# Institut Curie
## Laboratoire Physico-chimie Curie

**THESE DE DOCTORAT DE L'UNIVERSITE PIERRE ET MARIE CURIE**
**Ecole doctorale de Physique - ED389**

*Présentée par*:

M. Scott ATWELL

Pour obtenir le grade de

**DOCTEUR de l'UNIVERSITÉ PIERRE ET MARIE CURIE**

---

# Force et couple dans les pinces magnétiques: Paysage énergétique de la protéine hRad51 sur ADN double-brin

---

*Soutenue le 26 Septembre 2014 devant le jury composé de :*

| | |
|---|---|
| M. Giovanni CAPPELLO | *Directeur de thèse* |
| M. Gijs WUITE | *Rapporteur* |
| M. Marcello NOLLMANN | *Rapporteur* |
| M. Raphaël VOITURIEZ | *Examinateur* |
| Mme. Karen PERRONET | *Examinatrice* |

# Institut Curie
## Laboratoire Physico-chimie Curie

**THESE DE DOCTORAT DE L'UNIVERSITE PIERRE ET MARIE CURIE**
**Ecole doctorale de Physique - ED389**

*Présentée par*:

M. Scott ATWELL

Pour obtenir le grade de

**DOCTEUR de l'UNIVERSITÉ PIERRE ET MARIE CURIE**

---

# Force et couple dans les pinces magnétiques: Paysage énergétique de la protéine hRad51 sur ADN double-brin

---

*Soutenue le 26 Septembre 2014 devant le jury composé de :*

| | |
|---|---|
| M. Giovanni CAPPELLO | *Directeur de thèse* |
| M. Gijs WUITE | *Rapporteur* |
| M. Marcello NOLLMANN | *Rapporteur* |
| M. Raphaël VOITURIEZ | *Examinateur* |
| Mme. Karen PERRONET | *Examinatrice* |

# Thanks

I have so many people to thank for their help during my thesis that I am not sure where to start. First I would like thank Jean-Louis Viovy for giving me the opportunity to work within his unit, first by accepting as an intern and then by proposing and helping me to start a thesis. His input on my work has always been very valuable. The next person is of course my thesis director Giovanni Cappello. I thank him for his unending patience, his unwavering optimism and for always being there for me in spite of his having three young children to care for. I can also not forget Giulia Carzedda without whom I would have been lost in administrative paperwork on countless occasions.

Hideyuki Arata for training me in the use of magnetic tweezers. Ludovic Disseau for his significant contribution to my work, helping all along my thesis and always answering my questions even if I ended up asking the same questions several times. Remy Fert and Benoit Lemaire of the mechanical workshop for their input and help on the design and construction of the hybrid magnetic tweezers setup. Terrence Strick and Jordan Monnet of the institut Jacques Monod for their help in the fabrication of a new DNA construct. Daniel Migliozzi for his work during his internship. Axelle Renodon-Corniere and Masayuki Takahashi of the Universite de Nantes for providing the hRad51 proteins. Alicja and Andrzej Stasiak for their contribution with electron microscopy.

I would like to thank the entire Viovy team for being my colleagues and friends during my time there; In alphabetical order: Anais Ali-Cherif, Virginie Audonnet, Julien Autebert, Stefano Begolo, Nadege Bois, Nadia Bourouina, Jerome Champ, Benoit Coudert, Francois-Damien Delapierre, Morgan Delarue, Stephanie Descroix, Mohamed Diakite, Francesca Farina, Qihao He, Petra Juskova, Laurent Malaquin, Sandrine Misere, Reza Mohamadi, Sylvain Monnier, Fabien Montel, Guillaume Mottet, Iago Pereiro, Karla Perez-Toralla, Paolo Pierobon, Renaud Renault, Laure Saias, Sanae Tabnaoui, Velan Taniga, Bruno Teste, Ezgi Tulukcuoglu, Marine Verhusel, Maeva Vignes and Ayako Yamada

A special thanks to my friend Mathias Hottner and his wife Nina Hottner for their patient support and for being there when I most needed it. The same goes for my mother Gisele Atwell and my sister Alexandra Atwell. I also thank my friends Antoine Floride, Yannick Dechoux and David Lissmyr.

# Table of contents

# Introduction

In this thesis, we will be studying the mechano-chemical properties of hRad51-dsDNA nucleoprotein filaments using different types of magnetic tweezes setups. The hRad51 protein is a key actor in the homologous recombination process in humans. Its role in DNA repair qualifies it as a target in anti-cancer treatments. When in the presence of a DNA substrate, the hRad51 monomers self-assemble onto the DNA, forming the nucleoprotein filament, unwinding and stretching the DNA molecule in the process. This operation requires little to no energy as it does not require the hydrolysis of ATP.

This work is the continuation of the work accomplished by Judith Mine, Ludovic Disseau and Aurelie Dupont during their theses and Hideyuki Arata during his post-doctorate. Prior to starting the work on this thesis, there was to our knowledge no other study of the filament's response to torsion. We used magnetic tweezers for their ability to access simultaneously the torsion and extension of several single filaments. Our study focuses on the torsion to extension response of the filaments which changes depending on the nature of the cofactors present, specifically the bound nucleotide and the cations present.

This thesis is divided in four chapters. The first chapter focuses on general knowledge about the DNA molecule and on the homologous recombination process; biochemical studies of the hRad51 protein and the previous works in single molecules studies are presented. The second chapter presents the technical aspects of the magnetic tweezers and the main results one may obtain on naked dsDNA molecules. In the third chapter, we present our results on the filaments' torsion to extension response and we use a custom developed version of magnetic tweezers to measure the torques applied by the protein during its various transitions. We then attempt in the fourth chapter to draw the energy potentials of the protein using our results in correlation with existing literature and finally consider the steric effects for the previously unobserved structures of the filament.

# Chapter 1: Homologous recombination in humans

## A. Biological context

### A.I. Homologous recombination: role in the cell

Homologous recombination (HR) refers to the pairing and interaction of two DNA molecules of homologous sequences, usually to allow the exchange of information. Homologous recombination has many roles in the cell. First, it allows the accurate repair of missing information in the genome. This kind of repair is often required in the case of deleterious DNA lesions also called double-strand breaks (DSB). Secondly, HR plays an important role in DNA replication during the cell's S phase. It also promotes the pairing and information exchange between homologous chromosomes during meiosis. Finally, it is crucial for accurate chromosome segregation during meiosis and mitosis.

In summary, HR is needed for two important tasks: the preservation of genome integrity through the repair of DSB and the genomic diversity through allelic shuffling.

When studying the mechanics of homologous recombination, it is crucial to understand the DNA molecule. In this section, we will review the fundamentals of DNA structure, see how various DNA lesions may compromise genome integrity and how the cell solves this issue though HR. We will then review the main actors of HR and we will finish by the importance of studying HR for cancer research.

#### A.I.1. The DNA molecule

DNA stands for deoxyribonucleic acid. Discovered in 1869, it is now known to be the vector of heredity. The information it contains allows for the organization and activity of the cell. As a whole, this information is referred to as genome.

A DNA molecule is defined first by its sequence (primary structure), by what form it is in (secondary structure), and finally by what spatial conformation it adopts (tertiary structure). Here we will describe succinctly DNA's chemical structure and present the most common secondary structures. The only tertiary structure which will be of interest to us is the plectonem form which will be described later on.

##### Primary structure: nucleotide sequence

DNA is a linear polymer whose sequence of nucleotides codes information for the synthesis of proteins necessary to cell functioning. This sequence of nucleotides is the primary structure of DNA. Each unit is composed of a phosphorylated sugar (2-desoxyribose)

and one of four nitrogen bases (Adenine, Thymine, Guanine, Cytosine, noted respectively A,T,G,C) **[Figure 1]**.
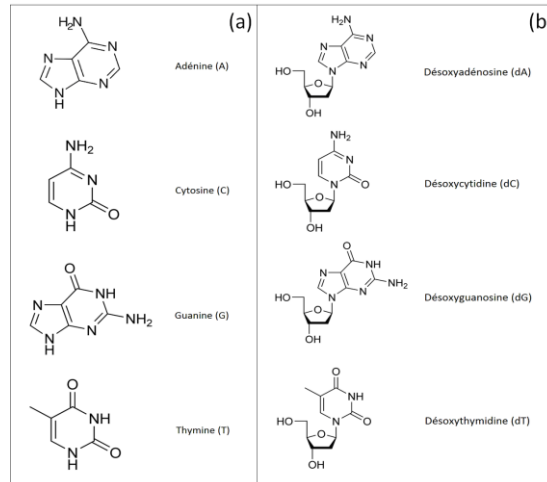


**Figure 1:** Chemical structure of DNA
(**a**) Chemical formula of the four nitrogen bases of DNA.
(**b**) Chemical structure of desoxyribonucleosides, the elementary bricks of DNA.

The desoxyribose phophaste sugars are linked to one another by phosphodiester bonds. Those bonds form the phosphate-desoxyribose backbone which carries the nitrogen bases **[Figure 2]**. They link the phosphate group attached to the 5' carbon of the desoxyribose sugar to the hydroxyl group attached to the 3' carbon of the next sugar. Thus the chain of nucleotides has a polarity, one end ending by a hydroxyl group attached to a 3' carbon and the other ending by a phosphate group attached to a 5' carbon. DNA sequences are conventionally read from 3' to 5'.
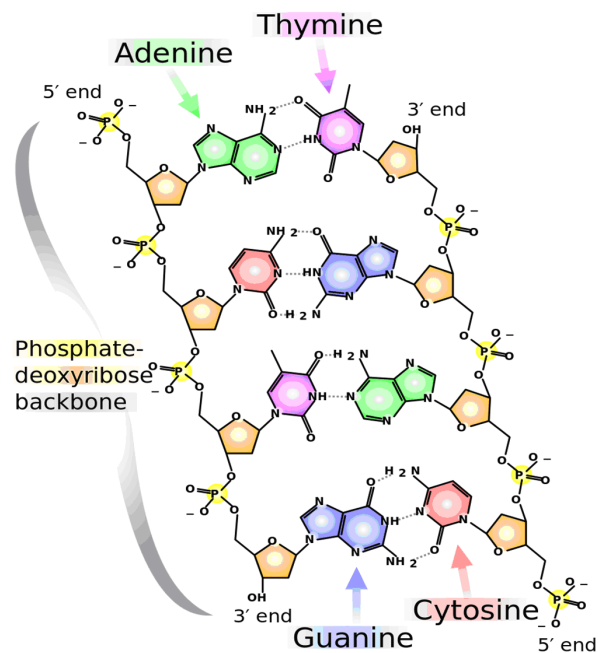


**Figure 2:** Chemical structure of DNA with the desoxyribonucleosides linked by phosphodiester bonds forming the phosphate-desoxyribose backbone. The complementary strands are linked by hydrogen bonds between nitrogen bases (A-T and G-C). Both strands are of opposite polarity.

Nitrogen bases are able to pair with one another through non-covalent bonds called hydrogen bonds. Those bonds are weak when compared to thermal energy and may be broken at high temperatures. The directionality of those bonds and the number of possible bonds for each nucleotide allows for specific pairing between nitrogen bases. Adenosine thus pairs preferentially with Thymine whereas Guanine pairs only with Cytosine. It is then said that A is complementary to T and G is complementary to C and vice versa. For any DNA sequence changing all nucleotides by their complements and changing the polarity direction results in the construction of the complementary sequence.

DNA replication is achieved by proteins called DNA polymerases. They synthesize new DNA strands by pairing the complementary nucleotides to a template sequence. This mechanism allows easy copying of the information of any DNA strand. A single-stranded DNA (ssDNA) is most commonly paired with its complementary sequence, thus forming a double-stranded DNA molecule (dsDNA) [Figure 2]. Therefore the information is present twice on the same molecule, offering a safeguard in case of DNA damage.

## Secondary structure: the B-DNA double helix

Using crystallographic studies by diffraction of X-rays on fibers of DNA, Watson and Crick propose in 1953 the right-handed double helix structure of dsDNA, referred to as B-DNA [Figure 3]. This form is considered to be the canonical state of any random DNA sequence *in vitro*. It contains two strands of opposite polarities and complementary sequences. Those strands are linked together through the hydrogen bonds of their complementary sequences. They twist around one another forming a right handed double helix. The nitrogen bases are oriented towards the inside of the structure.
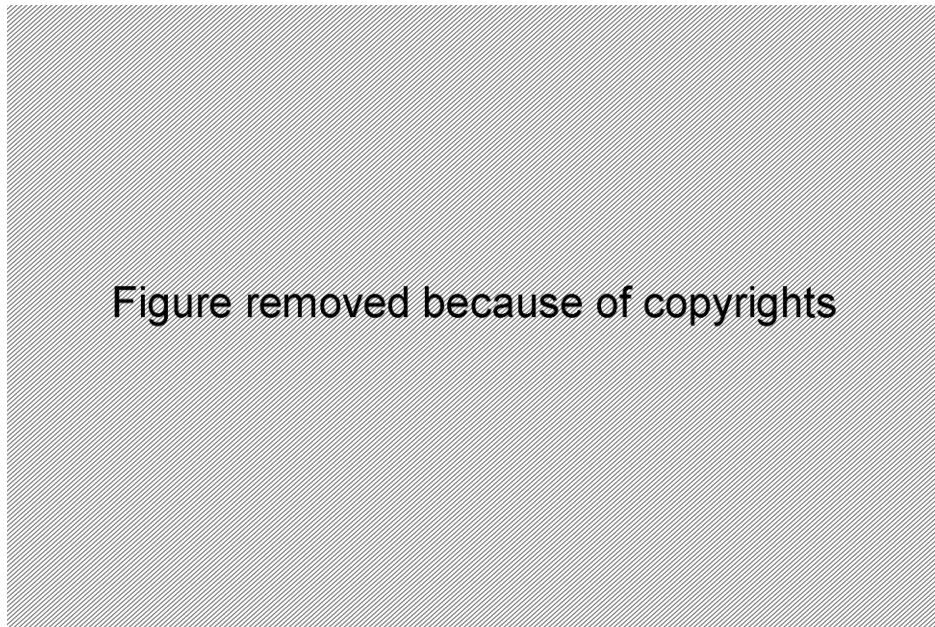


**Figure 3:** Extracted from [1]. Structural parameters of the double helix of B-DNA. Watson and Crick's double helix has around 10.5 base pairs per helical turn which amounts to a 34.3° rotation per base pair.

Watson and Crick's double helix has around 10.5 base pairs per helical turn which amounts to a rotation of 34.3° per base pair (twist angle). The helical pitch is of 35.7Å, the axial rise is then of 3.4Å. In normal physiological conditions, the helix diameter is around 20Å. However these values are strongly dependent locally on the sequence of the DNA and

on the immediate environment of the DNA molecule. Thus twelve different crystallographic studies show a twist angle between 24° and 51°, and axial rise values between 2.5Å and 4.4Å [2]–[4].

## Other secondary structures
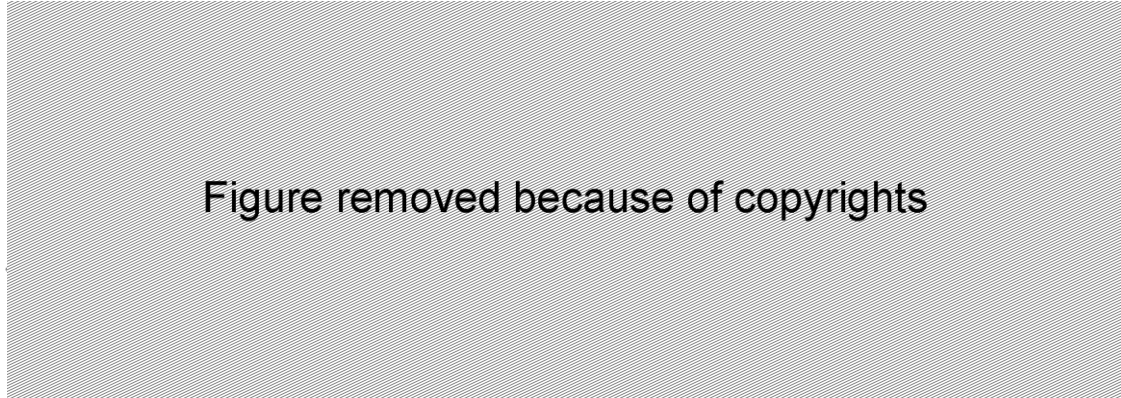


**Figure 4:** Adapted from [5]. On the left, representations of different secondary structures of DNA. On the right, simplified representations of the same structures, only the sugar backbone is seen. From left to right, those structures are A-DNA, B-DNA and Z-DNA.

Even though B-form is considered to be the canonical state of DNA, several other forms may be observed under specific conditions. We shall then present here a non exhaustive list of other secondary structures adopted by dsDNA. What follows is the description of four different secondary structures, two of them that are non-elongated, A-DNA and Z-DNA, and two others that are elongated, P-DNA and S-DNA.



**Figure 5:** Extracted from [6]. Average structural parameters of A-DNA, B-DNA and Z-DNA.

### A-DNA

Like B-DNA, A-DNA is a right handed double helix structure. It is observed *in vitro* in conditions of partial dehydration. It is presumed to exist in certain protein-DNA complexes or in the two strands of DNA-RNA during transcription [7]. A-DNA is slightly more compact than B-DNA with an axial rise of 2.9Å and 11 base pairs per helical turn. Yet the main differences between those two structures are the width and depth of the helix's major and minor grooves **[Figure 5]**.

### Z-DNA

Contrarily to the previously presented forms, Z-DNA is a left handed double helix structure. Short and very specific sequences of DNA are able to spontaneously take this form [8], [9], but for the vast majority of DNA molecules, this structure is accessible only through extensive underwinding of DNA [10]

### P-DNA

P-DNA (Pauling-DNA) has been modelized by Linus Pauling in 1953 [11]. This structure is heavily supercoiled, with only 2.62 base pairs per turn, and extended 2.7 times compared to B-DNA [12]. The bases are oriented towards the outside of the structure **[Figure 6]**. This secondary structure of DNA is observed in single DNA molecule manipulation experiments such as in magnetic tweezers setups which will be the main tool for the work presented in this thesis. It is achieved by strongly overwinding DNA thusly applying a strong positive torque on the molecules **[Figure 7]**. If the pulling force applied is not sufficient, then the DNA molecules adopting this form will also form plectonemes (scP standing for supercoiled Pauling DNA) which will be more extensively discussed later on.
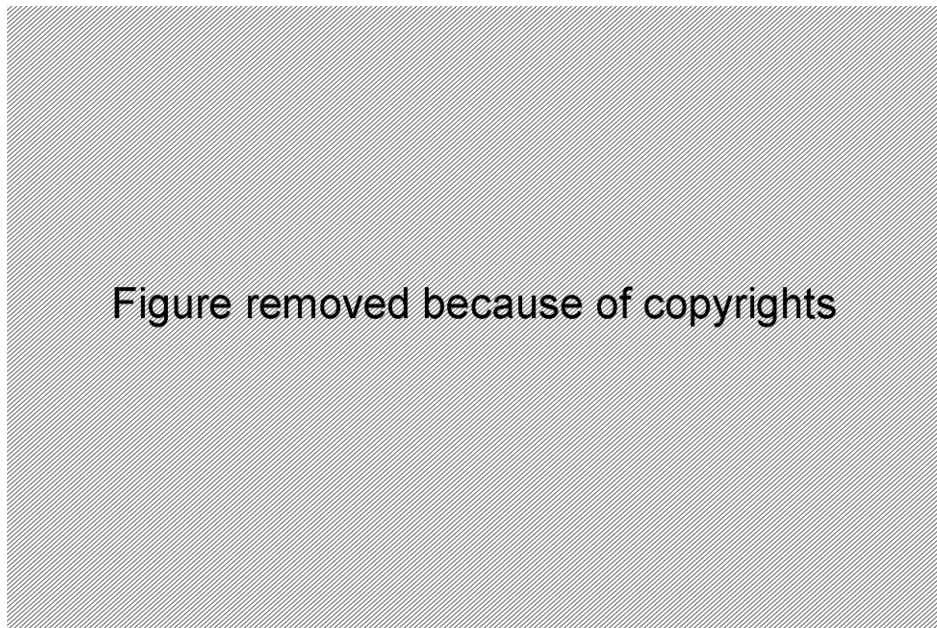


Figure removed because of copyrights

**Figure 6:** Adapted from [13].
(**a**) Representation of P-DNA.
(**b**) Representation of B-DNA (middle), S-DNA obtained by pulling on the 3' ends (left) and S-DNA obtained by pulling the 5' ends (right).

## S-DNA

S-DNA stands for stretched DNA. Anticipated as early as 1951 [14], the S-DNA structure has later on been proposed to explain the elongation observed when pulling on DNA molecules with high forces (F>65pN). Indeed, it was noticed that DNA molecules could reversibly go through a transition to a state extended up to 1.7 times compared to B-DNA. By numerically minimizing the energy of DNA molecules under stress, the S-DNA structure has been modelized [15], [16]. Stretched DNA molecules may be obtained by pulling on opposite strands of an unnicked dsDNA molecule, for example by pulling on the 3' ends or by pulling on the 5' ends. The exact structure of this form depends on which extremities are being pulled.

The existence of this structure has been for many years subject to controversy since the stretching observed could be explained by DNA denaturation (unpairing of the complementary nucleotides). Currently it is still impossible to observe these stretched forms of DNA in order to directly verify the existence of this structure. However some recent experiments tend to show the possibility of its existence. It has been shown, for short oligonucleotides (30 base pairs), that stretched DNA can withstand forces above 65pN before Watson-Crick ruptures [17]. Other experiments by the same group have been able to demonstrate a difference between DNA stretched by the 3'3' and 5'5' methods, showing that DNA molecules stretched through 3'3 pulling had a higher rupture force then the ones stretched through 5'5' pulling [18]. Furthermore, experiments of stretching long λ-DNA molecules have shown different mechanical behavior for both pulling methods [19]. These last results seem to support the existence of two different structures. Yet other studies on λ-DNA detecting bases not involved in Watson-Crick hydrogen bonds seem to favor the DNA melting hypothesis [20]. It has been argued however that in these experiments, single-strand nicks may occur, thus facilitating strand unpairing.

Figure removed because of copyrights

**Figure 7:** Adapted from [21]. DNA phase diagram in the torque-force space. The ScP phase refers to supercoiled P-DNA forming plectonemes.

## A.I.2. DNA lesions

Several tens of thousands DNA lesions happen in a single human cell each day. Those lesions may block genome replication and transcription or cause mutations that may affect the cell's viability. Multiple factors may cause DNA lesions such as replication induced mismatches, topoisomerase activity, hydrolytic reactions, non-enzymatic methylations, or chemical agents such as reactive oxygenated compounds. Ultraviolet sunlight is one the most potent lesion inducing factor, responsible for thousands of lesions per exposed cell and per day [22]. There are two types of DNA lesions: single-stranded and double-stranded.

### Single-stranded lesions

Single-stranded lesions are by far the most frequent. They occur when one of the strands is damaged while the complementary sequence remains intact. In this category are found single-strand nicks, oxidized or missing nitrogen bases and DNA mismatches.
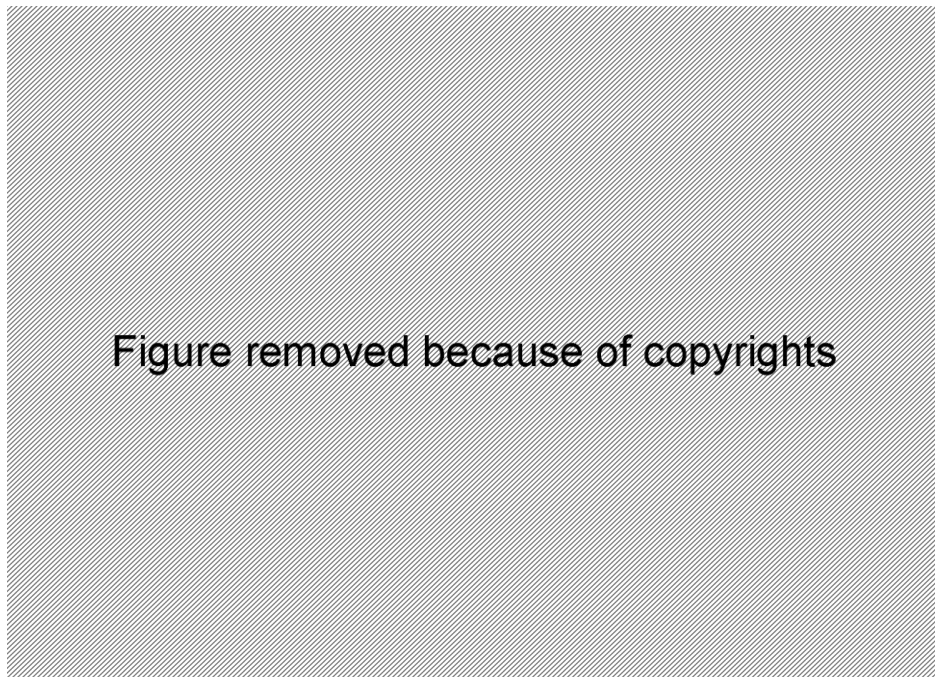


**Figure 8:** Extracted from[23].Generation of single-strand breaks (SSGs) and double-strand breaks (DSBs).

(**a**) DSBs may occur through various means, from left to right: ionizing radiations; DNA polymerase encountering a single-strand nick in the leading-strand template; DNA polymerase encountering a single-strand nick in the lagging-strand template; and replication of a linear chromosome in the absence of a mechanism to complete synthesis of the lagging strand.

(**b**) Single-strand gaps (SSGs) may occur when a DNA polymerase encounters an impediment in the leading strand template, but synthesis ensues further downstream, or when the polymerase encounters an impediment in the lagging-strand template. Nicking an SSG will convert it in a DSB.

In the case of single-strand nicks, one of the phosphodiester bonds of the DNA backbone is broken. It is noteworthy at this point to notice that those are single covalent bonds which allow free rotation around their axis. Thus it is impossible to accumulate torsion on a single-stranded DNA (ssDNA) or in a double-stranded DNA (dsDNA) presenting a single-strand nick anywhere in its sequence (commonly referred to as a nicked dsDNA molecule).

Repair of a single-strand break is easily achieved, either by the reparation of the sugar backbone in the case of single-strand nicks, or by using the complementary sequence as template to replace the damaged one. Unchecked, a single-strand break may lead to the apparition of a much more serious double-strand break, either through a nick occurring in the already damaged regions or through replication of the damaged sequence **[Figure 8]**.

## Double-stranded lesions

Double-stranded lesions affect both strands of DNA at the same place in the sequence. The most serious case is the deleterious double-strand break because the information necessary for repair is missing. While much less frequent, these double-strand breaks (DSBs) are the most problematic because they are difficult to repair, extremely toxic to the cell and may cause mutations of the genome [24].

Means to repair these DSBs can be classified in non-homologous and homologous processes. The non-homologous processes are the non-homologous end joining (NHEJ) and the single-strand annealing (SSA) pathways. The homologous processes are the double-strand break repair (DBSR), the synthesis dependent strand annealing (SDSA) and the break induced repair (BIR).

Figure removed because of copyrights

**Figure 9:** Extracted from[25]. Double-strand break repair models.

## DSB non-homologous repair

Non-homologous repair are relatively simple processes in which repair is achieved through loss of information in the sequence. NHEJ is the dominant pathway of non-homologous repair (NHR). It involves the rejoining of blunt ends or ends with short overhangs after recognition of the double-strand break **[Figure 9; F]**. This mechanism is rapid and efficient but may induce genome mutations; it is used mainly during the G1 phase of the cell just before DNA replication [26]–[28].

The SSA pathway is used in the case of breaks in regions of DNA composed of repetitive sequences such as telomeres [29]. The repeat sequence on both sides of the break is used as a welding point; all information between the two sequences is lost **[Figure 9; E]**. In this process, the extremities are digested in order to reveal the repeat sequences. Those sequences then anneal, superfluous extremities are digested and the DNA backbone is ligated [30].

## DSB homologous repair

Homologous repair allows for high fidelity in the replacement of the lost sequence of DNA. It uses a homologous sequence, generally the sister chromatid during the S/G2 phases [31], [32], as a template for the synthesis of the deleted DNA. Rarely, homologous recombination may occur between homologous chromosomes during the G1 phase, though the NHEJ pathway tends to be preferred in this case.

Models of homologous double-strand repair all have three phases. First comes a pre-synaptic phase during which the broken DNA molecules are prepared for recombination **[Figure 9; A]**. The broken ends are resected to leave short 3'-protruding overhangs. Recombinase proteins assemble on these overhangs to form the nucleoprotein filament which is then involved in the homology search. Once homology has been found comes the synaptic phase in which the nucleoprotein filament invades the homologous sequence forming a D-loop (displacement loop) structure. Last is the post-synaptic phase involving the propagation of the synapse, DNA synthesis using the homologous sequence as template, and the resolution of the synapse. In the end the recombined sequences are separated. It is in this last phase that the different models diverge.

In the case of the DBSR model **[Figure 9; B]**, once the first broken end has been captured, the second end is also captured, forming a structure known as double Holliday junction. The resolution of this structure may lead to non-crossover or crossover products [33].

In the SDSA model **[Figure 9; C]**, the 3' end of the invading strand acts as a primer for DNA replication by a DNA polymerase thus lengthening the D-loop. After replication the invading strand is ejected and captured by the second end of the break. This process can produce only non-crossover products [34], [35].

Recent studies imply that during mitosis only SDSA occurs, whereas during meiosis there are two waves of homologous recombination. The first wave uses exclusively SDSA and the second wave uses DBSR, in this case it seems DBSR gives rises mainly, if not exclusively, to crossover products [36], [37].

Last is the BIR model **[Figure 9; D]** which can occur when the second end of the break is absent. The D-loop intermediate assembles into a replication fork and the entire chromosome arm is copied [38].

### A.I.3. Importance of HR in cancer

Traditional anti-cancer therapies frequently use ionizing radiations or other agents to induce double-strand breaks (DSB) or inter-strand crosslinks (ISC). The objective is to damage the cancerous cell beyond repair to trigger apoptosis or necrosis. The ability of tumors to repair such damage is therefore an important factor in their resistance to those therapies. It has been suggested that the therapies' efficiency could be improved by inhibiting the damage response and repair pathways of the cancerous cell [39], [40]. The targeted pathways are mainly the homologous recombination (HR) and the non-homologous end joining (NHEJ) pathways that are involved in the repair of double-strand breaks.

The key protein of HR in humans, hRad51, is often over-expressed in tumors [41]–[43]. In fact, the expressed quantity of the hRad51 protein in a cancerous cell is 2 to 7 times higher than in a normal cell [43]. As this over-expression of hRad51 may contribute to the chemo- and radio-resistance of human cancers, it could be an important target in anti-cancer therapies. Some recent studies have therefore focused on the identification and study of molecules specifically inhibiting hRad51 or other proteins implicated in the homologous recombination process [44]–[49].

## A.II. The hRad51 protein

Homologous recombination is a complex mechanism involving many partners. Initially the genes of the *RAD52* group (RAD50, RAD51, RAD52, RAD54, RAD55, RAD57, RAD59, MRE11 and XRS2) were identified in yeast for their implication in the cell's X-ray sensitivity [50]. Later on, the homologues of RAD50, RAD51, RAD52, RAD54 and MRE11 were identified in other eukaryotes such as mice and humans [51]–[54].

The proteins of the *RAD52* group form a multi-protein complex called recombinosome [55]. Co-immunoprecipitation has shown that these proteins physically interact with one another [55]–[61]. Furthermore, in response to DNA damage (often voluntarily induced by ionizing radiations in experiments), several proteins of this group tend to co-localize in sub-nuclear structures called foci [32], [62]–[68]. In those foci is formed a joint molecule between the broken DNA and the homologous sequence used for the repair of the DSB. Biochemical analyses show a cooperation between the proteins of the *RAD52* group for the formation of this intermediate [58], [60], [61].

This thesis is centered on the study of the human protein Rad51which plays a key role in homologous recombination. In this section we will introduce the recombinase family that hRad51 is a part of. We will then review what role hRad51 plays in the cell. Finally, we will describe the mechanisms of homologous recombination and what partners are involved.

### A.II.1. The Rad51/RecA recombinase family

Homologous recombination is a highly conserved mechanism throughout the species. The main actors of this process are the proteins of the RecA/Rad51 recombinase family which are responsible for the formation of the pre-synaptic nucleoprotein filament. They all have very similar sequences and structures. Both prokaryotic RecA and eukaryotic Rad51 have two

domains: an ATPase domain (in yellow on **[Figure 10]**) and a domain for DNA binding. It is the former which is especially well conserved.
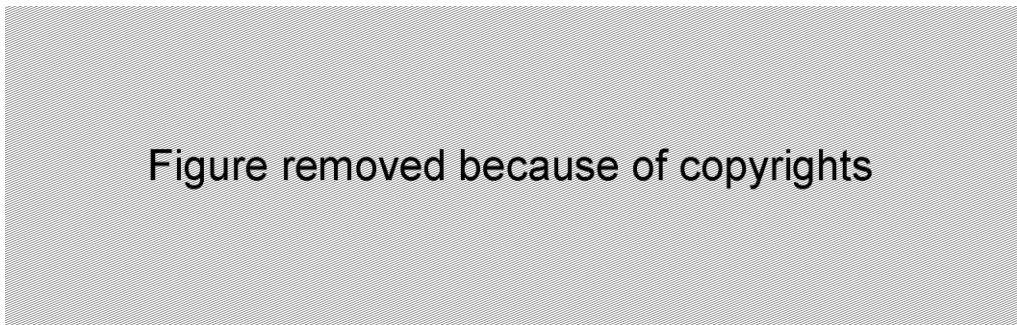


**Figure 10:** Extracted from [69]. Organization of the sequences of proteins of the recombinase family. From top to bottom, the Rad51 proteins from *Pyrococcus furiosus* (PfRad51), *Homo sapiens* (HsRad51), *Saccharomyces cerevisiae* (ScRad51) and the RecA protein from *Escherichia coli* (EcRecA). Regions of homology among Rad51-NDs and Rad51-ADs and RecA-AD are colored red and yellow, respectively. Walker A and B motifs are in green. Non homologous regions are in white or blue.

The first protein identified was RecA in *E. coli* in the 1960s [70]. It was first noticed for the effect its mutations would have on recombination events in the cell. It was then shown to play a central role in homologous recombination. The Rad51 proteins, structural homologues of RecA, were first identified in yeast in the 1990s [51], [71]–[76]. They were then found in other eukaryote organisms such as lily [77], Xenopus laevis [78], mice [51], [79] and humans [51], [80]. In fact, Rad51 homologues have been identified in every eukaryotic organism studied and other homologues have been identified in most of living organisms.

One can find many similarities between the prokaryotic and the eukaryotic process, or between the homologous proteins such as RecA, and the Rad51 proteins. However, one can find just as many differences, studies characterizing their behaviors find that those are significantly different from one another [81]. It is important to notice that there are great behavioral differences between the human protein hRad51 and its much more studied yeast homologue ScRad51. Therefore anyone wishing to compare those two proteins, as it is often done in literature, should tread carefully.

The human protein hRad51 will be the focus of this thesis; comparison of hRad51 with other homologous proteins will be kept to a minimum.

## A.II.2. The role of the hRad51 protein

Biochemical studies have shown that the human RAD51 gene codes for a 36.966 kDa protein containing 339 amino acids, called hRad51.

### hRad51 *in vivo*

Within the cell, the hRad51 protein is located mainly in the nucleus although it has recently been shown to be also present in human mitochondria [82]. Its involvement in the DNA damage response has been ascertained by the fact that it is recruited in response to various DNA damaging treatments [65], [83], [84]. Moreover mutant cell lines deficient in the

formation of the Rad51-dependent foci induced by DNA lesions are more sensitive to DNA damaging agents and are genomically instable [85]–[89].

It is also required during cell proliferation as is proven by the embryonic mortality induced in mice by the targeted disruption of the RAD51 gene [90], [91]. A similar phenomenon happens when it is expressed in chicken B-lymphocytes, suppression of the gene leads to an accumulation of cells in the G2/M phase and induces cell death [31].

Recruitment of hRad51 occurs mainly during the S phase from foci within the nucleus. hRad51 foci associate preferentially with post-replicative chromatin [92]. The hRad51 foci may be found in non irradiated cells in the S phase, they are thought to identify the sites where broken or stalled replication forks are being repaired [66], [93]. Those foci in non irradiated cells and those induced by radiation seem to be distinct from one another since BRCA2 is not required for the formation of the foci in the first case [94].

### hRad51 *in vitro*

*In vitro* hRad51 is observed in the form of oligomeric rings [95], [96]. It has been shown that hRad51 plays a vital role in homologous recombination, its main function is to allow homologous pairing and strand exchange [97]. It cooperatively assembles on the single-stranded extremities of dsDNA molecules [98]. It will do so in the presence or absence of a cofactor nucleotide [81]. It can by itself induce homologous pairing and strand exchange but those exchanges only occur on small portions of DNA in the absence of partners (inferior to 3000bp). The presence of cofactors such as a cation and a nucleotide are necessary for such an exchange [99]–[102]. Strand exchange may be achieved by hRad51 alone in the presence of ATP and $Mg^{2+}$, but only at a temperature of 37ºC. At 30ºC, it requires the presence of a partner such as hRad54 [97].

## A.II.3. Mechanism of homologous recombination

Many partners are involved in homologous recombination. Immunofluorescence experiments show that hRad51 co-localizes in nuclear foci with other proteins of the *RAD52* group such as hRad52 [32], [62], [63], [65], hRad54 [63]–[65], RPA [65], [66], and the tumor suppressors BRCA1 [67] and BRCA2 [65], [68]. Here we will try to describe as simply as possible the mechanism of the homologous recombination process. It can be separated into three separate stages: the pre-synaptic phase, the synaptic phase and the post-synaptic phase [Figure 11]. The pre-synaptic phase will be described in much more detail than the others because it involves the formation of the nucleoprotein filament which is of interest to us.

### The pre-synaptic phase

During the pre-synaptic phase, the break site of the DNA molecule is prepared by a combined action of enzymes which will detect the break and resect the ends of the DNA molecule to leave 3' single-stranded overhangs. This role is played by the Mre11 complex, composed of the Mre11, Rad50 and NBS1 proteins [103]. This complex has an affinity for DNA ends, nuclease activities and can migrate along DNA. It also allows both ends of the DNA break to stay close to one another in order to be easily reattached later on.

The single-stranded overhangs are then covered with the RPA protein (replication protein A). RPA has a high affinity for single-stranded DNA. It has been shown to interact with the hRad51 protein and to mediate the formation of the pre-synaptic filament [104]. Its presence stimulates the formation of the joint molecules [100], [101] and the strand invasion [98]. It is thought that RPA allows the loading of hRad51 on the single-stranded DNA by dislocating any proteins present and removing secondary structures of the ssDNA. However, the very strong affinity of RPA for ssDNA also prevents the loading of hRad51 which has a lower affinity.

Figure removed because of copyrights

**Figure 11:** Extracted from [103]. Schematic representation of DSB-initiated homologous recombination between DNA molecules. Duplex DNAs are indicated by the ladders with the rungs representing base pairs. Pre-synapsis spans from stages **A** to **C**. Synapsis spans from **D** to **E**. Post-synapsis spans from stages **E** to **G**.

During the pre-synaptic phase, the break site of the DNA molecule is prepared by a combined action of enzymes which will detect the break and resect the ends of the DNA molecule to leave 3' single-stranded overhangs. This role is played by the Mre11 complex, composed of the Mre11, Rad50 and NBS1 proteins [103]. This complex has an affinity for DNA ends, nuclease activities and can migrate along DNA. It also allows both ends of the DNA break to stay close to one another in order to be easily reattached later on.

The single-stranded overhangs are then covered with the RPA protein (replication protein A). RPA has a high affinity for single-stranded DNA. It has been shown to interact with the hRad51 protein and to mediate the formation of the pre-synaptic filament [104]. Its presence stimulates the formation of the joint molecules [100], [101] and the strand invasion [98]. It is thought that RPA allows the loading of hRad51 on the single-stranded DNA by dislocating any proteins present and removing secondary structures of the ssDNA. However, the very strong affinity of RPA for ssDNA also prevents the loading of hRad51 which has a lower affinity.

The loading of the hRad51 proteins therefore requires the action of several other proteins called recombination mediators. The main role of those mediators is to negotiate between the positive and negative effects of RPA on hRad51 assembly. Among those mediators are the Rad51 paralogs (Rad51B, Rad51C, Rad51D, XRCC2 and XRCC3), BRCA2 and the hRad52 protein. BRCA2 is considered to be the main mediator of hRad51. Part of its role is to target hRad51 to ssDNA and to prevent nucleation on dsDNA. It is also able to stabilize the nucleoprotein filament by downregulating hRad51 ATP hydrolysis, thus stabilizing the ATP-bound form [25]. The importance of the nucleotide state within the filament will be discussed in detail later on.

The hRad51 proteins cooperatively assemble on the single-stranded DNA to form a right handed helix called the nucleoprotein filament [98]. This filament is central in the homologous recombination as it will be involved in the search for homology and the formation of the joint molecule. The last protein involved in the pre-synaptic phase is hRad54 which at this point is used mainly to stabilize the nucleoprotein filament [105]. The hRad54 protein physically interacts with hRad51 in multiple stages of the homologous recombination process [106]. The pre-synaptic phase ends when the homologous sequence has been found.

## The synaptic phase

The synaptic phase is the formation of the joint molecule composed of the pre-synaptic filament and the homologous duplex DNA molecule. The nucleoprotein invades the homologous dsDNA and forms the intermediate form called D-loop **[Figure 12]**. This step is commonly referred to as strand invasion. Here again, the hRad54 protein plays a part using its chromatin-remodeling abilities that are stimulated by the nucleoprotein filament [107]. It is able to displace nucleosomes in order to facilitate access to the chromatin.

## The post-synaptic phase

The post-synaptic phase differs from one model to another as seen previously. In the DBSR model, the second end is captured to form a double Holliday junction. This junction then migrates with the help of the hRad54 protein to allow DNA synthesis for the repair of the deleted information. Resolution of this structure requires the intervention of proteins which we will not discuss here. In the SDSA model, the invading strand acts as a primer. The D-loop is lengthened as DNA is synthesized. The invading strand is eventually displaced to be annealed with the second end of the break. Here too, hRad54 is thought to play a role displacing the hRad51 protein since disassembly of the latter is slow and often incomplete.

Figure removed because of copyrights

**Figure 12:** Extracted from [108]. Mechanism of homologous recombination in humans.

# B. Biochemistry of hRad51

## B.I. Catalytic activity of hRad51

### B.I.1. Definition of catalytic activity

A large portion of the primary structure of the hRad51 protein is dedicated to its ATPase activity. It is paradoxical that this activity does not seem to have a strong impact on the function of the protein. In fact, the role of ATP hydrolysis for hRad51 in the homologous recombination process is poorly understood. In this section we will review what is known on the hRad51 ATPase activity and on its role in homologous recombination.

hRad51 is an ATPase protein, which means that it hydrolyses ATP molecules in an ADP+Pi (inorganic phosphate) form. This reaction produces mechanical work which can be used by the protein to perform its function. The ATP hydrolysis reaction is as follows:

$$hRad51 + ATP \underset{k_r}{\overset{k_f}{\longleftrightarrow}} hRad51 \oplus ATP \xrightarrow{k_{cat}} hRad51 + ADP + P_i$$
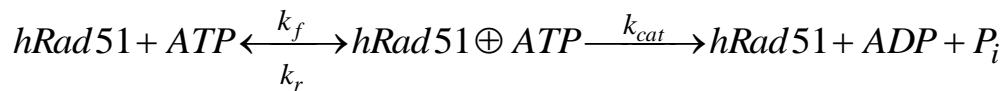
Where $k_f$ and $k_r$ (s$^{-1}$) represent the forward and reverse binding rates of the hRad51 enzyme and the ATP substrate. Here $k_{cat}$ is the reaction rate constant for ATP hydrolysis by hRad51, it is called the catalytic constant. It represents the number of catalytic cycles per second that the protein is capable of in the case of saturating ATP. The higher the $k_{cat}$ value is, the quicker the ATP to ADP+P$_i$ conversion is.

To describe ATPase activity, the catalytic constant alone is not enough. To describe enzymatic activities, the Michealis-Menten kinetics is most commonly used model. In this model, the reaction rate is described through the following equation:

$$V_i = \frac{V_{\max} \cdot [ATP]}{K_m + [ATP]}$$

Where $V_i$ (mol.s$^{-1}$) is the initial reaction rate for a given ATP concentration [ATP]. $V_{max}$ is the maximum initial reaction rate measured for a saturating ATP concentration. It is linked to the reaction constant $k_{cat}$ through the following relation:

$$V_{\max} = k_{cat} \cdot [hRad51]$$

$K_m$ is called the Michealis constant. It represents the concentration of substrate (here ATP) at which the initial reaction rate $V_i$ is half of the maximum rate $V_{max}$ which translates how much ATP in solution is required for the ATPase activity of the protein to be efficient. As such the value of this $K_m$ constant is inversely related to the protein's affinity for the ATP substrate; a high $K_m$ value indicates a low affinity for the substrate and a low value indicates a high affinity. It can be obtained through the following equation:

$$K_m = \frac{[hRad51] \cdot [ATP]}{[hRad51 \oplus ATP]} = \frac{k_r + k_{cat}}{k_f}$$

The full description of the catalytic efficiency is generally determined by the ratio $k_{cat}/K_m$. which is translates how fast ATP is hydrolyzed once it is bound multiplied by the protein's affinity for ATP. The higher this ratio, the more efficient is the ATP to ADP+$P_i$ conversion.

## B.I.2. Effect of the DNA substrate on ATPase activity

Studies show that the catalytic activity of hRad51 is dependent on the DNA substrate present. Thus the ATP turnover speed is much greater in the presence of ssDNA than in any other cases, whereas they are 3 to 5 times inferior when respectively dsDNA is present and no DNA is present. The ATP turnover speed in the presence of 5µM of hRad51 and 0.2mM of ATP were measured as follows [100]:

- In the presence of ssDNA: 0,16 ATP/min
- In the presence of dsDNA: 0,05 ATP/min
- Without DNA present: 0,03 ATP/min

hRad51 shows no ATP hydrolysis cooperativity [109] and variation of pH (between 6.2 and 8.2) seems to have no effect on its activity. It is to be noted though that a high concentration of salt (1.5M) seems to enhance it in the case of the absence of DNA [110]. A summary of hRad51 ATPase data can be found in [**Figure 13**].

Figure removed because of copyrights

**Figure 13:** Extracted from [110]. hRad51 ATPase data. RFI indicates a circular overwound dsDNA molecule and RFIII refers to a linearized dsDNA substrate.

The protein's affinity for ATP is greatly influenced by the presence of a DNA substrate as can be seen by the evolution of the $K_m$ constant for different DNA substrates. Indeed, the presence of DNA seems to increase the affinity by a factor 4. The nature of the DNA substrate present (ssDNA, circular or linear dsDNA) makes little to no difference. It does however affect the catalytic rate $k_{cat}$ which is much higher for ssDNA than for any other substrate (a factor of 2 to 3). The rates for dsDNA are similar, regardless of the state of the dsDNA (linear or circular), with a slight preference for circular dsDNA. The absence of DNA yields a catalytic rate close to the one in the presence of linear dsDNA.

In the end, catalytic efficiency is very low in the absence of a DNA substrate, moderate in the presence of dsDNA and high in the presence of ssDNA. Also, a high concentration of salt will result in very high catalytic efficiency in the absence of DNA. This

is a result of the catalytic rate increasing to a level comparable than with ssDNA, combined with an increase in ATP affinity.

### Comparison with RecA

If compared to its prokaryotic homolog RecA, hRad51 has a catalytic activity that is one to two orders of magnitude inferior to RecA in the presence of a DNA substrate. However, its activity in the absence of DNA is four times higher than its homolog. It also seems to have affinity for ATP that is equal or higher than that of RecA.

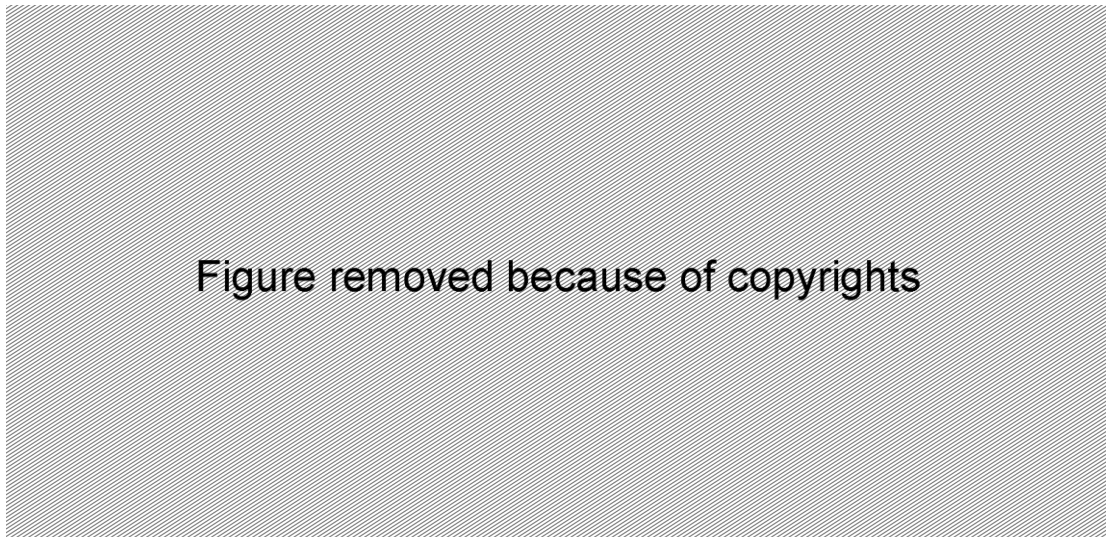## B.I.3. Effect of the cation cofactor

### Effect of magnesium concentration



Figure removed because of copyrights

**Figure 14:** Extracted from [109]. Effect of the $Mg^{2+}$ concentration and ATP concentration on the hRad51 ATPase activity in presence of (**A**) circular ssDNA or (**B**) linearized dsDNA. Measures are taken in the presence of 1.5μM hRad51 and 6μM of DNA substrate.

The hRad51 protein's ATPase activity is optimum for a $Mg^{2+}$ concentration for hRad51 between 0.08 and 0.12mM [**Figure 14**]. This optimum concentration is close to the 0.5mM of free magnesium ions typically found in a cell. This behavior suggests a non competitive inhibition of ATP hydrolysis by magnesium ions. This indicates that the nucleotides and the cations do not bind to the same sites on the protein but require compulsory ordered binding mechanisms in order to complete the catalytic cycle. Indeed, it seems that both the release of the $Mg^{2+}$ cation and the presence of exogenous ATP in solution are required for the release of ADP from the nucleoprotein filament [109].

The affinity of hRad51 for nucleotides is also affected by the magnesium concentration. High concentrations of $Mg^{2+}$ seem to enhance the affinity for ADP while the affinity for ATP seems unaffected [**Figure 15**]. ATP hydrolysis evolves accordingly diminishing as the percentage of bound ADP increases. This is true on both single and double-stranded DNA substrates. The effect of the magnesium concentration seems to be intrinsic to the protein, not affecting its ability to bind DNA nor the stability of the nucleoprotein filament.

Figure removed because of copyrights

**Figure 15:** Extracted from [109]. Effect of the $Mg^{2+}$ concentration on the binding of a nucleotide by hRad51 and its ATPase activity in presence of (**A**) circular ssDNA or (**B**) linearized dsDNA. Measures on ATPase activity (▲) are taken in presence of 2μM hRad51, 300μM ATP and 6μM DNA substrate. Measures on nucleotide binding, ATP-γS (○) or ADP (□), are taken in presence of 0.5μM hRad51 and 2μM DNA substrate.

## Effect of calcium cations

The calcium cation slows down considerably ATP hydrolysis within the nucleoprotein filament, even with the simultaneous presence of magnesium in solution **[Figure 16]**. Since ADP to ATP turnover is not inhibited by the presence of calcium, the overall effect is to have an exclusively ATP-bound nucleoprotein filament if exogenous ATP is present. In contrast, in the presence of $Mg^{2+}$, hRad51-ssDNA-ATP nucleoprotein filaments rapidly convert to an inactive hRad51-ssDNA-ADP form. This conversion is a result of a fast ATP hydrolysis and a slow ADP dissociation [111].

Figure removed because of copyrights

**Figure 16:** Extracted from [111]. The calcium prohibits the conversion of the hRad51/ssDNA/ATP filament into a hRad51/ssDNA/ADP filament by inhibiting ATP hydrolysis.
(**a**) Graphic representation of three independent experiments showing the evolution of the percentage of ADP molecules present in the hRad51/ssDNA/ATP filaments.
(**b**) Graphic representation of the evolution of ATP hydrolysis.

This effect of the calcium cation is specific to the human Rad51 protein. It does not exist for the yeast homolog ScRad51, where it neither slows down ATP hydrolysis nor does it enhance strand exchange activity. The slowing down of ATP hydrolysis is true for the

prokaryotic homolog RecA, but the presence of calcium does not improve strand exchange efficiency [112].

# B.I.4. Role of ATPase activity

The exact role of ATP hydrolysis in homologous recombination is an open question. Especially if one notices that hRad51 is able to accomplish all three steps of HR without hydrolyzing ATP such as it has been demonstrated through the use of mutant proteins. We do know however that ATP hydrolysis is required prior to protein dissociation

## The K133A and K133R hRad51 mutants

The proteins hRad51 K133A and K133R are mutants in which the lysine residue situated in the Walker A motif is substituted respectively with an alanine or an arginine. Studies of these mutants show that both are able to bind DNA but their ability to hydrolyze ATP is strongly impaired.

The K133R mutant retains the ability to bind ATP but not to hydrolyze it, whereas the K133A mutant has lost the ability to bind ATP [113]–[115]. The binding of the K133R mutant on DNA seems to be less efficient than the wild type and thus its assembly is much slower. *In vitro* studies demonstrate that the hRad51-K133R protein is capable of strand exchange and that its activity is superior to the wild type protein's. The hRad51-K133A mutant is compromised in this aspect [110].

From this we can deduce that the binding of ATP is crucial to strand exchange but ATP hydrolysis is not. In fact, it would seem that ATP hydrolysis is a hindrance to the process which would normally be regulated by mediator proteins such as BRCA2. The same is true for DNA unwinding and homologous pairing [113]. Experiments conducted *in vivo* confirmed these observations[116], [117].

## Hydrolysis and protein dissociation

Hydrolysis has been shown to correlate with the dissociation of hRad51 from ssDNA [113]. However, even though correlated, ATP hydrolysis does not necessarily induce hRad51 dissociation from DNA [118], [119]. In fact, all data suggest that ATP hydrolysis is a necessary but not sufficient condition for protein dissociation. Therefore hydrolysis and dissociation are correlated by the fact that the former always occurs prior to the latter.

## Effects of ATP hydrolysis on strand exchange

How ATP hydrolysis affects strand exchange efficiency is ambiguous. On one hand it hinders it by destabilizing the nucleoprotein filament on ssDNA and on the other it helps discriminate during the homology search by increasing the intolerance for heterology [120]. Attempting to elucidate the role of ATP hydrolysis in HR is one of the main goals of this thesis' work.

# B.II. Nucleotide binding and affinity for DNA

## B.II.1. ATP and ADP

The presence of ADP in solution inhibits the binding of ATP by hRad51 in the presence of ssDNA. For concentrations of ADP inferior to 50μM, inhibition is strictly competitive, suggesting that ADP and ATP bind to the same site of the protein. However at high ADP concentrations (>100μM), inhibition is no longer strictly competitive, suggesting that in these conditions ADP binds multiples sites of the protein in non specific modes [121].

Since the presence of a nucleotide does not affect the protein association rate but that it does affect its affinity for the DNA substrate, this suggests that the nucleotide affects directly the binding of the monomers to DNA. As such the nucleotide binding site is most probably very close to the DNA binding site.

## B.II.2. ATP-γS

Protein binding to ssDNA in the presence of ATP-γS is less efficient than with ADP or ATP [122]. However hRad51 completely and rapidly saturates with ATP-γS with great affinity (Kd ~ 3-5μM) regardless of the nature of the DNA substrate present [121]. Thus the ATP binding is probably not a limiting step in the formation of nucleoprotein filaments.

## B.II.3. Filaments in absence of nucleotides

It has been shown that the hRad51 protein will cooperatively assemble to form a nucleoprotein filament on ssDNA regardless of the presence or the absence of a cofactor nucleotide [81]. Their ability to bind to ssDNA substrates seems to be almost unaffected by the presence of ATP, ADP or none of the two [123]. In reality, the presence of a nucleotide cofactor actually reduces the protein intrinsic affinity for ssDNA but compensates this loss by increasing the cooperativity of self-assembling [122].

In the end, there is a slight reduction of the hRad51's overall affinity for ssDNA in the presence of a nucleotide [81], [124]. Filaments in the absence of nucleotides on ssDNA are subject to rapid protein dissociation.

# B.III. Strand exchange activity of hRad51

In order to form an active nucleoprotein filament, the hRad51 protein requires the presence of a nucleotide and of bivalent cation in solution. The nature and concentration of these cofactors will determine the behavior of the filament, affecting its efficiency in conducting successful strand exchanges. Strand exchange assays are often used as a measure of how well hRad51 operates in different conditions. Schematic examples of what are strand exchange experiments are represented in [**Figure 17**]. The principle is to put two homologous DNA substrates in presence of the hRad51 and measure the percentage of strand exchange between those sequences.

**Figure 17:** Extracted from [125]. Schematic examples of homologous pairing and strand exchange experiments involving RecA.
 (**a**) Formation of a joint molecule (D-loop).
 (**b**) Three-strand exchange experiment.
 (**c**) Four-strand exchange experiment.

## B.III.1. Effect of the cation cofactor on strand exchange

The most common bivalent ions found in the cell are the magnesium ($Mg^{2+}$) and the calcium ($Ca^{2+}$) ions. The concentration of magnesium in the cell is orders of magnitude superior to the concentration in calcium, the latter being extremely regulated throughout the cell as a means of chemical communication. It therefore stands to reason to study the effect of both these ions on hRad51 activity, especially the effect of magnesium which is probably the cation the protein normally interacts with.

### Influence of $Mg^{2+}$ cation

The efficiency of the hRad51 strand exchange activity in the presence of magnesium and ATP is optimum for a concentration of $Mg^{2+}$ between 0.2 and 1.5mM [**Figure 18; A**]. This optimum concentration is set after the optimum $Mg^{2+}$ concentration for ATPase activity [**Figure 14**]. In fact, the optimum efficiency of strand exchange coincides with when ATP hydrolysis is very low for the ssDNA substrate and its affinity for ADP is still low enough [**Figure 15**]. This all point towards the fact that an active hRad51-ssDNA nucleoprotein filament is ATP bound.

It also coincides with when ATP hydrolysis is low for the ssDNA substrate and still quite high on dsDNA [**Figure 15**]. This could suggest that the formation of hRad51-dsDNA nucleoprotein filaments is somewhat detrimental to the protein's activity.

Figure removed because of copyrights

**Figure 18:** (**A**) Extracted from [101]. Effect of the $Mg^{2+}$ concentration on the efficiency of strand exchange of hRad51. Reactions are made in the presence of ATP. (**B**) Extracted from [111]. Effects of bivalent ions on hRad51 strand exchange activity. The effects of $Ca^{2+}$ (10mM) and of $Mg^{2+}$ (20mM) on ScRad51 strand exchange activity are shown in the upper right corner.

### Influence of the Ca²⁺ cation

As illustrated by the results in **[Figure 18; B]**, the calcium cation promotes effective strand exchange much better than any other bivalent ion. We know that it modulates its ATPase activity but it also has been suggested that calcium promotes strand exchange activity through the stabilization of the protein's spatial conformation. Indeed $Ca^{2+}$ facilitates strand exchange even in conditions containing ADP **[Figure 19]**. The $Ca^{2+}$ cation being much larger than $Mg^{2+}$, it is thought that its size stabilizes one of the L2 loops responsible for DNA binding. This tighter binding of DNA would then facilitate homologous pairing and strand exchange [126].

## B.III.2. Influence of the bound nucleotide

### ATP vs ADP for strand exchange

Figure removed because of copyrights

**Figure 19:** Extracted from [126]. Effects of the nucleotides and the cations $Ca^{2+}$ and $Mg^{2+}$ on the hRad51 strand exchange activity.

Looking at the effect of the cation cofactor led us to suspect that an active nucleoprotein filament is ATP bound. Indeed, as can be surmised by the results in **[Figure 19]**, filaments formed in ATP are much more efficient than those formed in ADP. Also the presence of exogenous ADP in solution inhibits strand exchange if a high enough magnesium concentration is present [109]. This coincides with when the affinity for ADP is high **[Figure 15]**.

## ATP to ADP conversion

When forming nucleoprotein filaments in ATP in the presence of magnesium on ssDNA, two states of the filaments are observed, the first of them transitory. Since ATP hydrolysis on ssDNA is quite efficient, the transitory state may then be interpreted as a transient ATP-bound form, rapidly converting to an ADP-bound form. This effect explains, at least partially, why the presence of calcium cations increase the efficiency of strand exchange for filaments formed in ATP **[Figure 19]**.

Filaments in presence of ADP may be less efficient in strand exchange than those with ATP, but their capacity for homologous pairing is superior [118].

## B.III.3. Other factors: pH and temperature

Summarized in **[Figure 20]** are the results of strand exchange assays in function of temperature and pH. Strand exchange activity of hRad51 is optimum for a pH around 7.5 [101]. It is also efficient for temperatures ranging from 22ºC to 50ºC with an almost 100% efficiency for a temperature of 50 ºC. Rising the temperature above this limit to 55 ºC results in a drastic reduction of efficiency, probably due to protein denaturation [101]. Another assay shows that the hRad51 protein alone is able to efficiently promote strand exchange at 37 ºC but not at 30 ºC. At this temperature, the presence of hRad54 in solution is required [97].
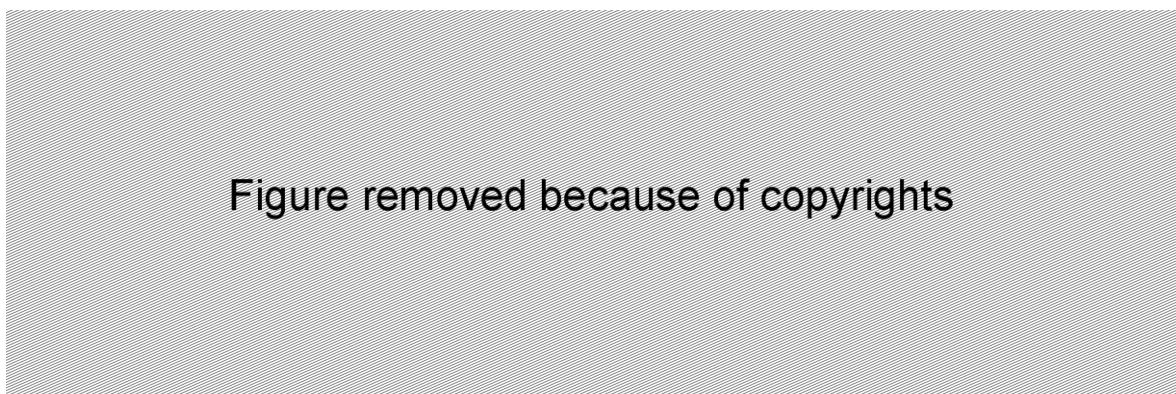
Figure removed because of copyrights

**Figure 20:** Extracted from [101]. hRad51 strand exchange efficiency in presence of ATP and $Mg^{2+}$ in function of (**A**) pH and (**B**) temperature.

# C. hRad51 in single molecule studies

## C.I. Single molecule techniques used for hRad51

In this section we will introduce the most commonly used single molecules techniques that have been applied to the study of the hRad51 protein.

The term single molecule here applies to techniques allowing the observation or manipulation of single DNA molecules on which hRad51 nucleoprotein filaments were formed. We will then not talk about techniques such as Nuclear Magnetic Resonance (NMR) or Site-Specific Linear Dichroism (SSLD) spectroscopy whose results will nonetheless be presented in the filament structure section. We will focus as much as possible on experiments aiming to study nucleoprotein filaments formed on dsDNA since it is what we'll be doing in our experiments.

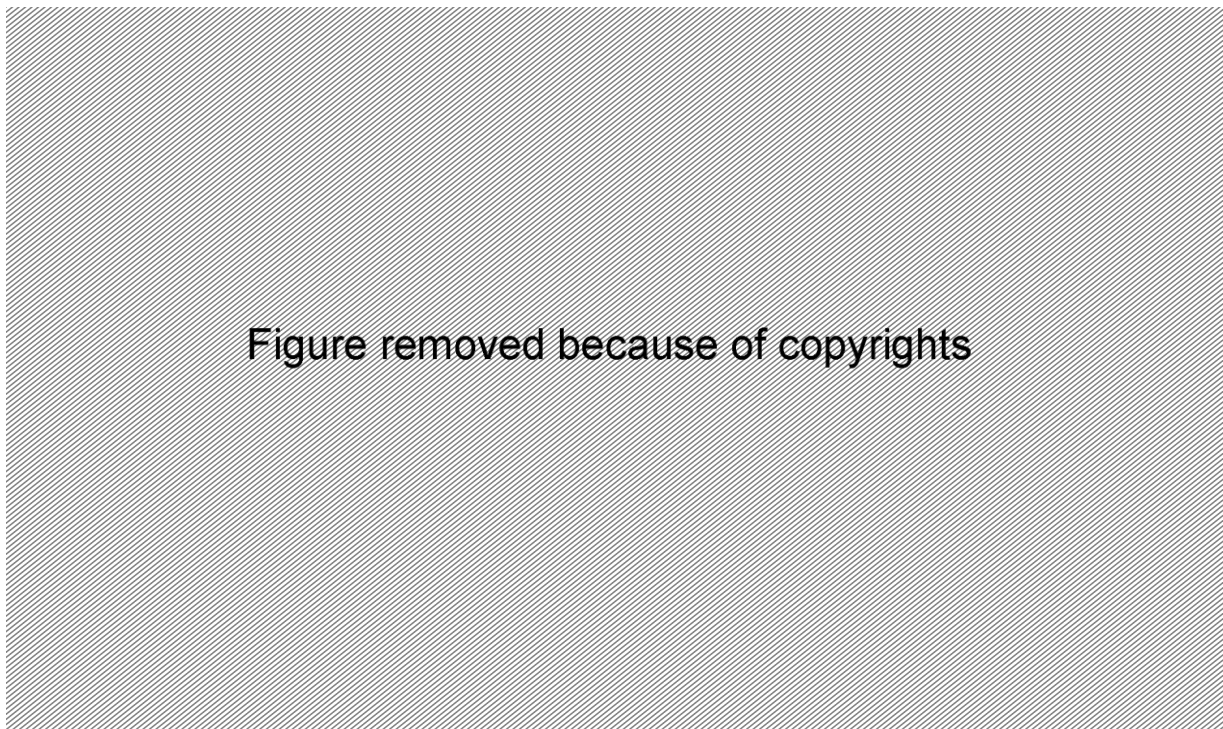### C.I.1. Electron microscopy and scanning force microscopy

Figure removed because of copyrights

**Figure 21:** Electron micrograph of hRad51 nucleoprotein filaments. In (**A**) is shown an hRad51-dsDNA filament formed in AMP-PNP + $Mg^{2+}$ (adapted from [127]). In (**B**) is a hRad51 formed on nicked circular dsDNA in ATP and $Mg^{2+}$ and stabilized by ATP-γS after formation (1000Å; adapted from [99]). In (**C**) and (**D**) are hRad51 filaments formed on ssDNA in the presence of ADP-AlF4$^-$ (**C**) or ATP-γS (**D**). (adapted from [128]). Scale bar on all images denote a distance of 1000Å.

Electron microscopy is a convenient way to directly observe the structure of hRad51 nucleoprotein filaments [**Figure 21**]. One may then measure their extension and even perform 3D-reconstructions by considering many segments issued from different filaments (generally more than 1000 segments are required for reconstruction). Much of what is known on the

filaments' structure comes from such experiments; results stemming from them will be presented in the next section.
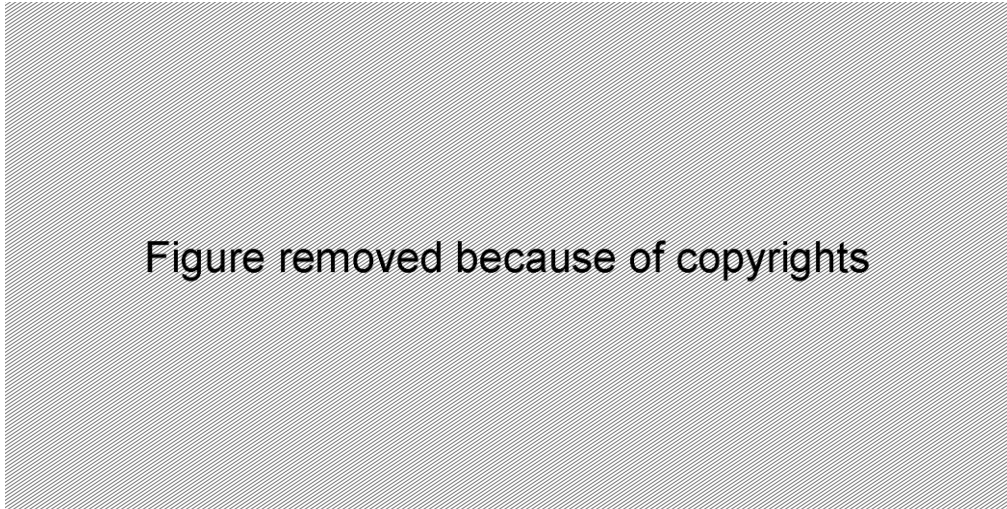


**Figure 22:** SFM images of filaments formed by hRad51 on dsDNA. The images from **A** to **E** show filaments formed in the presence of various nucleotide cofactors (Extracted from [129]). The images **F** and **G** show filaments assembled on a 1.8 kb dsDNA substrate in the presence of ATP and $CaCl_2$ (adapted from [130]). All images are 1µm x 1µm. Color indicates height (0–3 nm from red to white).

Samples for electron microscopy are generally applied to carbon-coated grids and negatively stained with uranyl acetate. The magnesium spreading method is incompatible with the use of calcium cations to prevent ATP hydrolysis which is why filaments are generally stabilized through the use of non-hydrolysable analogs of ATP such as AMP-PNP, $ADP-AlF_4^-$ or ATP-γS.

To circumvent such a restriction, the use of scanning force microscopy (SFM) is an option **[Figure 22]**. The effect of the cation cofactor on nucleoprotein filaments may then be observed. However the resolution of the technique is somewhat intrinsically inferior to electron microscopy when it comes to analyzing the structure of the filaments, due to an inferior resolution in the XY-plane.

## C.I.2. Fluorescence and microfluidics

### TIRFM

Total internal reflection fluorescence microscopy (TIRFM) uses an evanescent field to excite fluorophores in a region restricted to the proximity of the sample surface. The evanescent wave typically penetrates to a depth of 100 to 200nm. In those setups, DNA molecules are generally bound to neutravidin proteins immobilized on lipid bilayers. The DNA molecules are then tethered on one end and extended by the application of a buffer flow in the microfluidic chamber. When extended, the DNA molecules enter the evanescent field allowing their observation **[Figure 23]**.

Observation is achieved by staining the dsDNA molecules with YOYO1 [131] or by forming nucleoprotein filaments with fluorescent hRad51 proteins [132]. If one does not wish to mark the DNA or wants to use the wild-type non-fluorescent hRad51protein, then the

tracking of the molecules' extension may be achieved by tagging the free end of the dsDNA with a quantum dot (QD) [119].
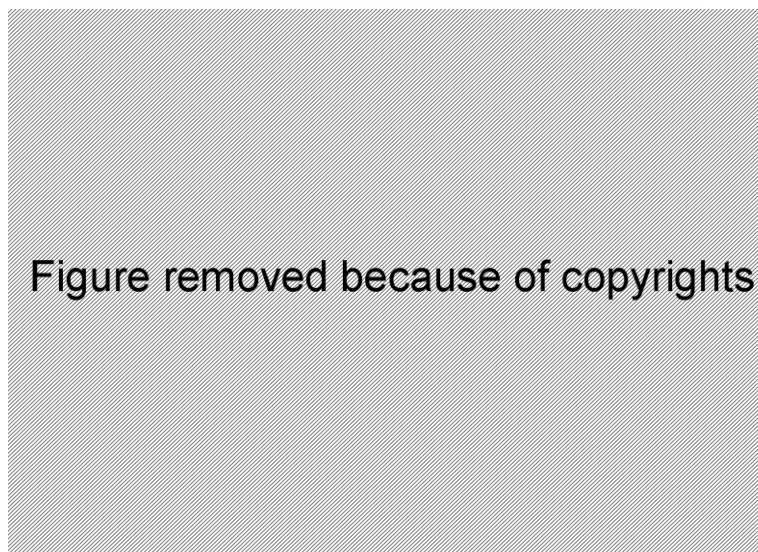
Figure removed because of copyrights

**Figure 23:** Adapted from [133]. Schematic illustration of the TIRFM system (**A**) and cartoon image of a QD-labeled dsDNA molecule and its response to variations in buffer flow (**B**).

High parallelization using this technique is possible by the construction of what has been called DNA curtains [134]. For such a construction, the surface is etched prior to the deposition of the lipid bilayer and the neutravidin proteins are no longer immobilized and allowed to diffuse on the surface. The application of a flow in the chamber results in an accumulation of tethered DNA molecules at the site of the etching **[Figure 24]**. It is even possible to tether the molecules to lipid bilayer at both ends to circumvent the use of buffer flow during observation [132].
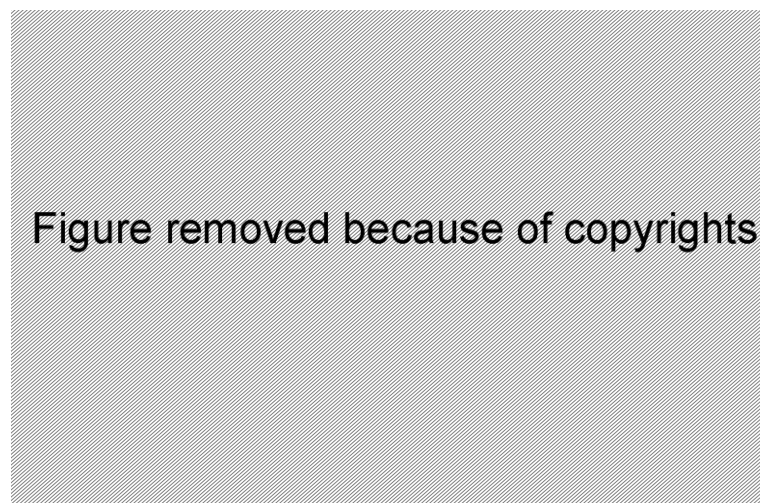
Figure removed because of copyrights

**Figure 24:** Adapted from [134]. Assembly of parallel DNA arrays in the TIRFM system. (**A**) Outline of the protocol for preparing arrays of surface-tethered DNA molecules. First, the fused silica surface was mechanically etched and the scratched slide was used to make a microfluidic sample chamber in which is formed the lipid bilayer. Neutravidin was added to provide attachment points for the DNA prior to the injection the biotinylated λ-DNA molecules which were then pushed into position along the diffusion barrier using hydrodynamic force. (**B**) Accumulation of DNA molecules along the leading edge of a diffusion barrier. After injecting the DNA molecules and allowing them to bind to the surface, buffer flow was initiated, and single images were collected at the indicated intervals. A 10μm scale-bar and time points are indicated.

Using the TIRFM setup to study hRad51 allows direct observation the nucleoprotein filaments when using fluorescent proteins or the tracking of the filaments' extension. This technique is currently the only one combining such an observation and high parallelization. The specifics of the surface coating in these experiments preclude the use of $Ca^{2+}$ cations.

## Optical tweezers and multichannel flow cells

Optical tweezers allow imposing the position of micrometric beads through the use of highly focused laser beams. When well calibrated those setups also allow the control and/or measurement of the force applied to the bead by the optical trap. Forces applied typically range from zero to several hundreds of piconewtons.

Application of optical tweezers to the study of hRad51 nucleoprotein filaments makes use of multichannel microfluidic flow cells where channels containing different buffers are separated by laminar flow. DNA molecules attached to antibodies-coated beads are captured by an optical trap in a capture channel containing a protein-free buffer before being dragged into a reaction channel containing a buffer with hRad51 and its cofactors **[Figure 25]**. Observation of the proteins on the DNA requires the use of fluorescent proteins which in contrast with the TIRFM system generates a lot of parasitic fluorescence signal coming from unbound proteins in solution. Therefore observation must be made in a protein-free channel.

If one wishes to wild-type non-fluorescent proteins, then observation may be made in the protein containing channel but the free end of the DNA molecule must be marked by a fluorophore such as Cy3 into order to be able to track the end-to-end extension [135].

Figure removed because of copyrights

**Figure 25:** Extracted from [135]. Diagram illustrating the assembly of hRad51 proteins on a single λ-dsDNA molecule; channels are separated by laminar flow border represented by hashed line. A single bead-DNA complex is captured in the capture channel by an optical trap. This complex is the moved to the reaction channel to allow hRad51 assembly on the DNA molecule. FluorescentRad51permits direct visualization of nucleoprotein filament formation in the observation channel.

When the DNA molecules are captured from one end, they are extended by the drag force of the buffer flow in the chamber much like in the TIRFM setup. One may also capture both ends of the molecules with beads through the use of a dual optical trap setup **[Figure 26]**. This allows the application of tension to the captured DNA molecule and thus the elasticity of a nucleoprotein filament may be probed [136] or protein dissociation may be stalled [137].

This technique is a powerful tool combining direct observation of and application of tension to nucleoprotein filaments. This goes hand in hand with the loss of parallelization.

Beads in optical traps are free to rotate along the axis of the captured DNA molecule, so no torsion restriction is applied.
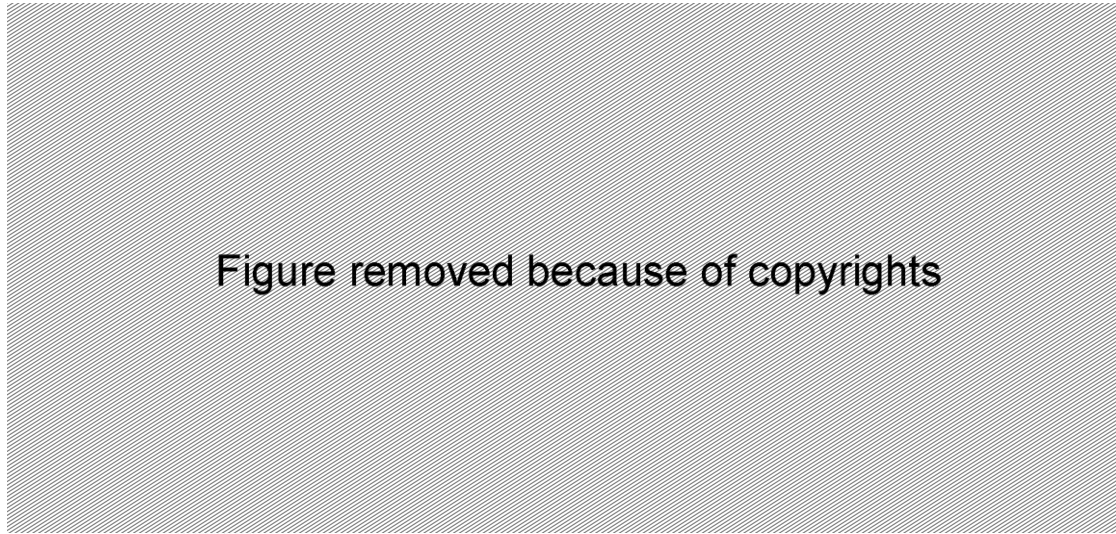


**Figure 26:** Extracted from [138]. (**A**) Schematic of the dual-trap assay. Two traps can be generated from a single laser source by splitting into two orthogonal polarizations, which may be independently steered in the sample. After suspending a single DNA molecule in between two trapped beads, the DNA can be manipulated without the application of force. In addition, optical tweezers can be employed to quantitatively detect the forces exerted on the DNA. The fluorescence from DNA-staining dyes or fluorescently labeled DNA-binding proteins can be detected using a CCD camera. (**B**) Assay employed in the study of the elasticity of (fluorescently labeled) hRad51 nucleoprotein filaments formed on double-stranded DNA.

## C.I.3. Magnetic tweezers

Magnetic tweezers is the one of the only tools allowing the simultaneous study of extension and torsion of single DNA molecules. The extension and torsion are the key mechanical parameters to be accessed in order to fully comprehend the mechanics of hRad51 nucleoprotein filaments. However, in contrast with length, torsion in those filaments has been seldomly studied previously.

Previous studies of hRad51 nucleoprotein filaments in classical magnetic tweezers **[Figure 27; A]** have been reported in particular the studies by van der Heijden *and al.* [139], Ristic *and al.* [129], and within our team by Miné *and al.* [140] and Disseau during his PhD [141]. However, except for the PhD work accomplished by Disseau, those experiments have focused on the formation and study of filaments formed on ssDNA or nicked dsDNA molecules thus lacking the study of simultaneously torsion and extension as is possible in magnetic tweezers.

Also within our team was developed, by Arata *and al.* [142] and Dupont during her PhD [143], a new generation of magnetic tweezers baptized free-rotation magnetic tweezers (FRMT) **[Figure 27; B]**. First introduced for the study of the RNA polymerase in *E.Coli* by Harada *and al.* [144], FRMT uses a magnetic tip to produce a vertical magnetic field thus allowing free rotation of the beads along the axis of the attached DNA molecules. The rotation of the beads was tracked by the addition of small polystyrene beads to the paramagnetic beads in order to produce non-spherical objects, however simultaneous tracking of extension was lost. Applied to the study of hRad51 nucleoprotein filaments, the binding or unbinding of proteins to the DNA produced spontaneous rotation of the beads.

Figure removed because of copyrights

**Figure 27:** Schematic diagrams of the different magnetic tweezers used for the study of hRad51. (**A**) Adapted from [139] Classical magnetic tweezers using a horizontal magnetic field and racking molecule extension. (**B**) Adapted from [142]. Free rotation magnetic tweezers using a magnetic tip to produce a vertical magnetic field. Rotation is tracked by adding polystyrene beads to the paramagnetic beads. Images of such beads are shown on the right of the diagram. (**C**) Same principle as (**B**) except for the use of cylindrical magnet instead of a tip. Extension is tracked as in (**A**) and rotation tracking is achieved by the tracking the center of the beads while they rotate in an off-centered fashion. (**D**) Modification of (**C**) by adding a small magnet to the side of the cylinder. It allows the application of small torques (~200pN.nm.rad$^{-1}$). Rotation of the magnets induces bead rotation. (**C**) and (**D**) are adapted from [145].

During my PhD, an evolution of FRMT was developed by Lipfert *and al.* [146] which they baptized freely orbiting magnetic tweezers (FOMT) **[Figure 27; C]**. Like us, they had the idea of using a cylindrical magnet instead of a tip in order to recover the simultaneous tracking of extension which was lost in FRMT. Rotation tracking was achieved through the tracking of the center of the beads as they turned in an off-centered fashion. They also added a small magnet on the side of the main cylindrical one **[Figure 27; D]** which allowed them to apply a small torque on the beads (typically around 200pN.nm.rad$^{-1}$). Measurement of the mean angle deviation within this small magnetic trap gave access to the measurement of the torques applied the DNA or the proteins on the DNA. Towards the end of my PhD, this technique was applied to the study of hRad51 nucleoprotein filaments by Lee *and al.* [145]. Contrarily to other results produced by other teams, the results stemming from these

experiments will not be presented in this chapter; they will be compared to our results in chapter 3.

The work presented in this thesis is the continuation and evolution of the work previously done in our team. We will use classical magnetic tweezers and an evolution of the FRMT/FOMT setup which I developed during my PhD. Using those tools, we will try to access information about extension and torsion evolution which are the pertinent parameters to obtain for the energies involved in hRad51 nucleoprotein filaments. The idea is to reduce the complex system that is homologous recombination to a simple *in vitro* system involving a single dsDNA molecule and hRad51 proteins in controlled chemical conditions and without any involvement of the many partners of HR.

# C.II. hRad51 filament structure

The nucleoprotein filament is formed when hRad51 monomers cooperatively assemble on the single-stranded overhangs of the broken DNA sequence. Its structure is function of its chemical state, especially the nature of the cations and of the cofactor nucleotides it contains. In this section we will review what electron microscopy tells us about the structure of this filament.

## C.II.1. Structure of various recombinase proteins on ssDNA



Figure removed because of copyrights

**Figure 28:** Extracted from [128]. Surface reconstruction of filaments from electron microscopy pictures.
    (**a**) hRad51+ssDNA in ADP-AlF$_4^-$, helical pitch 99Å, 6.39 units per turn
    (**b**) ScRad51+ssDNA in ATP-γ-S, helical pitch 94Å, 6.28 units per turn
    (**c**) RecA+dsDNA in ATP-γ-S, helical pitch 91Å, 6.16 units per turn

hRad51 monomers self-assemble into a right handed helix on ssDNA called the nucleoprotein filament. These filaments will form on DNA, preferably in the presence of $Mg^{2+}$, regardless of the presence or absence of a cofactor nucleotide and whatever the DNA substrate [99].

These filaments have been observed by electron microscopy and their surfaces reconstructed from the pictures. Those 3D surfaces reveal highly polar structures, the surface of one side of the groove being smooth whereas the other side exhibits pendular lobes. These structures are similar in the case of hRad51, ScRad51 and RecA **[Figure 28]**. Stochiometry within those filaments has been estimated to one hRad51 monomer for three base pairs [100]–[102]; the same is true for ScRad51 and RecA proteins.

## C.II.2. ATP hydrolysis and structure on ssDNA

Two different states of the hRad51-ssDNA filaments appear, depending on chemical conditions present during the filament formation **[Figure 29]**. First an extended state when formed in ADP-AlF$_4^-$ with a helical pitch of 99Å and 6.39 sub-units per turn. ADP-AlF$_4^-$ is used here as non-hydrolysable analog of ATP thus it is a safe assumption that this extended state corresponds to the active ATP bound form.

However using ATP-γS as another non-hydrolysable analog of ATP yields filaments in a compact state with a helical pitch of 76Å and 6.43 sub-units per turn. These filaments are similar to those obtained with ADP. The similarity between those ATP-γS filaments and those formed with ADP leads us to assume that this compact state is the non-active ADP bound form.
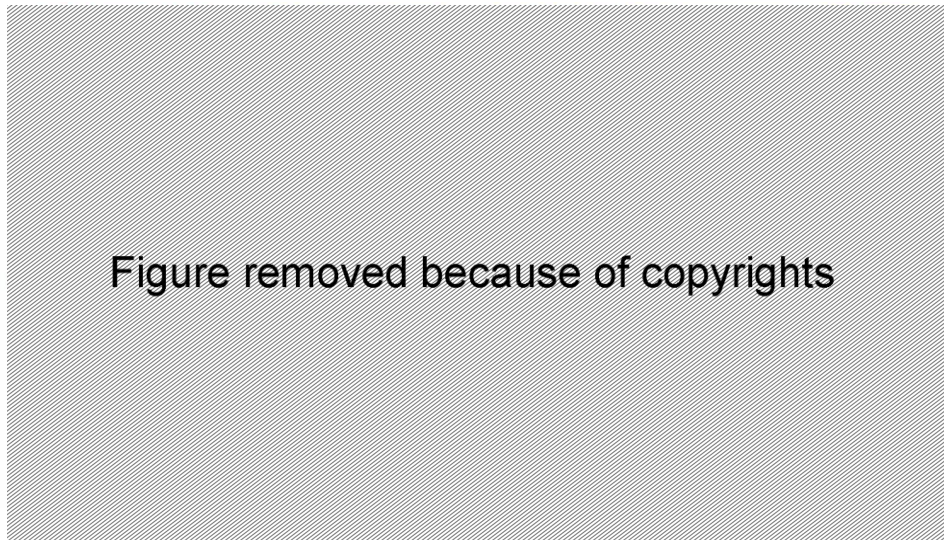


Figure removed because of copyrights

**Figure 29:** Extracted from [128]. On the left, hRad51+ssDNA in ADP-AlF$_4^-$, helical pitch 99Å, 6.39 units per turn. In the middle, hRad51+ssDNA in ATP-γS, helical pitch 76Å, 6.43 units per turn. On the right, comparison between both filaments (brought to the same helical pitch)

Thus we have an extended active ATP bound state and a condensed ADP bound one, both with a similar helicity with respectively 6.39 and 6.43 sub-units per turn. The main difference between these two states, apart from the helical pitch is a rotation of the pendular lobes present on one side of the helix's groove. The resolution by MNR spectroscopy of the

structure of the N-terminal domain of the protein shows a good apparent fit for the volume of these lobes [128].

## C.II.3. hRad51 structure on dsDNA

The previous results clearly show there is a correlation between the structural conformation of the filament and the cofactor nucleotide. In the case of hRad51-dsDNA nucleoprotein filaments, the nature of the nucleotide will also affect the unwinding of the DNA molecule.

In the presence of ATP, a filament on dsDNA will be unwound by approximately 43%. Extension of the DNA molecule when it is unwound in such a nucleoprotein filament is estimated at 150% of its original length in the B-DNA form. In reality, measurements using electronic microscopy yield an axial rise of 4.7Å which corresponds to an extension of only 138% [99]. This value however is probably underestimated due to the presence of heterogeneous regions of the filaments not completely covered with hRad51 proteins.

Electron microscopy on filaments formed from hRad51 on dsDNA in conditions containing AMP-PNP and $Mg^{2+}$ yielded structures similar to the ones obtained on ssDNA with ADP-AlF$_4^-$ [Figure 30]. The right-handed helix formed in this case had a pitch of 100Å and contained 6.4 subunits per turn [127]. If one assumes a stochiometry of three base pairs per hRad51 protein, this is equivalent to 19.2bp/turn which corresponds to an unwinding of 45.3%. Taken together with the value of the pitch, the extension of the filament is 1.53 times the length of B-DNA.
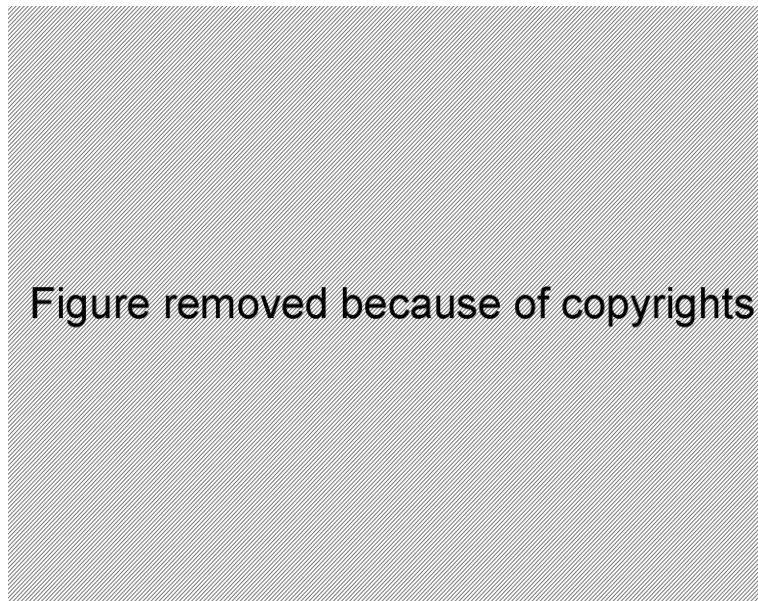
Figure removed because of copyrights

**Figure 30:** Adapted from [127]. The three-dimensional reconstruction of filament formed in 7μM hRAD51 (a hRad51 to DNA ratio of 40:1), 1.25mM AMP-PNP and 2.5mM $Mg(C_2H_3O_2)_2$. Reconstruction involved 2000 segments and has 6.4 subunits per turn of a 100Å pitch helix. The crystal structure of an intact ScRad51 subunit is fit into the filaments (red). A portion of the α-helix containing residues 146-156 in ScRad51 projects outside of the reconstruction (blue arrow), consistent with the suggestion that this region might be flexible in the filament [147].

Filaments formed on dsDNA with ATP and $Mg^{2+}$ are irregular and of variable length. Addition of $Ca^{2+}$ cations or the use of AMP-PNP instead of ATP yield filaments results in the formation of regular structures as can be observed from SFM images [Figure 22]. The regular

extended states are thought to be in the active ATP-bound form, whereas irregular structures are most probably ADP-bound. The use of ammonium sulfate also seems to yield regular structures, explaining why its use enhances hRad51 strand exchange activity by stabilizing active forms

No unwinding was observed in the presence of ADP or in the absence of nucleotides [99]. Compact filament structures states may be observed on dsDNA in conditions allowing ATP hydrolysis. The compact and extended states are thought to have the same protein/nucleotide stochiometry on the basis that complete covering of intact overwound circular dsDNA have been reported [99].

## C.II.4. Similarity with ScRad51

Structures formed by hRad51 on dsDNA are very similar to those formed by its yeast homolog ScRad51. The pendular lobes however are not as clearly visible in contrast to what can be observed with hRad51 and RecA [**Figure 31; A**]. The axial rise is of 5.1Å with an helicity of 18.6 base pairs per turn (6.18n monomers per turn) and a helical pitch is 98.9Å [75]. A crystallographic structure of filaments formed with ScRad51 has been resolved [**Figure 31; B**].

This structure shows a very high pitch value of 130Å which contrasts with the previously measured value of 98.8Å. In spite of these disparities, this structure is currently the one which has been fully resolved for the Rad51 proteins.



**Figure 31:** Reconstruction from electronic microscopy pictures of the surface of a dsDNA/ScRad51 filament formed in ATP extracted from [75] is shown in (**A**). The resolved crystallographic structure of ScRad51 monomers self-assembled into a helical structure, extracted from [147], is shown in (**B**). The presence of bound DNA in this crystal is unknown.

# C.II.5. Resolving hRad51 on dsDNA
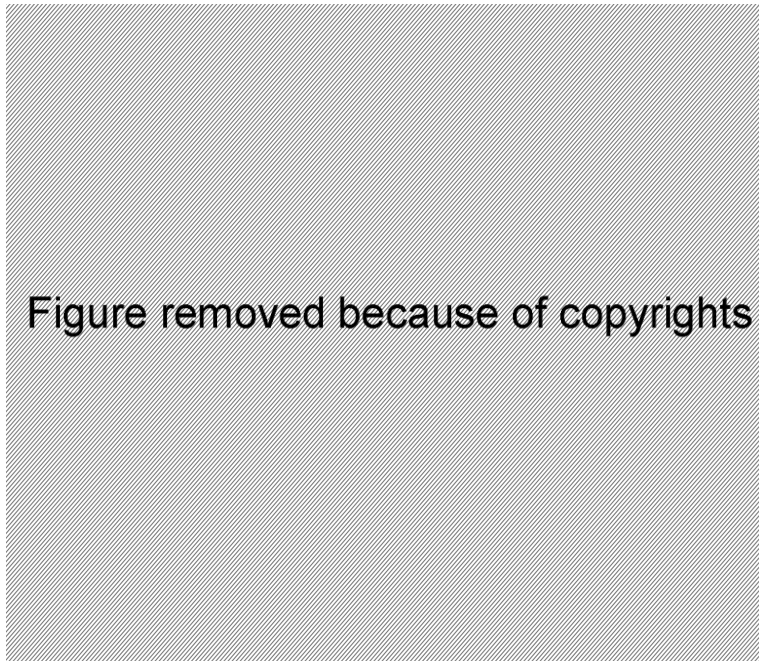
Figure removed because of copyrights

**Figure 32:** Extracted from [148]. Model of the structure of a helical hRad51 filament constructed by replication of the monomer structure by respecting 6.39 monomers per turns and helical pitch of 99Å [127].The angular orientations of the orthogonal transition moments, $L_a$ et $L_b$, are illustrated for Tyr-205.

More recently, a hRad51-dsDNA filament structure has been resolved using molecular modeling and experimental data from site-specific linear dichroism spectroscopy (SSLD) **[Figure 32]**. The molecular modeling was based on reported structures of the central [149] and N-terminal domains [150] of the uncomplexed hRad51 protein. Missing gaps in the known structure have been complemented by using the previously presented work of the crystallographic structure of the ScRad51 filament structure as a template [147]. To obtain information on the monomer orientation, SSLD was used on hRad51/dsDNA/ATP nucleoprotein filaments to measure the angular orientation of substituted Tyr residues on the protein. Model verification is achieved by optimally overlapping the obtained structure with the density of a 3D reconstruction of an electron micrograph [127] as shown in **[Figure 34]**.
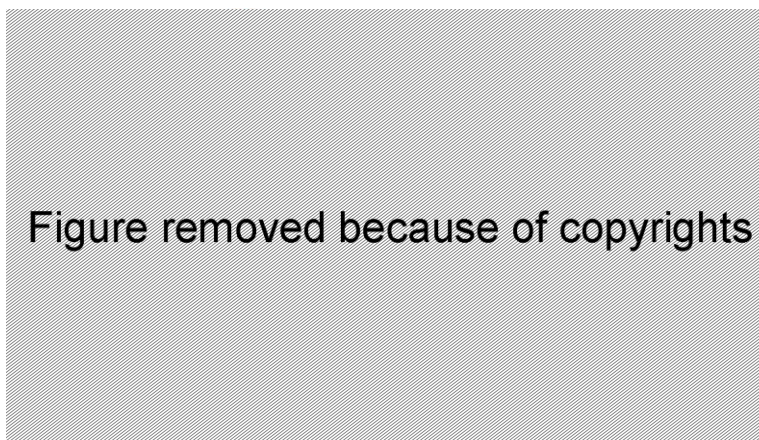
Figure removed because of copyrights

**Figure 33:** Extracted from [148] Oligomerization of hRad51. The filament assembly is coordinated by the β sheet of the interdomain connector (red) with the β sheet (bleu) of the adjacent monomer. The interaction between two neighboring monomers follows a "key-lock" principle: Phe-86 is inserted between Ala-190 and Ala-192.

**Figure 34:** Extracted from [148]. Model structure of a hRad51 nucleoprotein filament (monomers in blue and orange) aligned with the 3D surface reconstruction of the filament [127]. A dsDNA (pink), extended heterogeneously as proposed by [151] and observed in [152] is fitted to the structure of the filament.

The proposed structure [148] provides insights on how proteins interact with each other and with DNA substrates. It shows protein-protein interaction through the β-sheets of two neighboring monomers following a "key-lock" principle as the Phe-86 residue of one monomer is being inserted between the Ala-190 and the Ala-192 residues of the next monomer **[Figure 33]**. The Phe-126 and Phe-129 residues which are thought to be to the ATP binding site [153] are found in a pocket situated at the interface between two monomers and near the L2 loop which is thought to be one of the loops responsible for DNA binding. This proximity could explain how ATP hydrolysis would promote hRad51 disassembly from the filament by destabilizing both the monomer to monomer interaction and the monomer's interaction with DNA.



**Figure 35:** Extracted from [148]. Loop orientation and DNA binding. The modelized structure allows for a dsDNA molecule such as represented in the enlargement.. The L1 loops (magenta) and the L2 loops (green) are turned toward the inside of the filament and are available for interaction with the DNA: Tyr-232 is inserted between 2 bases of one of the strands and Arg-235 is located near the sugar backbone of the other strand.

The hRad51 contains two flexible loops, a short L1 loop and a longer L2 loop, which are thought to be responsible for DNA binding. The modification of the L1 loop, by substituting the Tyr-232 residue with an Alanine or Tryptophan, reduces the protein's affinity for DNA without affecting neither conformation nor ATP hydrolysis [154]. This strongly suggests that the L1 loop, and more specifically the Tyr-232 residue, is implicated in the binding of the DNA. On the other hand, modification of the L2 loop shows no apparent change. In this structure, the L1 loop is flexible and in a random coil conformation. The L2 loop shows some ordered α-helical structures. Both loops point towards the center of the helix and are in a position to be directly in contact with the DNA substrate. This is consistent with the L1 loop's implication in DNA binding and reports of the proximity of the L2 loop to the DNA binding site. The compact structure of the L2 loop and the fact its modification does not directly affect DNA binding leads to the conclusion that this loop provides additional, non-specific stabilization of the nucleoprotein complex.

The L2 loop in the presented structure is also host to a divalent cation [**Figure 36**]. Therefore a bound hRad51 monomer contains two divalent cations; one is attached to the cofactor nucleotide whereas the other is situated at the C-terminus of the L2 loop. In the presence of a cation at this latter site ($Ca^{2+}$ or $Mg^{2+}$), the α-helical domains of the L2 loop become stable. In the absence of a cation, these α-regions become elongated thus greatly disrupting DNA binding [126]. Moreover the nature of this cation seems to influence the filament differently. Indeed the calcium cation being much bigger than the magnesium cation, its residency time within the L2 loop would be much greater thus stabilizing the structure more efficiently. This stabilization would explain the previously reported favoring of strand exchange by the presence of $Ca^{2+}$ in solution.



**Figure 36:** Extracted from [126]. Model structure of a hRad51/ADNsb/ATP filament with and without a bivalent cation, (A) et (B) respectively, at the C-terminus of the L2 loop (orange). A cation (magnesium or calcium) coordinates the oxygen atoms and phosphates of the ATP (cation labeled 'ATP'), while the other coordinates the α helix regions of the L2 loop (cation labeled 'L2 loop'). The α helix region of the L2 loop, responsible for DNA binding, is stable in presence of a bivalent cation ($Ca^{2+}$ or $Mg^{2+}$). Without cations at the C-terminus of the loop, the α helix region becomes elongated disrupting the DNA binding.

# C.III. Filament formation

When a DNA molecule (ssDNA or dsDNA) is incubated with hRad51 proteins in the presence of ATP and of a divalent cation ($Mg^{2+}$ or $Ca^{2+}$), a nucleoprotein filament will form as the proteins self-assemble onto the DNA. The final result is an elongated form which reaches up to 150% of the DNA molecule's length in B-form [119], [129], [135], [139]. The DNA molecule will also be unwound by 43% in the case of a target dsDNA [99], [127].

## C.III.1. Nucleation-growth mechanism

The mechanism of this filament formation is thought to be of nucleation and growth. This mechanism is inspired by the JMKA (Johnson-Mehl-Avrami-Kolmogorov) model initially applied to crystal growth. Nucleation events consist of the loading of monomers or oligomers on a vacant spot of the DNA molecule without any cooperation with the proteins already present in the filament. Once this nucleus has reached a certain size, cooperative growth of the filament may occur by addition of supplementary monomers or oligomers to one of its extremities.

If one considers a formation mechanism solely based on nucleation events, then it would be expected to observe an exponentially asymptotic growth of the DNA molecule's length. The simplest case of this would be to imagine that a group of p monomers are required for nucleation and to disregard the possibility of dissociation. The reaction could then be described as an irreversible process with a probability of *k*:

$$p \cdot hRad51 + DNA \xrightarrow{k} (p \cdot hRad51) - DNA$$
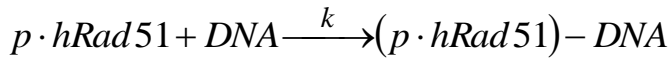
The total number *n(t)* of loaded proteins on the DNA would then follow a *p* order kinetics law:

$$\frac{dn}{dt} = k \cdot [hRad51]^p \cdot (n_{\max} - n(t))$$

Where $n_{max}$ represents the maximum number of monomers that can be loaded on the DNA molecule. The number of available spots as the reactions occurs is then ($n_{max}$ - *n(t)*). Solving this equation, by considering the concentration of [hRad51] constant throughout time leads to an exponential law:

$$n(t) = n_{\max} \cdot \left(1 - e^{-k't}\right) \text{ with } k' = k \cdot [hRad51]^p$$

The stochiometry of nucleotides per protein being 3:1, filaments formed only through nucleation should also not reach full extension. Indeed random placement of the proteins would give rise to 1 or 2 inaccessible nucleotides in between bound proteins.

Cooperative growth is assumed to be characterized by a constant rate of monomers or oligomers added to one nucleus. Now if one considers a very low probability for nucleation events and a fast cooperative growth, then it would be expected to observe a linear extension

of DNA molecules. The obtained filament should be very smooth and contain very little defects due to the high cooperativity of the assembly. Full extension should be then reached.
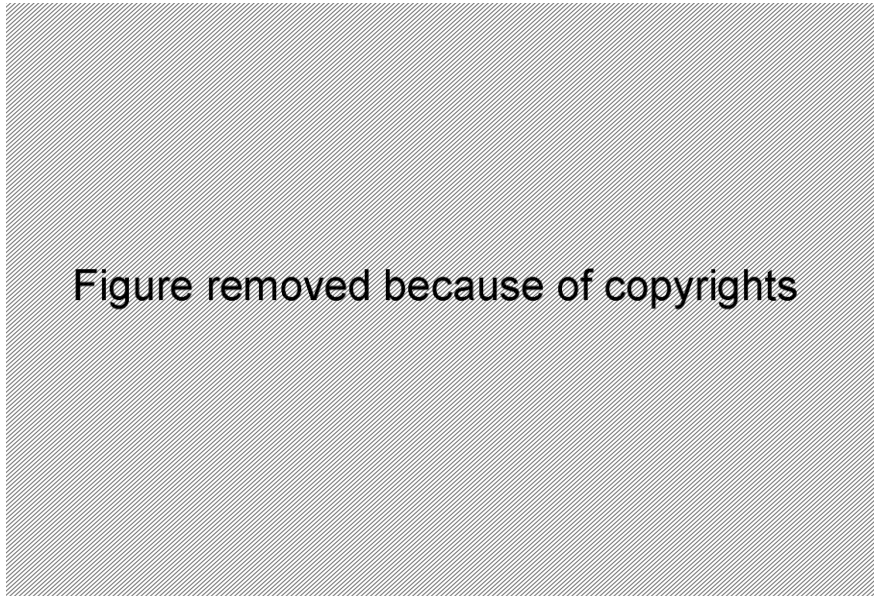


**Figure 37:** Extracted from [139]. Results from Monte Carlo simulations of nucleoprotein filaments formation. The extension is calculated by assuming that each monomer bound to 3 base pairs extends the dsDNA by 50%. The model used is nucleation-growth, the ratio between cooperative growth speed and nucleation rate is indicated on each curve.

Results from Monte Carlo simulations show us the existence of three different regimes depending on the value of the ratio between cooperative growth speed and nucleation rate **[Figure 37]**:
- The first regime, when the growth speed is very high compared to nucleation (ratio in the order of magnitude of 107). Very few nucleation events are then observed; they are preceded with long waiting periods and followed by rapid linear growth.

- The second regime, when the ratio is the 102-103 range, yields sigmoid shaped curves. The final extension of the molecule diminishes with the ratio.

- In the third regime, when the ratio is under 50, extension curves are exponential. Full extension is never reached.

## C.III.2. Hill coefficient

Originally applied by A.V. Hill in 1910 to describe the binding of oxygen to hemoglobin, the Hill coefficient is now commonly used to estimate the number of ligand molecules required to bind to a receptor in order to produce a functional effect. We have previously seen in **[Ch1.B.I.1]** the Michaelis-Menten model for enzymatic activity. This model predicts that if the conversion of a substrate (*S*) into a product (*P*) by an enzyme (*E*) is as follows:

$$E + S \underset{k_r}{\overset{k_f}{\longleftrightarrow}} E \oplus S \overset{k_{cat}}{\longrightarrow} P$$
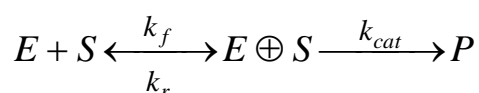
Then the conversion rate can be described by the following equation:

$$V_i = \frac{V_{\max} \cdot [S]}{K_m + [S]}$$

One can also predict with this model the concentration of the enzyme-substrate complex [E-S]:

$$[E \oplus S] = \frac{[E]_{total} \cdot [S]}{K_m + [S]}$$

Yet this model presupposes that only one enzyme-substrate binding is sufficient for conversion of the substrate into the product. In the case where *n* enzyme-substrate bindings are required ($n \geq 1$), the last equation becomes:

$$[E \oplus S] = \frac{[E]_{total} \cdot [S]^n}{S_{0.5}^n + [S]^n}$$

Where $S_{0.5}$ is the substrate concentration at which the enzyme-substrate concentration [*E-S*] is worth half of the total enzyme concentration [*E*]$_{total}$. n is called the Hill coefficient [155], [156].

## C.III.3. Nucleation in hRad51 filament formation



Figure removed because of copyrights

**Figure 38:** Extracted from [131]. Elongation versus of a dsDNA molecule incubated with hRad51 in presence of ATP and Mg$^{2+}$ in a TIRFM setup within a flow cell.

Elongation curves for dsDNA molecules incubated with hRad51 proteins in the presence of ATP and a divalent cation gives rise to sigmoid shaped curves **[Figure 38]**. This is incompatible with growth based solely on nucleation but also with slow nucleation and fast cooperative growth. However, an intermediate ratio between cooperative growth and nucleation would give rise to sigmoid curves such as been observed. Estimation of this ratio

by fitting Monte Carlo simulations results to experimental data obtained in magnetic tweezers experiments yields a value comprised between 200 and 250 for both ssDNA and dsDNA **[Figure 39]**.



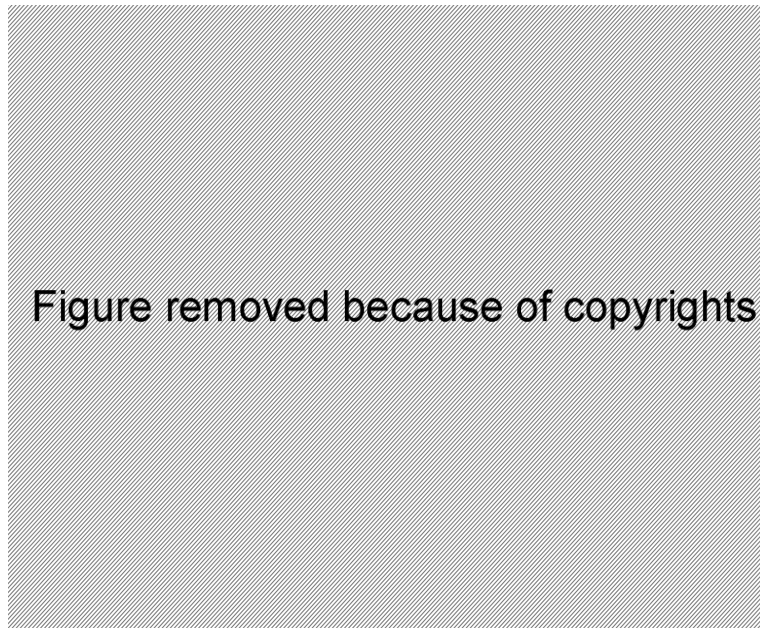Figure removed because of copyrights

**Figure 39:** Extracted from [139]. Rates and structural parameters for hRad51 filament formation on ssDNA and dsDNA at 187nM hRad51. Values deduced from Monte Carlo fits of experimental data from magnetic tweezers experiments.

Direct observations of filament formation by using fluorescent variant of the protein clearly show multiple nucleation sites **[Figure 40]**. Typical filament formation time is in the range of 10 minutes. The fast nucleation rate does not allow for the easy observation of nuclei formation. In order to slow down reaction speed, one can repeatedly incubate a single dsDNA molecule in sub-optimal conditions containing a high concentration of salt. Multiple single nucleation events are then easily observed **[Figure 40]**. Cooperative growth however is unclear since distinction between addition of oligomers to an existing nucleus and the formation of a new nucleus near a preexisting one requires resolution unavailable in fluorescence microscopy [135]
.

The Hill coefficient allows measuring the cooperativity between monomers during filament formation. Studies on filament formation on ssDNA with hRad51 showed a dependency of this coefficient on the nature of the nucleotide present. Values obtained of the Hill coefficient of hRad51 were 2.74±0.28 without nucleotides, 3.11±0.31 with ATP, 4.28±0.23 with ATP-γS [81]. Studies on dsDNA in magnetic tweezers yielded a Hill coefficient of 4.3±0.5 for assembly in presence of ATP [139]. These results lead to the conclusion that hRad51 nucleation occurs with oligomers ranging from 2-5 monomers on ssDNA and with pentamers on dsDNA.

Observing directly the nucleation events allowed characterizing of their time dependence as a function of protein concentration **[Figure 41]**. The rate's proportionality to the protein concentration gives direct access to the Hill coefficient of nucleation events. Experimentally this coefficient was estimated to a value of 2.4±0.2 [135]. Fitting experimental data to Monte Carlo simulations yields a Hill coefficient of 2.7±0.1. This latest results indicates that nucleation on dsDNA involves 2-3 monomers, not pentamers.

**Figure 40:** Extracted from [135]. Fluorescent hRad51 assembly on dsDNA (Scale bar = 2µm).

(**A**) Images from a video (time in seconds) showing nucleation and growth of a hRad51$_{FAM}$ filament on a single dsDNA molecule. Reactions occurs in presence of 100nM hRad51$_{FAM}$, 2mM Ca(OAc)$_2$ and 1mM ATP.

(**B**) Images from a video (time in minutes) of hRad51$_{FAM}$ assembly in sub-optimal conditions. The same dsDNA molecule is repeatedly incubated in 300nM hRad51$_{FAM}$, 2mM Ca(OAc)$_2$, 1mM ATP and 200mM NaCl. The yellow arrows indicate new nucleation sites whereas magenta arrows indicate nucleation sites occurring near a preexisting nucleus.



**Figure 41:** Extracted from [135].

(**A**) Images from a video (time indicated in minutes) of hRad51$_{FAM}$ assembly. The same dsDNA molecule is repeatedly incubated in 300nM hRad51$_{FAM}$, 2mM Ca(OAc)$_2$, 1mM ATP and 150mM NaCl.

(**B**) Time dependence of hRad51$_{FAM}$ cluster formation at various protein concentrations. Deduced from images shown in (**A**).

(**C**) Nucleation site formation frequency as a function of protein concentration. The solid line is a fit with the function: 5.2e-6*[hRad51$_{FAM}$]$^{2.4}$. Standard deviations are the size of data points.

Filament formation requires a protein concentration superior to 50nM. No formation of nucleus or filament elongation has been observed for concentrations under this limit [131], [140], [142]. In experiment monitoring several single dsDNA molecules simultaneously, all filament start expanding at the same time with no delay between protein insertion and filament extension. This is the case for protein concentrations ranging from 50nM to 1µM [131]. These results indicate that hRad51 nucleation is probably not a limiting step in filament formation.

## C.III.4. Cofactors influence on filament formation

Cofactors present in solution during filament formation greatly influence the conformation it will adopt. Effects of these cofactors may also be observed in the dynamics of hRad51 filament formation.
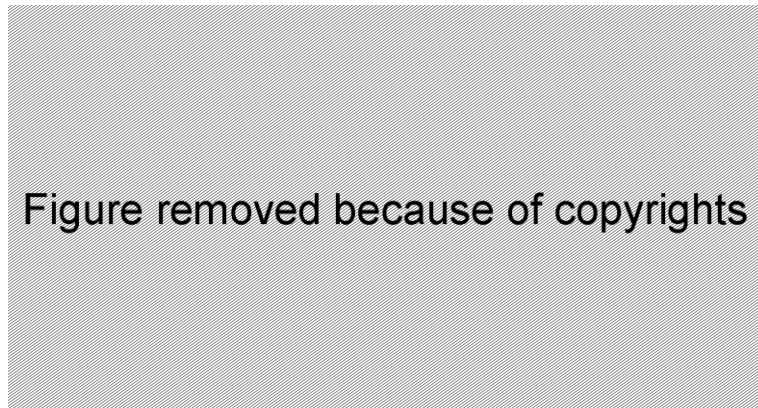
### Effects of the hRad51 concentration



**Figure 42:** Adapted from [131]. hRad51 assembly rates on dsDNA molecules in presence of ATP and $Mg^{2+}$ as a function of hRad51 concentration.

It was shown that the filament assembly rates increase with the concentration of hRad51 proteins present in solution during filament formation **[Figure 42]**. Protein concentration will also affect the final extension of the formed filament. It is thought this effect is caused by the variation of the final protein coverage of the DNA in the resulting filament **[Figure 43]**.
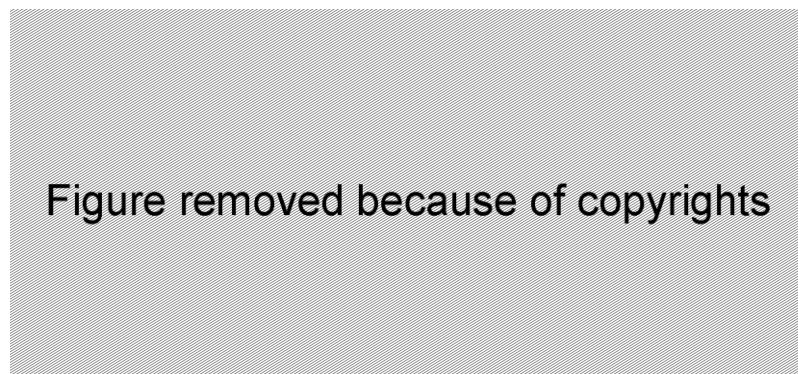


**Figure 43:** Extracted from [140]. Effect of hRad51 concentration (in nM) during filament formation on dsDNA molecules. The initial polymerization velocity (in $nm.s^{-1}$ and $monomers.min^{-1}$) and the filaments' final hRad51 protein coverage (in percentage of DNA length) increase as a function of hRad51 concentration.

## Effects of pulling force

The effect of the pulling force applied to the dsDNA molecule during filament assembly is similar to the effect of protein concentration. Both the assembly rate and the final protein coverage increase as stronger pulling forces are applied [**Figure 44**].

Figure removed because of copyrights

**Figure 44:** Extracted from [140]. Effect of pulling force during filament formation on dsDNA molecules. The initial polymerization velocity (in $nm.s^{-1}$ and $monomers.min^{-1}$) and the filaments' final hRad51 protein coverage (in percentage of DNA length) increase as a function of the pulling force.

## Effects of ATP concentration

To determine the role of ATP concentration plays in hRad51 filaments formation, dsDNA molecules were incubated with 100nM hRad51 in the presence of $Mg^{2+}$ and various concentrations of ATP [131]. Assembly rates were measured by TIRFM, averaged on several tens of molecules [**Figure 45; a**]. Rates remained more or less constant for ATP concentration ranging from 10µM to 1mM. However, for ATP concentrations under 10µM, the assembly rate declined rapidly in a linear fashion. This suggests that ATP binding probably becomes a limiting step for low concentrations of ATP due to limited supplies.

Figure removed because of copyrights

**Figure 45:** Extracted from [131]. Filament assembly in TIRFM with various cofactor nucleotides and ATP concentrations.
(**a**) A total of 100nM hRad51 along with various concentrations of ATP was injected into a flow cell containing a DNA curtain. Rates of filament assembly were obtained from the TIRFM experimental data and plotted as a function of ATP concentration.
(**b**) Kinetic plots of hRad51 filament assembly in the presence of ATP (black squares), ATP-γS (green triangles), AMP-PNP (blue inverted triangles) and ADP (red circles). All nucleotide co-factors were used at 1mM final concentration and each reaction contained 100nM Rad51.

## Nature of the nucleotide

The effect of the nature of the nucleotide was also investigated with the same setup, incubating the molecules with 100nM hRad51 in the presence of $Mg^{2+}$ with 1mM of various cofactor nucleotides **[Figure 45; b]**.

The presence of ATP yielded the typical ATP-bound filament conformation showing an extension of approximately 46%.

Assembly in the presence of ADP however did not produce any filament extension, even when protein concentration was increased ten-fold. This does not mean however that the protein does not bind the DNA in these conditions and in fact, presence of the proteins on the molecules was ascertained by gel-shift experiments.

Experiments using ATP-γS showed a very slow assembly rate, 5 times lower than ATP. These results are in good agreement with those obtained in a magnetic tweezers setup [140]. This is the main reason why ATP-γS is seldomly used as a non-hydrolysable analog of ATP in single molecule studies involving hRad51-dsDNA filaments.

Using an non-hydrolysable analog of ATP such as AMP-PNP yielded filaments longer than in the case of ATP, with an extension of approximately 64%. The assembly rate was 2.4 times higher than with ATP.

In the case of AMP-PNP, it is noteworthy to mention that similar experiments in classical magnetic tweezers have yielded the formation of not fully extended hRad51-dsDNA nucleoprotein filaments with a slow assembly rate [140], [157]. However one should be cautious of this result since measures using the same setup are in contradiction [141].
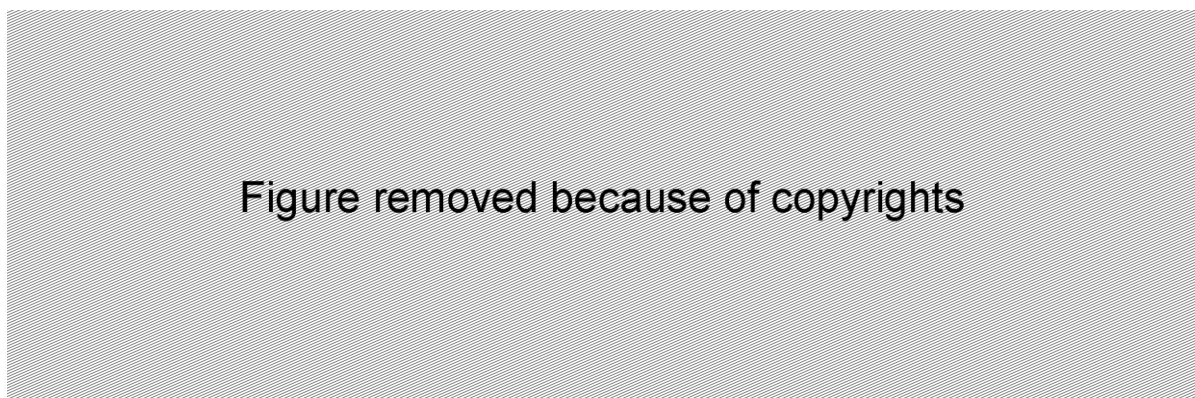
## Effects of temperature and cation nature



Figure removed because of copyrights

**Figure 46:** Adapted from [131]. hRad51 assembly on dsDNA molecules in presence of ATP and $Mg^{2+}$ at two different temperatures 25°C (black profile) and 37°C (red profile) (**A**). hRad51 assembly on dsDNA in ATP-$Mg^{2+}$ (black profile) and ATP-$Ca^{2+}$ (**B**).

Temperature also increases assembly rates as shown in **[Figure 46; A]** but this effect is very slight. Changing the divalent cation from $Mg^{2+}$ to $Ca^{2+}$ yields a slight increase in assembly rates and in final extension of the molecules **[Figure 46; B]**.

# C.III.5. Unwinding during filament formation



**Figure 47:** Adapted from [142]. Formation of hRad51-dsDNA nucleoprotein filament in conditions containing ATP and $Mg^{2+}$ in a FRMT setup.

(**A**) Rotation rate of the bead at different hRad51 concentrations. Inset: Traces of 3 DNA–beads in the presence of 100nM (black), 50nM (red), and 10nM (green) hRad51. Because of the viscous drag of the bead, the speed saturates at high hRad51 concentration.

(**B**) Stepping traces of 3 different DNA–beads at 10nM (black), 75nM (red), and 50 nM (blue) [hRad51]. Sixty-five-degree steps are emphasized by the gray trace issued from a semiautomated step-finding algorithm (see text). [Warning: the rotation seems faster at 10 nM, but averaging polymerization speed on such a short period is meaningless owing to the strong polymerization speed fluctuations apparent in (**A**)]

We know from the structural studies that the formation of an active ATP-bound hRad51-dsDNA nucleoprotein filament unwinds the DNA molecule by approximately 43%. The formation of filaments in conditions containing ATP-$Mg^{2+}$, in a magnetic tweezers setup allowing rotation, shows that indeed the DNA molecule unwinds spontaneously under the action of the hRad51 proteins **[Figure 47]**.

The unwinding speed increases with the concentration of hRad51 until it reaches a maximum value imposed by the force of the viscous drag **[Figure 47; A]**. This suggests that the transition to an unwound extended conformation of the filament may only occur with the application of a limited torque at saturating concentrations of hRad51. Characterizing and measuring this torque will be one of the objectives of the work presented in this thesis.

Studying the unwinding of the filaments at low concentrations of hRad51 showed the existence of angular steps **[Figure 47; A]**. Those angular steps proved to be 65°±15° in size. The meaning of such a result is currently not well understood.

# C.IV. Heterogeneity and elasticity

## C.IV.1. Filament heterogeneity

Several experimental studies reveal that hRad51 filament formation starts from multiple nucleation sites. The obtained filaments alternate between regions of hRad51-dsDNA and regions of naked DNA [130], [135], [136]. This is a result of rapid nucleation of hRad51 proteins onto the DNA substrate and weak cooperative assembly. The existence of these multiple nucleation sites can be clearly seen by assembling successively hRad51 proteins marked with two different fluorophores **[Figure 48]**.

**Figure 48:** Adapted from [130]. Visualization of multiple nucleation sites during formation of hRad51/dsDNA filaments by using fluorescent hRad51 proteins labeled with two different fluorophores (here represented in green and red). Filaments are formed in solution on λ DNA in presence of fluorescent hRad51, ATP and $Ca^{2+}$. They are then deposited on a glass slide for observation. The image on the left is formed with a low concentration of hRad51-AF488 and the image on the right shows the filament obtained after incubation of the first one with hRad51-AF555.

The resulting filaments are then in fact composed of a multitude of short fragments. The mean length of these fragments was estimated by Monte Carlo simulations to be of 21±25 hRad51 monomers (63±45 base pairs) for conditions containing $Ca^{2+}$ and 30±24 monomers (90±72 base pairs) with $Mg^{2+}$ [139]. The same simulation results predict nucleation and growth by pentamers and gaps between fragments up to 14 base pairs. However observation of hRad51-dsDNA filaments formed in ATP and $Ca^{2+}$ by scanning force microscopy (SFM) revealed filament fragments of approximately 500 base pairs (~166 monomers) [130].

It is noteworthy at this point to cite that a mechanism of lateral diffusion of dsDNA bound fluorescent hRad51 complexes has been reported [132]. This mechanism could lead to filament rearrangements, thus compensating for the heterogeneity induced by the dynamics of filament formation. However several other studies have not been able to observe such a behavior, indicating fixed binding of the protein to DNA [130], [135], [136].

## C.IV.2. Filament elasticity

Using a double optical trap setup coupled with fluorescent microscopy, it was possible to study the force-extension curves of those heterogeneous hRad51-dsDNA filaments and to uncouple the contribution of the filaments fragments from the contribution of naked DNA regions [136]. For easier uncoupling of these contributions, partially coated filaments are used instead of fully extended filaments.

**Figure 49:** Extracted from [136]. Elastic properties of a single linear 48kbp dsDNA partially covered with fluorescent hRad51 (labeled with Alexa fluor 555).

 (**A**) Force extension curve of the composite filament. The light gray curve shows the reference curve of a naked linear dsDNA.

(**B-D**) Force extension curves of the naked portion (**i**), the continuous fluorescent portions (**ii**) and the composite fluorescent portions (**iii**).

The first observation stemming from such a study is that the behavior of partially coated DNA molecules differs from the one of a naked DNA molecule as can be seen in [**Figure 49; A**]. However the naked DNA behavior is found if only the non-coated regions are considered [**Figure 49; B**]. The continuous fluorescent regions, assumed to be fully covered in hRad51 proteins, are strictly non-elastic, meaning that they do not extend under tension [**Figure 49; C**]. The composite fluorescent zones are most probably not fully covered with proteins. They display a more complex behavior [**Figure 49; D**] which can be interpreted as a linear combination of the elastic behavior of the naked DNA and the rigid behavior of the continuous regions.

These results lead to the conclusion that dsDNA is rigidly maintained by hRad51 proteins precluding any elasticity. The non coated regions behave exactly like naked DNA.

# C.V. State transitions and protein dissociation

The hRad51-dsDNA nucleoprotein filaments are dynamic systems, capable of exchanging their chemical cofactors with the ones present in solution. Doing so changes their conformation or even triggers protein dissociation. In this section we will review how they behave in single molecule studies when the unbound proteins are removed after filament formation.

## C.V.1. Changing filament conformation

### Converting ATP to ADP

Assembling hRad51 nucleoprotein filaments on dsDNA molecules in conditions containing ATP-$Mg^{2+}$ results in the formation of active ATP-bound conformations extended to approximately 1.5 times the length of the DNA in its B-form. Evacuating both the unbound hRad51 proteins and the free ATP, by insertion of a new buffer containing neither, triggers a decrease in the filaments' extension [**Figure 50**]. Filament decrease continues until an extension approximately 1.25 times the length of B-DNA is reached [119]. Checking at the outlet of the

microfluidic chamber revealed this effect was not solely a consequence of protein dissociation.

Figure removed because of copyrights

**Figure 50:** Extracted from [119]. Experiment in TIRFM showing the evolution of an ATP-Mg$^{2+}$ hRad51-dsDNA nucleoprotein filament when unbound hRad51 proteins and ATP are evacuated. Filaments were assembled in 1µM hRad51, 1mM ATP, 1mM MgCl$_2$, 40mM Tris (pH 7.8), 0.2mg/mL BSA, and 1mM DTT and chased by the same buffer lacking hRad51 proteins and ATP. The assembly and chase phases of the reaction are denoted by respectively blue and yellow backgrounds.

Since ATP hydrolysis is permitted in these conditions, this leads us to the conclusion that the shortening is in fat an expression of the filaments' conversion to an ADP-bound conformation. However formation of filaments in conditions containing ADP **[Figure 45; b]** yields filaments that are barely extended (~1.07 times B-DNA) [131], [135]. Then if both conformations are ADP-bound, the question arises of why their extensions are different.

The obvious conclusion comes that there is a difference between filaments formed in ADP and those which hydrolyzed their ATP. The exact nature of this difference is, to our knowledge, currently unknown. One assumption would be to assume that the first is truly ADP-bound whereas the second still contains the inorganic phosphate and thus is (ADP+Pi)-bound.

## Recycling ATP

Figure removed because of copyrights

**Figure 51:** Adapted from [119]. Experiments conducted in TIRFM showing the evolution of ATP-Mg$^{2+}$ hRad51-dsDNA nucleoprotein filaments' extension in the presence or absence of ATP. ATP stabilizes the elongated hRad51 filaments whereas in its absence the filament contracts to a condensed form (**A**). Filaments were formed as in **[Figure 50]**. They were then chased with buffers that contained varying concentrations of ATP but lacked free Rad51. Reversible transitions between elongated and compressed filaments are shown in (**B**). The filaments were assembled with ATP-Mg$^{2+}$ and then chased with a buffer lacking nucleotide cofactor leading to formation of compressed filaments. Cycles of successive injections of 2mM ATP each followed by washes with buffer lacking nucleotide cofactor are applied.

The conversion of ATP-Mg$^{2+}$ hRad51-dsDNA nucleoprotein filaments from their extended to their condensed conformation requires that no free ATP nucleotides are available. Indeed if ATP is left in solution, the decrease of the filament's extension will not occur **[Figure 51; A]**. Furthermore, re-injecting ATP after the conversion will trigger an inverse conversion where filaments re-extend to almost the length of the extended state **[Figure 51; B]**.

These results indicate that proteins within the filament are able to exchange their hydrolyzed nucleotides with the exogenous ATP. Such an exchange triggers a conversion back to the extended ATP-bound form although full extension is not reached probably due to protein dissociation effects.
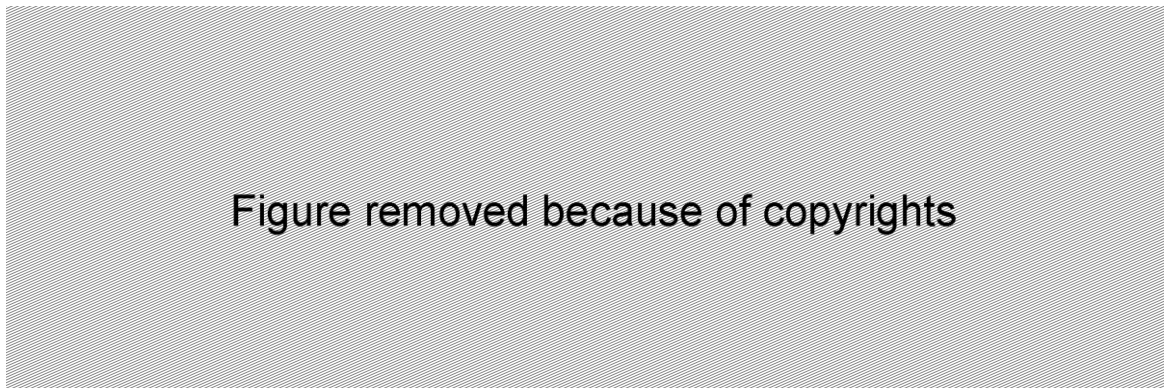
## Inhibiting ATP hydrolysis

Figure removed because of copyrights

**Figure 52:** Adapted from [119]. (**A**) hRad51 nucleoprotein filaments were assembled with ATP and then chased with buffer lacking nucleotide cofactor leading to formation of compressed filaments. 1mM AMP-PNP was then injected into the sample chamber revealing re-elongation of the compressed filaments.
(**B**) Non-hydrolysable nucleotide traps human Rad51 in an elongated conformation. hRad51 filaments were assembled 1μM hRad51, 1 mM AMP-PNP, 1 mM MgCl$_2$, 40mM Tris (pH 7.8), 0.2 mg/mL BSA, and 1mM DTT. The filaments were chased with buffer that contained either 1mM AMP-PNP, ATP, ADP or neither.

Much like the compressed filament are able to replace their hydrolyzed ATP with free ATP in solution, they also may do so with exogenous AMP-PNP, a non-hydrolysable analog of ATP **[Figure 52; A]**. Binding of AMP-PNP by the filament will result in the transition to the extended conformation. Once this state has been reached, no further transition is observed if nucleotides are removed from solution once again. In fact no changes are observed whatever the nucleotide or absence of is injected in the channel afterwards **[Figure 52; B]**.

So contrarily to ATP-bound filaments, AMP-PNP-bound filaments do not convert to the condensed conformation. This result further confirms that conversion from the extended to the condensed conformation requires ATP hydrolysis.

## Transition and torsion

Observation of torsion of filaments formed in ATP-Mg$^{2+}$ in a FRMT setup showed that when in a buffer containing neither protein nor nucleotides, the filament started to wind itself back **[Figure 53]**. The insertion of exogenous ADP in solution completely inhibited this rotation [142].

**Figure 53:** Extracted from [142]. Rotating trace of a hRad51-dsDNA nucleoprotein filament formed in ATP-Mg$^{2+}$. After approximately 20 min of clockwise rotation (polymerization) at 100nM hRad51, rotation became irregular and very slow for approximately 50 min until the bead finally stopped (this latter section was cut in the graph to more clearly display the other sections). After intense rinsing with a protein- and nucleotide-free buffer, rotation started counterclockwise at a slower rate. Inset: histogram of step sizes for 75 steps obtained during depolymerization on 3 different molecules. The best-fit normal distribution has a mean of 67° and standard deviation of 23°.

The interpretation for such a torsion change may go one of two ways. The effect could be a consequence of protein dissociation with the naked DNA molecule winding itself back to its natural torsion. Or the filament could be converting itself to the condensed form as was seen in the TIRFM experiments; such an assumption would lead to the conclusion that the condensed conformation has a twist superior than the extended conformation. The inhibition of the phenomenon by exogenous ADP suggests that nucleotide release is necessary for such a process. A study of the step size during this winding of the filaments yielded an angular value of 67°±23°.

## C.V.2. Protein dissociation

### Protein dissociation and ATP hydrolysis

The behavior of filaments formed in ATP-Mg$^{2+}$ and those formed in ATP-Ca$^{2+}$ differs when unbound hRad51 proteins are absent **[Figure 54]**. Indeed both filaments form in an extended state but evolve differently when unbound hRad51 proteins are washed from the chamber by a buffer containing ATP and one of the two cations but no hRad51. The filaments formed in Ca$^{2+}$ stay locked in their extended state showing no difference with when hRad51 was present. In contrast evacuating the proteins triggers the ATP-Mg$^{2+}$ filaments' extension decrease. This decrease will continue until the initial extension of the naked DNA molecule has been reached.

For the ATP-$Mg^{2+}$ filaments, the presence of exogenous ADP or the absence of nucleotides did not seem to modify dissociation dynamics [139].



**Figure 54:** Extracted from [139]. Filament assembly of hRad51 onto nicked dsDNA (8kbp) in classical magnetic tweezers. The solid lines represent fits based on Monte Carlo simulations.

(**A**) In presence of 25 mM Tris-HCl (pH 7.5), 5mM MgCl2, 25mM KCl, 1mM DTT, 1mM ATP and 187nM hRad51, the molecule extends by approximately 45%.

(**B**) After removal of the hRad51, the molecule's length decreases in presence of ATP-$Mg^{2+}$.

(**C**) In presence of $Ca^{2+}$, behavior is similar to the one with $Mg^{2+}$.

(**D**) After removal of the protein, the molecule's length remains constant in presence of $Ca^{2+}$.

Since free ATP is left in solution in both cases, the decrease in filaments' extension in ATP-$Mg^{2+}$ may not be explained by the conversion to the condensed state. The decrease rate is in fact much slower than what was observed for conversion. This phenomenon is much better explained by dissociation of the hRad51 proteins from the dsDNA molecule. The fact that is does not occur in ATP-$Ca^{2+}$ suggests that ATP hydrolysis is required for protein dissociation. Combined with the facts that this dissociation is slower than the conversion to the condensed conformation and that this conversion may occur without dissociation, it leads us to the conclusion that ATP hydrolysis triggers conformation change before inducing dissociation.

## Effect of salt concentration

The effect of NaCl concentration on the hRad51-dsDNA filaments in the absence of proteins or ATP in solution is shown in [**Figure 55**]. Three regimes can be identified:

- For low NaCl concentrations ($\leq$ 50mM), the conversion the filament to the condensed conformation occurs with its rate decreasing as the concentrations increases.

- At an intermediate NaCl concentration of 100mM, the conversion seems to be stalled.

- For high NaCl concentrations (≥ 250mM), the filament's extension decreases until the length of the naked DNA molecule is reached. This effect may occur as well on filaments that are already condensed **[Figure 55; D]**. Insertion of nucleotides after this phenomenon induces no lengthening of the molecule. Checking for proteins at the outlet of the chamber reveals that this effect is due to protein dissociation.

The logical conclusion one could come to is that the effect of salt concentration on the filament's dynamic are a consequence of the modulation of ATP hydrolysis. However, an ATPase assay on hRad51 proteins in presence of DNA substrates shows no meaningful effect of salt concentration on its ATPase activity. Therefore the effect of salt could be solely a consequence of ionic strength.
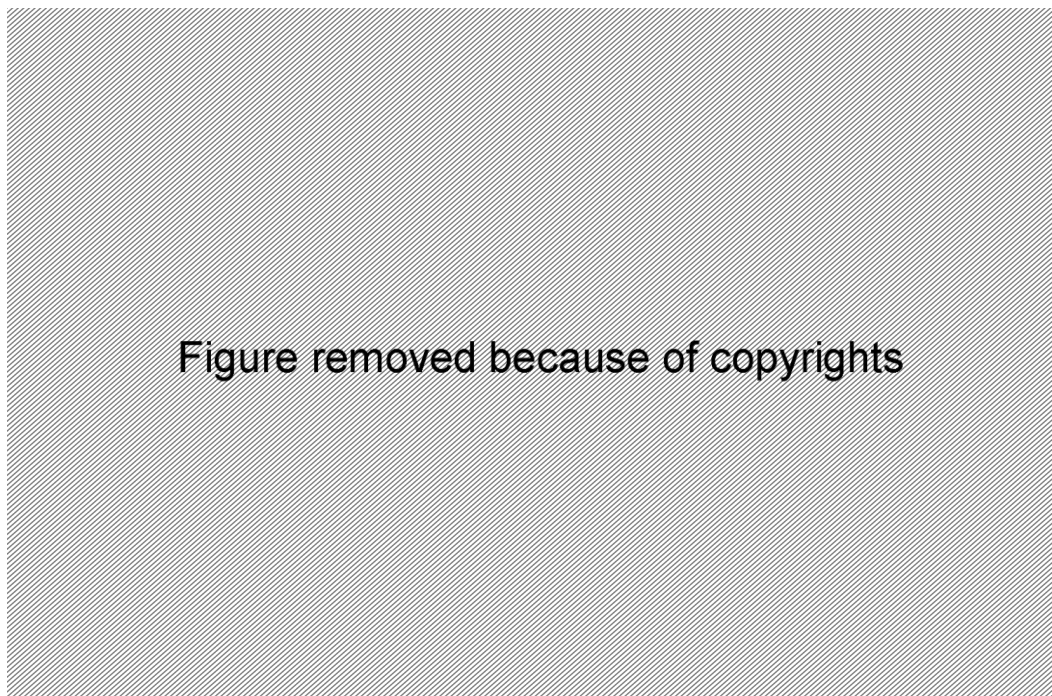
Figure removed because of copyrights

**Figure 55:** Extracted from [119]. Nucleoprotein filaments were assembled with 1μM hRad51, 1mM ATP, 1mM MgCl$_2$, 40mM Tris (pH 7.8), 0.2mg/mL BSA and 1mM DTT. All reactions are performed at 37°C. After assembly, free protein is chased with buffer that lacked hRad51 and ATP and that contained various amounts of NaCl. The assembly and chase phase are marked in blue and yellow respectively.
(**A**) Representatives traces of filament behavior at different NaCl concentrations.
(**B**) Filament shortening rates derived from (**A**)
(**C**) Results from an ATPase assay with hRad51 at various NaCl concentrations.
(**D**) hRad51 nucleoprotein assembled, then chased with 1mM MgCl$_2$, 40mM Tris (pH 7.8), 0.2mg/mL BSA and 1mM DTT. Second chase with buffer containing 500mM NaCl 10 minutes later.

## Stalling protein dissociation

It has been shown in magnetic tweezers experiments that the protein dissociation rate is a function of the pulling force applied on the filament, the rate being slower as the pulling increases [140]. Experiments conducted by van Mameren *and al.* [137] go further. Using a dual optical trap combined with a multichannel flowcell to observe protein dissociation via a

fluorescence signal **[Figure 56]**, they showed that the application of tension to an hRad51-dsDNA nucleoprotein filament could stall protein dissociation.
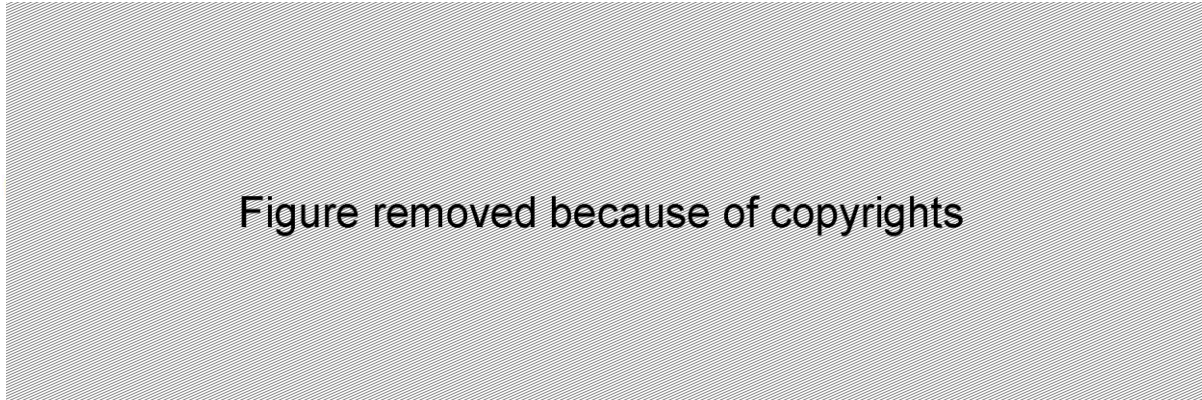


**Figure 56:** Adapted from [137]. Experiment done by van Mameren *and al.* showing the stalling of hRad51 proteins from dsDNA by the application of pulling force. The setup used is a dual optical trap combined with a multichannel flow cell (**A**). Channels are separated by laminar flow; beads are captured in the first channel and are used to capture dsDNA molecules which are in presence of hRad51 and ATP-$Ca^{2+}$. Filament disassembly is triggered by moving the $Ca^{2+}$-stabilized complexes to a buffer containing $Mg^{2+}$ only. Filament disassembly is tracked through the evolution of the fluorescence signal (**B**; kymograph and red profile). Disassembly is associated with an increase of tension as the filament contracts while keeping the positions of the optical traps constant (**B**; blue profile).This experiment shows a correlation between tension and disassembly rate.

Their filaments were formed on dsDNA molecules in conditions containing ATP-$Ca^{2+}$. ATP hydrolysis was then triggered by moving the resulting filament in a buffer containing $Mg^{2+}$ only. Thus their filaments are originally ATP-bound and allowing ATP hydrolysis triggers the conversion to the condensed state and eventually protein dissociation. As protein dissociation occurred, since the positions of the optical traps was kept constant, the tension along the filament increased as it attempted to contract in order to revert back to the length of naked DNA. The most interesting part of these results is that tension increase slowed down and even stalled the dissociation process as a pulling force of F=48±3pN was reached. They of course checked successfully that releasing the tension resumed the dissociation process thus demonstrating that it was indeed the application of force that stalled it in the first place.

The rate decrease versus the force applied was well fitted by a single exponential, suggesting a dependency according to Arrhenius's law:

$$k(F) = k(0)\exp\left(-\frac{x_B F}{k_B T}\right)$$

In which k is the decrease rate, $k_B T$ is the thermal energy, F is the tension, and $x_B$ denotes the distance to the transition state along the relevant reaction coordinate. They further determined this distance to have a value of:

$$x_B = 0.27 \pm 0.04 nm$$

This latest result will be of particular interest to us, and we will come back to it during the discussion in chapter 4.

## C.V.3. Cofactor turnover



**Figure 57:** Extracted from [130]. Constructs were assembled by incubation of one-end biotinylated 48kbp dsDNA molecules with Alexa Fluor 488-labeled C319S RAD51 in the presence of ATP and $CaCl_2$ and tethered on streptavidin-coated glass. The tethered end corresponds to the fixed end of the construct that is attached to the glass. On the left are shown kymographs from time-lapse movies showing the behavior of a construct under $CaCl_2$-ATP conditions for 15 min (top) and for 45 min after switching to $MgCl_2$-ATP conditions (bottom). On the right is the representative plot of the disassociation of Alexa Fluor 488-labeled RAD51 from a 48kbp dsDNA molecule. Disassociation in presence of $MgCl_2$-ATP (red, bold line: fit to first order exponential decay) or $CaCl_2$-ATP (blue, bold line: fit to linear regression).

Multiple experiments on hRad51-dsDNA nucleoprotein filaments in single molecule studies show the possibilities of cofactor turnover. We've already seen that exogenous ATP is able to replace the hydrolyzed ATP in the filament **[Figure 51]** and that the same is true for exogenous AMP-PNP **[Figure 52]**.



**Figure 58:** Extracted from [135]. Experiments showing the evolution of hRad51-dsDNA nucleoprotein filaments' extension in response of various chemical conditions change.

(**A**) Nucleoprotein filaments of hRad51 proteins on dsDNA (hRad51 on the left and hRad51FAM on the right) are formed in the presence of 2mM $Ca(OAc)_2$ and 1mM ATP and allowed to disassemble in the presence of 5mM $Mg(OAc)_2$ and 2mM ATP.

(**B**) hRad51-dsDNA filaments (hRad51 on the left and hRad51FAM on the right) are formed in the presence of 2mM $Mg(OAc)_2$ and 1mM ATP and allowed to disassemble in the presence of 5mM $Mg(OAc)_2$.

(**C**) hRad51-dsDNA filaments (hRad51FAM) are formed in the presence of 2mM $Mg^{2+}$ and 1mM ADP and allowed to disassemble in the presence of 5mM $Mg^{2+}$. In A–C, still images of the nucleoprotein filaments at the start and end of the reactions are indicated above and below the kymographs. The original length of the DNA in this experiment was slightly shorter at 13.5µm and extended to only 14.5µm.

(**D**) Trajectories for the data shown in **A–C**. Experiments using hRad51 are in black; those using hRad51FAM are in green. Solid blue lines represent linear ($Ca^{2+}$-ATP) and nonlinear ($Mg^{2+}$-ATP and $Mg^{2+}$-ADP) fits to the data.

It can also be shown that exogenous $Mg^{2+}$ cations are able to replace the $Ca^{2+}$ cations within the filament. Such an exchange will trigger ATP hydrolysis which was previously prevented by the calcium resulting in the decrease of the filaments' extension as protein dissociation occurs **[Figure 57 and Figure 58; A]**.

Formation of filaments on dsDNA in conditions containing ADP resulted in the formation of very slightly extended conformations (~1.07 times the length of B-DNA). Removing the exogenous ADP from solution triggers extension decrease back to the length of the naked DNA molecule **[Figure 58; C]**. This effect may be explained by protein dissociation, further confirming that the presence of ADP in solution stabilizes nucleoprotein filaments [118]. This stabilizing suggests that protein dissociation requires the prior release of the nucleotide; the presence of free ADP would then prevent its release through the modification of the chemical potential.

# Chapter 2: Magnetic tweezers

## A. Building the setup

### A.I. Functioning principle

Initially developed in the 1990s to study DNA response to tension and torsion [158], the magnetic tweezers is a technique for the manipulation of multiple single dsDNA molecules. The main advantage of magnetic tweezers is the ability to apply controlled torsion and tension to the DNA while measuring its end to end extension. Magnetic tweezers remain to this day one of the only ways to apply torsion to single dsDNA molecules.

Experiments take place within a microfluidic chamber which grants control of chemical conditions around the manipulated DNA. Buffer flow may be modulated at will through the use of an electric syringe pump, used to aspirate buffers out of the chamber. Use of the pump in aspiration mode avoids unnecessary buffer contamination in contrast with buffer injection where buffers are placed within the syringe prior to insertion.

The bottom of the chamber is made out of a thin glass cover slide approximately 170µm thick, allowing optical observation from the bottom through a 100x oil microscope objective. The image is projected onto a CCD camera whose signal is sent in real time to a computer interface. A monochromatic light source is placed above the chamber.

In our case, the extremities of the dsDNA molecules have been modified by construction to include digoxygenin-marked nucleotides at one end and biotin-marked nucleotides at the other. The glass slide is coated with anti-digoxygenin protein fragments which specifically bond to the digoxygenin-marked end of the molecules. The biotin-marked ends specifically bond to streptavidin-coated paramagnetic beads. Since both strands of the extremities of the dsDNA molecule are marked, both are bonded to their respective receptors. Thus if no single-strand nicks are present, the dsDNA molecules are torsionally constrained.

Control over the beads is achieved through their interaction with permanent magnets placed over the chamber. The shape and configuration of those magnets vary depending on the type of magnetic tweezers used.

### A.I.1. Classical magnetic tweezers

What is being referred to here as "classical" magnetic tweezers is a setup where two identical permanent magnets are placed symmetrically with opposite polarities over the microfluidic chamber **[Figure 59]**. The one used in the institut Curie has been developed by Aurélien Bancaud during his phD [159] in collaboration with Vincent Croquette and David Bensimon's team (Laboratoire de Physique Statistique, Ecole Normale Supérieure).
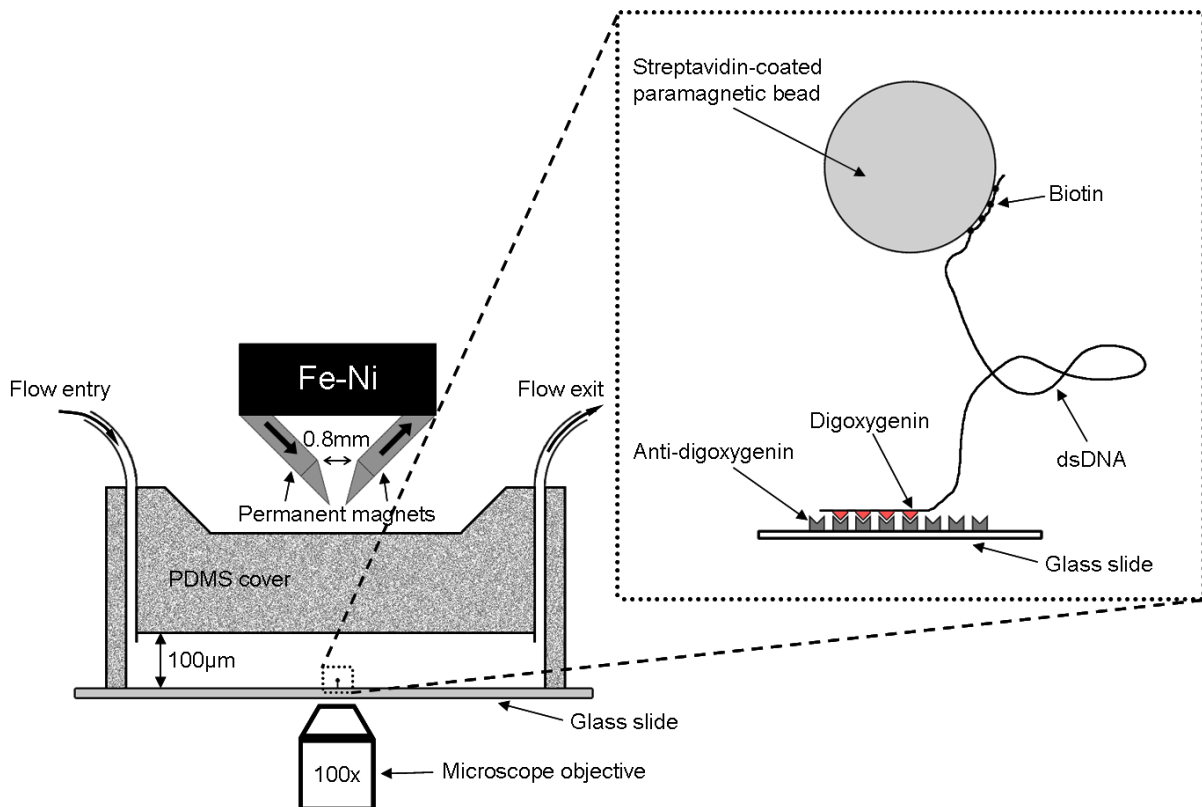
**Figure 59:** Schematic representation of the classical magnetic tweezers setup developed by Aurélien Bancaud. The framed representation on the right is a zoom of the small frame on the left.

Two parallelepiped shaped permanent magnets composed are placed symmetrically over the chamber with a 45° angle with opposite polarities. They are composed of a Neodymium-Iron-Boron alloy (NdFeB) and possess a persistent magnetic field of about 1.3T. In order to guide to the field lines, two pieces of Iron-Cobalt alloy (FeCo), shaped as tips, are placed at the ends of both magnets so that the air gap between them is of 0.8mm. This alloy has a very high magnetic permeability and its saturation field exceeds 2T. The magnetic circuit is closed on top by a block of Iron-Nickel alloy (FeNi). This configuration allows for the creation of magnetic fields within the chamber of approximately 0.3T and vertical gradients around 0.4T.mm$^{-1}$ when the magnets are placed 500µm over the chamber (minimal distance to which the magnets can be brought to) [159].
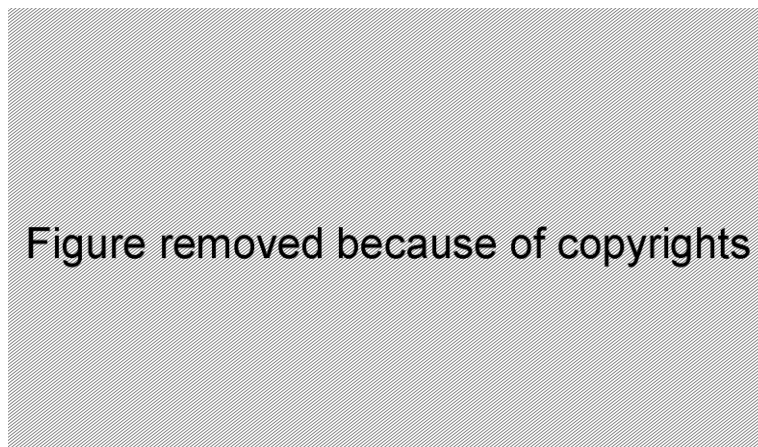


**Figure 60:** Adapted from [160]. Hysteresis loops (magnetization versus magnetic field) at room temperature for M-280 Dynabeads in the field range ±1T. Inset figure shows the hysteresis loops in the field range ±10 mT.

For DNA binding, streptavidin-coated paramagnetic beads of 2.8μm in diameter are used (M-280 Dynabeads®). Those beads display a high magnetization response even with relatively low magnetic fields. Indeed, almost 80% of their saturation magnetization is reached for fields of approximately 0.1T [Figure 60]. One of their characteristics is to display a preferential direction for magnetization. Therefore, if allowed to freely rotate, the beads will tend to align this specific direction with the magnetic field to which they are exposed. In the classical configuration, the generated field is horizontal and relatively homogeneous in the horizontal directions over the observed area (200μm x 200μm) [Figure 61].

The magnets are able to rotate around the vertical axis; their rotation is controlled by a modified step by step micrometric controller (M-126.PD1, PI Instruments). Magnet rotation induces the modification of the magnetic field direction within the chamber. The bead will tend to align its preferential direction with the field and thus follow the rotation of the magnets. Both strands of the dsDNA molecule are bound by multiple nucleotides to the bead and to the bottom of the chamber by multiple nucleotides. Thus rotation of the bead results in a simultaneous rotation of both strands which leads to the application of a torsional constraint to the DNA. Accumulation of torsion is of course possible only if the sugar backbone of both strands is intact. If not, then the molecule will be able to release torsion through the free rotation around the monovalent phosphodiester bond at the site of the single strand nick. Nicked dsDNA molecules are used in magnetic tweezers when one wishes to not apply any torsional constraints.
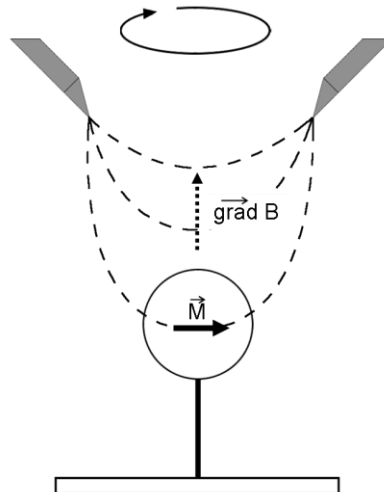


**Figure 61:** Schematization of the magnetic field lines in a classical magnetic tweezers setup. The magnetization moment aligns with the horizontal magnetic field and the field gradient is vertical.

The field gradient is vertical inducing a vertical magnetic force applied on the bead. If the $u_z$ is the unit vector in the vertical direction and $u_x$ the unit vector in the horizontal direction given by the magnets, then the magnetic force applied to the beads may be expressed as follows:

$$\vec{F}_{mag} = \vec{\nabla}\left(\vec{M} \cdot \vec{B}\right) = M \cdot \frac{dB}{dz}\vec{u}_z, \ \text{ if } \vec{B} = B\vec{u}_x \text{ and } \vec{M} = M\,\vec{u}_x$$

The height of the magnets is controlled by a step by controller with a 25mm translation range (also M-126.PD1, PI Instruments). The closer the magnets are to the chamber, the higher is the force applied. Those forces range from 0 to 15pN when using the M-280 Dynabeads.
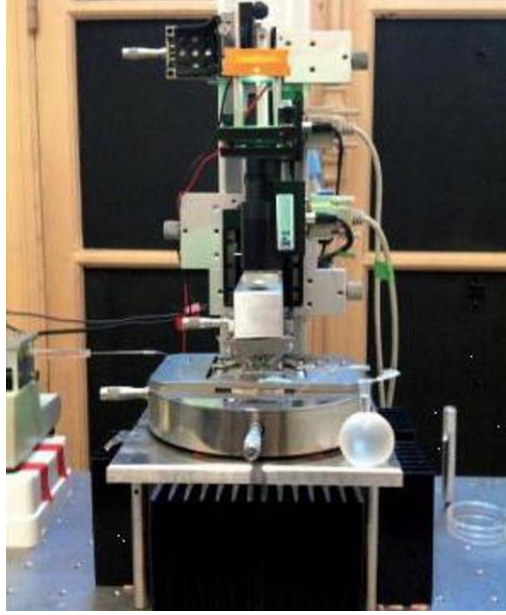
**Figure 62:** Photograph of the classical magnetic tweezers experimental setup used at the institut Curie.

Illumination comes from above, through the gap between the two permanent magnets. A high power LED (LUXEON 5-Watt Star; LXHL-LM5C) is used, giving off a monochromatic light centered on 520nm and concentrated by a converging lens. The position of the light source at the zenith is essential for the formation of the beads' diffraction patterns, which is used for the elongation tracking.

The microscope objective is mounted on a piezoelectric translation motor in order to offer nanometric control of the focus position. The setup has also been modified by Pierre Recouvreux during his phD [161] to include thermal control through the use of a Pelletier module and a thermocouple sensor. I used this setup as it was, except for changing the optic block between the microscope objective and the CCD camera in order to expand the observation field; the final observation field was 120 x 120μm wide (originally 80 x 80μm).

## A.I.2. Allowing rotation in magnetic tweezers

In classical magnetic tweezers, the horizontal magnetic field generates a very high torque on the bead (~$10^7$ pN.nm.rad$^{-1}$). In most instances such a high torque is an advantage, as it erases the thermal fluctuations and allows the experimentalist to fix the DNA topology in a deterministic manner. However, it becomes a limitation when one wants to measure the very small torques generated by the biological enzymes associated to the DNA molecule (~10-30pN.nm.rad$^{-1}$). During my thesis, I developed a new generation of magnetic tweezers imposing a vertical magnetic field with a vertical gradient. This configuration allows minimizing the torque on the bead. If this torque is small enough, the application of small biological torques on the DNA molecule will induce the rotation of the bead. Thermal angular fluctuations are then no longer negligible and may be used to measure the strength of the applied magnetic torque. The vertical gradient of the field ensures the application of a vertical magnetic pulling force:

$$\vec{F}_{mag} = \vec{\nabla}\left(\vec{M} \cdot \vec{B}\right) = M \cdot \frac{dB}{dz}\vec{u}_z, \ \text{ if } \vec{B} = B\,\vec{u}_z \text{ and } \vec{M} = M\,\vec{u}_z$$

In an ideal situation, the torque applied to the bead has no component along the axis of rotation. In reality, the position of the magnets over the chamber is adjusted to minimize the horizontal component of the magnetic field for the beads of interest. Two magnet configurations are possible for the creation of such a magnetic field: a magnetic tip or a hollow cylindrical magnet [**Figure 63**]. Both configurations will result in the creation of vertical magnetic field lines directly under the magnets.
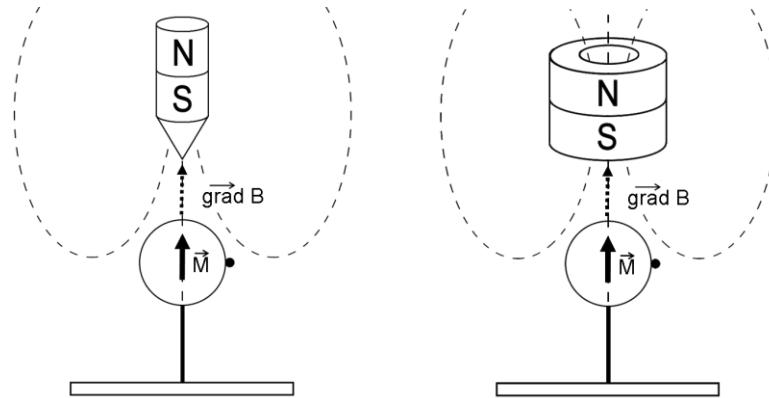


**Figure 63:** Schematization of the magnetic field lines (dotted lines) in free-rotation magnetic tweezers setups. The magnetization moment aligns with the vertical magnetic field and the field gradient is vertical. On the left is shown a schematic of the FRMT setup using cylindrical magnets and an iron tip. On the right is shown the schematic of a setup using hollow cylindrical magnets. The field lines are the same as in the previous setup in the vicinity of the bead.
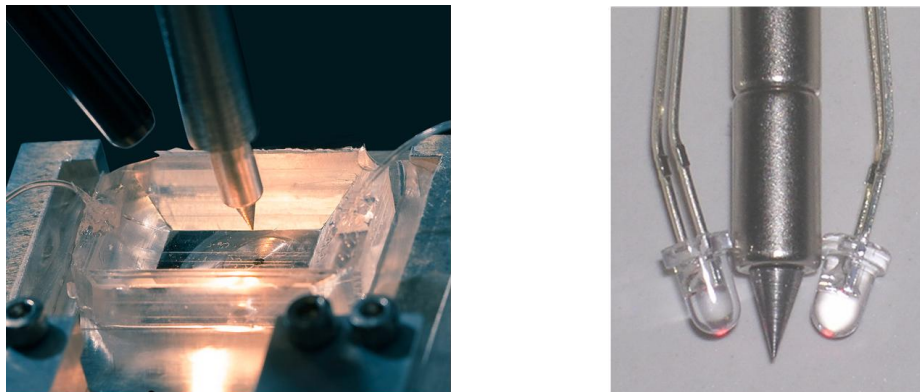
## Free rotation magnetic tweezers



**Figure 64:** Adapted from [143]. On the left, photography of the FRMT experimental setup; illumination is achieved by the use of an optical fiber (top left on the photo). On the right, photography of the magnetic tip coupled with two LED to achieve better homogeneous illumination.

The free rotation magnetic tweezers (FRMT) were originally developed by Harada *and al.* [144] for the study of DNA rotation during the transcription by the *E.Coli* RNA polymerase. The setup was then reproduced and adapted to the study of hRad51 by Arata Hideyuki during his post-doctorate at the institut Curie [142] and improved by Aurélie Dupont during her phD [143]. These tweezers made use of neodymium cylindrical magnets with an iron tip on the end to concentrate the magnetic field lines.

One the main problems associated with such a setup was the illumination method, which could no longer come from the top along the axis of rotation as in the classical

magnetic tweezers. In their first version, the light source was a helium lamp whose light was directed by an optic fiber **[Figure 64; left]**. This solution resulted in the loss of the diffraction pattern and inhomogeneous shading of the beads' images rending rotational tracking difficult. A second version aiming to compensate for this problem was designed with a pair of LED adjusted on the side of the tip **[Figure 64; right]**.
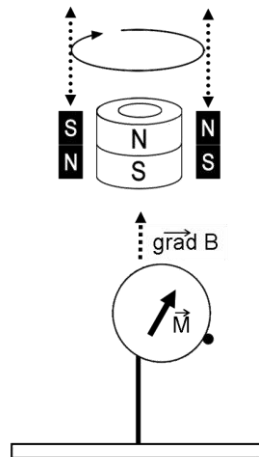
## Hybrid magnetic tweezers



**Figure 65:** Schematization of a hybrid magnetic tweezers. Small magnets on either of the main hollow cylindrical magnet are mobile in the vertical direction and able to rotate. The magnetization moment aligns with the quasi vertical magnetic field which also has a small horizontal component. The field gradient remains vertical.

During my phD, I built a new magnetic tweezers setup aiming to easily switch between a classical configuration allowing to impose a supercoiling degree and a free-rotation configuration allowing the rotation of the beads around the vertical axis. In order to achieve such flexibility we chose to build a setup with a main hollow cylindrical magnet coupled with a pair of smaller cylindrical magnets which can be raised or lowered at will **[Figure 65]**. When raised, the contribution of the smaller magnets is considered to be negligible and thus the setup is equivalent to a configuration with a single hollow cylindrical magnet producing a vertical magnetic field. If lowered, the smaller magnets add a small horizontal component to the magnetic field so as when they rotate, the beads follow this horizontal component through the action of the magnetic torque applied to them.
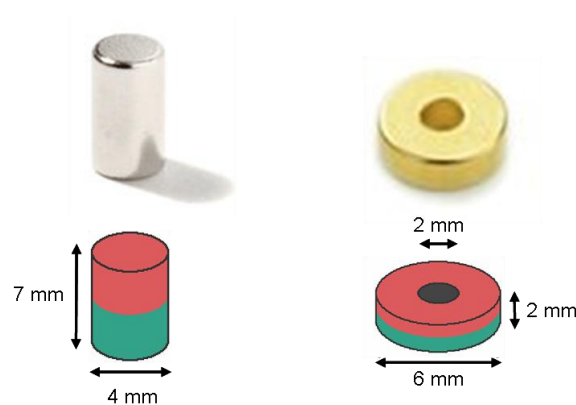


**Figure 66:** Photographs and outlines of the magnets used in the hybrid magnetic tweezers setup. The cylindrical magnet (S-04-07-N) on the left and the ring magnet (R-06-02-02-G) on the right. The north poles of the magnets are shown in red and the south poles in green.

For the construction of the main hollow cylindrical magnet, we stacked three ring magnets (Supermagnete; R-06-02-02-G) which are 2mm thick with a diameter of 6mm and a hole diameter of 2mm [Figure 66; right]. For the smaller magnets, we used two cylindrical magnets (Supermagnete; S-04-07-N) which are 7mm high with a diameter of 4mm [Figure 66; left]. Those magnets were placed on diametrically opposed sides of the main magnet with opposite polarities such as shown in [Figure 65].
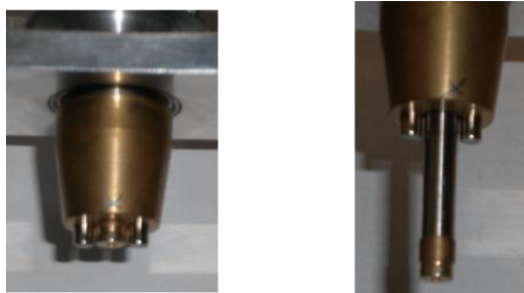


**Figure 67:** Photography of the magnet configuration in the hybrid magnetic tweezers setup. The smaller magnets are lowered on the left are raised on the right. The height difference is of 25mm. The smaller magnets are separated from the main one by gaps of 0.2mm.

A customized holder made of tin was fabricated by Rémy Fert (mechanical workshop of the institute Curie) [Figure 67]. This holder allows the small cylindrical magnets to be kept at distance of 0.2mm from the main magnet. The latter is held by a small tin component attached to a hollow quenched steel rod (custom ordered from A.M.P.L. SARL) of 15cm in length, with an external diameter of 6mm and an internal diameter of 3mm. The steel rod goes through the small magnets' tin holder and is guided by a linear ball bearing (LBBR6A, SKF) within the holder. This setup allows for the tin holder to slide along the steel rod and to rotate around it. The relative height between the main and the small magnets is controlled by a linear translation stage (M-126.PD1, PI Instruments). The maximum value for this height is 25mm.
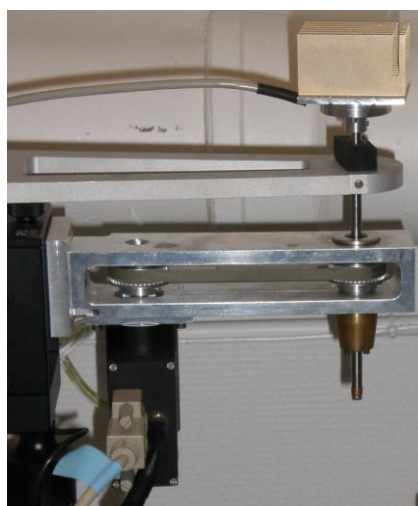


**Figure 68:** Photograph of the structure holding the magnets in the hybrid magnetic tweezers setup. An aluminum overhang holds the quenched steel rod in position and a power LED is attached to the top of the rod (not visible under the radiator). The tin holder for the small magnets is attached to an aluminum component which is connected to a linear translation stage. This stage controls the relative height between the small magnets and the main one. Both the linear stage and the overhang for the steel rod are connected to a second linear stage (out of the picture on the left) controlling the height of the whole setup relatively to the microscope. A third motor (modified M-126.PD1) controls the rotation of the small magnets' tin holder through a driving belt.

The structure maintaining the magnets over the microscope is shown in [**Figure 68**]. The whole setup is connected to a linear translation stage (M-126.PD1, PI Instruments) with a travel range of 25mm. This stage controls the height of the setup relatively to the microscope. When lowered to the maximum, the main magnet almost touches the microscope objective.

On this translation stage is fixed an aluminum component with an overhang which holds the quenched steel rod in place. The latter is fitted with a high power LED (LUXEON 5-Watt Star; LXHL-LM5C) so that the emitted light is transmitted through the hollow steel rod and comes out through the hole of the main hollow cylindrical magnet. This allows for a homogeneous monochromatic lighting favorable for the observation of the diffraction patterns of the beads needed for the extension measurements.

Connected to the aluminum component is a second translation stage which controls the height of the small cylindrical magnets without affecting the height of the main one. It also carries a third motor (modified M-126.PD1) which controls the rotation of the small magnets' tin holder through a driving belt. The tin holder is allowed to rotate around and slide along the steel rod.

This whole structure is connected to a pair of translation stages which allows the precise placement of the magnets in XY-plane. These stages are controlled through step by step microcontrollers (NewStep Linear Actuators, Newport) which have a travel range of 11mm. They rest upon a customized aluminum linking piece which provides the connection of the whole setup to a supporting column fixed to an optical table.
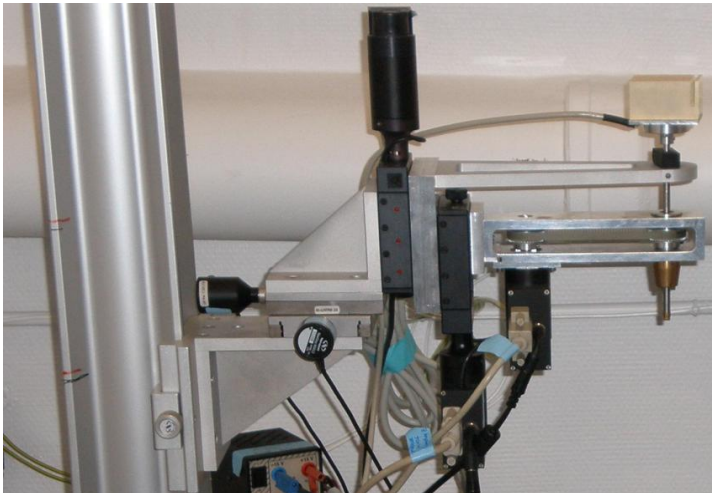


**Figure 69:** Photograph of the structure for holding the magnets. The structure is linked to two translation stages allowing for displacement in the XY-plane (photograph on the right). Those are in turn connected to a supporting column which is fixed directly on an optical table.

Under the magnet-holding setup is a custom-built microscope made out of solid aluminum. On top of it rests manual linear translation stages for the placement of the microfluidic chamber over the objective [**Figure 70; right**]. A 100X oil microscope objective (Olympus UPlanSPpo 100x / 1.40 Oil) with a numerical aperture (NA) of 1.4 is mounted on a piezo nanopositioning device (P-721.CLQ, PI Instruments) with a travel range of 140μm to control the objective's focus. The image from the objective is projected onto a CCD camera (Pike F-421B, Allied Vision Technologies) placed on the side via reflection on a mirror placed at an angle of 45°. The observation field is slightly over 200μm x 200μm allowing for a bead of 2.8μm in radius to be represented by a width of over 30 pixels.
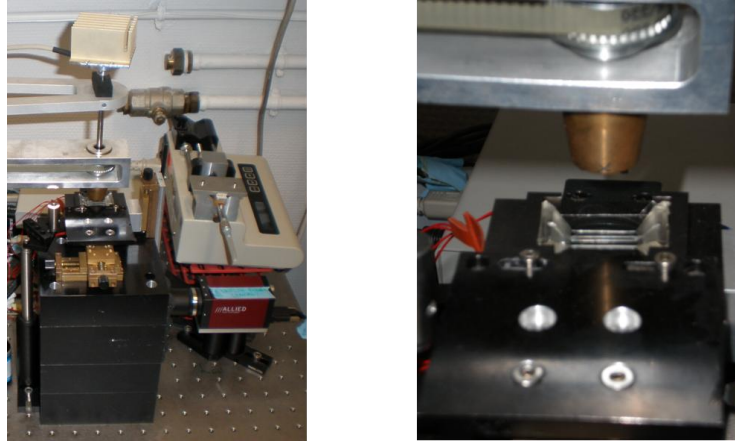
**Figure 70:** Photographs of the microscope used in the hybrid magnetic tweezers setup.

As it was done in the previous versions of the free-rotation magnetic tweezers, thermalisation is achieved through three heating resistor of approximately 50Ω each (MINCO) placed on the inside of the specimen holder **[Figure 71]**. The latter is made out of aluminum and is in direct contact with the microfluidic chamber. Thus the specimen is heated by convection through the contact with the holder, the microscope objective, the oil and the heated air inside the holder. The temperature is controlled by PID controller (custom built by Jean-Hugues Cordabox, Electronic Workshop of the insitut Curie). The precision in the set temperature is of approximately 0.1°C.
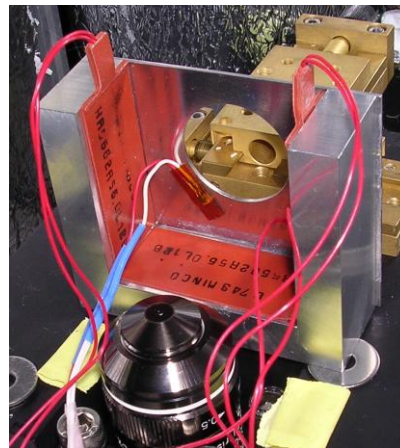


**Figure 71:** Photograph of the inside of the specimen holder in the hybrid magnetic tweezers setup. Three heating resistors are placed on the vertical sides of the inside of the holder. The temperature is measured by a platinum resistance thermometer placed directly under the holder, where the microfluidic chamber is positioned.

The six motors and the CCD camera are interfaced with a computer through a program I developed during my phD in Matlab **[Figure 72; right]**. It allows to control the XYZ- position of the main magnet (X, Y and MainZ), the relative position of the small magnets compared to the main one and their rotation (SecondZ and Rot) and the focus height of the microscope objective (Focus). The images from the CCD camera (1024x1024 pixels, 30 images per second) are stored directly on hard drive for post-experiment analysis. With our current computing power, using our algorithms to track one bead takes about a tenth of the experiment time. So it is currently impossible to track in real time more than 3 to 5 beads (some of the computing power is not available during an experiment, it is needed for the running of the program).
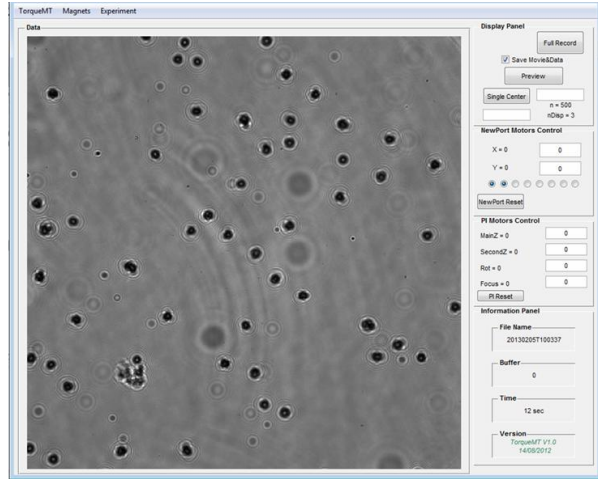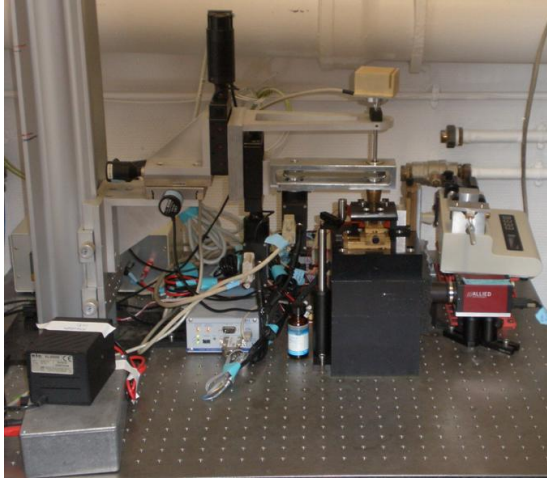
**Figure 72:** On the left, photograph of the full hybrid magnetic tweezers setup (PC excluded). On the right, snapshot of the program used to control the setup during an ongoing experiment.

# A.II. The microfluidic flowcell

## A.II.1. Flowcell design

Our magnetic tweezers experiments take place within a microfluidic flowcell allowing us to control the buffer conditions at all time. This chamber is comprised of a PolyDiMethylSiloxane (PDMS) cover on top of silanized glass slide **[Figure 73]**; an inverted pyramidal shape with carved out sides was adopted in order to achieve a PDMS layer as thin as possible over the channel while maintaining an easy to manipulate PDMS cover for assembly. The thickness of the PDMS over the channel is of 300µm which means the magnets may approach the DNA-bead complexes at a minimum distance of 500µm (the channel in itself is 100µm high).



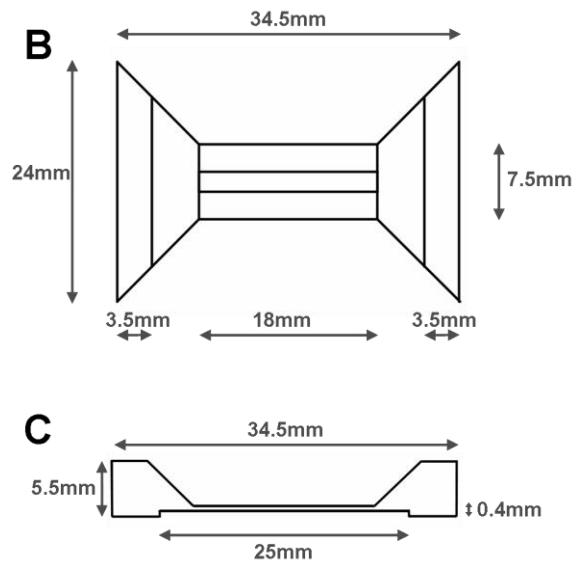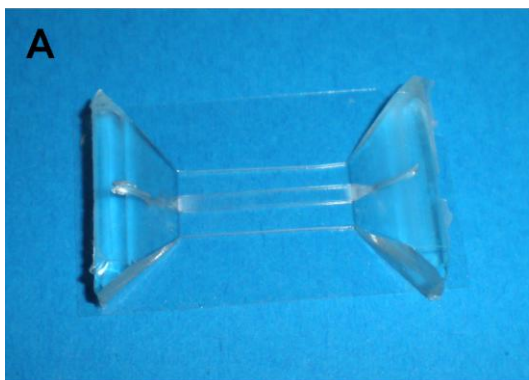**Figure 73:** The microfluidic chamber is made out of a PDMS cover on a silanized glass slide. A photograph of the chip is shown in (**A**). Schematic views from the top (**B**) and transversal cut (**C**) are shown with the dimensions of the chip (the transversal cut is not entirely drawn to scale). The PDMS layer over the channel was made to be as thin as possible with a thickness of 300µm (the channel is 100µm high).

The chamber design does not need to be overly complicated to suit our needs; a single channel of 25mm in length, 2mm wide and 100μm high allows us to form the DNA-bead complexes and effectuate buffer exchanges. The total volume of the chamber contains a little over 4μL. A few special modifications were made to the original design in order to improve efficiency.

First, the ends of the channel were narrowed in order to allow a better evacuation of buffers and air bubbles [**Figure 74; A**]. This design limits the dead volume of the chamber at both the entrance and the exit.
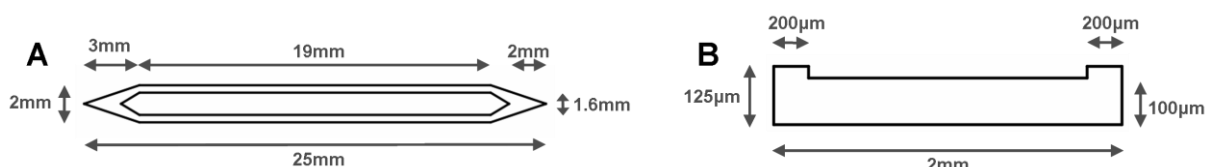


**Figure 74:** Schematic views of the microfluidic channel from the top (**A**) and from a traversal cut (**B**) with the dimensions indicated. Drawings are not to scale. The channel is 25mm long, 2mm wide and 100μm high. It narrows at each end to allow a better evacuation of buffers. The top of the channel is patterned so that the sides of the channel are higher than the middle in order to trap unevacuated paramagnetic beads.

Also, we tried to address the recurring problem of bead clouds during magnetic tweezers experiments. In order to form the DNA-bead complexes, a great deal of paramagnetic beads is inserted into the flow chamber and only a small portion of those beads are connected to a DNA molecule (less than 10%). The rest of the beads need to be evacuated from the chamber prior to starting the experiment. For this reason, long rinsing times are required. Unfortunately, due to the beads' weight, they have a strong tendency to sediment at the bottom of the chamber even during buffer exchange. The Poiseuille profile of the directly implies that the buffer flow speed is minimal near the edges of the chamber. This effect is even greater on the sides of the channel, since the beads are near the channel walls and on the floor of the chamber. Therefore, despite meticulous rinsing steps, there always remains a number of unattached beads in the channel. When the magnets are lowered near the chamber, those unattached beads are pulled towards the ceiling. When the magnets are left immobile, the effect is negligible and one can minimize the inconvenience by choosing an observation field far from the channel's sides. However, as the magnets are instructed to rotate, motion is given to all these unattached beads and they tend to converge horizontal towards the point where the magnetic field gradient is the greatest, right under the magnets. This also coincides with where the experimenter's observation field is. The overall effect is that as the experiment progresses in time, more and more unattached beads appear in the observation field on the ceiling of the chamber where they tend to aggregate and form clouds. While those beads do not interact with the DNA-bead complexes situated on the floor, they have an annoying tendency to obstruct the view, rendering difficult or impossible to track the movement of the beads we are interested in. Since most of the unattached beads come from the sides of the chamber, the ceiling above them was patterned to be higher than the rest of the chamber [**Figure 74; B**]. The idea is that when the magnets pull the beads towards the ceiling, they would stay trapped inside those structures and would not be able to move horizontally towards the observation field.

## A.II.2. Flowcell fabrication and surface treatment

In order to produce a PDMS cover with the desired form, a custom PMMA casing was constructed to impose the inverted pyramidal shape. The channel was originally formed using

a master composed of a glass wafer with a shaped negative photoresist (SY355) on top. However, to accommodate for the patterned ceiling, we switched to a mechanically patterned aluminum wafer custom made by Remy Fert (institut Curie mechanical workshop). After PDMS curing, the sides of the pyramid are manually carved out to allow for the magnet size of the hybrid magnetic tweezers setup.

The bottom of the chamber is made with a 24x40mm glass cover slip (BB024040A1, Menzel-Gläser) whose thickness is comprised between 130 and 160μm. A thickness of less than 200μm is required for observation with 100X microscope objective.

After thoroughly washing the glass cover slip in 5M sodium hydroxide for 2h, it is coated with a silane solution (Sigmacote, Sigma) during 15min and cured for 1h at 150°C. These silanized glass slides may be kept for a few weeks after coating.

Usually, the bonding between PDMS and glass slides is achieved through plasma treatment. However this solution is not possible due to the previous coating of the glass slides, because the plasma treatement will strip the silane from the surface. Therefore bonding of the glass and the PDMS is achieved solely by depositing the PDMS cover on top of the glass slide and curing at 65°C in order to remove any residual humidity between the two which could weaken the bond.

Two silicon tubes inserted at each end of the channel to allow the control of flow through the use of an electric syringe pump. The pump is connected to the exit tube and buffers are being sucked out the chamber by the syringe. The use of the syringe in an aspiration mode limits buffer contamination by the syringe.

The final steps in surface treatment take place inside the chamber. The first consists of non-specific bonding of anti-digoxygenin fab fragments (Roche) to the silane coat for 2h at 37°C. The anti-digoxygenin will allow the specific bonding of the DNA constructs to the chamber floor. The second step aims to limit non-specific adhesion of the paramagnetic beads by coating the surface with poloxamers (Pluronic F-127, Invitrogen).

# A.III. DNA construct
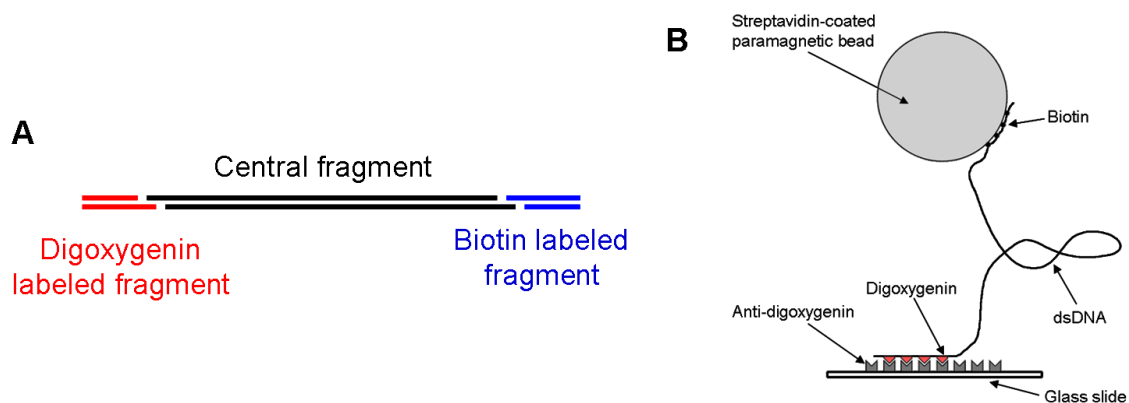


**Figure 75:** The DNA contruct (**A**) is composed by a long central fragment (10 to 15 kbp) to which are attached on one end a digoxygenin labeled fragment and on the other end a biotin labeled fragment (approximately 200 bp each). The digoxigenin labeled fragment allows for specific adhesion of the dsDNA to the anti-digoxygenin coated glass slide that forms the bottom of the microfluidic chamber. The biotin labeled fragment bonds to the streptavidin coated paramegentic beads (**B**). Both strands of the dsDNA fragments on each end are labeled so that the DNA construct is torsionally constrained between the glass slide and the bead,

The principle of the DNA construct in magnetic tweezers experiments is always the same. A long central fragment of DNA constitutes the core of the DNA construct. On each

end of this central fragment are attached labeled fragments that will allow for specific bonding of the construct to the bottom of the microfluidic chamber on one end and the paramagnetic bead on the other **[Figure 75]**.

The labeled fragments are fabricated through PCR (Polymerase Chain Reaction) with a portion (typically 25%) of modified nucleotides present during the DNA formation. As such, both strands of the fragments are randomly labeled with their respective markers. This results in a bond with both strands of the DNA attached on each end of the construct. Therefore the dsDNA molecule is torsionally constrained by the bottom of the chamber and the paramagnetic bead. Thus rotating the bead is equivalent to changing the twist of the attached dsDNA.

## A.III.1. Fabrication by PCR
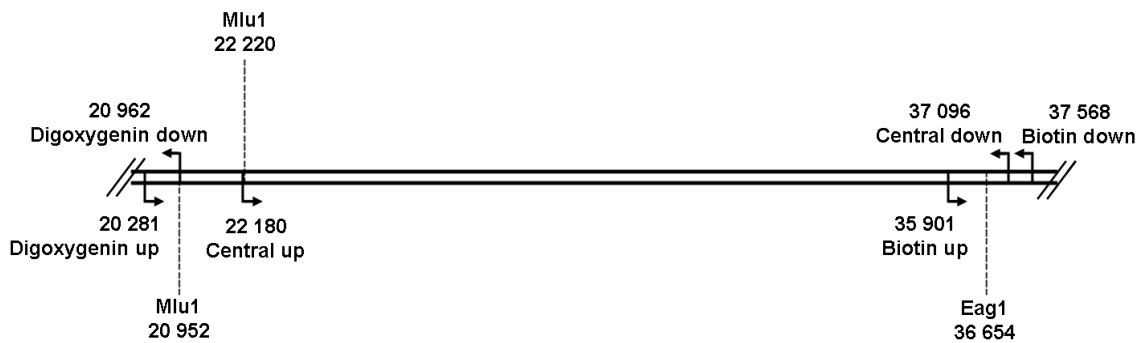


**Figure 76:** Map of the λ phage's DNA in the area of interest with primer positions and enzyme nicking sites.

### Central fragment

Originally [157] the central fragment was produced by amplification through PCR of 14917bp fragment of the λ phage's DNA between the positions 22180 and 37096 **[Figure 76]**. Since the sequence is especially long for PCR amplification, a special PCR kit for long sequences was used: *Expand Long Template PCR System* (Roche). The sequences of the primers used are as follows:

Central up: 5' GAC CAT CGG GGT AAA ACC GTC TAT GAC 3'
Central down: 5' GCG ACT TAC CGC AGC AAA AAT AAA GGG 3'

For the PCR reaction of the central fragment, the following protocol is followed; for a total reaction volume of 50µL, the solution contains:

- 330nM of each primer (Central up and Central down)
- 350µM of each nucleotide (dATP,dTTP,dGTP and dCTP)
- 2ng of the λ phage's DNA (ie 4pg.µL$^{-1}$)
- 3.75 units of the DNA polymerase enzyme of the *Expand Long Template PCR System* kit
- 50mM Tris-HCl (pH 9.2@25°C), 16mM $(NH_4)_2SO_4$ and 1.75mM $MgCl_2$

The following parameters for the thermal cycles were used:

| Cycles | Step | Temperature | Time |
|--------|------|-------------|------|
| 1X | 1 | 94°C | 2' |
| 10X | 2 | 94°C | 10" |
| | 3 | 59°C | 30" |
| | 4 | 68°C | 12' |
| 15X | 5 | 94°C | 10" |
| | 6 | 59°C | 30" |
| | 7 | 68°C | 12' + 20" |
| 1X | 8 | 68°C | 7' |
| | 9 | 4°C | ∞ |

The PCR product is then purified on purification columns (BD Chroma Spin 1000) to remove the primers, nucleotides and enzymes. The end product is kept in 10mM Tris-HCl (pH 7.5). The resulting quantity of DNA is quantified by spectroscopy (Nanodrop).

## Labeled end fragments

Two other fragments are produced by PCR, one is made to be labeled with digoxygenin and the other is labeled with biotin. They are obtained by amplificating the λ phage's DNA between the positions 20281 and 20962 for the digoxygenin fragment and between the positions 35901 and 37568 for the biotin fragment [Figure 76]. Labeling is achieved by replacing 25% of the dTTP nucleotides by marked dUTP nucleotides (Digoxygenin-11-dUTP or Biotin-16-dUTP, Roche Applied Science) during the PCR reaction. The primers used are as follows:

Digoxygenin up: 5' CTG CAG CGT CAC AAC AAT CAG C 3'
Digoxygenin down: 5' AGG TGA CGC GTC GAT AAC ATC TG 3'

Biotin up: 5' CCG ATG GCG ATA GTG GGT ATC ATG T 3'
Biotin down: 5' GGT GAT GCG GAG AGA TGG GTA AGC 3'

For the PCR reaction of the labeled end fragments, the following protocol is followed; for a total reaction volume of 100µL, the solution contains:

- 300nM of each primer (Digoxygenin up and down or Biotin up and down)
- 200µM of each nucleotide except dTTP (dATP,dGTP and dCTP)
- 150µM of dTTP
- 50µM of labeled dUTP (Digoxygenin-11-dUTP or Biotin-16-dUTP)
- 2ng of the λ phage's DNA (ie 4pg.µL$^{-1}$)
- 2.5 units of the Taq DNA polymerase
- 20mM Tris-HCl (pH 8.8@25°C), 10mM $(NH_4)_2SO_4$, 10mM KCl, 2mM $MgSO_4$ and 0.1% Triton X-100

The following parameters for the thermal cycles were used:

| Cycles | Step | Temperature | Time |
|---|---|---|---|
| 1X | 1 | 94°C | 2' |
| 10X | 2 | 94°C | 40" |
| | 3 | 58°C | 1' |
| | 4 | 72°C | 1' |
| 15X | 5 | 94°C | 40" |
| | 6 | 58°C | 1' |
| | 7 | 72°C | 1' + 20" |
| 1X | 8 | 72°C | 5' |
| | 9 | 4°C | ∞ |

As before, the PCR products are then purified on purification columns (BD Chroma Spin 100). The end products are kept in 10mM Tris-HCl (pH 7.5). The resulting quantity of DNA is quantified by spectroscopy (Nanodrop).

## Digestion

The DNA fragments obtained must then digested by restriction enzymes and ligated together to form the final DNA construct such as schematized in **[Figure 75; A]**. In order to do so, two palindromic restriction enzymes, Mlu1 and Eag1 (New England Biolabs), are used. The positions at which they cut the DNA fragments are shown in **[Figure 76]**.

The digestion of the DNA fragments occurs in 50µL containing 50mM Tris-HCl (pH 7.9@25°C), 100mM NaCl, 10mM $MgCl_2$ and 1mM DTT for 3 hours at 37°C. The quantity of enzymes used depends on the quantity of DNA (10 units of enzymes for 1µg of DNA). When digestion is over, the restrictions enzymes are inactivated by heating at 65°C for 20 minutes. The product is then purified to remove enzymes and the undesirable small fragments.

The enzymes cut the central fragment at the positions 22220 and 36654, thus the end product is 14435bp long. The digoxygenin fragment is cut by Mlu1 at the position 20952, leaving two fragments, one which is 672bp long and another of 10bp. The shorter one needs to be evacuated before the next step. The Eag1 enzyme cuts the biotin fragment in two at the position 36654, resulting in 754bp and 915bp fragments. Since the Eag1 is a palindromic enzyme, both fragments are capable of linking with the central fragment, so both are usable for our needs.

## Ligation

All that remains then is to attach the different fragments to form the final DNA construct. Ligation occurs in 20µL containing 50mM Tris-HCl (pH 7.5@25°C), 10mM $MgCl_2$, 10mM DTT, 1mM ATP and 40 units of T4 DNA ligase. The DNA fragments must be present at equal quantities of fragments; the concentrations of the different fragments must be pondered by their respective molecule weights in order to achieve 1:1:1 stochiometry for the 3 different fragments. The reaction lasts for 1 hour at 37°C then the ligase is inactivated by heat at 65°C for 20 minutes. The ligation product is purified through gel extraction (QiaQUICK

Gel extraction kit, QIAGEN) in order to remove any cross-over products (linking of two biotin fragments for example).

The end product is a DNA construct of 15941±81bp which is 5.42±0.03μm long in its B-DNA form. Finally, it is diluted in 10mM Tris-HCl (pH 7.5) to 30ng.μL$^{-1}$ (concentration of approximately 3nM).

## A.III.2. Fabrication by transformation and PCR

Creating the DNA construct through PCR can be hazardous, essentially because of the PCR of the long central fragment whose efficiency is limited. Moreover a too long DNA construct increases the chances of single-strand nick formation along the dsDNA, rendering those nicked molecules useless if one wishes to study their elongation as a function of their twist.

For this reason, I developed during my phD, with the help of Terrence Strick and Jordan Monnet of the institut Jacques Monod, a new shorter DNA construct where the central fragment was no longer produced through PCR but through transformation in *E.Coli* cells.
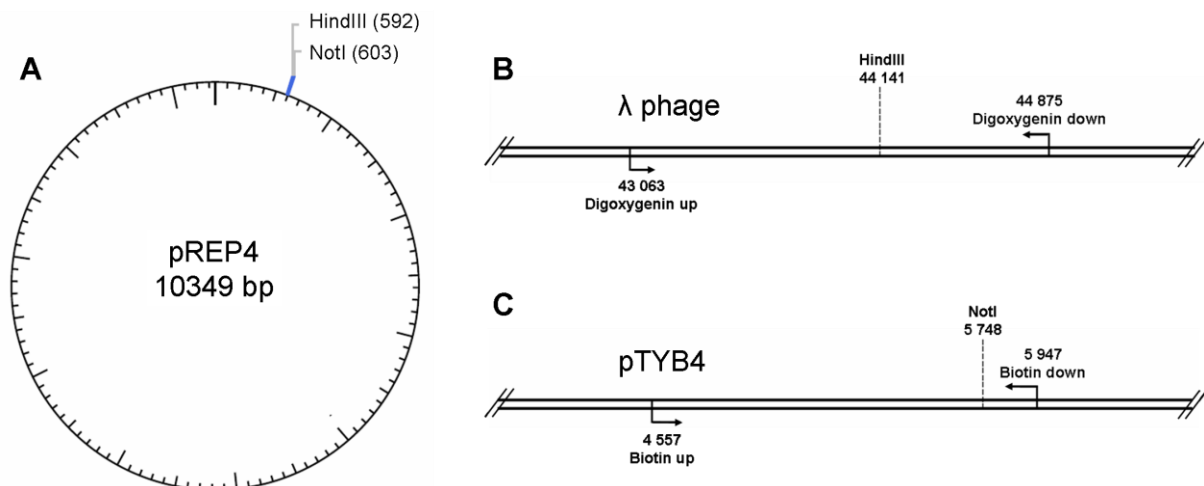


**Figure 77:** Maps of the pREP4 vector (**A**), the λ phage's DNA (**B**) and the pTYB4 vector (**C**) with the enzymes' restriction sites and for (**B-C**) the primers' positions for the PCR amplification.

### Transformation of central fragment

The principle of transformation is to transfect the target vector in bacteria cells which are then made to grow. As the bacteria replicate, they also replicate the transfected DNA; selection of the cells which have successfully transfected the vector is achieved through the presence of a resistance gene to antibiotics on the target vector.

The central fragment is formed from the episomal mammalian expression vector pREP4 (Invitrogen). This vector is transformed in *E.Coli* cells (Turbo Competent E.Coli cells, New England Biolabs) following the NEB High Efficiency Transformation Protocol:

- E.Coli cells are thawed on ice for 10 minutes.
- 100ng of pREP4 DNA is added to 50μL of Turbo Competent E.Coli cells and the solution is kept on ice for 30 minutes

- The pREP4 vectors are transfected in to the E.Coli cells through means of a heat shock at 42°C for exactly 30 seconds. The solution is then kept on ice for 5 minutes.
- 950µL of SOC (Super Optimal broth with Catabolite repression: 2% w/v bacto-tryptone, 0.5% w/v bacto-yeast extract, 10mM NaCl, 2.5mM KCl, 10mM MgCl$_2$ and 20mM glucose) is added to the solution which is then kept at 37°C for 60 minutes.
- After a 10 fold dilution, 50-100µL are spread on several selection plates containing LB medium (Lysogeny Broth: 1% w/v bacto-tryptone, 0.5% w/v bacto-yeast extract and 5.84mM NaCl) and 50µg/mL ampicillin at 37°C. Those plates are incubated 8-12 hours at 37°C. Since the pREP4 vector carries the hygromycin B resistance gene, cells that have successfully transfected it will be able to survive despite the concentration ampicillin.
- After incubation, one of the surviving colonies of cells is picked and inserted in 2-5mL of LB medium for pre-culture. This solution is incubated at 37°C for 8 hours.
- The cell culture is then made by inserting 1mL of the pre-culture in 250mL of LB medium containing 2.5µg of carbenicillin (Sigma). The solution is incubated for 12-16 hours at 37°C.
- The cells are then centrifugated for 15min at 4°C with an acceleration of 6000G.

The pREP4 vectors are then extracted from the *E.Coli* cells using a plasmid purification kit (QIAFilter Palmid Purification Maxi-Prep, QIAGEN). In then end, the vectors are suspended in 10mM Tris-HCl (pH 7.5).


## Labeled end fragments

The labeled end fragments are fabricated as before by PCR. The digoxygenin fragment is obtained by amplification of the λ phage's DNA between the positions 43063 and 44873 **[Figure 77; B]**. The biotin fragment is obtained by amplification of the pTYB4 vector (New England Biolabs) between the positions 4557 and 5947 **[Figure 77; C]**.

The protocol for PCR amplification is the same as before, only the thermal cycles vary:

| Cycles | Step | Temperature | Time |
|:------:|:----:|:-----------:|:----:|
| 1X | 1 | 94°C | 3' |
| 35X | 2 | 94°C | 1' |
| | 3 | 56°C (Digoxygenin) or 58°C (Biotin) | 1' |
| | 4 | 72°C | 2' |
| 1X | 5 | 72°C | 10' |
| | 6 | 15°C | ∞ |

The primers used are as follows:

Digoxygenin up: 5' TCC AGA CAT GCT CGT TGA AG 3'
Digoxygenin down: 5' TCG CTT AAT TCA GCA CAA CG 3'

Biotin up: 5' CGA CTC CTG CAT TAG GAA GC 3'
Biotin down: 5' GGG CTC TGT GCT GAC TTT TC 3'

## Digestion and ligation

The pREP4 vectors are digested by the HindIII and the NotI-HF restriction enzymes (NEB) which cut it respectively at the positions 592 and 603 **[Figure 77; A]**. After digestion, the central fragment is 10338bp long.

The digoxygenin fragment is cut in two by HindIII at the position 44141 **[Figure 77; B]**, creating two fragments 1079bp and 735bp long. Since the enzyme is palindromic, both fragments are usable for ligation.

The biotin fragment is cut in two by NotI-HF **[Figure 77; C]**, creating two fragments 1192bp and 200bp long. NotI-HF is also palindromic, and even the short fragment may be used for ligation.

The digestion and the ligation protocols are the same as before. The end product is a DNA construct containing 11941±668bp, its length in B-form is 4.06±0.23µm. It is diluted in 10mM Tris-HCl (pH 7.5) at a concentration of 3nM.

## A.III.3. Forming the DNA-bead complexes

In order to from the DNA-bead complexes, the DNA constructs and the paramagnetic beads are put together prior to insertion in the chamber in a binding buffer containing 10mMTris-HCl (pH 7.5), 1mM EDTA and 50mM NaCl. Originally, we thought that an optimal stochiometry would be given by one DNA construct for ten beads, thus limiting the risk of multiple binding of DNA molecules to the same bead. However experimentally, we found that a stochiometry of 5 DNA molecules for one bead works best indicating that the binding rate of the DNA to the beads is quite low.

The buffer containing the beads and the DNA is then inserted into the microfluidic flowcell and the flow is stopped when the chamber is saturated with beads. The complexes are then left in the chamber for 10-15 minutes with the magnets far from the flowcell. Therefore the beads sediment to the bottom of the chamber and eventually some of the DNA molecules specifically bind to the anti-digoxygenin coated floor. After incubation, the chamber is thoroughly rinsed with a buffer containing 10mM Tris-HCl (pH 7.5) and 1mM EDTA. This rinsing step is crucial to a successful magnetic tweezers experiment and should not be neglected or hastened. Through the action of the flow, the unattached beads are evacuated from the chamber while the beads connected to DNA molecules which have bound with the floor of the chamber remain tethered.

A note for future users, at this point it is crucial that no air bubbles enter the chamber. Indeed an air bubble will rip all the DNA-bead complexes from the floor by dragging the beads as the air-liquid interface progresses in the channel. Buffers are usually kept

refrigerated for conservation purposes. Those buffers should be let at room temperature for at least 2 hours before insertion into the flowcell. Indeed, at low temperatures gases tend to dissolve more in the liquid buffer. As the buffer attain the experimenting temperature, these dissolved gases are released from the liquid and if one inserts those refrigerated buffers inside the channel, air bubbles will spontaneously appear and ruin the entire experiment.

# B. Describing DNA topology in MT

## B.I. Persistence length and crystallographic length

### B.I.1. Definition of the persistence length

The persistence length of a polymer characterizes its bending energy. The longer its persistence length is, the more rigid the polymer is. Statistically, it is defined through the correlations of angular orientations of the tangents to the curve [5]. If $\theta(L)$ is the angle between tangents at two points separated by a distance $L$ along the curve [**Figure 78**], then the square average of those angles is given by :

$$\left\langle \theta^2(L) \right\rangle = \frac{L}{L_P} \quad , \text{where } L_P \text{ is the persistence length.}$$

Another way to look at it is to notice that the average cosine of tangent angular orientations decrease exponentially with a characteristic length equal to twice the persistence length:

$$\left\langle \cos \theta(L) \right\rangle = \exp\left( -\frac{L}{2L_P} \right)$$
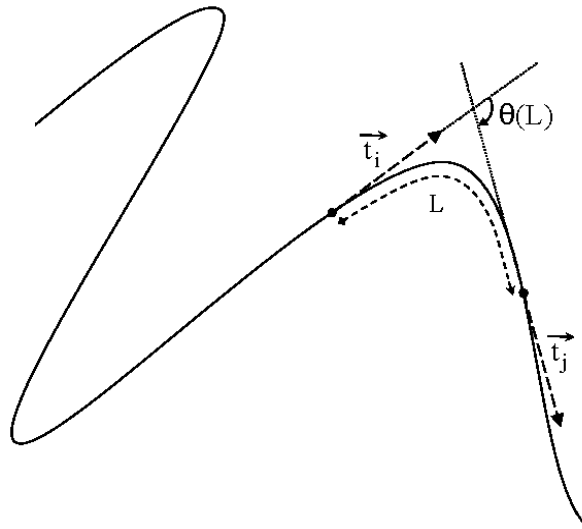


**Figure 78:** Angle $\theta(L)$ between the tangents of two points spaced apart of the distance $L$ along the curve.

In the end, the persistence length $L_P$ is the characteristic length after which angular correlations are lost. In physiological conditions (10mM phosphate buffer (pH 7.5), 10mM NaCl), a dsDNA molecule's persistence length is of $L_P = 52\pm2$nm [162]. This value may vary depending on DNA sequence and physicochemical properties of the solvent the DNA molecule is in, such as pH value and the nature and concentration of ions in solution.

## B.I.2. Force-extension curves

The mechanical behavior of DNA molecules in magnetic tweezers has already been studied in detail [162]. DNA is a polymer, i.e. a linear chain made of repeating structural units. Double-stranded DNA however differs from most polymers in that it is formed by the winding around each other of strands locked by hydrogen bonding between their complementary bases. This double helical structure prevents the relaxation of torsional stress by rotation around a single covalent bond as is common with most polymers. Moreover, the stacking of the bases on top of each other confers unto dsDNA an unusually large flexional rigidity. As a consequence, the force-extension curve of a dsDNA molecule is significantly different from that of a ssDNA molecule **[Figure 79]**. We'll focus here only on the behavior of dsDNA molecules, since we will not use ssDNA in our experiments.
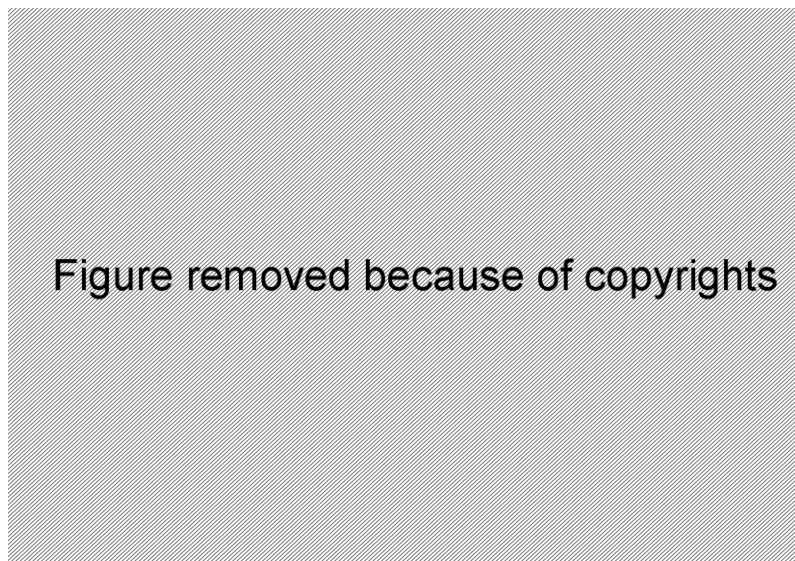
Figure removed because of copyrights

**Figure 79:** Adapted from [21]. Force-extension behavior of dsDNA compared to ssDNA and the inextensible WLC model.

DNA molecules behave in solution like a chain of polymers and form random coils to minimize their entropy [163]. Applying tension to a molecule supplies energy to the system and therefore reduces its entropy, effectively reducing the number of possible configurations the system can adopt. When the molecule is fully stretched, only one configuration remains with the polymer chain as a straight line with an extension corresponding to the crystallographic length of the DNA. This extension is attained for a relatively low stretching force of approximately 10pN. The dsDNA molecule's elasticity with forces ranging from 0 and 10pN is called the entropic regime **[Figure 80; A]**.

For forces over 10pN, the dsDNA molecules' extension remains sensibly close to the value of crystallographic length. Further extension results from stress being applied to the chemical bonds of the DNA backbone. This kind of elasticity corresponds to the enthalpic regime, any entropic contribution becomes negligible. The DNA's elasticity is then comparable to a spring's and is characterized by its Young modulus.

If the pulling force is strong enough, the DNA molecule goes through an overstretching transition, extending it to approximately 1.7 times its crystallographic length. This transition is cooperative and a very slight augmentation in force results in an important

stretching of the molecule. The force at which this transition occurs depends on whether or not the molecule is torsionally constrained as is attested by the different behaviors of dsDNA molecules containing a single-strand nick and non-nicked molecules [**Figure 80; B**]. The force required for the transition is higher in the case of torsionally molecules going from 65pN to 110pN (values obtained from [164]). It is thought that this transition corresponds to conversion from b-DNA to the S-DNA as presented in chapter 1.
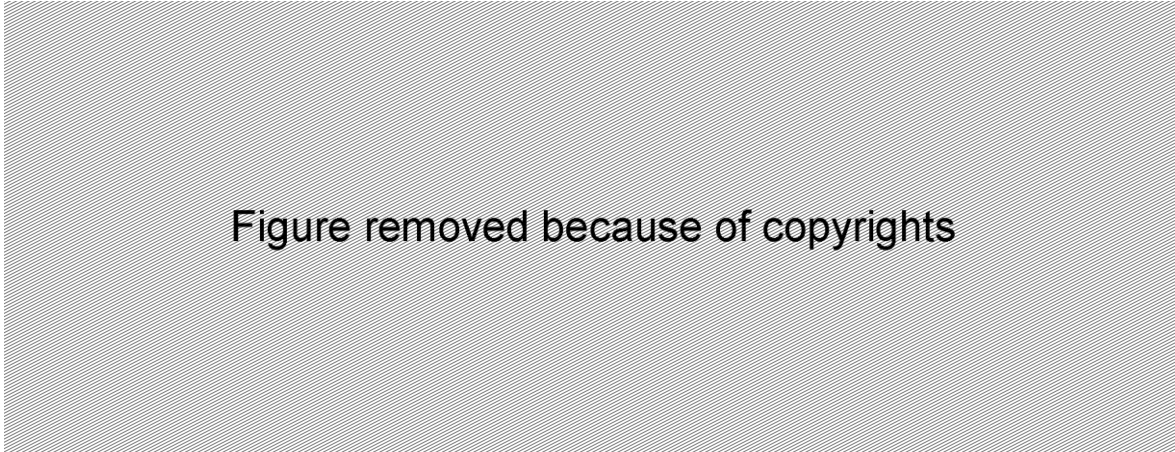
Figure removed because of copyrights

**Figure 80:** Adapted from [165], force-extension behavior of a nicked dsDNA molecule (**A**). At low forces (F≤6pN) is the entropic regime, then for 6pN≤F≤65pN come the enthalpic regime. Over 65pN comes the overstretching transition. Adapted from [162], force extension-behavior of torsionally dsDNA molecules (**B**), one with a single-strand nick and one without. Torsionally constrained the dsDNA molecule raise the transition force from 65pN to 110pN (values obtained from [164]).

## B.I.3. Worm like chain model

There currently exist no exact models simultaneously describing the entropic and the enthalpic regimes i.e. for forces under 50pN. The forces in our magnetic tweezers experiments range from 0 to 15pN, thus corresponding mainly to the entropic regime. We therefore used the improved Marko-Siggia model to fit our force-extension curves, also known as the Worm-Like Chain model (WLC). It should be kept in mind however that not taking into account the enthalpic contribution may result in an underestimation of the persistence length $L_P$.

The WLC model was first treated numerically in 1973 [166] before a preliminary analytical approach was performed [167]. Its complete treatment was achieved by Marko and Siggia and reported in 1994 [168].

In this model, this energy $E_{WLC}$ of a stretched DNA molecule is given by a line integral of a bending energy term $e_B$ and a stretching energy term $e_S$. The bending term $e_{B}(s)$ describes the chain's resistance to bending and is proportional to the inverse square of the curvature radius R. If one describes $R$ as a function of the arc length s and the unit tangent vector $t(s)$ then the term becomes:

$$e_B(s) = \frac{k_B T}{2} L_P \left| \frac{dt(s)}{s} \right|^2$$

The second term $e_S(s)$ describes the stretching energy resulting from the application of a force F to the extremities of the molecular chain.

$$e_S(s) = -F\cos\theta(s)$$

The resulting energy for a molecule of a length of $L_0$ can be written as the line integral of both these contributions:

$$E_{WLC} = \int_0^{L_0} ds \left( \frac{k_BT}{2} L_P \left| \frac{dt(s)}{s} \right|^2 - F\cos\theta(s) \right)$$

The way to solve this equation is presented in [169], [170]. John Marko and Eric Siggia propose an estimate of the force-extension relationship $F(l)$, $F$ being the force applied to the polymer and $l$ being the distance between both ends of the molecule projected on the direction in which the force is applied. This estimation interpolates the exact solution of the WLC model for low ( $F \ll k_BT/L_P$ ) and high ( $F \gg k_BT/L_P$) forces which leads to the following expression:

$$F = \frac{k_BT}{L_P} \left( x + \frac{1}{4(1-x)^2} - \frac{1}{4} \right) \quad \text{with} \quad x = \frac{l}{L}$$

Where $L$ is the full length of the polymer. This formula fits reasonably well experimental data obtained in magnetic [158] and optical [171] tweezers with however up to a 10% deviation in the intermediate extension regime ($x \approx 0.5$ which corresponds to a force $F \approx 0.1$pN). Another analytical solution to the WLC model which approximates the exact solution with a margin inferior to 0.01% in the interval $0.06 \le x \le 0.97$ was proposed [170].

$$F = \frac{k_BT}{L_P} \left( x + \frac{1}{4(1-x)^2} - \frac{1}{4} + \sum_{i=2}^{7} a_i x^i \right)$$

The coefficients $(a_i)_{2 \le i \le 7}$ are determined numerically. This estimation fits the previously mentioned experimental data better than the former one for forces inferior to 6pN. This equation will be referred to as the improved Marko-Siggia model for the fitting of force-extension curves in magnetic tweezers experiments.

| $a_2$ | -0.5164228 |
|-------|------------|
| $a_3$ | -2.737418 |
| $a_4$ | 16.07497 |
| $a_5$ | -38.87607 |
| $a_6$ | 39.49944 |
| $a_7$ | -14.17718 |

**Figure 81:** Values of the $a_i$ coefficients for the improved Marko-Siggia model [170].

# B.II. Supercoiling degree

A dsDNA molecule is composed of two opposite strands which coil around each other to form a double helix structure (**see Chapter 1**). This structure, when rotated around its axis is capable of accumulating torsion if both ends of both strands are held. Topological description of a dsDNA molecule then rests upon two quantities: the twist and the writhe.

The twist number $T_w$ characterizes the number of turns the two strands make around each other along the axis of the DNA molecule. The twist number may be positive or negative depending on the orientation of the turns. Right handed turns account for positive twist numbers and left-handed turns for negative twists. In its B-DNA form, DNA molecules display a one right-handed turn for every 10.5 base pairs. Therefore, if the number of base pairs of the molecule is given by $N$, then the mean intrinsic twist number of B-DNA can be deduced by $T_{w0} = N/10.5$.

The write number $W_r$ translates the number of times the axis of the molecules crosses with itself, taking into account the direction of the crossing. The writhe number is positive for left handed crossings and negative for right handed crossings. B-DNA in its unconstrained form does not display any writhe ($W_{r0} = 0$).
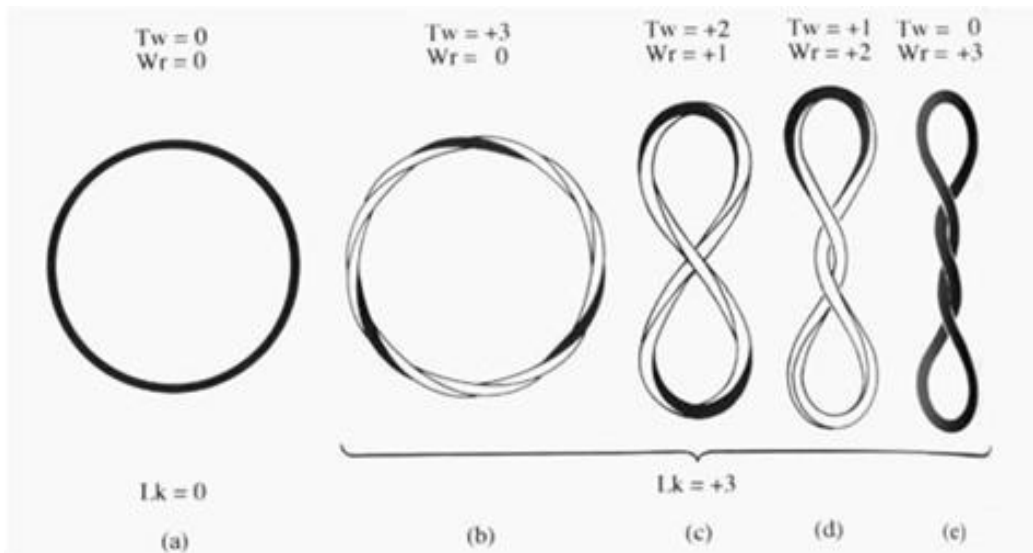


**Figure 82:** Representation of a circular tube with a square section which has one black side. In (**a**) is shown the unconstrained tube ($L_k$=0). (**b**)-(**e**) show the tube with a linking of number $L_k$=3. Conversion between twist ($T_w$) and writhe ($W_r$) allows four different conformations respecting $L_k$=$T_w$+$W_r$=3.

The sum of those quantities form a topological constant called the linking number ($L_k = T_w + W_r$). It is possible to convert twist into writhe and vice versa by modifying the pulling force applied to the molecule [**Figure 82**]. This conversion occurs at a constant linking number if no extra rotation is applied to the molecule [172]. Since unconstrained B-DNA displays no writhe, its intrinsic linking number is equal to its twist number ($L_{k0} = T_{w0} = N/10.5$). When extra rotation is applied to the molecule, the linking number is modified ($L_k \neq L_{k0}$), the molecule is then said to be supercoiled. Supercoiling is represented through a normalized algebric value σ called the supercoiling degree:

$$\sigma = \frac{L_k - L_{k0}}{L_{k0}}$$

Thus unconstrained B-DNA has a null supercoiling (σ=0). Positive supercoiling means overwinding the molecule (adding right-handed turns) and negative supercoiling means unwinding it (adding left-handed turns).

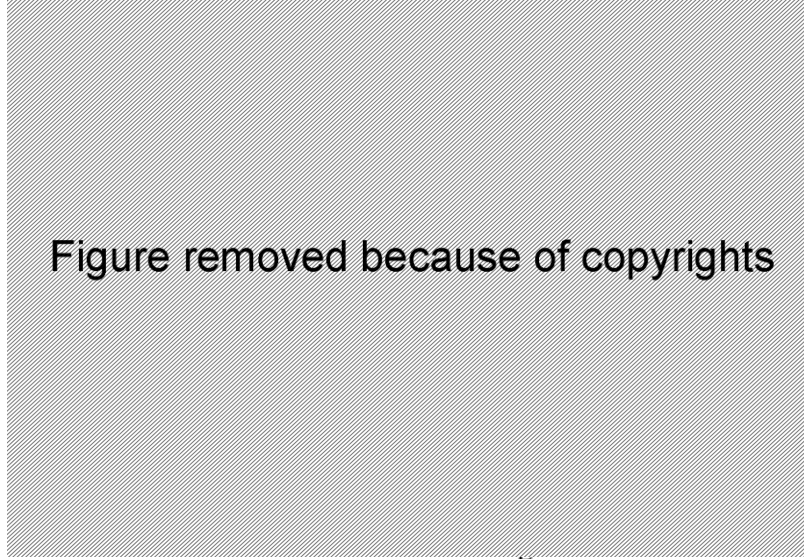# B.III. DNA conformation in magnetic tweezers



**Figure 83:** Extracted from [162]. Relative extensions of dsDNA molecules in magnetic tweezers experiments as a function of the η (proportional to the supercoiling degree σ). For low forces (*F*<0.5pN), the response curve is symmetrical as the molecule forms plectonems for both negative and positive supercoiling. At intermediate forces (*F*≈1-5pN), the response becomes asymmetrical, plectonems are still formed for positive supercoiling, but denaturation bubbles form for negative supercoiling. For high forces (*F*>5pN), denaturation occurs for negative supercoiling and P-DNA forms for positive supercoiling.

## B.III.1. Plectonem formation

At low forces (typically under 0.5pN), the response of the relative extension of dsDNA molecules as a function of the supercoiling degree is a symmetrical curve called a hat curve **[Figure 83; F= 0.116, 0.197 and 0.328pN]**. The maximum extension is reached for a null supercoiling degree (σ=0). If the molecule is wound away from that value, the extension decreases until its reaches an almost null value.

This behavior may be understood by considering the DNA molecule as a rod flexible in curvature and torsion. When torsion is applied to the rod by rotating one of its extremities relatively by an angle θ, an elastic energy E$_{torsion}$ is stocked within the system:

$$E_{torsion} = \frac{1}{2}\frac{C \cdot k_B T}{L}\theta^2$$

Where L is the contour length of the rod and *C* is its effective torsional persistence length. The compensating torque associated with such an energy is:

$$\Gamma = \frac{C \cdot k_B T}{L}\theta$$

**Figure 84:** Adapted from [173]. Schematic view of the buckling transition for a DNA molecule. The DNA molecule starts buckling and forming plectonemes after $n_b$ turns have been added. The plectonemes grow linearly with subsequent twisting and the torque remains constant.

For the dsDNA molecule, the accumulation of torsion results in the modification of its twist number $T_w$ with a variation depending on the imposed $\theta$. Thus as the imposed angle $\theta$ increases, the accumulated torque grows stronger until a critical value of $\Gamma_b$ is reached [**Figure 84**]. This value is called the buckling torque, and corresponds to the torque necessary to form buckles called plectonems in the DNA. The formation of plectonem modifies the writhe number $W_r$ instead of the twist and reduces the end to end extension of the molecule. Further winding of the molecule will result in the formation of more plectonems thus linearly decreasing the extension.

The energy associated with the formation of plectonems is the sum of the bending energy associated with the creation of a buckle of a radius $R_b$ and the work necessary to produce an extension decrease equal to the length of the buckle under the pulling force $F$. Thus the energy associated with the formation of one plectonemic buckle is:

$$2\pi\,\Gamma = \frac{1}{2}\frac{k_B T \cdot L_P}{R_b^{\,2}} * 2\pi R_b + F * 2\pi R_b$$

Minimizing this energy in regards with the buckling radius $R_b$ yields the following expressions for the buckling radius and the buckling torque:

$$R_b = \sqrt{\frac{k_B T \cdot L_P}{2F}} \quad \text{and} \quad \Gamma_b = \sqrt{2k_B T L_P F}$$

## B.III.2. Denaturation induced by negative σ

For forces over 1pN, the dsDNA no longer form plectonems when unwound to negative supercoiling degrees. As a result, at intermediate forces (1pN<$F$<5pN) the extension-rotation curve becomes asymmetrical [**Figure 83; F= 1.2pN**].

At such forces, plectonems are still formed at positive supercoiling degrees, but at negative values the molecule remains extended. This effect is due to the formation of denaturation bubbles in the DNA. In denatured DNA (dDNA), the strands of the dsDNA are no longer linked through the hydrogen bonds between the base pairs. No torsion is accumulated in dDNA and as such the supercoiling degree of dDNA is $\sigma_d$=-1 (completely

unwound DNA). The critical torque for the formation of dDNA is estimated at approximately 9pN.nm.rad$^{-1}$ [162]. Thus the formation of dDNA is favored if the buckling torque $\Gamma_b$ is over this value.

### B.III.3. B-DNA to ScP-DNA transition at positive σ

At pulling forces over 5pN, the dsDNA molecules no longer form plectonems at positive supercoiling degrees **[Figure 83; F= 8pN]**. The formation of denaturation bubbles still occurs with negative supercoiling. For supercoiling degrees above σ=+0.037, the DNA molecule goes through a transition from B-DNA to P-DNA (**presented in chapter 1**).

This form has an extension of 1.7 times the length of B-DNA. However, no such extension of the molecule is observed. This suggest that the P-DNA is actually forming plectonems (ScP-DNA) in this force range, probably stabilized by non-specific interactions between base pairs [12].

# C. Tracking the bead

In magnetic tweezers experiments, the user controls the buffer conditions, the temperature and the positions of the magnets. The height of the magnets will indirectly give control of the pulling force applied and the rotation of the magnets gives control over the linking number of the DNA molecules. Since the DNA is not directly visible, all measurements in MT are made through the tracking of the bead attached to the molecules.

Here we will present how the beads may be tracked in the three-dimensional space through analysis of the images projected onto the CCD camera through the microscope objective. In the end, the XYZ positions and the angle of rotation of the bead may be known.

## C.I. Tracking the center

Tracking the center of the beads on the image gives us access to the XY positions. Knowing these exact positions is crucial for the tracking of all the other parameters and for the measurement of all the deduced values. It is essential that this tracking be achieved as precisely as possible and if one wishes for real-time tracking, as quickly as possible.

### C.I.1. 1D mirror correlation
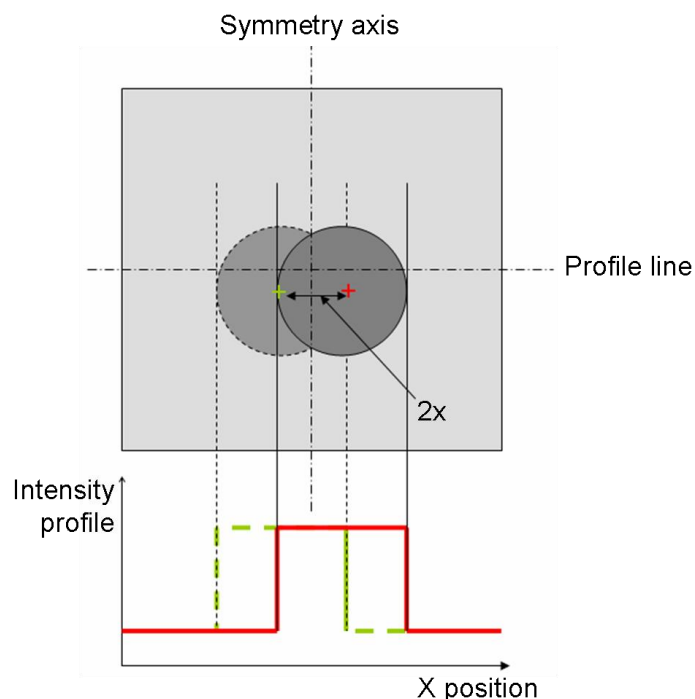
**Figure 85:** Simplified diagram of the center tracking through mirror correlation in 1D for the X-position. A square image sample is centered on the approximate position of the bead's center and is mirrored along a vertical symmetry axis. The intensity profiles are extracted along a horizontal profile line for both the image of the bead (red profile) and its mirror image (yellow profile). The maximum of the cross-correlation between the two profiles is found when the two profiles coincide at a distance equal to $2x$, $x$ being the distance along the X-axis between the bead's center and the center of the image sample.

Finding the center of the bead can be done by using the fact that bead is a spherical object. As such, its image coincides with a mirror image whatever the direction of the symmetry axis used to create the mirror image. The inconvenient is that prior knowledge of the approximate position of the bead's center is required. For the first image, the approximate position is inputted manually. For all the others, the center obtained for the previous image is used; this is based on the fact that the images are acquired at short fixed intervals of time and thus the bead cannot move more than a short distance during that lap of time.
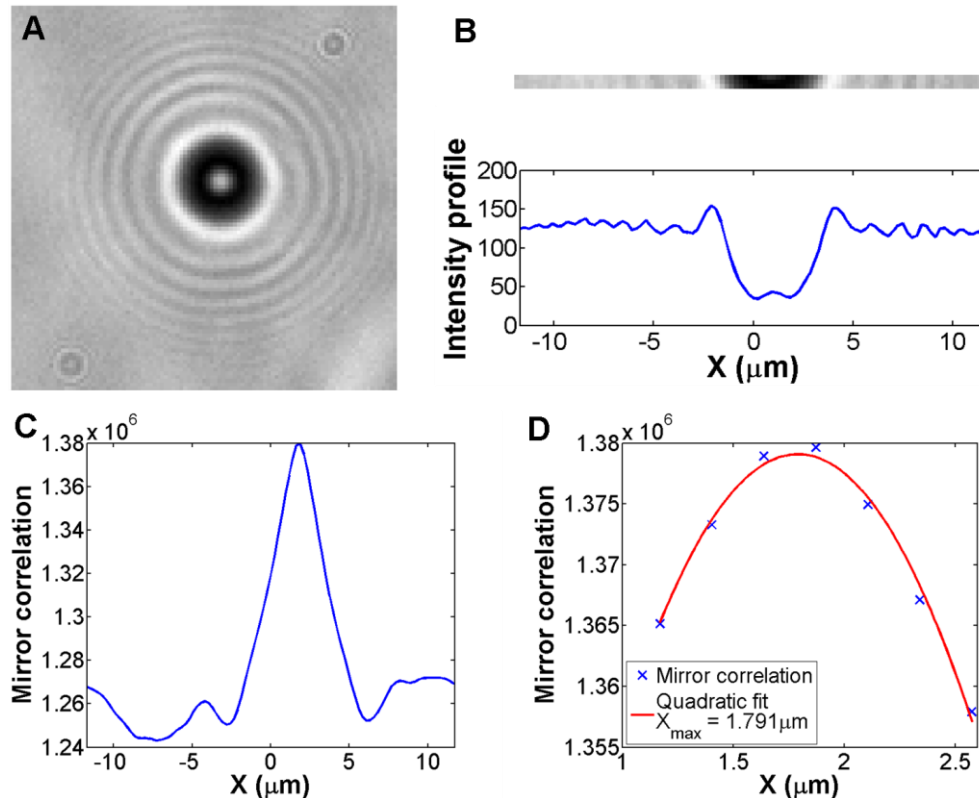


**Figure 86:** 1D mirror correlation process for the measure of the X-position of the bead's center. A square sample image of the bead is centered on the bead's approximate center position (**A**). A horizontal profile is extracted form the center of the image (**B**). The mirror correlation of this profile is computed (**C**). The maximum of this mirror correlation is fitted by a quadratic function for sub-pixel precision (**D**). The $X_{max}$ value must be divided by 2 to obtain the distance between the bead's center and the center of the image along the X-axis.

When the bead is perfectly spherical, it is convenient to use one-dimensional cross-correlation **[Figure 85]** to find the center in order to reduce computing time. Thus a square image sample is centered on the bead's approximate center position **[Figure 86; A]**. For the X-position, a 1D intensity profile is extracted from this image along a horizontal profile line situated at the center of the image (vertical line for the Y-position) **[Figure 86; B]**. Another intensity profile is extracted along the same profile line from the mirror image created by mirror symmetry along a vertical symmetry axis situated at the center of the image (horizontal for the Y-position). Thus the two profiles are separated by a distance equal to twice the distance $x$ between the bead's center and the symmetry axis. This distance $x$ is the value we need to position the bead's center along the considered axis. A cross-correlation of those profiles will yield a maximum at the distance $2x$ separating the two profiles **[Figure 86; C]**. Therefore dividing by two the position of the maximum of the cross-correlation yields the distance of the center's position to the center of the sample image. A sub-pixel precision may

be achieved by fitting the cross-correlation around its maximum by a quadratic function [**Figure 86; D**].

The process is done twice, once for the measurement of the center's X-position and a second time for the Y-position. We'll refer to the process of cross-correlating a profile with its mirror image as mirror correlation. If *f(x)* is the considered profile, then the expression of the mirror correlation function *M* of this profile as a function of the transition distance *d* is:

$$M(d) = [f(-x) \otimes f(x)](d) = \int_{-\infty}^{+\infty} \overline{f}(-x)f(x+d)dx$$

Where $\otimes$ represents the cross-correlation product and $\overline{f}$ is the complex conjugate of function. For easy computation, one can use the fact that the Fourier transform of the mirror correlation is the product of the Fourier transform of the profile and of the Fourier transform of its complex conjugate:

$$F\{M\} = F\{f\} * F\{\overline{f}\}$$

Where *F{}* is the Fourier transform function. Since the profiles are real functions, the computation of the Fourier transform of the mirror correlation is then achieved by squaring the Fourier transform of the profile.

## C.I.2. 2D mirror correlation
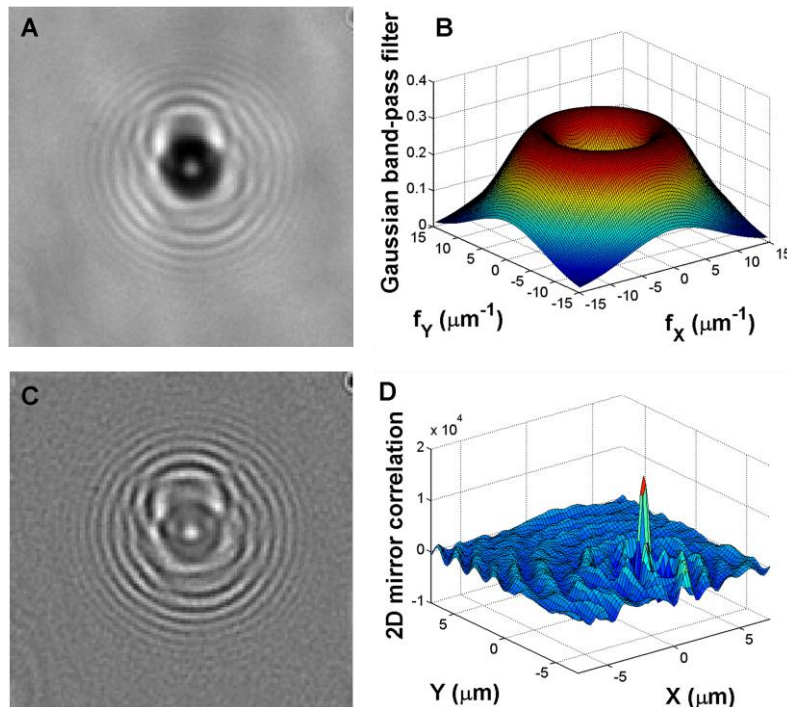


**Figure 87:** 2D mirror correlation process for the measure of the X-position of the bead's center. A square sample image of the bead is centered on the bead's approximate center position (**A**). A Gaussian band-pass filter (**B**) is applied to the image to obtain a filtered image (**C**). The 2D mirror correlation function of this filtered image is computed, the position of the maximum relatively to the center of the mirror correlation is indicative of the bead's center position (**D**).

When the beads are not perfectly spherical as will be the case in some of our experiments, limiting the center tracking to a 1D mirror correlation is no longer an option. We then use a 2D mirror correlation coupled with a band-pass Gaussian filter to find the center [**Figure 87**]. The principle remains the same but for the mirror image which is now constructed by point mirror symmetry using the center of the sample image as a reference point. The Gaussian band-pass filter [**Figure 87; B**] is applied in the spatial frequency space. It is formed by the difference of a low-pass filter, for eliminating the non-spherical defects of the bead, and a high-pass filter for eliminating the background's contribution. The parameters of the band-pass filter are chosen as to maximize the contrast of the ring diffraction pattern around the bead in the filtered image [**Figure 87; C**]. The computation formula for the mirror correlation function is the same as before, expect for the Fourier transform which is now in 2D. As before, sub-pixel precision may be achieved through 1D-fitting of the maximum of the mirror correlation by quadratic curves.

## C.I.3. Microscope horizontal drift and center precision
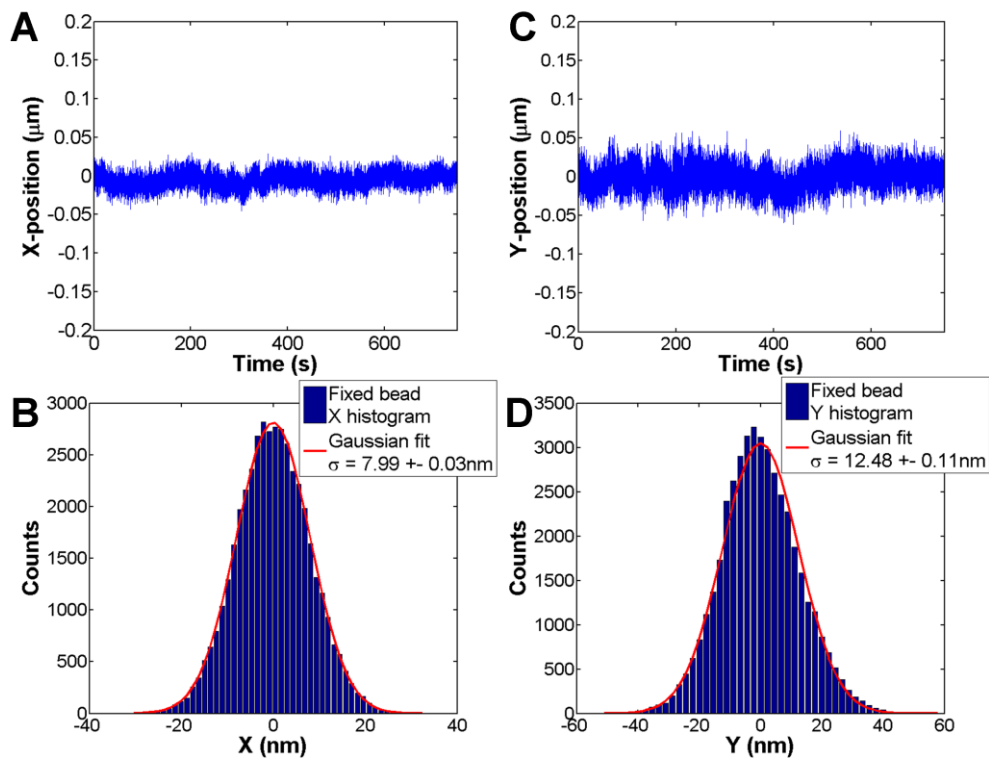


**Figure 88:** Temporal drift of a fixed bead in the XY-plane (**A** and **C**). Once corrected for the drift, the histograms of the center's fluctuations are drawn (**B** and **D**) and fitted with Gaussian curves with standard deviations of $\sigma_x$=8nm and $\sigma_y$=12.5nm.

We will see later that the precise tracking of the absolute position of the center is necessary for the tracking of the angular positions. As such, it becomes necessary to correct any thermal drifting of the sample in the XY-plane by tracking beads that are non-specifically attached to the chamber floor. Those beads are referred to as fixed beads. The evolution of their centers' positions is smoothed to remove fluctuations induced by tracking imprecision and then used for data correction by subtraction from the center positions of the beads of interest during analysis. In normal conditions, the horizontal drift of the sample is minimal and should not exceed 100nm [**Figure 88; A and C**].

A fixed bead is completely immobile on the surface of the sample therefore rapid fluctuations of its tracked position can result only from errors in tracking. We've seen that sub-pixel precision may be achieved through quadratic fitting and image interpolation. Since a pixel corresponds to approximately 200nm, we expect tracking errors to be lower than this value. The tracking of a fixed bead's center yields, once the temporal has been removed, fluctuations with standard deviations of the order of 10nm [**Figure 88; B and D**]. These deviations are good estimates of the tracking error for the center positions.

# C.II. Tracking extension through bead height

## C.II.1. Diffraction patterns and calibration

The fluctuations of the molecule's end to end extension along the Z-axis are measured through the fluctuations of the bead's height. In order to measure the bead's height, the form of the diffraction pattern formed by the bead is considered. The microscope is illuminated by a parallel light beam emitted from a high-brightness LED. Under these conditions, the bead's image is decorated with a series of diffraction rings whose shape and number depends on the distance between the bead and the focal plane [**Figure 89**]. LED illumination provides a very stable light source whose spatial coherence is sufficient to obtain a sharp ring pattern.
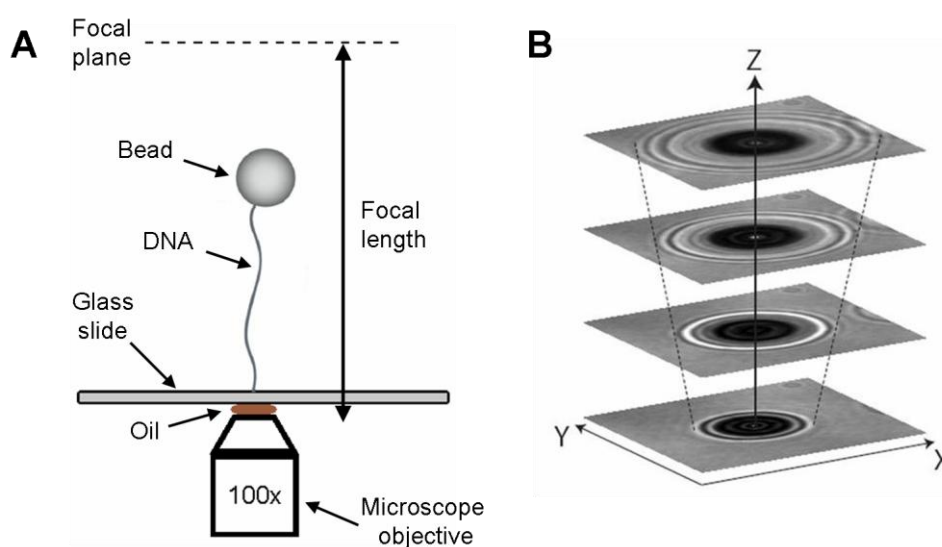


**Figure 89:** In magnetic tweezers, the microscope objective is situated under the observed bead and parallel illumination comes from above. The focal plane of the objective is kept above the bead's position (**A**) even when the molecule is fully stretched, that way the bead's image is always defocused. The ring pattern around the bead is highly sensitive to the distance between the bead and the focal plane; the pattern widens as this distance increases (**B**).

The diffraction patterns of the bead's images will be compared to a set of calibration images taken at regular intervals of the bead to focal plane distance. In order to obtain these calibration images, the magnets are lowered as much as possible near the microfluidic chamber so that a high pulling force is applied to the bead. This pulling force aims to limit as much as possible the vertical fluctuations of the bead induced by thermal agitation. The set of images of the diffraction pattern is taken each at different bead to focal plane distance which is modified by lowering or the raising the position of the objective. Each image is line profile of the ring pattern centered on the XY-position bead. These images may be taken simply

along one direction (typically the X-axis) or by calculating the mean intensity along the diameters of the beads thus obtaining the radial profile of the diffraction pattern. This last method is convenient if the considered beads are not perfectly spherical and allows to minimize the contribution of the background to intensity profile. To minimize the effects of vertical fluctuations, the calibration images are averaged over several images (typically 16 images). The final calibration image is a set of line profiles for which the relative bead to focal plane distances are known. It is important to mention that since theses distances are deduced from the displacement of the oil microscope objective a corrective factor of 0.878 must be applied to them. This factor corrects the focus shift due to the refractive index mismatch between the solution in the chamber (water: $n_{water}$=1.33) and the oil/ glass slide ($n_{oil/glass}$=1.515 [174]) (1.33/1.515 ≈ 0.878).



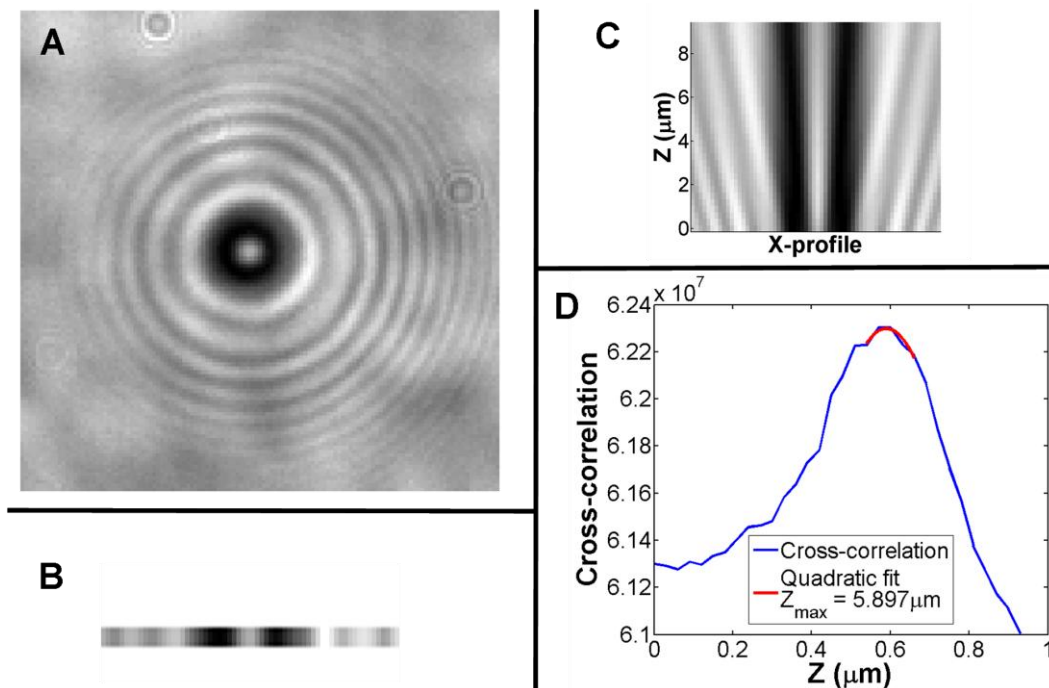**Figure 90:** Process for the measurement of a bead's height on a single image (**A**). A horizontal profile centered on the bead is extracted (**B**) and compared to a set of 32 calibrated profiles (**C**) which were taken with steps of 0.3µm in focal plane distance. The cross-correlation (**D**) of the extracted profile with the calibration profiles gives us the distance between the bead and the focal plane relatively to that of the calibration images. Greater precision is achieved through fitting the maximum of the cross-correlation with a quadratic curve. In this case, the bead's height is evaluated comparatively with distance of the first calibration profile; a precision of 50 to 100nm is achieved.

In order to measure the bead to focal plane distance in an image [**Figure 90; A**] relatively to the calibration images, an intensity profile of the ring pattern is extracted [**Figure 90; B**]. Here again, this profile may simply be taken along the X-axis or averaged on a series of diameters of the bead. This line profile is then compared to the calibration images [**Figure 90; C**] through cross-correlation [**Figure 90; D**]. The maximum of the cross-correlation gives us the calibration image to which the ring pattern of the image is the most similar. Greater precision may be achieved by interpolating the calibration images and/or by fitting the maximum of the cross-correlation with a quadratic curve. In the end, a precision of the order of 10nm may be achieved.

Yet this method only yields the distance relatively to the calibration images. To obtain the absolute measure of the bead's height, the position of the glass slide must be ascertained during the calibration process. In order to do so, the magnets are raised away from the

chamber so that the pulling force applied to the bead becomes negligible. In these conditions, the bead sediments to the bottom of the chamber and rests on the glass slide. The height of the bead is then averaged over multiple images (500 images) and only the lowest values of these heights are considered. The error on the position of the glass slide is of the order of 100nm and is the greatest source of error in the height measurement process. In the end, the extensions of the molecules attached to the beads may be known through the computation of the distance of the bead to the focal plane relative to the calibration images, compared to the position of the floor and taking into account the position of the microscope objective at the moment of the image's acquisition relative to the positions of the objective during the calibration.

## C.II.2. Microscope vertical drift and height precision

Even though every effort has been made to limit the vertical drift of the microscope, the phenomenon still needs to be accounted for if one wishes to accurately measure the molecule's extensions. This is particularly important since the experiment times generally range in the order of the a few hours which is more than enough time to generate a non-negligible drift.

To take in account this temporal vertical drift, the heights of fixed beads are tracked during the experiments **[Figure 91]**. The measure of their height gives us access to the evolution of the height of the glass slide in time. The drift is then deducted from the measures of the heights of the beads of interest. A typical drift during an experiment is of the order of 100nm for a period of time of one hour.
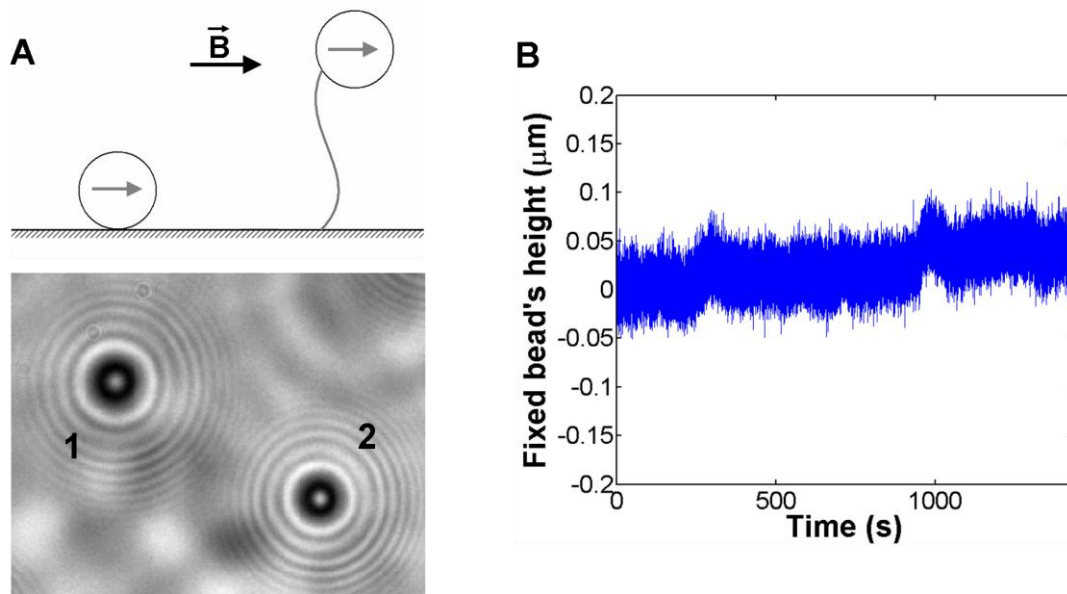


**Figure 91:** The extension of the molecule of interest (**A; 2**) is corrected for the vertical drift of the microscope in time through the tracking of a bead which is non-specifically attached to the glass slide (**A; 1**) usually referred to as the "fixed" bead. A typical drift in time is shown in (**B**); over a period of 25 minutes, the microscope drifted about 50nm.

After subtracting the vertical drift from the microscope, we can draw the histogram of the vertical positions measured for the fixed bead **[Figure 92]**. The histogram is well fitted by a Gaussian curve with a standard deviation of $\sigma=15$nm. This standard deviation is a good approximation of the measuring error in the relative vertical position. It is one order of

magnitude smaller than the error on the position of the chamber's floor making this source of error negligible when compared to the error on the absolute vertical height of the bead.
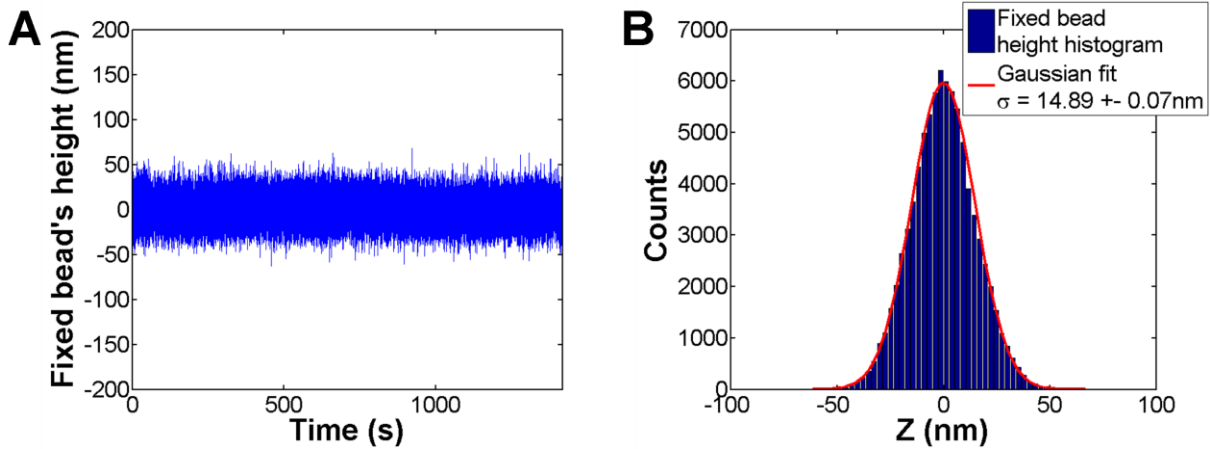


**Figure 92:** The vertical drift of the microscope is subtracted from the fixed bead's height temporal curve (**A**). The histogram of the vertical positions is well fitted by a Gaussian curve with a standard deviation of σ=15nm.

## C.II.3. From bead height to molecule extension
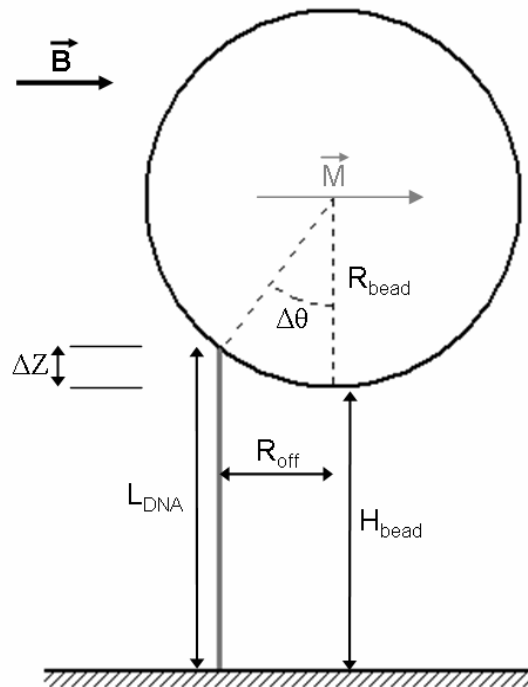


**Figure 93:** Schematic view of the decentered attachment of the DNA molecule on the bead. The bead has a preferential magnetization direction and it aligns its magnetic moment *M* with the horizontal magnetic field *B*. The DNA molecule has no particular reason to be attached the bead so that its attach point is right under the bead when the moment is aligned. Therefore there is difference between the height of the bead $H_{bead}$ and the length of the DNA $L_{DNA}$ ($L_{DNA} - H_{bead} = \Delta Z$).

Using the method we just described, one can know the height of the bead relatively to the glass slide. However, this height does not necessarily reflect the end to end extension of the attached molecule. Indeed, the molecule has no particular reason to be attached to the

bottom of the bead [**Figure 93**]; in the vast majority of cases, an additive correction must be applied to obtain the actual molecule extension.

The additive correction $\Delta Z$ is the difference between the height of the bead $H_{bead}$ and the length of the DNA molecule $L_{DNA}$ ($L_{DNA}$ - $H_{bead}$ = $\Delta Z$). We will see later that the off-center radius $R_{off}$ resulting from the position of the attach point may be deduced from the tracking of the bead's center. Thus, knowing this radius and the radius of the bead ($R_{bead}$ = 1.4µm for M-280 Dynabeads), the additive correction may be calculated:

$$\Delta Z = R_{bead} - \sqrt{R_{bead}^2 - R_{off}^2}$$

# C.III. Tracking rotation

In free-rotation magnetic tweezers, the bead's rotation is no longer controlled through the direction of the horizontal magnetic field; it is instead influenced by the DNA molecule's twist and whatever cofactors interact with the DNA. Therefore the angular fluctuations of the bead carry some energetic information on the attached system and the tracking of angular positions becomes paramount. This section focuses on techniques allowing the access to those positions through image analysis. The methods involve either a fiducial marker for visual reference or the tracking of the center's position relatively to the off-centered rotation center.

## C.III.1. Breaking the beads' symmetry

Tracking the angular fluctuation of a spherical object is a problem in itself since no visual markers are present to allow for a directional differentiation. We therefore used biotin-coated polystyrene nanobeads (PC-B-0.8; G. Kisker GbR; 810nm in diameter) as fiducial markers for visual reference.

Suspended in a binding buffer (10mMTris-HCl, pH 7.5; 1mM EDTA; 50mM NaCl), those beads were injected in the microfluidic channel once the DNA-bead constructs were assembled, where they would bind with the streptavidin-coated paramagnetic beads (2.8µm in diameter).

One cannot stress enough the importance of rinsing the channel to evacuate the non-attached streptavidin beads prior to the marker beads' insertion for binding. Since the marker beads are biotin-coated, they will, if given the chance, bind with any non-attached streptavidin beads left in the chamber, ultimately forming huge aggregates which have the potential to bind with the DNA-bead complexes. These aggregates can therefore ruin an entire experiment before it even started, wasting hours of preparation.

Apart from thorough rinsing, another precaution is to keep the magnets lowered near the chamber at all times from the moment the marker beads are introduced in the chamber. Those beads are non-magnetic, so the presence of the magnets will not affect their behavior. The magnetic field will however pull all unattached paramagnetic beads to the ceiling of the chamber and thus potential aggregates are kept as far as possible from the DNA-bead constructs. Keeping the magnets lowered also has the effect of pulling the constructs off of the chamber's floor, increasing the probability for binding by a marker bead.

After a while, the excess marker beads are evacuated before starting the actual experiment. The concentration of marker beads used and the incubation time left for binding in order to obtain one and only one fiducial marker bead per construct remains an elusive art which is perfected only through trial and error. What seemed to work in our experiments was introducing 0.5µL of a 0.3% w/v solution of the marker beads (the commercial solution is at 1% w/v) and incubating for 5 to 10 minutes. One should keep in mind that many binding events happen during the evacuation step.
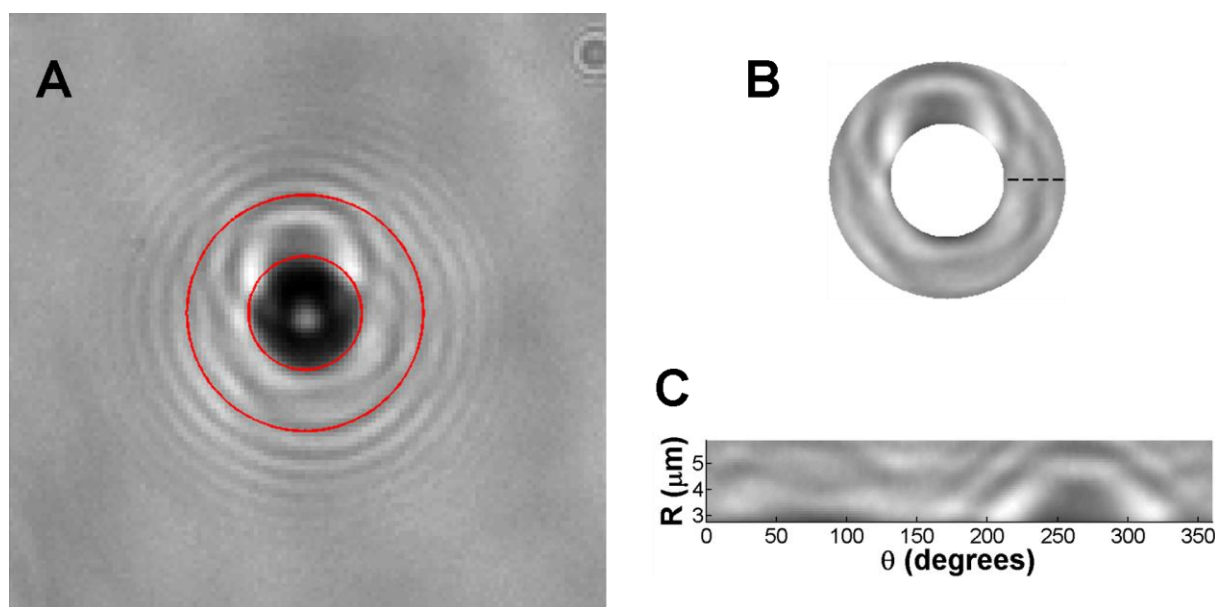


**Figure 94:** The image of a paramagnetic bead marked with a polystyrene marker bead (**A**) is interpolated along circles whose radiuses are comprised between two user-set values to form a ring image (**B**). The limit values are chosen so that the ring contains the image of the fiducial marker bead. This ring image is then linearized (**C**) as a function of the angle θ for easy comparison with other images through cross-correlation.

The image of paramagnetic beads marked with a polystyrene bead retain the diffraction pattern necessary for the tracking height [**Figure 94; A**]. To track the angular position of the bead, a ring image around the bead is extracted though linear image interpolation [**Figure 94; B**]. The parameters of this ring are chosen so that the image of the fiducial marker is contained within the ring while keeping out as much as possible any parasite information. The ring is then linearized along the angular axis to allow for easy analysis [**Figure 94; C**]. The angular positions may thus be tracked by one of two ways, either by differential tracking or by ring symmetry.

## C.III.2. Differential angular tracking

Differential tracking refers to the comparison of the linearized ring images extracted from consecutive video frames. The relative angular position of these consecutive frames is given by the shift of the ring image along the angular axis. This shift may be calculated through the cross-correlation of those rings. In order to achieve a 1D cross-correlation of 2D images, the 2D cross-correlation of these images is calculated and a line profile corresponding to a null shift in the radial direction is extracted from the surface [**Figure 95; A**]. The maximum of this cross-correlation profile is direct measure of the angular shift between the consecutive

frames **[Figure 95; B]**. Greater precision may be achieved through finer interpolation and/or through fitting the maximum by a quadratic curve.
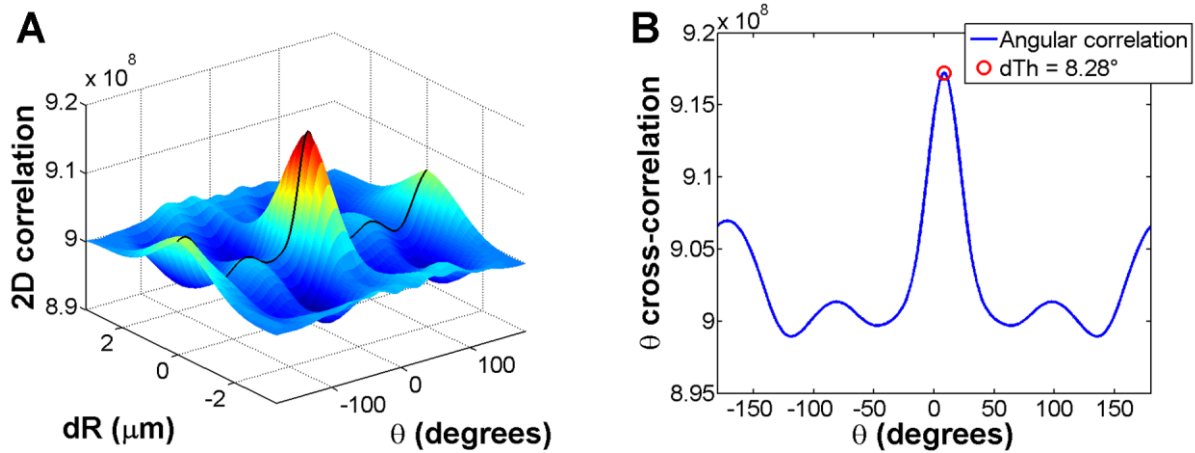


**Figure 95:** The 2D cross-correlation (**A**) of the ring images from consecutive frames is calculated. The line profile (**black profile in A**) corresponding to a null shift in the radial direction is extracted from the surface. The maximum of this line profile (**B**) is direct measurement of the relative angular shift between the two frames.

## Consequence of center error on angular precision
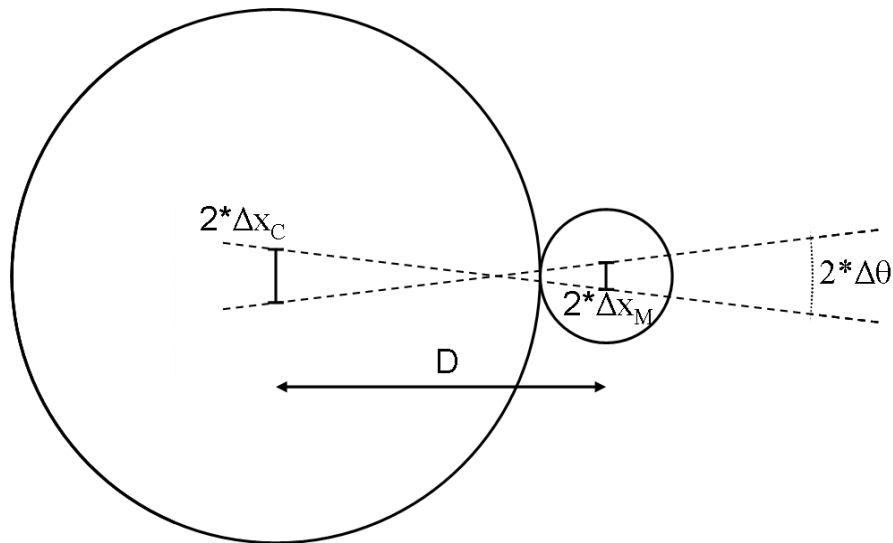


**Figure 96:** Simple geometric model linking the uncertainty on the angular position $\Delta\theta$ induced by the uncertainty on the position of the bead's center $\Delta x_C$ and the uncertainty on the position of the fiducial marker bead $\Delta x_M$. This model shows the worst case scenario when both errors are in the same direction, perpendicular to the axis between the bead's center and the marker's position.

To estimate theoretically how the uncertainty on the bead's center position affects the precision on angular tracking, we'll use a simple geometric model **[Figure 96]**. In this model, we'll consider that the angular tracking is achieved through the positioning of the fiducial marker bead's center relatively to the center of the bead. The uncertainty on the angle is greatest when the uncertainties on both centers are perpendicular to the axis between the bead's and the marker's centers. Then the greatest angular difference is found both situations when the uncertainties on the centers are in opposite directions. Simple geometry will then

show the following relationship between the angular imprecision $\Delta\theta$, the uncertainty on the bead's center $\Delta x_C$ and the uncertainty on the fiducial marker bead's center $\Delta x_M$:

$$\tan(\Delta\theta) = \frac{\Delta x_C + \Delta x_M}{D}$$

Then using the properties of the tangent function, it comes that:

$$\Delta\theta \leq \frac{\Delta x_C + \Delta x_M}{D}$$

We've seen that the standard deviation on center tracking in our experiments is of th order of 10nm. Then if one is to be pessimistic, the uncertainty on the bead's center position can be up to three times this value. We'll consider that the uncertainty on the position of the fiducial marker bead's center is the same as the one on the bead's center. Thus we'll consider $\Delta x_C = \Delta x_M = 30$nm. The beads used in our case are 2.8μm in diameter for the paramagnetic beads and 810nm in diameter for the fiducial marker beads. Therefore the distance D between both centers is $D = 1.805$μm. It then comes that the angular imprecision stemming from the error on the centers' tracking is:

$$\Delta\theta \leq \frac{30nm + 30nm}{1805nm} = 0.0332 rad \approx 2°$$

## Accumulation of error in differential tracking

When the images are sequentially compared to one another by measuring the angle of the bead in one image relatively to the bead of the precedent image, it comes that the absolute value of the angular position carries the errors in tracking of all the images before it. With an acquisition rate of 30 images per second, the error stemming from such an effect becomes rapidly problematic. For this reason, the images are not actually compared to the one directly before it but to sample reference images taken every 1000 images or more. This precaution allows to significantly reduce the error on angular tracking but with experiment times up to 3 hours long the error is still important: $10^5$ images, divided by 1000 from sampling results in errors 100 times the angular precision.

To further reduce the error propagation, the sample images are then all compared to one another to accurately determine their angular positions. Every reference image is compared to all the others and the angular positions are determined through averaging in a recursive algorithm. The precision achieved through such a process is then better than the intrinsic tracking precision. The error propagation on a regular image is then the error on the sample image added to the intrinsic angular uncertainty $\Delta\theta$. A precision better than 4° is thus achieved at all times through this process.

It is also possible to compare all images to a single reference image in order to achieve the intrinsic tracking precision of 2° for all images. This process is possible if the images were acquired intelligently with the focal plane of the microscope objective far above the beads' heights. Indeed the evolution a bead's height will change its relative distance to the focal

plane thus changing its image as it becomes more focused or unfocused. If the focal plane was placed far enough, the image modification induced will be minimal.

## C.III.3. Tracking through ring symmetry

In the cases where one and only one fiducial marker bead is attached to the bead of interest, it is possible to track the angular positions of the bead without comparing them to other images. This process relies on the fact that since the marker bead is spherical, the resulting ring image will be symmetrical in the angular direction. The positioning of the marker bead is then possible by using a mirror correlation process [Figure 97]. Due to the nature of the mirror correlation function, this process requires a forehand knowledge of the marker bead's angular position with a precision of ±90°. This type of precision is easily achieved by any other type angular tracking methods or alternatively the angular position for the precedent image can be used as reference. This process has the advantage of not propagating errors as was the case with differential tracking. However it presupposes a symmetry which is not always achieved. The uncertainty of this method results mainly from the error on the center's positions and is therefore of the order of ±2°.
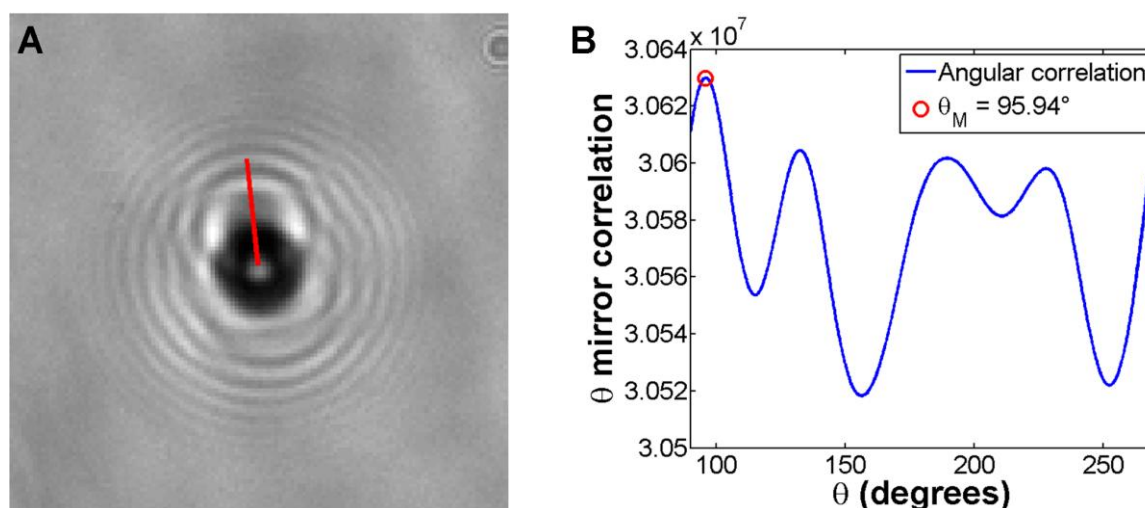


**Figure 97:** Tracking of the position of the fiducial marker (**A**) by ring symmetry through mirror correlation (**B**) of the ring intensity profile.

## C.III.4. Tracking through off-centered rotation

As we've discussed previously, the center of the bead does not coincide with the axis of rotation imposed by the attached DNA molecule [Figure 93]. The result is an off-centered rotation of the bead's center around the axis of the DNA molecule [Figure 98]. The radius $R_{off}$ of this off-centered rotation is dependent on the position of the attach point of the DNA molecule onto the bead. Its value is necessarily inferior to the radius of the bead ($R_{bead} = 1.4\mu m$). This phenomenon occurs whether the magnetic field is horizontal or vertical therefore it is possible to use this property for angular tracking in free-rotation magnetic tweezers.

The off-centered rotation tracking method is simple enough; it requires no comparison of images to each other and therefore has no error propagation. It uses only the center positions which we already have with no additional computing. Yet its most attractive feature

is that it does not require the presence of fiducial marker bead which are troublesome to implement. We will see however in this section that its biggest flaw is a lack of precision.



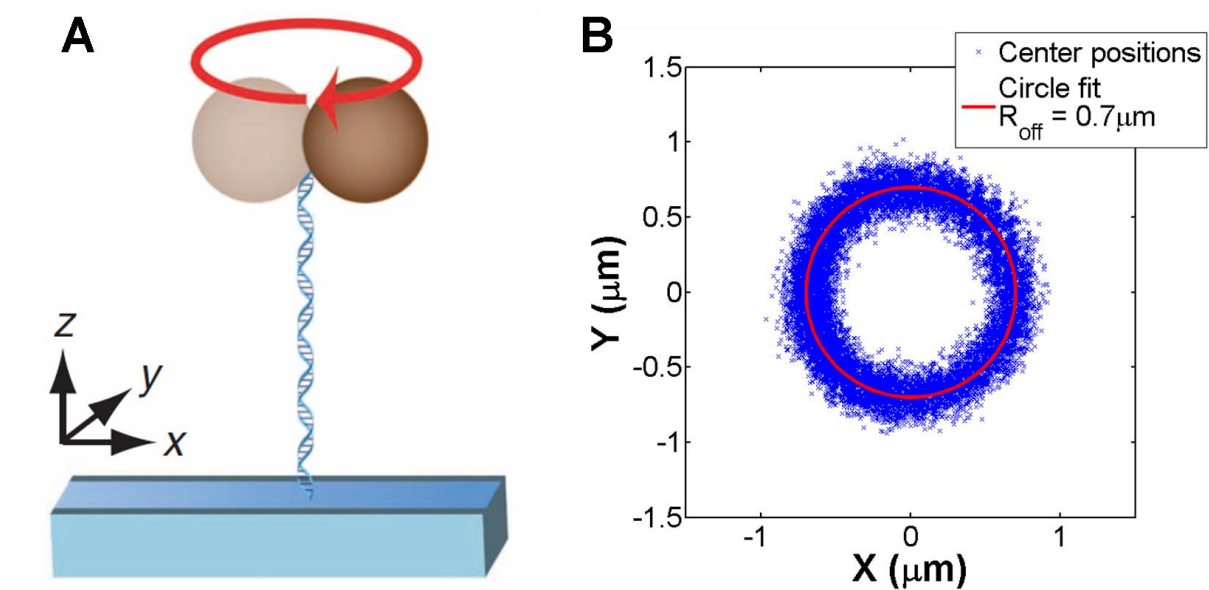**Figure 98:** The bead rotates in an off-centered manner around the axis of the attached DNA molecule (**A**). The bead's center positions are located along a circle centered on the attach point of the DNA molecule onto the bead (**B**). The off-centered rotation radius $R_{off}$ may be measured by fitting those positions by a circle, this radius has a value inferior to the bead's radius ($R_{bead} = 1.4\mu m$).

In order to characterize the off-centered rotation, the XY-positions of the bead's center are fitted to a circle whose center and radius $R_{off}$ are thus determined. Since the bead strives to align its magnetic moment with the magnetic field at all times, the position of the bead on the circle is directly related to its angular position. The center of this circle is then taken as a reference point for the bead centers. The expression of the angular position is thereafter given by the arctangent of the ratio of the Y position over the X position:

$$\theta = \tan^{-1}\left(\frac{Y}{X}\right) + (1 - sign(X)) * \frac{\pi}{2}$$

The last term of this expression is necessary to correct the fact that the arctangent function only returns values comprised between -π and +π.

The error on the estimation of the angle by this method results mainly from the error on the bead's center position. We'll assume that the error on the center of the circle is negligible due to the great number of the bead's center positions used to determine its position. Therefore if $\Delta x$ is the error on the center's position, the error $\Delta\theta$ on the angle in the worst case scenario is given by:

$$\tan(\Delta\theta) = \frac{\Delta x}{R_{off}} \quad \Rightarrow \quad \Delta\theta \leq \frac{\Delta x}{R_{off}}$$

The error on the bead's center is in the worst case somewhere around $\Delta x = 30$nm. We'll assume the highest value possible for the off-center radius $R_{off} = 1.4$µm. Then the maximum error becomes:

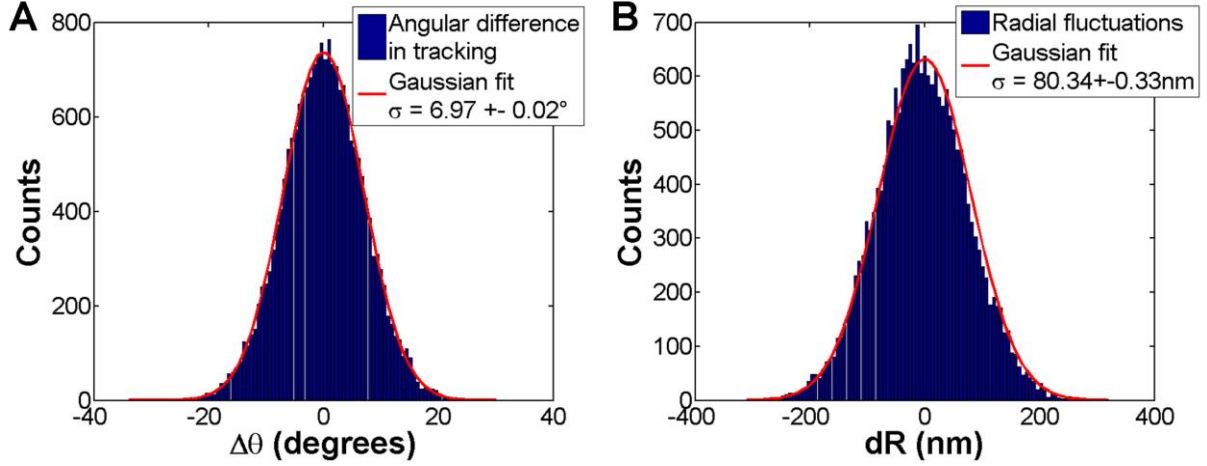$$\Delta \theta \leq \frac{30nm}{1400nm} = 0.0214\,rad \approx 1.3°$$



**Figure 99:** (**A**) Histogram of the difference in the angular position values obtained by differential tracking and the ones obtained by off-center tracking for a single experiment with a pulling force of $F$=2pN. (**B**) Histogram of the radial fluctuations of the bead during this experiment.

The uncertainty on the center is not however the only source of error of this tracking. A much more problematic aspect results from the translational Brownian motion of the bead. The bead's movements in translation due to Brownian motion are several orders of magnitude faster than its rotation. Therefore for a given angular position, the bead will fluctuate many times around its theoretical center position with an amplitude that is a function of temperature and of the magnetic pulling force applied to the bead.

To estimate the error on angular tracking stemming from such an effect we tracked a bead's rotation using both differential tracking and off-center tracking. The difference between the values obtained by the two methods showed a standard deviation of $\sigma_\theta = 7°$ **[Figure 99; A]**. The pulling force during this experiment was measured to $F$=2.01±0.49pN. In order to characterize the translational Brownian in these conditions, we observed the fluctuations of the bead along the radial direction around its mean value $R_{off}$. These fluctuations showed a standard deviation of $\sigma_R = 80$nm **[Figure 99; B]**. This standard deviation of the translational Brownian motion may be considered as an uncertainty on the positioning of the bead's center. Therefore, since the off-center radius is in this case $R_{off} = 0.7$µm, the resulting angular imprecision can be expressed as before by:

$$\Delta \theta \leq \frac{\sigma_R}{R_{off}} = \frac{80nm}{700nm} = 0.1143\,rad \approx 6.6°$$

We effectively find a value close to the standard deviation $\sigma_\theta$ for the angular difference between the tracking methods. This effect of Brownian motion is the biggest source of error for the off-center tracking method. This error added to the uncertainty on the bead's center

positions makes this method highly imprecise when low pulling forces are involved. It could be argued nonetheless that the errors stemming from Brownian motion are intrinsically null in average and would therefore not impact on measures such as torque estimation when large numbers of data points are considered. We chose however no to trust this method regardless of its convenience. Instead we used it only as a watch-dog mechanism to check that the other tracking methods were staying on course during analysis.

# D. Measures in MT

## D.I. Pulling force

### D.I.1. Compensating force

Due to the presence of the magnets over the microfluidic chamber, the paramagnetic beads are submitted to a magnetic field gradient which varies along the Z-axis. Under this influence of this gradient, the beads are pulled towards the magnets by a magnetic pulling force $F_{mag}$. The measuring of this pulling force relies on the analysis of the bead's Brownian fluctuations.
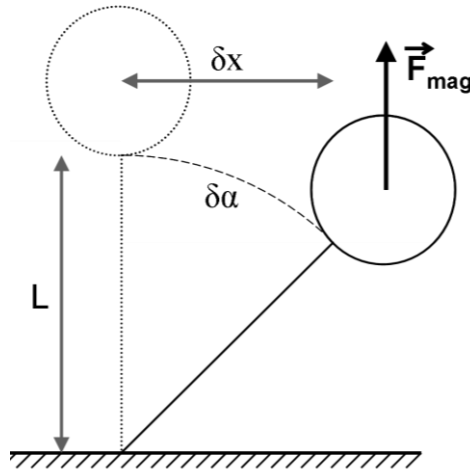


**Figure 100:** Geometric model for the fluctuations of the bead in the XY-plane.

The fluctuations of the bead under the influence of thermal agitation will result in the application of a compensating force $F$ due to the application of the magnetic pulling force $F_{mag}$. The components of this compensating force may be separated as a parallel component $F_{//}$ along the axis of the DNA molecule and a component $F\perp$ perpendicular to the axis of the DNA. Since the fluctuations are small when compared to length $L$ of the DNA molecule, we'll make the approximation that the parallel component $F_{//}$ is along the Z-axis and the perpendicular component $F\perp$ is in the XY-plane (along the X-axis in our example).

For fluctuations in the XY-plane, a deviation $\delta x$ will induce a compensating force in the XY-plane function of the deviation angle $\delta\alpha$ between the DNA molecule and the Z-axis **[Figure 100]**:

$$F_\perp = F_{mag} \cdot \sin(\delta\alpha)$$

Since we are considering small $\delta x$ fluctuations, and consequently small values of $\delta\alpha$, the following approximation may be made:

$$\sin(\delta\alpha) \approx \tan(\delta\alpha) = \frac{\delta x}{L}$$

This approximation would seem to preclude the validity of the model in cases where the extension $L$ of the molecule is too small. It is however possible to demonstrate rigorously that the model remains true even for low values of the molecule's extension [175]. Using this approximation, it comes that the perpendicular component of the compensating force may be written as that of a spring:

$$F_\perp = K_\perp \cdot \delta x \qquad \text{with} \quad K_\perp = \frac{F_{mag}}{L}$$

## D.I.2. Anisotropy of the Brownian motion

When the magnetic field is horizontal, an anisotropy of the bead's Brownian motion in the XY-plane appears. This anisotropy is the result of the paramagnetic bead striving to align its magnetic moment $M$ with the magnetic field $B$ at all times.
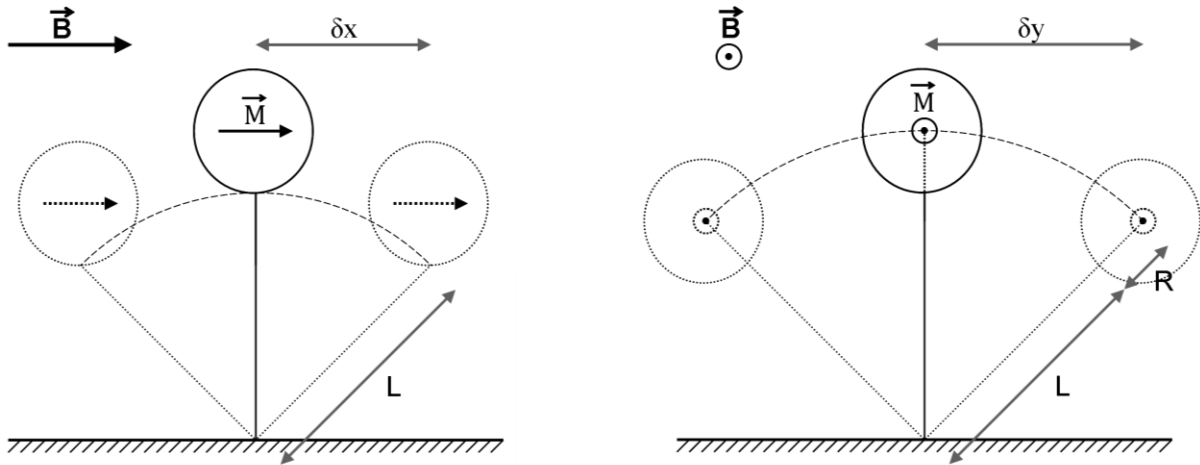


**Figure 101:** Anisotropy of the Brownian motion in the XY-plane resulting from an horizontal magnetic field $B$ along the X-axis. For the fluctuations parallel to the axis of the magnetic field (**diagram on the left**), the length to be considered for the deviation angle is the length of the DNA molecule $L$. For fluctuation perpendicular to the axis of the magnetic field (**diagram on the right**), the length to be considered is the sum of length $L$ and the radius of the bead $R$.

When the fluctuations are parallel to the axis of the magnetic field (the X-axis in our example), the bead will move by translation only due to its angle in the YZ-plane being imposed by the direction of $B$ **[Figure 101; left]**. In this case the pertinent length for the expression of the deviation angle $\delta\alpha$ is the length $L$ of the DNA molecule. Therefore the expression of the stiffness of the compensating force in this direction remains:

$$K_x = \frac{F_{mag}}{L}$$

The situation is different for the fluctuations along the Y-axis, perpendicular to the axis of the magnetic field in our example. In this case, the angle of the bead in the XZ-plane is not locked by the magnetic field and the bead will move by translation and rotation around the X-axis **[Figure 101; right]**. The pertinent length for the expression of the deviation angle $\delta\alpha$

becomes the sum of the length $L$ of the DNA molecule and the radius $R$ of the bead. The stiffness of the compensating force is then lesser in this direction and its expression becomes:

$$K_y = \frac{F_{mag}}{L + R}$$

For vertical magnetic field as in free-rotation magnetic tweezers setups, there is no anisotropy of Brownian motion in XY-plane. The situation is the same as for the fluctuations parallel to the magnetic field in the case of the horizontal field. The direction of the magnetic moment is locked in the direction of the Z-axis. The bead moves by translation only [**Figure 102**]. Then the pertinent length to consider is the length $L$ of the DNA molecule.

Another phenomenon to consider in this case is the translation of the bead along the off-center circle stemming from the rotational Brownian motion. Therefore, only the radial fluctuations around the off-center radius $R_{off}$ are considered for the measurement of the force when the field is vertical.
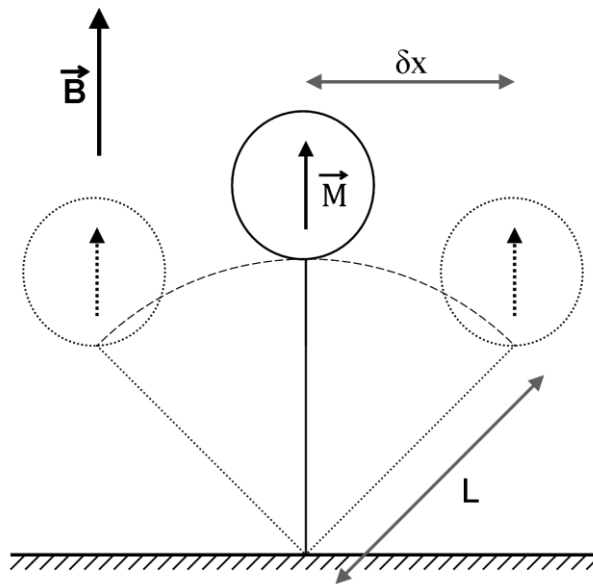


**Figure 102:** Brownian fluctuations of the paramagnetic bead in a vertical magnetic field.

## D.I.3. Equipartition of energy

The simplest way to evaluate force from the Brownian fluctuations of the bead is to use the equipartition theorem which states that the average kinetic energy is shared equally among all degrees of freedom. Since the compensating force resulting from the application of the magnetic pulling force is equivalent to a spring, the energy associated to the Brownian motion in a given direction may be expressed as:

$$\frac{1}{2} K_\perp \left\langle \delta\perp^2 \right\rangle = \frac{1}{2} k_B T$$

Where $\delta\perp$ are the fluctuations of the bead in the considered direction and $K\perp$ is the associated stiffness of the compensating force to the same direction. Obtaining the stiffness of

the compensating force becomes a matter of measuring the mean square of the bead's fluctuations in a given direction. The magnetic pulling force may then be deduced by simultaneously measuring the average extension of the molecule:

$$F_{mag} = k_B T \frac{L_\perp}{\left\langle \delta\perp^2 \right\rangle}$$

Where $L\perp$ is the measured pertinent length to consider for the given direction.

## D.I.4. Frequency analysis

### Equation of motion

Our system is a bead with a radius R submitted to an elastic compensating force characterized by a spring stiffness $K$, the Stockes drag force and the Langevin force resulting from thermal agitation. The equation of motion for this system can thus be written as follows:

$$m\frac{d^2 x(t)}{dt^2} = -\xi \frac{dx(t)}{dt} - K \cdot x(t) + \eta(t)$$

Where $x(t)$ is the instantaneous position of the bead, $m$ is its mass, $\xi$ its drag coefficient and $\eta(t)$ is a noise term called the Langevin force representing the collisions of the bead with the molecules of the fluid. The uncorrelated force $\eta(t)$ has a Gaussian probability distribution and is characterized by the following relations stemming from the fluctuation-dissipation theorem:

$$\left\langle \eta(t) \right\rangle = 0 \quad \text{and} \quad \left\langle \eta(t) \cdot \eta(t') \right\rangle = 2k_B T \xi \delta(t - t')$$

Where $\delta(t)$ is the Dirac delta function. Due to the small size of the system, the inertial term of the equation of motion is negligible in front of the drag force, which means that the equation to solve becomes:

$$\xi \frac{dx(t)}{dt} + K x(t) = \eta(t)$$

### Autocorrelation

The equation of motion of motion cannot be solved for the fluctuations x(t) because of the random noise term $\eta(t)$. It is however possible to solve the equation and find a solution for the autocorrelation $R_{xx}(t)$ of the fluctuations. The autocorrelation function is the cross-correlation of a signal with itself:

$$R_{xx}(\tau) = [x(t) \otimes x(t)](\tau) = \int_{-\infty}^{+\infty} \overline{x(t)} \cdot x(t + \tau) dt$$

For a causal real function whose total acquisition time $T$ is not infinite, the expression of the autocorrelation becomes:

$$R_{xx}(\tau) = \frac{1}{T} \int_{0}^{T} x(t) \cdot x(t + \tau) dt = \langle x(t) \cdot x(t + \tau) \rangle_t$$

Where $\langle \ \rangle_t$ is the average over the variable $t$.

In order to solve the equation of motion for the autocorrelation, we will have to modify the form of the equation. We will start by multiplying all terms by a temporally shifted fluctuation signal $x(t+\tau)$:

$$\xi \frac{dx(t)}{dt} \cdot x(t + \tau) + K x(t) \cdot x(t + \tau) = \eta(t) \cdot x(t + \tau)$$

All terms are then averaged over time:

$$\xi \left\langle \frac{dx(t)}{dt} \cdot x(t + \tau) \right\rangle_t + K \langle x(t) \cdot x(t + \tau) \rangle_t = \langle \eta(t) \cdot x(t + \tau) \rangle_t$$

With the equation in this form, each of these three terms may be simplified so as to be expressed in a convenient form:

- The term stemming from the elastic force may now be expressed directly as a function of the autocorrelation function:

$$K \langle x(t) \cdot x(t + \tau) \rangle_t = K \cdot R_{xx}(\tau)$$

- The averages in the term containing the random noise may be dissociated due to $x(t)$ and $\eta(t)$ being completely uncorrelated. Thus the whole term is null due to the null average of the random noise:

$$\langle \eta(t) \cdot x(t + \tau) \rangle_t = \langle \eta(t) \rangle_t \cdot \langle x(t + \tau) \rangle_t = 0 \qquad \text{because} \qquad \langle \eta(t) \rangle_t = 0$$

- The term stemming from the drag force is more complicated. It can be shown that the average term is actually the expression for the derivative of the autocorrelation in regards of the variable $\tau$:

$$\xi \left\langle \frac{dx(t)}{dt} \cdot x(t + \tau) \right\rangle_t = \xi \frac{dR_{xx}(\tau)}{d\tau}$$

In the end, the equation of motion becomes a first order linear differential equation for the autocorrelation *Rxx(τ)*:

$$\xi \frac{dR_{xx}(\tau)}{d\tau} + K \cdot R_{xx}(\tau) = 0$$

The solution of this equation is a single exponential function:

$$R_{xx}(\tau) = R_{xx}(0) \cdot e^{-\frac{K}{\xi}\tau}$$

Since the origin of the autocorrelation function is equal to the mean square of the fluctuations, the equipartition theorem tells us [**Chapter 2; D.I.3**]:

$$R_{xx}(0) = \left\langle x(t)^2 \right\rangle = \frac{k_B T}{K}$$

Therefore, the expression for the fluctuation's autocorrelation function is:

$$\boxed{R_{xx}(\tau) = \frac{k_B T}{K} \cdot e^{-\frac{K}{\xi}\tau}}$$



**Figure 103:** Semi-logarithmic representation of the autocorrelation of the radial fluctuations of a bead in free-rotation magnetic tweezers. The data is fitted with a single exponential as predicted by the model. The stiffness K of the compensating force and the drag coefficient $\xi$ of the bead are deducted from the fit values. The DNA molecule in this case has a length $L_{DNA}$=3.5μm, so the magnetic pulling force is estimated to $F_{mag}$=2.18±0.03pN.

The stiffness *K* of the compensating force and the drag coefficient $\xi$ may then be deduced from fitting the data with the final expression of the autocorrelation [**Figure 103**]. The

magnetic pulling force $F_{mag}$ can then be known through the model previously presented. We will also use the drag coefficient's value for certain measures of torques in later sections.

## Power spectrum density

Fitting the autocorrelation is fickle, essentially because the data points significant for the form of the exponential function represents a very small fraction of the data which is why the autocorrelation is usually shown in a semi-logarithmic scale [**Figure 103**]. It is much more convenient to switch to the frequency domain by studying the form of the power spectral density of the fluctuations. The power spectral density (*PSD*) is defined as the Fourier transform of the autocorrelation:

$$PSD_{xx}(f) = \int_{-\infty}^{+\infty}\int_{-\infty}^{+\infty} \overline{x(t)}\,x(t+\tau)\,e^{-2i\pi f\tau}\,dt\,d\tau$$

$$PSD_{xx}(f) = \int_{-\infty}^{+\infty} R_{xx}(\tau)\,e^{-2i\pi f\tau}\,dt\,d\tau$$
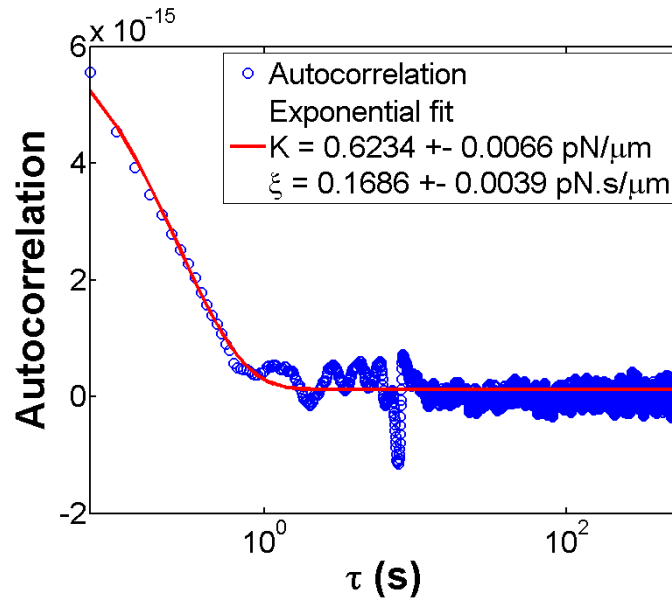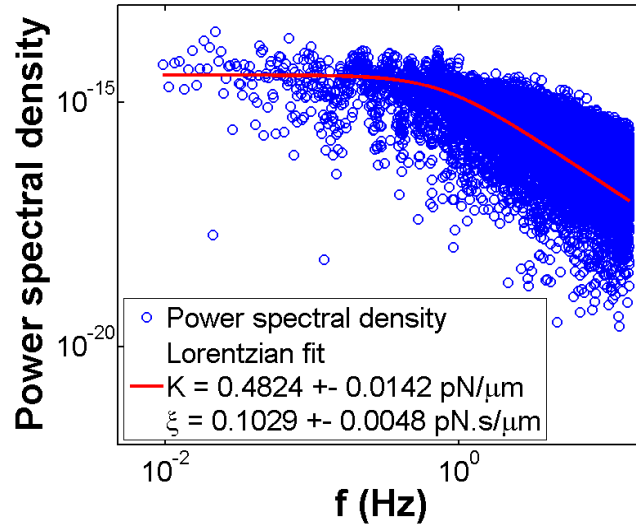


**Figure 104:** Logarithmic representation of the power spectral density of the radial fluctuations of a bead in free-rotation magnetic tweezers. The data is fitted with a Lorentzian function as predicted by the model. The stiffness *K* of the compensating force and the drag coefficient $\xi$ of the bead are deducted from the fit values. The DNA molecule in this case has a length $L_{DNA}$=3.5µm, so the magnetic pulling force is estimated to $F_{mag}$=1.69±0.05pN.

Where *f* is the spatial frequency. Knowing the expression of the fluctuations' autocorrelation, we can deduce the expression for the *PSD*. We'll need to use the fact that the autocorrelation is even ( $R_{xx}(-\tau) = R_{xx}(\tau)$ ):

$$R_{xx}(\tau \geq 0) = \frac{k_B T}{K}\cdot e^{-\frac{K}{\xi}\tau} \quad \text{and} \quad R_{xx}(\tau \leq 0) = \frac{k_B T}{K}\cdot e^{\frac{K}{\xi}\tau}$$

Thus the expression of the *PSD* is the sum of two integrals:

$$PSD_{xx}(f) = \frac{k_B T}{K} \int_0^{+\infty} e^{-\frac{K}{\xi}\tau} e^{-2i\pi f\tau} \, d\tau \quad + \quad \frac{k_B T}{K} \int_{-\infty}^0 e^{\frac{K}{\xi}\tau} e^{-2i\pi f\tau} \, d\tau$$

$$PSD_{xx}(f) = \frac{\dfrac{k_B T}{K}}{\dfrac{K}{\xi} + i\,2\pi f} \quad + \quad \frac{\dfrac{k_B T}{K}}{\dfrac{K}{\xi} - i\,2\pi f}$$

$$PSD_{xx}(f) = \frac{2\dfrac{k_B T}{\xi}}{\left(\dfrac{K}{\xi}\right)^2 + (2\pi f)^2}$$

In the end, the power spectral density has the form of a Lorentzian function with a cutoff frequency $f_c$ which is function of the compensating force's stiffness $K$ and of the drag coefficient $\xi$:

$$\boxed{PSD_{xx}(f) = \frac{PSD_{xx}(0)}{1 + \left(\dfrac{f}{f_c}\right)^2}}$$

with $\quad PSD_{xx}(0) = 2\dfrac{k_B T \xi}{K^2} \quad$ and $\quad f_c = \dfrac{1}{2\pi}\dfrac{K}{\xi}$

A Lorentzian function is much easier to fit accurately than an exponential function. As before with the autocorrelation, the compensating stiffness and the drag coefficient may be deduced from fit values **[Figure 104]**.

## Advantages of the frequency analysis

Aside from obtaining more accurate values from the fitting of data, the frequency analysis has multiple advantages. First it is possible to obtain hydrodynamic information on the system by measuring the bead's drag coefficient. This measure will be useful for later analysis for studying the bead's rotation speed. Secondly, the measure of the cutoff frequency allows us to test if the acquisition time for the force measurement was long enough for the measure to be pertinent. It will also tell us if the frame acquisition rate of the camera is high enough for the measure. Last but not least, the analysis in the frequency space allows for frequency filtering thus ridding the measure of any low frequency, long term drifts that might falsify the data.

# D.II. Torques

## D.II.1. Plotting the potential of a magnetic torque

Paramagnetic beads trapped in an energy potential by a magnetic field induced torque fluctuate in rotation around their equilibrium position due to thermal energy resulting in Brownian motion. Through these fluctuations we may gain access to the form of this potential. In our experimental conditions, we'll assume that these angular fluctuations obey a Maxwell-Boltzmann statistics. If so, the repartition of the angular fluctuations will follow a Boltzmann distribution in which the probability $p(\theta)$ for the bead to be at the angle θ is given by:

$$p(\theta) = \frac{e^{-\frac{U(\theta)}{k_B T}}}{Z}$$

Where U(θ) is the potential energy associated with the angle $\theta$, $k_B$ is the Boltzmann constant, $T$ the temperature in Kelvin and $Z$ is the partition function. Then the equation for the potential energy becomes:

$$U(\theta) = -k_B T \ln(p(\theta)) - k_B T \ln(Z)$$

And since potential energy is always defined up to an additive constant, we may ignore the term containing the partition function, thus we obtain:

$$U(\theta) = -k_B T \ln(p(\theta)) + cte$$
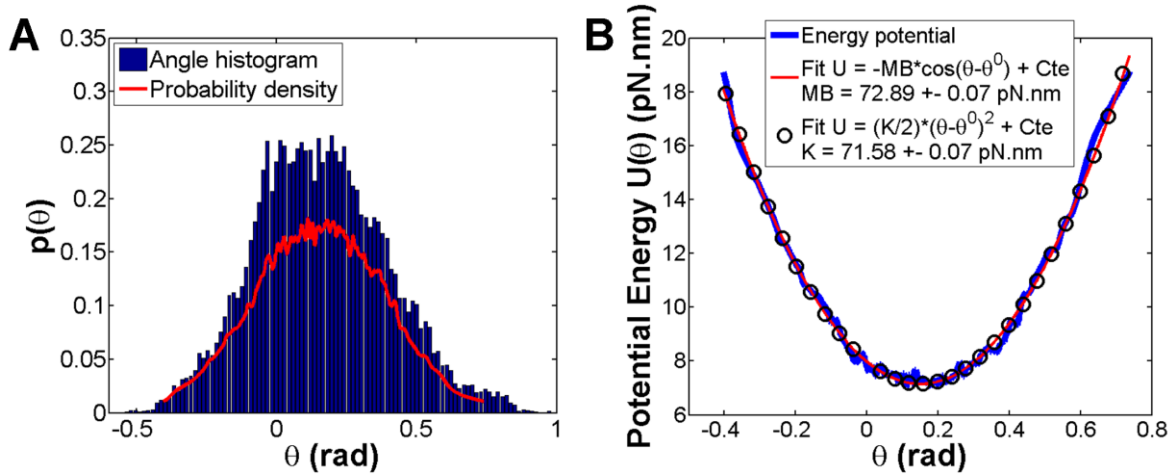


**Figure 105:** Experiment showing the measure of the magnetic energy potential to which a paramagnetic bead linked to a naked dsDNA molecule is subjected. (**A**) The probability density function (**red profile**) has been superposed over the histogram (**blue**) of the bead's angular positions. (**B**) The deduced energy potential (**blue profile**) is fitted by the magnetic potential formula (**red profile**) and the spring approximation model (**black profile**).

Obtaining the probability associated with the angles $\theta$ from our data comes down to drawing the histogram of angular position or calculating the probability density function

[Figure 105; left]. The latter may be obtained through derivation of the function giving the probability for the angle $\theta$ to have a value inferior to $x$:

$$f(x) = P(\theta \leq x)$$

The normalization of the histogram or of the probability density function does not matter for analysis since it will only affect the additive constant of the potential. The magnetic torque applied by a magnetic field $B$ on a paramagnetic bead with a magnetic moment $M$ is given by:

$$\Gamma_{mag}(\theta) = -MB\sin(\theta - \theta_0)$$

Where $\theta_0$ is the angular orientation of the magnetic field. Thus we can deduce the potential energy through the knowledge that the torque is the derivation of the potential:

$$\Gamma_{mag}(\theta) = -grad(U(\theta))$$

Therefore we finally obtain the equation for the potential energy of a magnetic torque:

$$\boxed{U_{mag}(\theta) = -MB\cos(\theta - \theta_0)}$$

We may then use this equation to fit our data [Figure 105; B red profile] and thus obtain the value of $MB$ which represents the maximum torque applicable by the magnetic field on the bead.

## D.II.2. The spring approximation

If the magnetic trap is strong enough and thus if the angular fluctuations of the bead are small enough, then we may approximate the magnetic field by a rotational spring applying a torque proportionate to the angular deviation:

$$\Gamma_{spring}(\theta) = -K(\theta - \theta_0)$$

Where $K$ is the spring constant. This holds true only in angle ranges in which the sine function may be approximated by a linear function ( $\sin(x) \approx x$ ). In this case, $K$ is equivalent to $MB$ and also represents the maximum torque. The potential energy of a rotational spring is given by:

$$\boxed{U_{spring}(\theta) = \frac{K}{2}(\theta - \theta_0)^2}$$

Using this function to fit energy potentials makes little difference for magnetic traps with a strength over 16pN.nm (approximately four times the thermal energy) [Figure 105; B black profile].

Making this approximation allows us, exactly as in the case of force measurement, to estimate the spring constant through the form of the power spectral density of the angular fluctuations. We then benefit from all the advantages frequency analysis and may thus access the bead's hydrodynamic drag coefficient in rotation. The data is well fitted by Lorentzian functions thus confirming the validity of the model; however the values of the trap stiffness *K* are always a bit underestimated when compared to the maximum torque value *MB* [**Figure 106**].
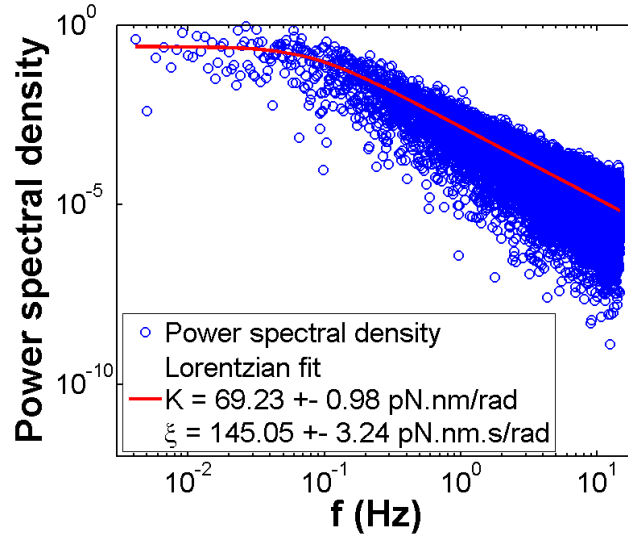


**Figure 106:** Power spectrum density of the angular fluctuations of the bead presented in [**Figure 105**]. The *PSD* is fitted by a Lorentzian function (**red profile**) as per the spring approximation model.

# D.III. Bootstrapping

In order to ascertain the error in measurement of forces or torques, we apply bootstrapping algorithms on our data to effectuate several measures on the same data set. The point of these algorithms is to ascertain the effect of data sampling on the various deduced values. It allows to reasonably compensate for the lack of multiple measurements of the same value.

The temporal beginning and end of the data sample on which the measure is made are chosen randomly within the pertinent data range. Some precautions are taken to insure that the samples are large enough to allow pertinent measures. This process is repeated several times (typically 100 different sampling) and the final measure is considered to be the average of all measures. The error on the measure is estimated by the standard deviation.

For example, the parameters for the torque measurement shown in [**Figure 106**] are after bootstrapping on 100 samples:

$$K = 69.91 \pm 1.28 \, pN.nm.rad^{-1}$$

$$\xi = 139.35 \pm 4.00 \, pN.nm.s.rad^{-1}$$

# E. Results on naked DNA

## E.I. Force-extension curves



**Figure 107:** (**A**) XY-positions of a bead at five different forces; as the force decreases, so does the mean height $Z$ of the bead and the fluctuations become wider. The measured forces are th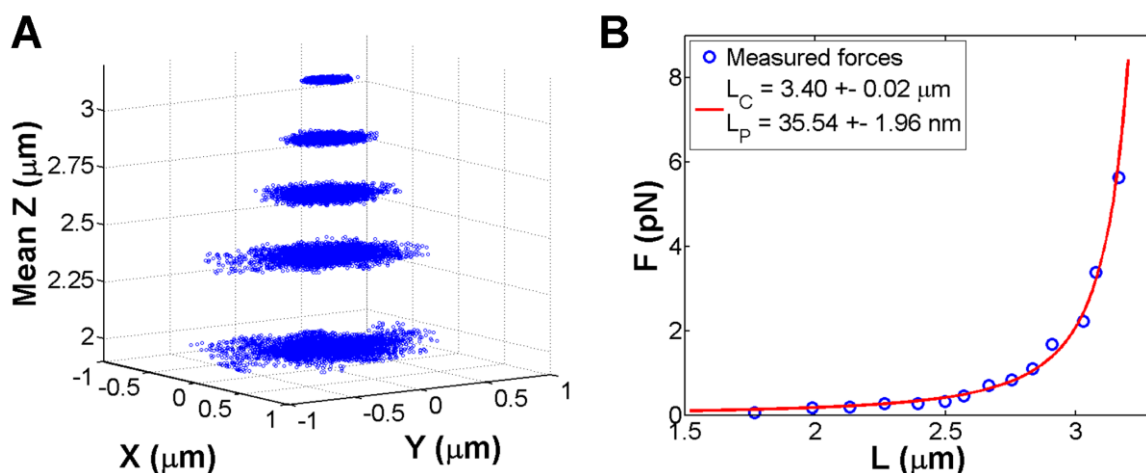en fitted by the worm-like chain model to extract the crystallographic length $L$ of the DNA molecule and its persistence length $L_P$ (**B**).

Before each experiment, a certain amount of calibration is required for future use during data analysis. Therefore once the calibration for the beads' height is made **[Figure 90]**, a force-extension curve is measured for each bead **[Figure 107]**. The XYZ-positions of the beads are measured during a set acquisition time for a range of values of the magnets' height $Z_{mag}$. The forces are then deduced from the centers' position fluctuations in the XY-plane and the height of the bead is averaged over time. These measures are used to plot the magnetic pulling force $F$ as a function of the length $L$ of the DNA molecule. These force-extension curves are then fitted by the improved Marko-Siggia formula based on the worm-like chain model **[Chapter 2; B.I.3]** in order to extract the crystallographic length $L_C$ and the persistence length $L_P$ of each DNA molecule. For the fit to be accurate, the force range of the force-extension curve must be chosen as to include the curved part of the response which is in our case between $F$=0.5pN and $F$=5pN. Our setup allowed for forces ranging from 0 to 10pN.

Once calibrated, the relation between the magnetic pulling force $F$ applied to the bead and the height $Z_{mag}$ of the magnets relatively to the microfluidic chamber is fitted by a power law **[Figure 108]**. This allows us to interpolate the force applied to the bead for any value of the magnets' height dispensing with the need for any further force measurement. This is especially useful for low forces where the force measurement requires a very long acquisition time and for which the error is important.

Knowing the value of the crystallographic length is necessary for normalization of the molecules' extensions and for the calculation of the supercoiling degree. The persistence length is used as a test for knowing the nature of what is attached to the paramagnetic bead. The value of $L_P$ for a single dsDNA molecule is expected to be around 50nm. If the measured persistence length is greatly different from this value, then the bead is probably not attached

to a DNA molecule but to a dust particle or something alike. The measurement of $L_P$ also allows discriminating between beads attached to single dsDNA molecules and beads attached to multiple molecules. The persistence length of a double dsDNA molecule is in our case half the normal value and yields results around $L_P \approx 25$nm.
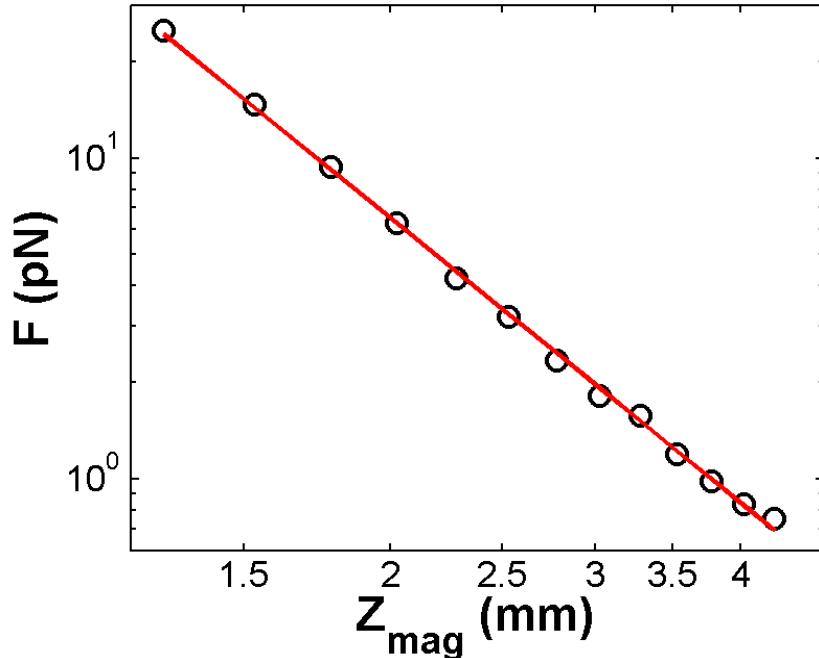


**Figure 108:** Measured forces $F$ as a function of the height $Z_{mag}$ of the magnets relatively to the microfluidic chamber in a logarithmic scale. The relation is linear in a logarithmic scale which means the force is proportional to a power law of the height ($F \propto Z_{mag}{}^{\alpha}$). Here the power coefficient was measured to $\alpha = -2.95$.

During my thesis, I used two types of dsDNA construct, one fabricated by PCR from the λ-phage's DNA and the other fabricated by transformation form the pREP4 vector. The λ-construct had 15941±81 base pairs and its crystallographic length was measured at $L_\lambda$=4.71±0.20µm **[Figure 109; A]**. The pREP4-construct had 11941±668 base pairs with a measured length $L_{pPREP4}$=3.32±0.35µm **[Figure 109; B]**. The persistence lengths of both constructs gave measures around $L_P$=47.1±14.0nm **[Figure 109; C]**. Any DNA molecules yielding values of $L_P$ equal or inferior to 25nm were not considered during analysis.
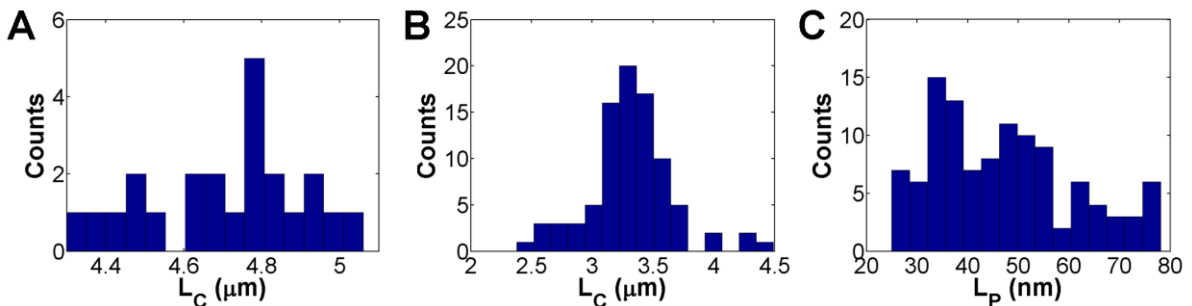


**Figure 109:** (**A**) Histogram of 23 measured crystallographic lengths $L_C$ for the DNA construct made by PCR from the λ-DNA. The average length was measured to $L_\lambda$=4.71±0.20µm. (**B**) Histogram of 87 measured crystallographic lengths $L_C$ for the DNA construct made by transformation from the pREP4 vector. The average length was measured to $L_{pREP4}$=3.32±0.35µm. C) Histogram of 110 measured persistence lengths $L_P$ on both DNA construct. The average persistence length was measured to $L_P$=47.1±14.0nm. All values were obtained by fitting our force-extension curves with the worm-like chain model.

# E.II. Torsionally constrained DNA

The work of this thesis will focus on the study of the behavior of nucleoprotein filaments formed by assembly of hRad51 proteins onto dsDNA molecules. In order to fully understand the results of such a study, it is necessary to know how naked dsDNA molecules behave for comparison. Their behavior in magnetic tweezers was previously described in this chapter **[Chapter 2; B.III]**, by using references to the work of other teams. However the specifics of the behavior are dependent on the buffer conditions, especially on the concentrations of ions present. It is therefore important to present the results on naked DNA in our experimenting conditions.
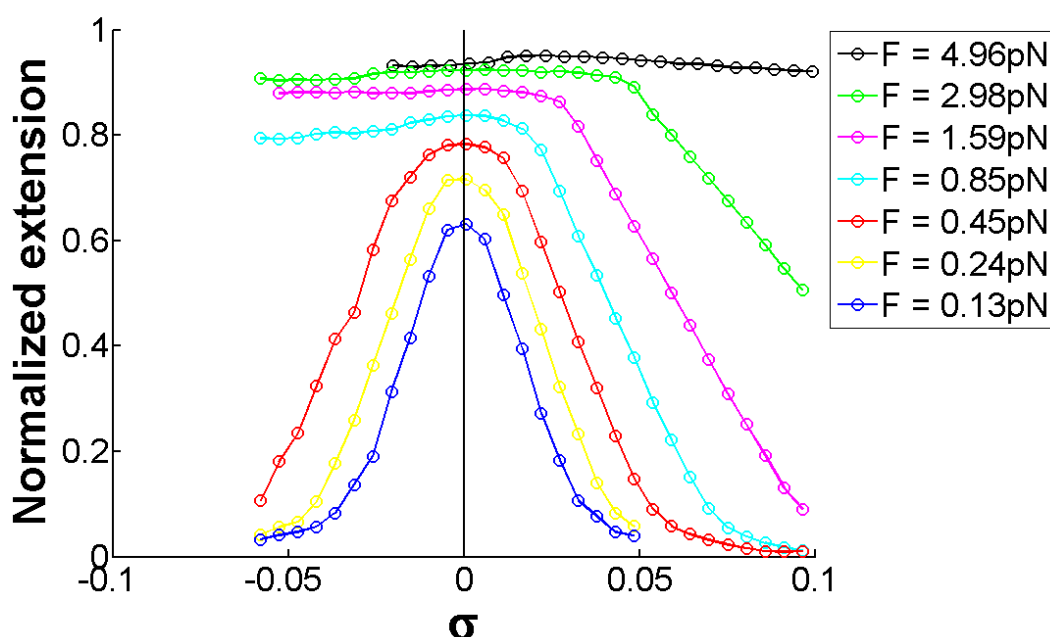


**Figure 110:** Normalized extension of naked dsDNA molecules in magnetic tweezers at various pulling forces as a function of the supercoiling σ. The extensions were normalized by the crystallographic length. Buffer conditions: 15mM Tris (pH 7.5), 2mM MgCl$_2$, 25mM NaCl, 0.05% Tween 20, 1mM DTT and 1mM ATP.

We placed naked dsDNA molecules in our experimenting buffer containing everything except for the hRad51 proteins: 15mM Tris (pH 7.5), 2mM MgCl$_2$, 25mM NaCl, 0.05% Tween 20, 1mM DTT and 1mM ATP. The torsion-extension response was measured at various pulling forces **[Figure 110]**. For forces under $F$=0.5pN, the response was a symmetrical hat curve indicating the formation of plectonems for positive and negative supercoiling degrees. The curves became asymmetrical for forces over $F$=0.5pN due to the denaturation of DNA for negative supercoiling degrees. Plectonems still formed for positive supercoiling degrees until $F$=4pN, value over which the formation of ScP-DNA was favored.

During most of our experiments with nucleoprotein filament, we chose to apply pulling forces ranging from 2pN to 4pN. The pertinent supercoiling range for the study of filaments is -0.5 < σ < 0.1. The behavior of a naked dsDNA molecule at a pulling force of $F$=3pN over a wide range of supercoiling degree is shown in **[Figure 111]**. The formation of dDNA for negative supercoiling values induces an increased extension due to the more elastic behavior of dDNA. The factor of extension does not exceed 10% for supercoiling degrees σ>-0.5.
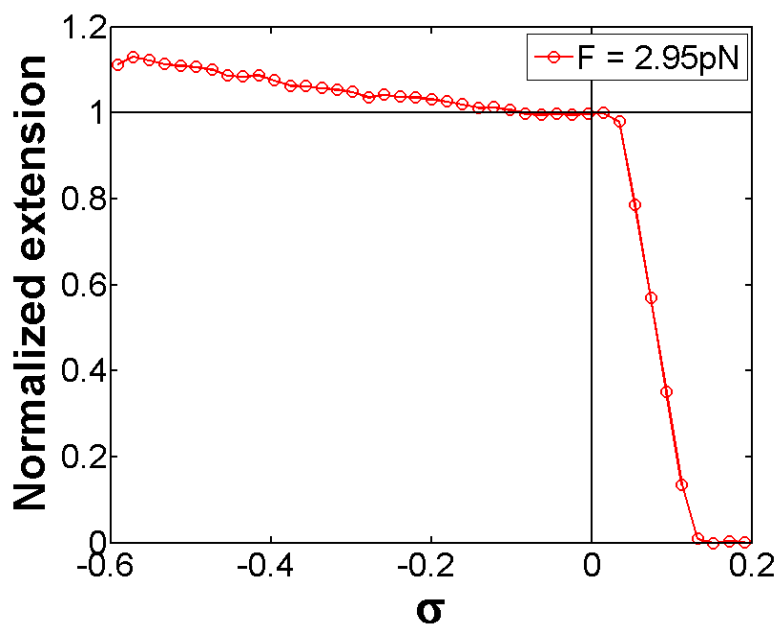
**Figure 111:** Normalized extension of a naked dsDNA molecule in magnetic tweezers at a pulling force of 2.95pN over a wide range of supercoiling degree σ. The extension was normalized with the molecule's length at σ=0. Buffer conditions: 15mM Tris (pH 7.5), 2mM $MgCl_2$, 25mM NaCl, 0.05% Tween 20, 1mM DTT and 1mM ATP.

## E.III. Plectonem formation torque
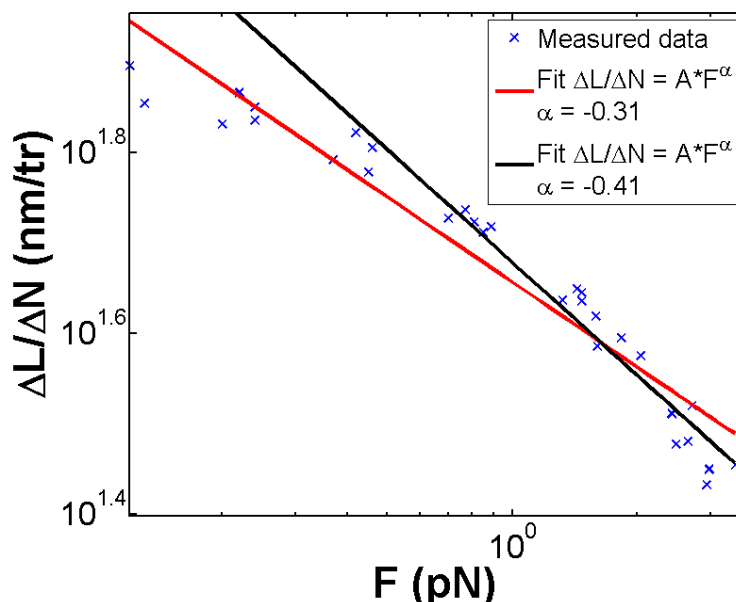


**Figure 112:** DNA extension decrease rate during plectonem formation $\Delta L/\Delta N$ as a function of the magnetic pulling force $F$ (**blue data points**). The measured data is fitted by a power law (**red profile**) showing a dependency to the force with a power coefficient $\alpha$=-0.31. The second fit (**black profile**) is also fitted by a power but it disregards the measured data for low forces (cutoff force = 0.4pN) for which the relative error on the force is the greatest; the data for high forces is fitted much better and the power coefficient becomes $\alpha$=-0.41.

When measuring torques on DNA molecules such as we will be doing later on, it is always necessary to have an idea, at least approximately, of the value buckling torque associated with the formation of plectonems. We've seen qualitatively that this buckling

torque is dependent on the pulling force applied to the molecules, the value of the torque increasing with the force. The effect of the change in buckling torque value may be observed in the behavior of naked dsDNA molecules at positive supercoiling degrees. The molecules' end to end extension decreases as the supercoiling degree increases; this decrease starts at higher values of the supercoiling degree and the decrease rate is lower as the pulling force increases **[Figure 110]**.

Since the buckling torque is also highly dependent on the buffer conditions, it becomes necessary to characterize it in our buffer. Therefore we've measured the torsion-extension response of several DNA molecules in our buffer containing 15mM Tris (pH 7.5), 2mM MgCl2, 25mM NaCl, 0.05% Tween 20, 1mM DTT and 1mM ATP. The decrease rates were measured at different pulling forces **[Figure 112]**. When fitted with a power law, the data showed a dependency to the pulling force with a power coefficient $\alpha=-0.41$. The decrease rate is proportional to the buckling radius, therefore the previously presented model would suggest a force dependency with a coefficient $\alpha= -0.5$. This coefficient was measured experimentally by another team with a value of $\alpha=-0.4$ [176].

The buckling torque $\Gamma_b$ may be deduced from the value of the supercoiling degree $\sigma_b$ at which the extension decrease starts. When a positive twist $\theta$ is applied to the DNA molecule, a torque $\Gamma$ is applied to the DNA. The value of this torque increases as the applied twist increases until the torque reaches the value of the of the buckling torque $\Gamma_b$ for a twist value $\theta_b$:

$$\Gamma_b = \frac{C_{DNA} \cdot k_B T}{L_C} \theta_b$$

Where $L_C$ is the contour length of the DNA and $C$ is its effective torsional persistence length. Increasing the twist further no longer results in torque increase but induces the formation of plectonemic buckles while keeping the torque applied to the DNA constant **[Figure 84]**. To convert the measured buckling twist values $\theta_b$ into values of the buckling torque, we need to estimate the value of the effective torsional persistence $C_{DNA}$. We used the third order approximation from the model derived by Moroz and Nelson [177], [178]:

$$C_{DNA} = C_{\lim} \left( 1 - \frac{\dfrac{C_{\lim}}{L_P}}{4\left(\dfrac{L_P F}{k_B T}\right)^{1/2}} + \frac{\left(\dfrac{C_{\lim}}{L_P}\right)^2 - 2\left(\dfrac{C_{\lim}}{L_P}\right)}{16\left(\dfrac{L_P F}{k_B T}\right)} \right.$$

$$\left. - \frac{4\left(\dfrac{C_{\lim}}{L_P}\right)^3 - 16\left(\dfrac{C_{\lim}}{L_P}\right)^2 + 21\left(\dfrac{C_{\lim}}{L_P}\right)}{256\left(\dfrac{L_P F}{k_B T}\right)^{3/2}} + O\left(F^{-3/2}\right) \right)$$

Where $C_{lim}$ is the DNA's intrinsic torsional persistence length and $L_P$ is its persistence length. This model has been frequently used for theoretical analyses [179] and for comparison with experimental data [146], [180], [181]. The value of the intrinsic torsional persistence length was considered to be $C_{lim}=109$nm as was found by Moroz and Nelson [178] when comparing their model with the data from magnetic tweezers experiments [158]. This value has been shown to be in good agreement with data from a rotary bead assay in optical tweezers [182] and data from magnetic tweezers experiments [146], [181].
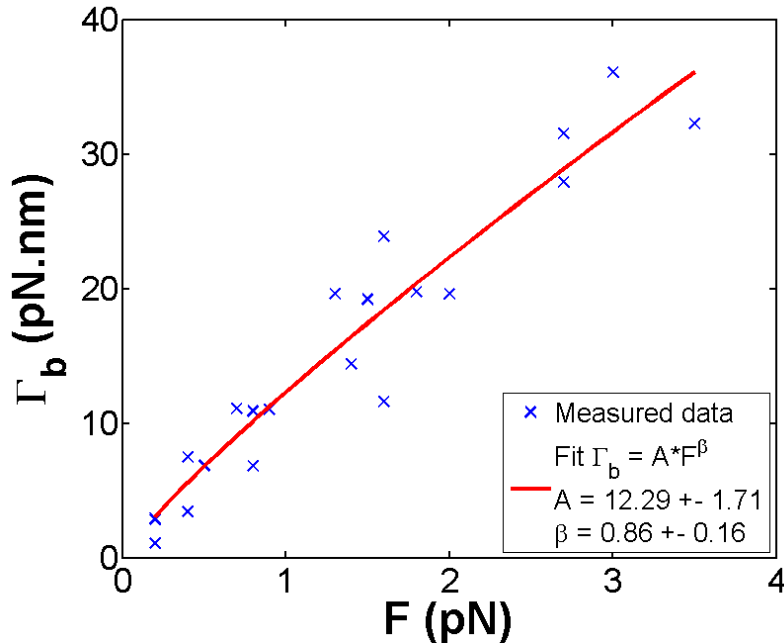


**Figure 113:** Buckling torque $\Gamma_b$ as a function of the magnetic pulling force $F$ (**blue data points**). The measured data is fitted with a power law (**red profile**) showing a dependency to the force with a power coefficient $\beta=0.86$.

Converted values of the buckling torque derived from our measured data shows an almost linear dependency of the torque relatively to the pulling force [**Figure 113**]. Fitting the data with a power law shows a dependency with a power coefficient $\beta=0.86$. Our findings are in good agreement with a previous study in magnetic tweezers measuring the buckling torque of dsDNA at different pulling forces for various salt conditions [**Figure 114**].

The values of the buckling torque for values of the pulling forces over $F=2$pN are superior to 20pN.nm which is the order of magnitude of the torques that we will measure later on. It is therefore safer for experiments on torque measurement to be made in conditions where the pulling force is $F>3$pN.

However this condition has not always been achieved in our experiments where the pulling force is sometimes around 2pN. It should be noted that the hRad51-dsDNA nucleoprotein filament has a much higher persistence length at least one order of magnitude higher than naked DNA molecules [140], [141]. Hence the formation of plectonems on filaments should happen at much higher values of torque. This remains true even if portions of DNA are left uncovered by the protein since the portions of naked DNA in the filament should not be long enough to allow the formation of a plectonemic buckle without also bending the covered parts of the filament. In fact, in all our experiments and in previous experiments made in our team [141], [157], filaments only form plectonems for forces well under $F=0.5$pN.

Figure removed because of copyrights

**Figure 114:** Extracted from [180]. Buckling torque of dsDNA as a function of the magnetic pulling force for different salt conditions. The continuous lines fitting the monovalent salt series yield exponents of 0.72±0.07.

# Chapter 3: Studying of the hRad51 protein

## A. Two filament structures

It is known that helical hRad51-DNA filaments can assemble in different forms depending on the bound cofactors such as adenosine triphosphate (ATP) or adenosine diphosphate (ADP) [135]. Earlier studies revealed that proteins of the RecA recombinase family, which hRad51 is a part of, can form two principal types of helical complexes: stretched and non-stretched [183]. The stretched filaments form in the presence of ATP or its non-hydrolyzable analogs on ssDNA or dsDNA. The DNA in these complexes adopts an unusual structure with ~19 bases or base pairs per ~95Å pitch [128], [152], [184]. The stretched filaments were shown to constitute the active state in the process of pairing and strand exchange [113], [185]–[187]. Non-stretched filaments have a less well-defined structure and it is likely that there are several distinct forms of them [183]. Structural studies of one of the forms of non-stretched RecA filaments indicated that it had different protein:DNA stochiometry than stretched filaments [188]. This finding decreased the interest in non-stretched filaments because it seemed to exclude their participation in the catalytic cycle of DNA pairing and strand exchange. However, relatively recent studies using total internal reflection fluorescence microscopy (TIRFM) revealed that human Rad51 filaments formed on linear dsDNA molecules can reversibly transit several times between stretched and non-stretched forms depending on whether ATP was added or removed from the reaction buffer [119]. Because there was no free hRad51 in the flow cells used for the experiments, these reversible transitions strongly indicated that stretched and non-stretched helical filaments constitute simply different allosteric forms of hRad51-dsDNA complexes where the transition between the two forms is regulated by ATP binding and hydrolysis. This finding reinitiated interest in non-stretched forms of the hRad51-DNA filaments and in the mechanism by which helical Rad51-DNA complexes can switch between stretched and non-stretched forms.

### A.I. Torsion-dependent states

The experiments shown in this section aim to demonstrate the existence of two distinct conformations of hRad51-dsDNA-ATP nucleoprotein filaments: a stretched state exhibiting an extension of approximately 1.5 times the length of B-DNA and a condensed state with an extension of ~1.05 times the length of B-DNA. We will also show that the formation of one or the other conformation depends solely on the supercoiling degree imposed to the dsDNA molecule during filament formation. The stretched state being unwound with a supercoiling degree of $\sigma=-0.43$ and the condensed state having the same twist as B-DNA with $\sigma=0$.

## A.I.1. The stretched state: S

It is known that the active form of hRad51 nucleoprotein filaments is stretched by 50% and unwound by 43% compared to B-DNA [99], [127], [128]. All data also suggest that the active form contains ATP because stretched forms were observed only in the presence of ATP or one of its non-hydrolyzable analog during filament formation (AMP-PNP or ADP-ALF$_4^-$).

Therefore in magnetic tweezers, we investigated the formation of hRad51-dsDNA nucleoprotein filaments on non-nicked DNA molecules on which we imposed prior to protein insertion a supercoiling degree of $\sigma = -0.43$. Those experiments confirmed the existence of a stretched state dsDNA-hRad51 nucleoprotein filament underwound by 43% and stretched by 50% when compared to B-DNA. These filaments were formed in conditions containing ATP and a divalent cation ($Mg^{2+}$ or $Ca^{2+}$).

### Forming stretched filaments on constrained dsDNA
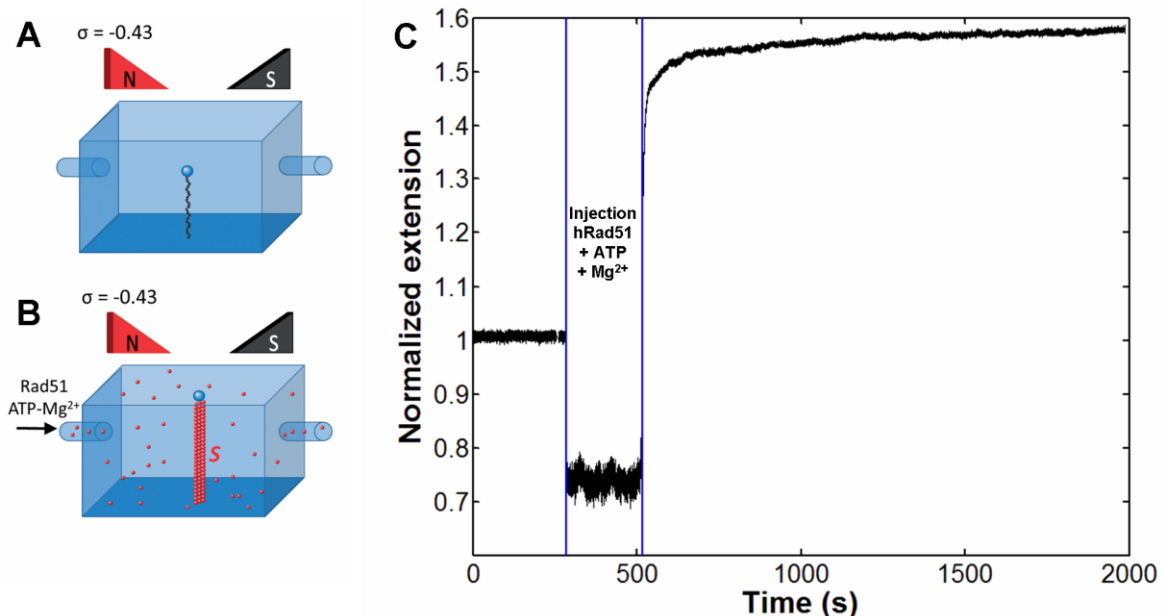


**Figure 115:** Experiment showing the formation of the unwound stretched state of the hRad51-dsDNA nucleoprotein filament in ATP and $Mg^{2+}$. Initially the flow chamber contained naked DNA molecules (**A**), torsionally constrained with an imposed supercoiling degree of $\sigma = -0.43$. A buffer with 200nM hRad51, 1mM ATP, 2mM MgCl$_2$, 1mM DTT, 0.05% Tween 20, and 25mM NaCl was inserted into the flow chamber (**B**). The tracking of the relative extension of a dsDNA molecule during hRad51-ATP-Mg nucleoprotein filament formation is shown in (**C**). The molecule was extended by a pulling force of $F$=3.25pN. Extension is apparently shortened during buffer insertion due to the drag force of the flow. After insertion, a stretched state nucleoprotein filament was formed; molecule extension went up by ~50%.

The tracking of the bead's vertical position during the experiment gives us the evolution in time of the DNA molecule's extension [**Figure 115**]. When unwound to this degree, naked DNA molecules are slightly stretched by factor not exceeding 10% [**Figure 111**]. Thus, here the naked DNA is initially stretched by 2%. The protein was inserted by applying a flow in the microfluidic chamber which takes roughly 200 seconds to effectuate buffer exchange. The protein reaction buffer contained 15mM Tris-HCl (pH 7.5), 25mM NaCl, 0.05% Tween 20, 2mM MgCl$_2$, 1mM DTT, 1mM ATP and 200nM hRad51. When flow is present, the molecule's apparent extension is artificially lowered due to the drag force exerted

on the bead. During buffer exchange, after approximately 200 seconds, the molecule started extending, indicating that the protein had entered the canal and come into contact with the DNA molecule. The flow was then stopped and accurate measurement of the molecule extension could resume. The molecule extended rapidly at first and slowed down until it reached a plateau value. The typical filament formation time was observed to be around 15-25 minutes.

The final extension was approximately 1.5 times the length of B-DNA at $\sigma = 0$ under the same pulling force, it was reached at this protein concentration in a little less than 15 minutes. Other experiments using the same buffer conditions but with 2mM $CaCl_2$ instead of $MgCl_2$, showed similar filament behaviors, with a slightly increased extension rate. Measurements of several nucleoprotein filaments' extension at $\sigma=-0.43$ yielded final stretchings, when compared to the initial length of the naked DNA at $\sigma=0$ at the same pulling force, as follows:

- In presence of ATP and $Mg^{2+}$: final stretching of 53.1±1.4% (measured on 34 DNA molecules with a standard deviation of 7.7%).

- In presence of ATP and $Ca^{2+}$: final stretching of 55.2±1.2% (measured on 28 DNA molecules with a standard deviation of 6.1%).

The length used to normalize the data presented above is the length of the naked DNA molecule under the same pulling force at a null supercoiling degree. At the typical pulling forces used during our magnetic tweezers experiments (2-8pN), the DNA extension is approximately 90% of the crystallographic length of the molecule.

## Normalized extension measurement
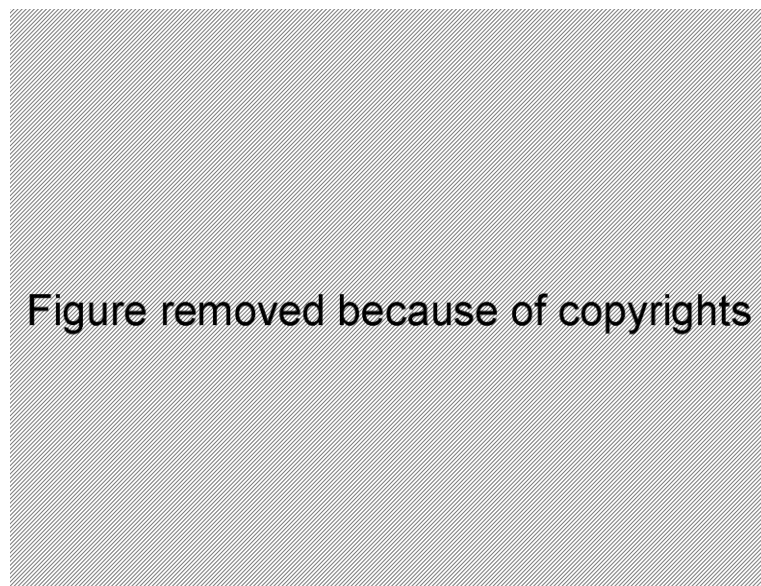


**Figure 116:** Extracted from [139]. Force-extension responses in classical magnetic tweezers setups. The force-extension behavior of dsDNA is fit using the worm-like chain model (red line) yielding a contour length of 2.9±0.1µm and a persistence length of 49±3 nm, whereas ssDNA displays a different flexibility behavior (black line) which cannot be described by worm-like chain. After filament formation in the presence of ATP-$Ca^{2+}$, the DNA molecule is elongated and stiffened yielding a contour length of 4.0±0.1µm and a persistence length of 268±17nm (blue line) for this particular case.

Measurement of stretchings exceeding the expected 50% can be explained by the entropic coil behavior of a DNA molecule. Indeed considering the force-extension of a naked dsDNA molecule compared to the one of a hRad51-dsDNA nucleoprotein filament [139]–[141], the naked DNA requires a stronger pulling force to reach its maximum than a filament **[Figure 116]**. Therefore the ratio of the filament's extension compared to the initial length of the DNA at the same pulling force decreases with the pulling force tending to a limit value when the pulling force is infinite. By studying these force-extension responses, we estimate that it requires a pulling force of at least 10pN or above to correctly evaluate the actual normalized extension. A normalized extension measured with a pulling force inferior to that would be overestimated as is the case in our experiments where pulling forces range from 2 to 8pN.

## Comparison with other single molecule studies

We can compare our data to normalized extensions given or deduced from published single molecule studies on hRad51-dsDNA nucleoprotein filaments. When the pulling force was not given by the study, it was deduced from the initial length of the naked dsDNA before filament formation, using the worm-like chain model as an estimation of the force.

Thus, for the stretched state in ATP-$Mg^{2+}$, our normalized extension was 1.53±0.02 times the length of the naked DNA. Studies in TIRFM show results of 1.57 [131] and 1.55±0.09 [119]; the pulling forces in those experiments were estimated at 0.6±0.1pN. A study in optical tweezers yields a result of 1.49±0.03 [135], with an estimated pulling force of 1.2±0.2pN.

For the stretched state in ATP-$Ca^{2+}$, we obtained a normalized extension of 1.55±0.02. This can be compared to measurement stemming from optical tweezers experiments yielding extensions of 1.64±0.03 [135], with a pulling force of 1.2±0.2pN, and 1.48±0.04 [136]. That last measurement is actually more accurate than ours or the others, because it compares the asymptotes of the force-extension curves while considering only fully hRad51-coated regions of the filament. We may also compare the extensions obtained for AMP-PNP-bound filaments, measured to 1.63±0.06 in optical tweezers , with a pulling force of 1.2±0.2pN, and 1.55 measured in TIRFM [119], with a pulling force of 0.6±0.1pN.

## Normalizing with crystallographic length

If one is to normalize the data with the crystallographic length of the DNA, obtained from the asymptote of the force-extension curves for the naked DNA, instead of the initial length at the same pulling force, then the our data becomes:

- In presence of ATP and $Mg^{2+}$: final stretching of 40.8±1.6% (measured on 34 DNA molecules with a standard deviation of 9.3%).

- In presence of ATP and $Ca^{2+}$: final stretching of 42.4±1.4% (measured on 28 DNA molecules with a standard deviation of 7.4%).

These crystallographic lengths normalized stretchings may be compared to a previous study in magnetic tweezers [139], which yielded stretchings of 44.1±0.8% in the case of ATP-Mg$^{2+}$ and 45.3±1.5% for ATP-Ca$^{2+}$. The pulling force in this study was 5pN.

## Protein coverage

It has been shown by fluorescence microscopy in optical tweezers experiments that parts of hRad51-dsDNA filaments completely covered with hRad51 proteins show an strictly non-elastic response to tension whereas non-covered parts behave exactly like naked DNA [136]. Therefore if filaments were completely covered with proteins, we should observe a filament extension equal to 150% of the DNA molecule's crystallographic length. Observing stretchings inferior to that when compared to the crystallographic length suggest that the DNA molecules are only partially covered in our experiments. The very fact that these filaments display an elastic behavior **[Figure 116]** confirms that are only partially coated.

Since the covered parts of the filaments are non-elastic, they should show an extension equal to 150% of the crystallographic length independently of the force applied (if this force is high enough, typically over 1pN). The naked DNA parts however are extended to a fraction of the crystallographic length and this fraction is function of the pulling force.

One solution to estimate the protein coverage is to compare the crystallographic length of the filaments with the crystallographic length of the DNA molecules as previously done in earlier magnetic tweezers studies [139], [140]. This process however is time-consuming and not adapted to the study of filaments' response to torsion since the filaments' crystallographic lengths should be measured for each data point. To estimate the protein coverage in our experiments, we are going to assume that the filaments' extension is a linear combination of fully extended protein covered sections and partially extended naked DNA sections as follows:

$$l_{fil} = p \cdot 1.5 \cdot l_{crys} + (1-p) \cdot l_{DNA}$$

where $l_{fil}$ is the filament's extension, $l_{crys}$ is the crystallographic length of the DNA molecule, $l_{DNA}$ is the DNA molecule's extension at the used pulling force and $p$ is the protein coverage (0≤$p$≤1). Since $l_{crys}$ and $l_{DNA}$ are measured prior to any protein insertion on our experiments, we can deduce the protein coverage by applying the following formula:

$$p = \frac{\dfrac{l_{fil}}{l_{crys}} - \dfrac{l_{DNA}}{l_{crys}}}{1.5 - \dfrac{l_{DNA}}{l_{crys}}}$$

Applying this formula to our data yields the following protein coverages:

- In presence of ATP and Mg$^{2+}$: protein coverage of 84.9±2.9% (34 molecules, standard deviation of 16.4%).

- In presence of ATP and $Ca^{2+}$: protein coverage of $87.6 \pm 2.4\%$ (28 molecules, standard deviation of 7.4%)

These results are consistent with previous studies on torsionally unconstrained dsDNA molecules in magnetic tweezers. The protein coverages obtained by theses studies were of $88.1 \pm 1.6\%$ [139] and $82 \pm 2\%$ [140] for ATP-$Mg^{2+}$ with pulling forces of respectively 5pN and 6pN. For ATP-$Ca^{2+}$, a protein coverage of $91 \pm 3\%$ [139] was found, with a pulling force of 5pN.

Moreover, our results were obtained by imposing a supercoiling degree of $\sigma = -0.43$ to the molecules, confirming that hRad51-dsDNA extended filament structure induces an unwinding by approximately 43% compared to the B-DNA conformation. Such a measurement should taken as $\sigma = -0.43 \pm 0.05$. Indeed, exact measurement of the supercoiling degree is error prone in magnetic tweezers even though the exact number of turns imposed to the DNA molecule is known. To convert the number of turns into the supercoiling degree, normalization by the total number of turns present in the DNA molecule in its B-form is required. This last quantity is deduced from the contour length of the DNA molecule which as an absolute extension value may only be known with a certain experimental error.

## A.I.2. The compact state: C
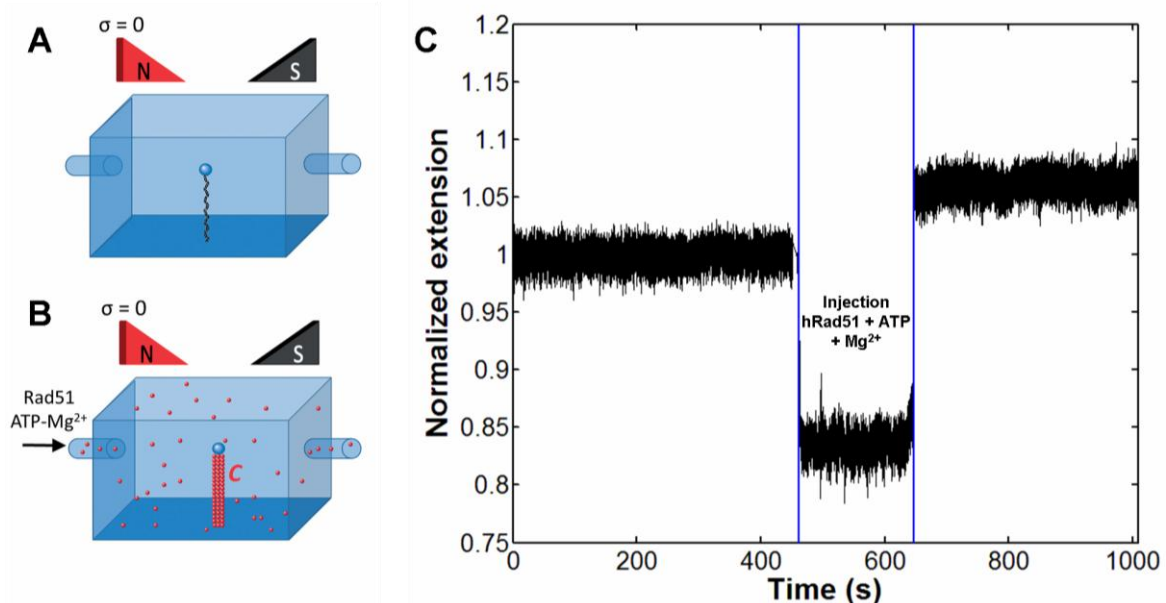


**Figure 117:** Experiment showing the formation of the null torsion condensed state of the hRad51-dsDNA nucleoprotein filament in ATP and $Mg^{2+}$. In a flow chamber containing naked DNA molecules whose supercoiling degree was kept at $\sigma = 0$ (**A**), a buffer with 200nM hRad51, 1mM ATP, 2mM $MgCl_2$, 1mM DTT, 0.05% Tween 20, and 25mM NaCl was inserted to form nucleoprotein filaments (**B**). The tracking of the relative extension of a dsDNA molecule during hRad51-ATP-Mg nucleoprotein filament formation is shown in (**C**). The molecule was extended by a pulling force of $F = 2.68$pN. Extension is shortened during buffer insertion due to the drag force of the flow. After insertion, a compact state nucleoprotein filament was formed; molecule extension went up by ~5%.

Earlier electron microscopy studies have shown that hRad51 is able to completely cover torsionally constrained dsDNA molecules [99]. In order to study filament formation in these conditions, the same experiments as in the previous section were conducted but with an imposed supercoiling degree of $\sigma = 0$ **[Figure 117]**. We showed that forming filaments on

torsionally constrained DNA molecules with the same supercoiling degree as B-DNA led to a condensed state filament. The extension of such a filament is close to the naked DNA molecule's crystallographic length. Those filaments were observed in conditions with ATP nucleotides and with $Mg^{2+}$ or $Ca^{2+}$ cations in solution.

As before, the protein reaction buffer containing 15mM Tris-HCl (pH 7.5), 25mM NaCl, 0.05% Tween 20, 2mM $MgCl_2$, 1mM DTT, 1mM ATP and 200nM hRad51 was injected into the flow chamber which originally contained naked dsDNA molecules. After protein insertion, the filament formed immediately displayed an increased end to end extension stretched by approximately 5% when compared the naked B-DNA's length at the same pulling force. No further stretching was observed after this initial extension.

Our measurements of normalized extensions are as follows:

- In presence of ATP and $Mg^{2+}$: Normalized extension of 1.046±0.005 (measured on 37 DNA molecules with a standard deviation of 0.028) when compared to initial length. This becomes 0.959±0.012 (37 molecules, standard deviation of 0.022) when compared to crystallographic length.

- In presence of ATP and $Ca^{2+}$: Normalized extension of 1.115±0.035 (measured on 3 molecules with a standard deviation of 0.061) when compared to initial length. This becomes 0.965±0.014 (3 molecules, standard deviation of 0.047) when compared to crystallographic length.

As with the stretched state, relative extensions inferior to 1 can be explained by the not fully stretched parts of the filaments that are not covered by hRad51 proteins. It may also be that some of the non-coated regions of the DNA are forming plectonemes to compensate for the protein trying to unwind the DNA molecule. These results suggest that the extension of this condensed state is actually very close to the crystallographic length of the dsDNA.

## A.I.3. Observation by electron microscopy

To elucidate the structural nature of *S* and *C* states, we directly observed how the structure of Rad51-DNA complexes changes when the DNA is permitted or prohibited from freely changing its twist. With this aim, in collaboration with Alicja Stasiak and Andrzej Stasiak (Centre Intégratif de Génomique, Faculté de Biologie et de Médecine, Université de Lausanne, CH-1015 Lausanne, Switzerland), we studied by electron microscopy hRad51-dsDNA complexes formed on circular DNA molecules that were either covalently closed and thus restricted in their change of twist or were nicked and thus could freely change their twist. The images obtained allowed direct observation of both the stretched and the condensed state.

To form the nucleoprotein filament, hRad51 proteins were bound to commercial pUC18 preparations (Fermentas) that contained ~5% of nicked DNA circles. Reactions were performed in a buffer containing 200nM hRad51, 15mM Tris–HCl (pH 7.5), 25mM NaCl, 1mM ATP, 1mM DTT and 0.05% Tween 20. After 30 minutes of incubation at 20°C, the formed complexes were stabilized with 1 mM ATP-γS for 1 minute. Afterwards the samples were diluted 10 times in 4mM magnesium acetate and were adsorbed to glowdischarged carbon grids. Specimens were then negatively stained with 2% uranyl acetate solution.

The use of calcium salts is not suited for the magnesium spreading method [189], which is why ATP hydrolysis was inhibited by adding ATP-γS to the complexes initially formed in the presence of ATP and $Mg^{2+}$.

Images obtained are shown in **[Figure 118]**. We observed that all DNA molecules formed complexes with hRad51proteins but that there were two types of complexes:

- Stretched filaments **[Figure 118, A and B]**, with a contour length of ~1300nm (1314±115, measured on 3 molecules). Which gives us a normalized extension of 1.44±0.13 when compared to the crystallographic length.

- Non-stretched filaments **[Figure 118, C-E]** with a contour length of ~900nm (890±26, measured on 11 molecules). Normalized extension of 0.97±0.03 when compared to the crystallographic length.
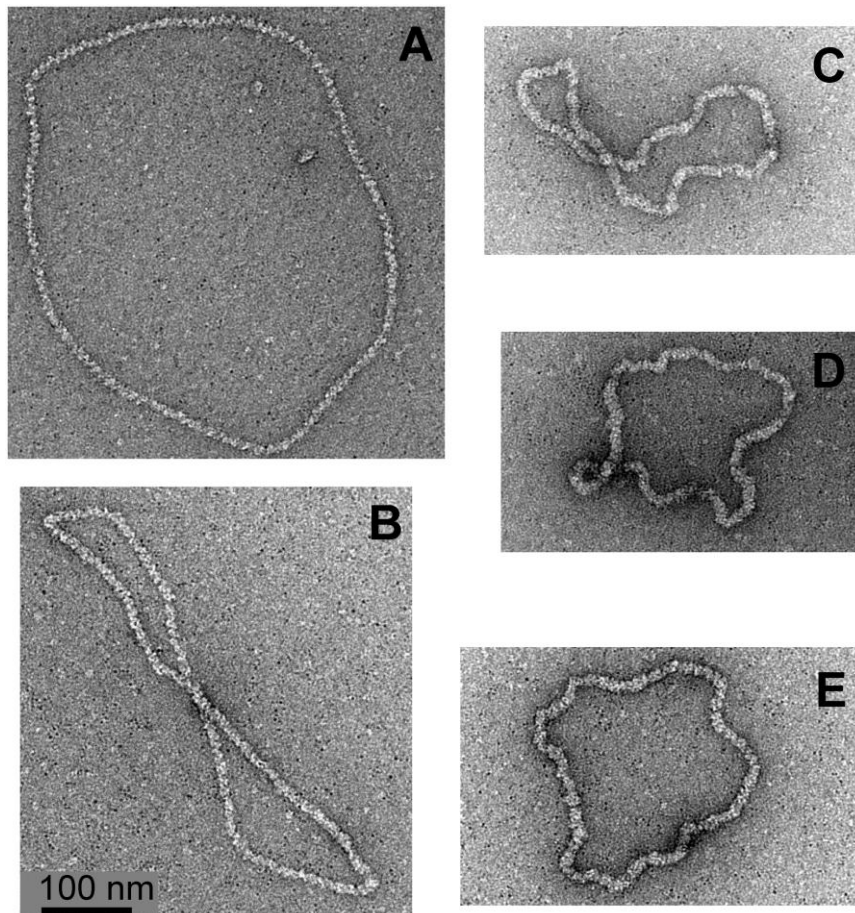


**Figure 118:** Electron micrographs of hRad51-dsDNA complexes in stretched (**A**, **B**) and non-stretched form (**C**–**E**).

Non-stretched complexes constituted the great majority, and their length was close to the expected length of protein-free pUC18 DNA (913 nm). The stretched complexes constituted ~5% of observed molecules and clearly showed their helical structure typical, for example, of RecA-DNA complexes formed in the presence of ATP-γS [186], [190], [191]. Non-stretched complexes had a much smoother and denser structure than stretched complexes. From the relative frequency of observed stretched and non-stretched complexes, we concluded that DNA molecules were nicked and thus could freely change their twist to

form stretched Rad51-DNA filaments, whereas covalently closed DNA molecules that were unable to freely change their twist formed non-stretched hRad51-dsDNA filaments. Electron microscopy observations therefore corroborated magnetic tweezers experiments, in which dsDNA molecules that were not permitted to change their twist formed complexes that stretched the DNA slightly, whereas a unwinding of DNA permitted these complexes to adopt a stretched form.

It is important to mention that the negative staining technique applied here allows us to unambiguously visualize protein-free DNA [99]. Therefore, it is unlikely that there are substantial uncovered portions of DNA molecules, in contrast to the situation where RecA protein interacts with covalently closed DNA molecules and leaves a substantial portion of uncovered DNA.

# A.II. Transition between states

In this section we will show that passage between the stretched and the condensed conformations may be achieved through torsion modification. The end result being that, as long as unbound proteins are available in solution and ATP hydrolysis is allowed, the hRad51-dsDNA-ATP filaments' extension is function only of the imposed supercoiling degree. We will also demonstrate that this holds true even if no unbound protein are available, indicating that the stretched and condensed state are in fact allosteric forms of the same dsDNA-hRad51 complex, containing the same amount of bound proteins.

## A.II.1. A torsion-dependent transition

We investigated the nucleoprotein filament's response to torsion change. Filaments were formed in presence of 200nM hRad51, 1mM ATP and 2mM $MgCl_2$. Keeping the hRad51 proteins in solution, the supercoiling degree imposed to the filament was changed by rotating the magnets while maintaining a constant pulling force of 2-5pN. Experiments were conducted for both the stretched and the condensed state filaments.

Those experiments showed that torsion change allowed the filaments to convert from the stretched state to the condensed state and vice-versa. In fact, we show that while hRad51 proteins are kept in solution, the filament's extension is function only of the supercoiling degree imposed as long as ATP hydrolysis is allowed. Therefore there is a direct correlation between the torsion state and the extension of dsDNA-hRad51 nucleoprotein filaments.

An example of transition from the stretched state to the condensed state is shown in **[Figure 119]**. The filament is formed in ATP and $MgCl_2$ at a constant pulling force of 4pN. During filament formation a supercoiling degree of $\sigma$=-0.43 is imposed to the DNA molecule. As before, the relative extension extends to approximately 1.5 times the initial length of the molecule at the same pulling force and at a null supercoiling degree ($\sigma$=0). Protein buffer injection is halted after approximately 200s as soon as some molecule extension seems to increase.

Filament extension reached its maximum after ~25 minutes. At this points, the supercoiling degree was gradually increased from $\sigma$=-0.43 to $\sigma\approx0.5$. Overwinding of the filament extension up to until $\sigma\approx0.1$ led to a decrease in filament at a proportional rate. Past this value, filament decrease rate significantly dropped. The value of filament extension

obtained for σ=0 was approximately 1.05 times the initial length of the DNA molecule, consistent with the extension of the condensed state of the filament. The rate of decrease in filament extension changed around the time filament extension reached the initial length of the DNA molecule (normalized extension equal to 1).
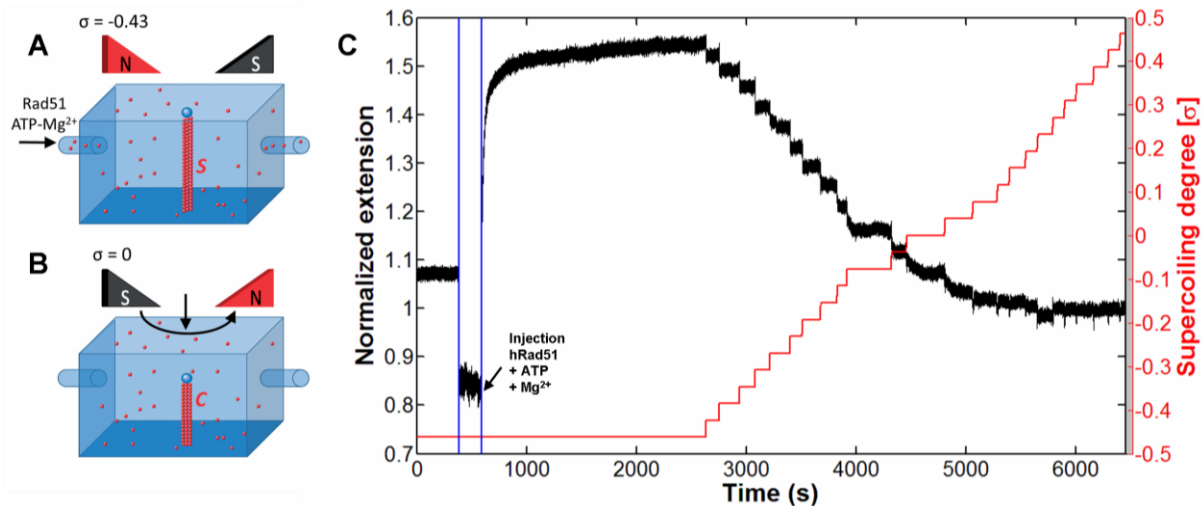


**Figure 119:** Experiment showing the transition from the stretched to the condensed state of the hRad51-dsDNA nucleoprotein filament in ATP and $Mg^{2+}$ through torsion modification while protein remains in solution. A buffer with 200nM hRad51, 1mM ATP, 2mM $MgCl_2$, 1mM DTT, 0.05% Tween 20, and 25mM NaCl was inserted into the flow chamber containing naked DNA molecules whose supercoiling degree was kept at σ = -0.43 (**A**). The imposed supercoiling degree was then increased while hRad51 proteins remained in solution (**B**). The tracking of the relative extension of a hRad51-ATP-Mg nucleoprotein filament in response to torsion change is shown in (**C**). A pulling force of *F*=3.25pN was maintained throughout the experiment. After insertion, a stretched state nucleoprotein filament was formed. Increasing the supercoiling degree resulted in filament extension decreasing proportionally. During experiments involving torsion change, some technical complications may arise preventing accurate tracking. Data points corresponding to such events and others considered to be non-pertinent were removed for easier comprehension by the reader. The time scale was rearranged appropriately, so the one presented here should be considered as an indicative value. The full experiment lasted a little over 2 hours.

An example of transition from the condensed state to the stretched state is shown in [**Figure 120**]. The filament is formed in ATP and $MgCl_2$ at a constant pulling force of 2.68pN. During filament formation a supercoiling degree of σ=0 is imposed to the DNA molecule. As before, the relative extension extends to approximately 1.05 times the initial length of the molecule at the same pulling force.

Filaments only partially coated with hRad51 proteins display a reduced extension; their normalized extension is always inferior to 1.05 and often inferior to 1 (data not shown). Since there is no delay between the end of buffer injection and the reaching of the condensed state extension, this observation allows us to assume that the filament is already fully formed at that point. The filament formation time is thus inferior to the buffer insertion time (~200s).

Unwinding of the filament led to filament extension increase at a proportional rate up until σ≈-0.4. As the supercoiling degree decreased further, the filament extension increase rate diminished until a maximum extension for σ=-0.45±0.05. Further unwinding past this value resulted in filament extension decrease at a lower rate than for values of the supercoiling degree between 0 and -0.4.

Repetition of such experiments revealed that the behavior of filaments formed in ATP and $MgCl_2$ was independent of the filament's history as long as the hRad51 proteins, the $Mg^{2+}$

cations and ATP remained in solution. Thus filament extension in these conditions is function solely of the supercoiling degree σ. The correlation between torsion and extension over a wide range of supercoiling degree (σ = -0.8 to σ = 0.4) is shown in **[Figure 121]**.
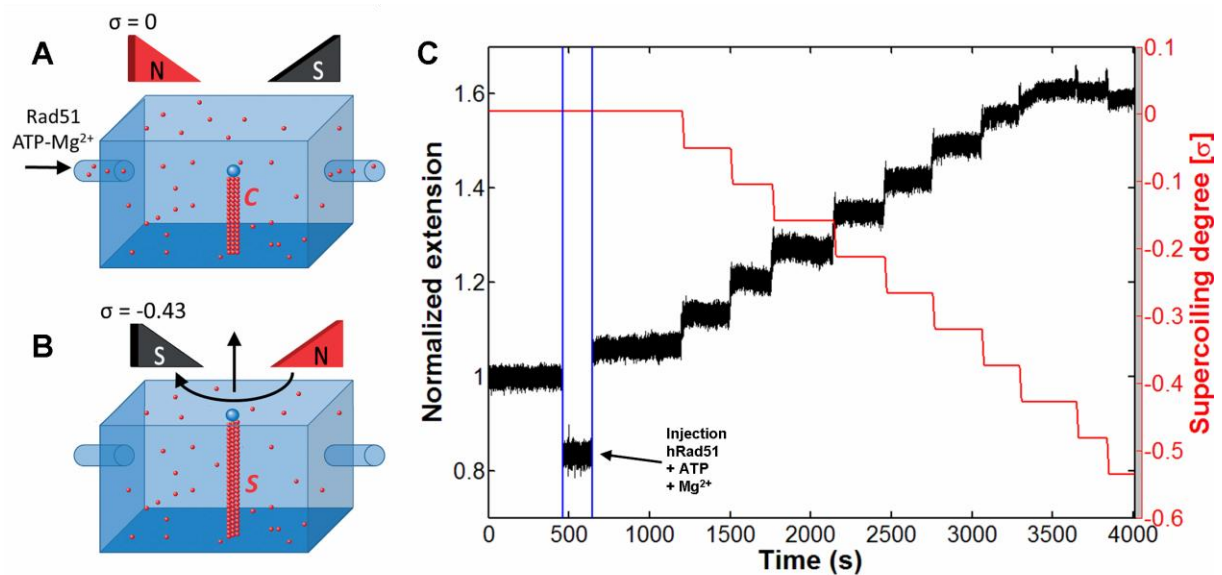


**Figure 120:** Experiment showing the transition from the condensed to the stretched state of the hRad51-dsDNA nucleoprotein filament in ATP and $Mg^{2+}$ through torsion modification while protein remains in solution. A buffer with 200nM hRad51, 1mM ATP, 2mM $MgCl_2$, 1mM DTT, 0.05% Tween 20, and 25mM NaCl was inserted into the flow chamber containing naked DNA molecules whose supercoiling degree was kept at σ = 0 (**A**). The imposed supercoiling degree was then decreased while hRad51 proteins remained in solution (**B**). The tracking of the relative extension of a hRad51-ATP-Mg nucleoprotein filament in response to torsion change is shown in (**C**). A pulling force of $F$=2.68pN was maintained throughout the experiment. After insertion, a condensed state nucleoprotein filament was formed. Decreasing the supercoiling degree resulted in filament extension increasing proportionally. Some data points were removed, total experiment time was 1h30.

Between the supercoiling degrees σ=0 and σ=-0.43 occurs a transition between the stretched and the condensed state. This transition is gradual and characterized by a constant extension to torsion variation rate of -3.91±0.06nm/turn (51 measures; standard deviation of 0.40nm/turn). This rate does not appear to depend on pulling force as long as this pulling force is kept over 1pN.

For supercoiling degrees inferior than the filament's natural unwinding (σ<-0.43), the filament's extension decreases with torsion at a proportional rate of 1.21±0.09nm/turn (3 measures; standard deviation of 0.15nm/turn). The reason for this shortening is not clear at this point and one would have to resort to speculation in order to explain the phenomenon.

For supercoiling degrees superior to σ=0.1, the filaments' behaviors varied greatly from one another. Filaments' extensions always decreased as the supercoiling increased but with varying proportional rates ranging from -0.15nm/turn to -1.2nm/turn. Exploration of this supercoiling range always resulted in extreme hRad51 dissociation suggesting that such an overwinding is not natural state for the nucleoprotein filament.

At low forces (typically 0.1pN and under), the filament extension collapses when it is wound too far away from σ=-0.43. The torsion/extension correlation curve forms a quasi-symmetrical hat curve centered on σ=-0.5±0.1 (5 measures; standard deviation of 0.1). The shortening in this case may be explained by the formation of filament plectonemes.

It is to be mentioned that while relative measures such as extension differences and twist changes are precise in magnetic tweezers experiments, absolute measures such as the

absolute lengths of the molecules and filaments are subject to non-negligible measurement errors. Those errors are greatly lessened through normalization of lengths by other measured lengths which are subjected to the same measurement errors. However the calculation of the supercoiling degree allows no such normalization, thus the values measured are subjected to important errors, generally of the order of 15-20%.
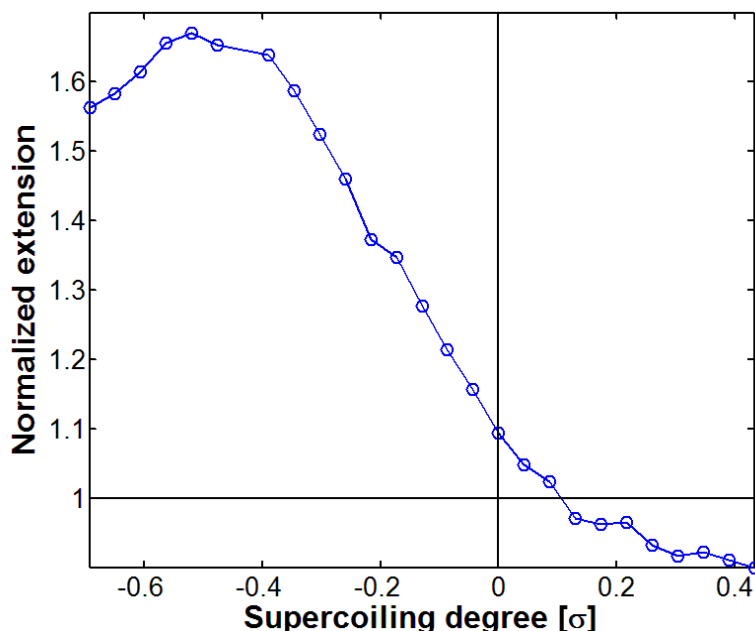


**Figure 121:** Torsion-dependent behaviour of hRad51-dsDNA complexes over a broad range of DNA twist changes. The hRad51-dsDNA complexes formed in the presence of ATP reach their maximum extension for the enforced DNA helicity corresponding to ca. 18.6 bp/turn ($\sigma = -0.43$). When the DNA was overwound above $\sigma = 0$, we observed shortening of the end-to-end distance, which may be explained by progressive dissociation of hRad51 and formation of localized plectonemes. There is a partial dissociation of hRad51 as DNA is overwound above $\sigma = 0$ or underwound below $\sigma = -0.5$.

## A.II.2. Reversible states

The next step was to analyze the behavior of dsDNA-hRad51 nucleoprotein filaments formed in ATP and $Mg^{2+}$ in response to torsion but without any free proteins in solution. In the following experiments, after filament formation, the protein was washed from the flow chamber using the same buffer the filament was formed in but without the protein. The volume of buffer used was at least 10-20 times the volume of the flow chamber in order to be sure no free protein remained in solution.

Data from the experiments conducted suggests that, apart from phenomena due to protein dissociation, there is no significant difference between the behaviors of filaments with and without protein present. Protein dissociation induced phenomena appear essentially if the filament is wound out of the $-0.43 < \sigma < 0$ supercoiling range or if the experiment lasts for a long enough time so that time-dependent protein dissociation is no longer negligible.

The conversion from the stretched state to the condensed the protein's absence is shown in **[Figure 122]**. The filament is formed in presence of ATP and $Mg^{2+}$ on DNA molecules unwound to $\sigma=-0.43$. The formation of the filament takes approximately 15 minutes after which the protein-free buffer was injected into the flow chamber. The

evacuation of the protein triggered a slight filament extension decrease; the normalized extension went from 1.57±0.03 to 1.56±0.03. Such shortenings are not uncommon when working with hRad51 proteins absent from solution. We assume they are caused by protein dissociation because re-injection of the proteins in solution restores the initial length (data not shown). Winding the filament towards σ=0 causes the extension to decrease much as it was observed before. The decrease rate however is slightly more elevated than the mean rate (-4.18nm/turn in the case of this experiment to compare with the mean of -3.91±0.06nm/turn measured for this transition). This modification of rate decrease can be attributed to time-dependent protein dissociation which is to be expected given the long experiment time. Thus the length obtained for the condensed state is lower than expected with a normalized extension 1.00±0.03.
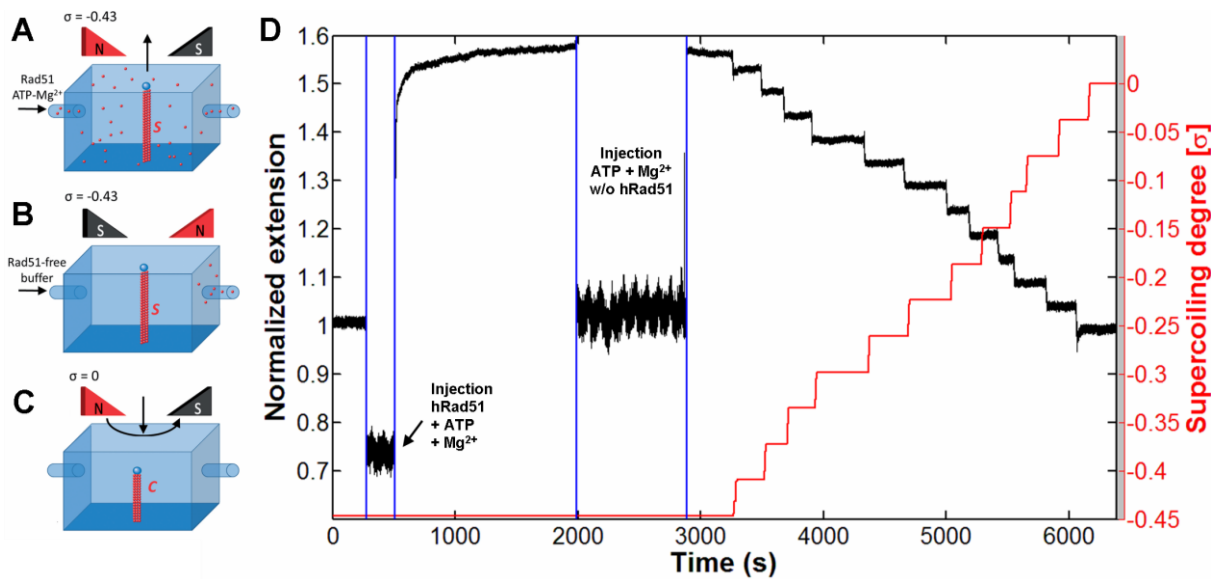


**Figure 122:** Experiment showing the transition from the stretched to the condensed state of the hRad51-dsDNA nucleoprotein filament in ATP and $Mg^{2+}$ through torsion modification in the absence of protein in solution. A buffer with 200nM hRad51, 1mM ATP, 2mM $MgCl_2$, 1mM DTT, 0.05% Tween 20, and 25mM NaCl was inserted into the flow chamber and a stretched state nucleoprotein is formed (**A**). The same buffer without the protein was then inserted in order to evacuate any unbound hRad51 protein from the flow chamber (**B**). The supercoiling degree was then gradually increased (**C**). The tracking of the extension of the molecule shows the decrease of the length as the filament converts to the condensed state (**D**). A pulling force of F=3.25pN was maintained throughout the experiment. Some data points were removed, total experiment time was 1h45.

The fact that the stretched to condensed transition is unaffected by protein absence is not surprising. One of the hypotheses commonly made for hRad51 filaments is that the condensed state is a product of protein dissociation and thus has a different protein to base pairs stochiometry than the stretched state. If that hypothesis were correct, the condensed state filament would contain fewer proteins than the stretched state and therefore should not be able to convert to the stretched state if no proteins are present in solution for filament reassembly. In order to investigate that matter, we conducted such an experiment of which an example is shown in **[Figure 123]**.

The filament was formed in ATP and $Mg^{2+}$ at σ=0 and the proteins were washed away from the chamber after that. The data shown starts after protein evacuation, the supercoiling degree is decreased from σ=0 to σ=-0.43. Filament extension increases with a proportional rate of -3.90nm/turn up until σ=-0.43 where the filament reached a normalized extension of

1.496±0.030. Winding the filament back to σ=0 resulted in filament extension behaving almost exactly the same way as when unwinding **[Figure 124]**.

This type of experiment is rendered difficult by strong protein dissociation during the protein-free buffer exchange. It should be noted that, for reasons not understood, very few of our attempts to reproduce this type of experiments have worked when using the DNA from pTYB4 constructed by transformation due to heavy protein dissociation. The experiments which have worked were conducted with the λ-DNA constructed by PCR. We do not know if this change in DNA sequence and synthesis method is likely to have the observed effect. A higher pulling force (higher than 4pN) maintained during the experiment seems to help prevent some of the protein dissociation. It also helps to not wind the filament as far as σ=0 as in the experiment shown in **[Figure 134; red profiles]** or to rinse the protein with the filament in an unwound stretched state, since most of protein dissociation occurs during protein evacuation when the filament is in its condensed state.

However, regardless of the DNA construct used, a transition from condensed to stretched state with no proteins present in solution is observable when forming the filament at σ=0 in conditions preventing ATP hydrolysis such as in the presence of $Ca^{2+}$. We think that preventing ATP hydrolysis greatly reduces protein dissociation from the filament which occurs during the protein-free buffer exchange.
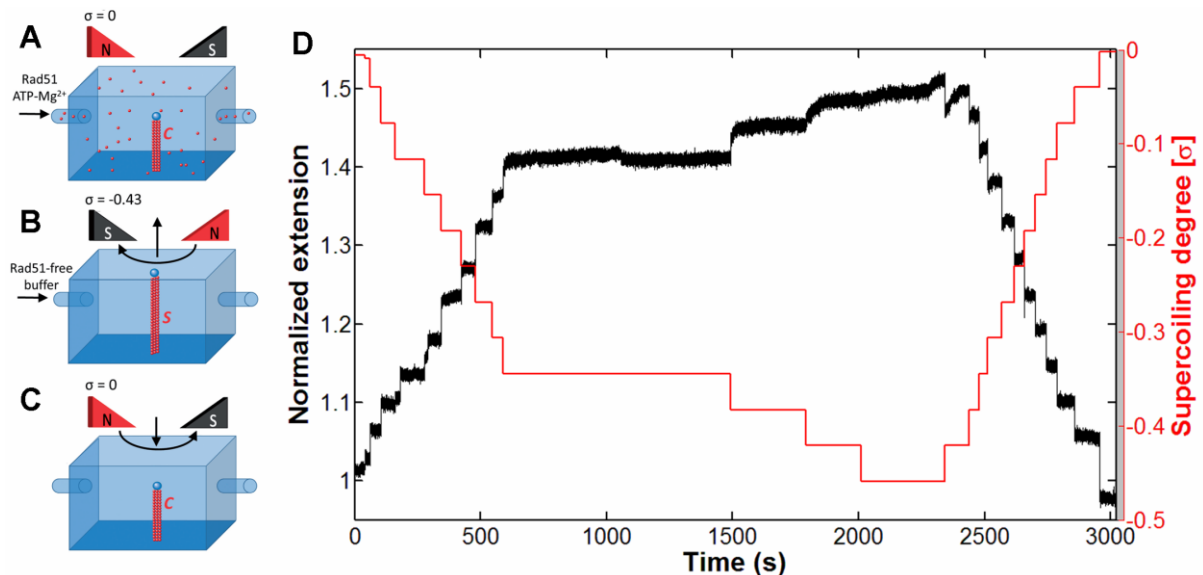


**Figure 123:** Experiment showing the transition from the condensed to the stretched state and vice-versa of the hRad51-dsDNA nucleoprotein filament in ATP and $Mg^{2+}$ through torsion modification in the absence of protein in solution. A buffer with 200nM hRad51, 1mM ATP, 2mM $MgCl_2$, 1mM DTT, 0.05% Tween 20, and 25mM NaCl was inserted into the flow chamber containing naked DNA molecules whose supercoiling degree was kept at σ = 0 (**A**). Free proteins in solution were then washed away by a protein-free buffer and the imposed supercoiling degree was decreased gradually to reach σ=-0.43 (**B**). The filament was then rewound back to σ=0 (**C**). The tracking of the relative extension of a hRad51-ATP-Mg nucleoprotein filament in response to torsion change is shown in (**D**). A pulling force of F=5.16pN was maintained throughout the experiment. Tracking data is shown after insertion of the protein-free buffer. Unwinding the filament resulted in filament extension and reaching σ=-0.43 yielded a stretching of ~50%, thus the stretched state was attained. Winding the filament back to σ=0 converted it back to the condensed state. For experimental reasons, the supercoiling degree modifications in this experiment were conducted at a pulling force approximately of 0.5pN. Data points corresponding to those events and others during tracking error events were removed for an easier reading. Total experiment time was of 1h45.

Taken together, these experiments suggest that the stretched and the condensed states are in fact allosteric state of one filament. Both states contain the same amount of hRad51

proteins, so logically their protein to base pairs stochiometries are the same. The conversion between both states is then merely a change in conformation.

We've also shown that all behavioral changes of the filament from when the protein is present in solution to when it is absent can be attributed to protein dissociation. This similitude in behavior is the reason why many of our experiments were conducted, when possible, with proteins present in solution in order to eliminate dissociation induced phenomena.
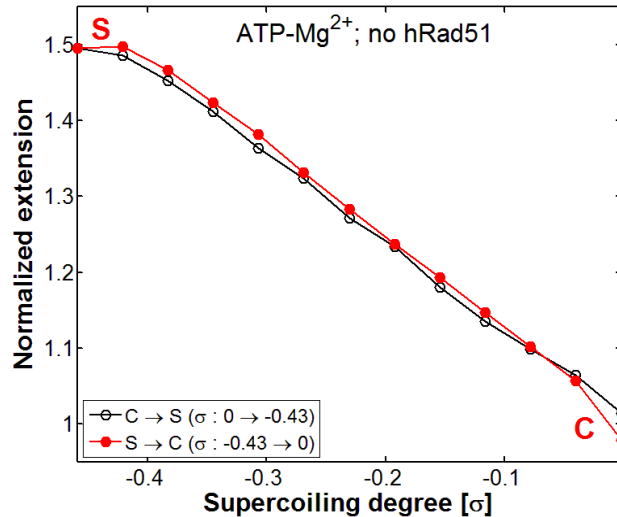


**Figure 124:** Extension response to torsion change of the filament in the experiment shown in [**Figure 123**].

# A.III. Cofactor influence

The experiments presented in this section aim mainly to determine the state of the nucleotide within the nucleoprotein filament as it transitions between the different states. We will first demonstrate that ATP hydrolysis is required only for the transition from the stretched to the condensed conformation. In conditions preventing ATP hydrolysis, once a stretched form has been reached, the filament is thereafter locked in various stretched conformations. We will then study the behavior of ADP-bound filaments and show that, while similar to ATP-bound filaments when unbound proteins are available, it differs as soon the proteins are evacuated. As such, they are more prone to protein dissociation and they try to reach a state which is somewhat less extended and less unwound than the stretched state.

In the end, we will deduce that the stretched conformations are naturally ATP-bound while the condensed ones are ADP-bound. We will also reach the conclusion that ATP hydrolysis seems to be a prerequisite to protein dissociation.

## A.III.1. ATP hydrolysis and transition

It is well known that the $Ca^{2+}$ divalent cation impairs greatly ATP hydrolysis by the hRad51 protein [111]. To investigate the role of ATP in filament conformation, we conducted experiment probing the behavior of filament formed in $Ca^{2+}$. In doing so, we found that ATP hydrolysis is required for only one the filament transitions, stretched to condensed.

Filaments were formed on DNA molecules at σ=0 in conditions with ATP and $Ca^{2+}$ present in solution. We've already seen that in these conditions the filaments form in a

condensed state. The protein was then removed from solution and the supercoiling degree decreased from σ=0 to σ=-0.43. Much like before with ATP and $Mg^{2+}$, the filament extension increased up to approximately 50% when underwinding reached 43% (see the red curve with full circles in [**Figure 125**]). Once stretched, the filament did not go through the reverse transition, stretched to condensed. Instead the increase in supercoiling degree triggered almost no extension shortening (red curve with empty circles in [**Figure 125**]). This new transition is reversible multiple times without the effects induced by protein dissociation (blue curves in [**Figure 125**]).
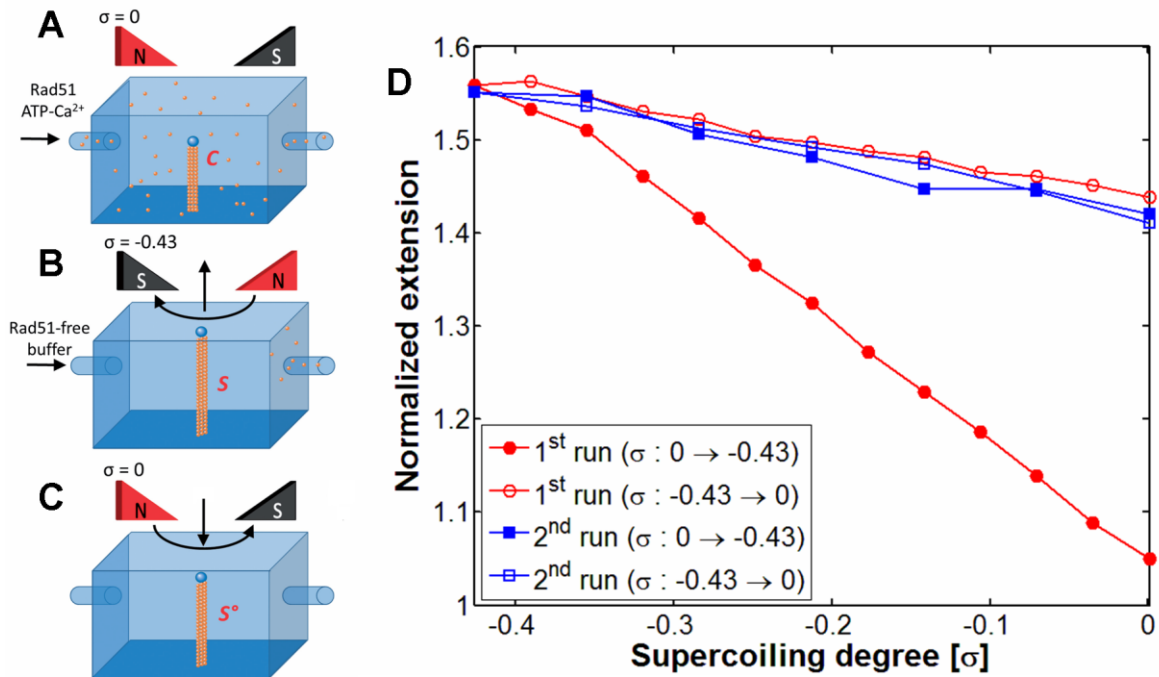


**Figure 125:** Experiment showing the behavior of hRad51-dsDNA nucleoprotein filaments in ATP and $Ca^{2+}$. hRad51 in a buffer containing ATP and $Ca^{2+}$ was added to the DNA that was prevented from rotation and thus maintained its natural twist (**A**). After elimination of unbound Rad51, the preformed complex progressively increased its length on DNA unwinding towards a stretched structure (**B** and **D**; the lowest red profile). Rewinding of stretched complexes did not convert them back to a non-stretched form, although some shortening was observed (**C** and **D**; the upper red profile and the blue profile). A pulling force of $F$=2pN was maintained during the experiment.

The slope of this new hydrolysis-free transition is inferior (in absolute value) to the one observed in $Mg^{2+}$ with a value of -1.12±0.04nm/turn (measured on 29 molecules; STD of 0.19nm/turn). Thus the filament converts in these conditions from an unwound stretched state to a less extended state with a null supercoiling degree (σ=0) and a normalized extension of 1.384±0.045 (measured on 21 molecules; STD of 0.045). It should be noted however that this new state is actually not a state at all since the slope of this transition is unaffected if the filament is wound further into the positive supercoiling degrees. In fact, the slope is constant for as far we have probed the supercoiling range (from σ=-0.43 to σ=0.3) [**Figure 126; A**].

Similar results may be obtained when using a AMP-PNP, a non-hydrolysable analog of ATP, as a cofactor [**Figure 126; B**].

The fact that the transition to condensed does not occur in these conditions but is possible when $Mg^{2+}$ is present strongly suggests that ATP hydrolysis is required for this particular transition. If so, then the stretched state filament should contain ATP whereas the condensed one should contain ADP. In this case, it is surprising that it is possible to form

condensed state filaments in presence of $Ca^{2+}$. Two possible explanations emerge; either the $Ca^{2+}$ condensed state differs from the one in $Mg^{2+}$, the former containing ATP while the latter contains ADP; or the formation of the nucleoprotein filament on torsionally constrained DNA molecules with an imposed supercoiling degree of $\sigma=0$ forces ATP hydrolysis even in presence of $Ca^{2+}$. Unfortunately our experiments did not allow differentiating between those two cases.
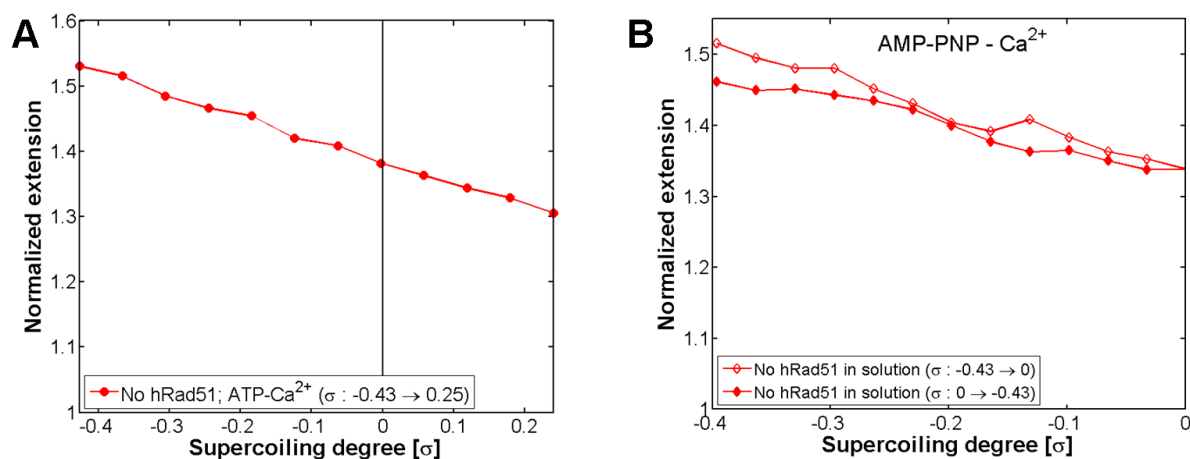


**Figure 126:** (**A**) Experiment showing the torsion response of a hRad51-dsDNA-ATP-$Ca^{2+}$ filament locked in over a wide range of supercoiling degree. (**B**) Experiment showing the torsion response of a hRad51-dsDNA-AMP-PNP-$Ca^{2+}$ filament locked in stretched state. The filament was formed while imposing $\sigma=-0.43$ by adding a buffer containing 50nM hRad51, 100µM AMP-PNP, 2mM $CaCl_2$, 1mM DTT, 0.05% Tween 20, and 25mM NaCl. The protein was then evacuated by the same buffer protein-free prior to torsion modification.

In summary, $Ca^{2+}$-stabilized hRad51-dsDNA-ATP complexes get locked in the stretched form, indicating the need for ATP hydrolysis in order to reach the condensed state. The same holds true when AMP-PNP is used instead of ATP. One could argue that the size of the cation is responsible for locking the stretched forms, the $Ca^{2+}$ cation being much larger than the $Mg^{2+}$. However the use of calcium cations in the presence of ADP does not seem to affect filament behavior at all [**Figure 129**]. With those indications, we can safely assume that the state of the nucleotide within the filament is solely responsible for this effect. These results suggest the stretched states of the filaments are ATP-bound and the condensed state is ADP-bound.

## A.III.2. Behavior of ADP-bound filaments

To further probe the role of ATP hydrolysis in filaments' transitions, we experimented in conditions containing ADP instead of ATP. The buffer used was strictly the same as in previous experiments apart for the nature of nucleotide.

With $Mg^{2+}$ present and the protein still in solution, the filaments' behavior is exactly the same as with ATP and $Mg^{2+}$ [**black curve in Figure 127**]. Whereas we strongly suspected the condensed state could be formed in ADP (normalized extension of $1.051\pm0.007$, measured on 6 molecules with an STD of 0.017), the existence of an ADP stretched state with a normalized extension of $1.487\pm0.033$ (21 molecules; STD of 0.051) comes as a surprise.
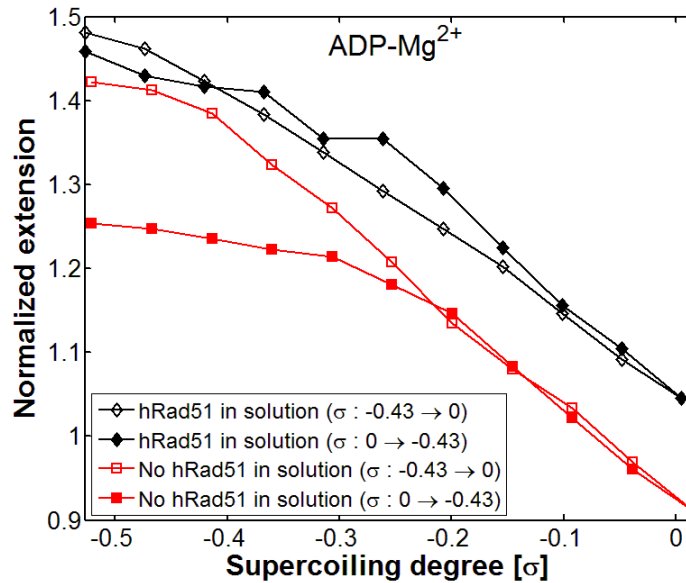
**Figure 127:** Response to torsion of filaments formed in ADP and $MgCl_2$. When protein remains in solution (black curves), filaments formed in ADP-Mg are able to interconvert between the stretched and the condensed state (experiment with a pulling force of $F$=2.35pN). When protein is no longer in solution (red curves), conversion from a condensed form to a stretched form is rendered is no longer possible, probably due to hRad51 dissociation from the filament (experiment with a pulling force of $F$=3.23pN).

When the protein was washed away from solution, strong protein dissociation induced phenomena appeared **[red curve in Figure 127]**. Thus the slope of the stretched to condensed transition was at first higher (absolute value) than when the protein was present is solution. This increased slope value may be explained with the simultaneity of both the transition and protein dissociation resulting in further filament extension decrease.

After a certain supercoiling degree value (approximately σ=-0.2 on **[Figure 127]** , the slope became the same as when the protein was present. We can therefore assume that the protein dissociation in those experiments occurred mainly during buffer exchange and the transition from σ=-0.43 up to a variable value of σ (here σ≈-0.2). Past this supercoiling degree the behavior of the filament was the same as when the protein was present but with an offset of extension due to dissociation. The result was a partially coated condensed state filament whose extension was often lower than the naked DNA molecule's length.

Further unwinding of the same filament in the same conditions resulted at first in a reversible behavior up to approximately the same supercoiling degree value as before. Unwinding even further resulted in slower filament extension increase. The end result was a much shorter stretched filament. The shorter extension was not entirely accounted for by protein dissociation; the injection of a protein-free buffer containing ATP resulted in a slight filament extension increase **[Figure 128]**.

We've thus shown that hRad51-dsDNA-ADP filaments behave exactly the same as ATP-filaments when unbound proteins are available in solution, freely able to pass between non-stretched and stretched forms. This behavior differs however as soon as the protein is removed from solution as a result of protein dissociation and the formation of a structure shorter than the stretched state. Furthermore, the shorter extension of these filaments is not solely accounted for by protein dissociation. Overall behavior of the ADP-bound filaments is unaffected by the nature of cation **[Figure 129]** except perhaps for a lesser tendency to protein dissociation in the presence of calcium.

- 144 -
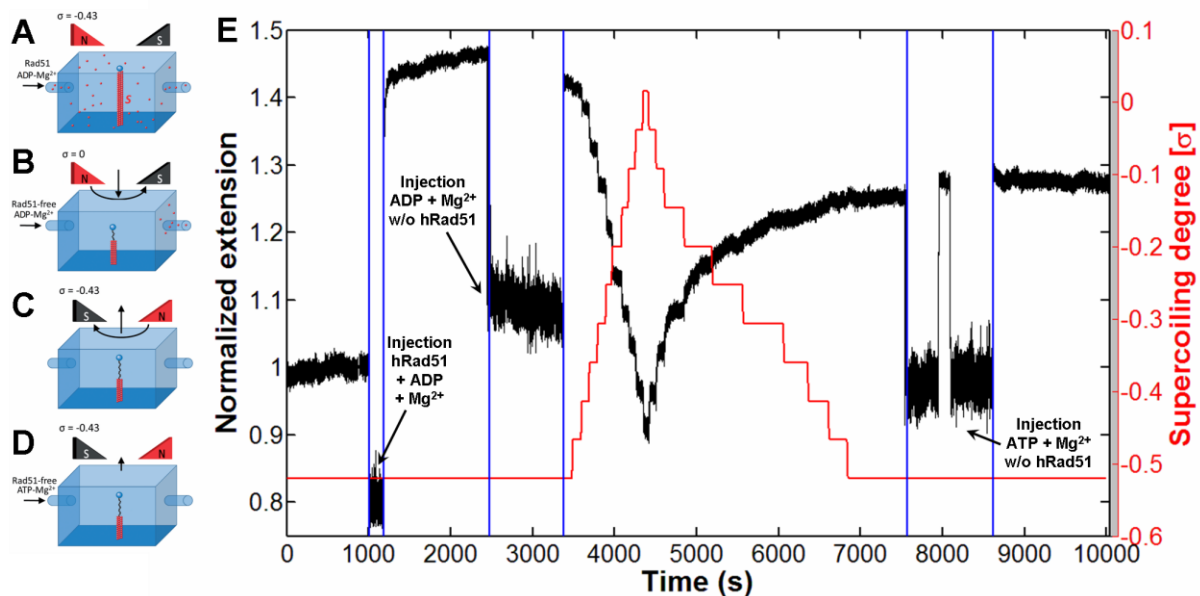
**Figure 128:** Experiment showing the elongation tracking (**D**) of the experiment whose result was shown in [**Figure 127 ; red profiles**]. The filament was formed on a dsDNA molecule at σ=-0.43 in ADP-Mg$^{2+}$, a stretched state was reached (**A**). Rinsing the protein with an ADP-Mg$^{2+}$ protein-free buffer resulted in slight length decrease. Winding the filament to σ=0 yielded a somewhat shorter length than the condensed filament state, probably due to protein dissociation (**B**). Unwinding the filament back to σ=-0.43 resulted a shorter stretched state (**C**). Insertion of an ATP-Mg$^{2+}$ protein-free buffer triggered a slight increase in filament length (**D**). A pulling force of *F*=3.23pN was maintained throughout the experiment.
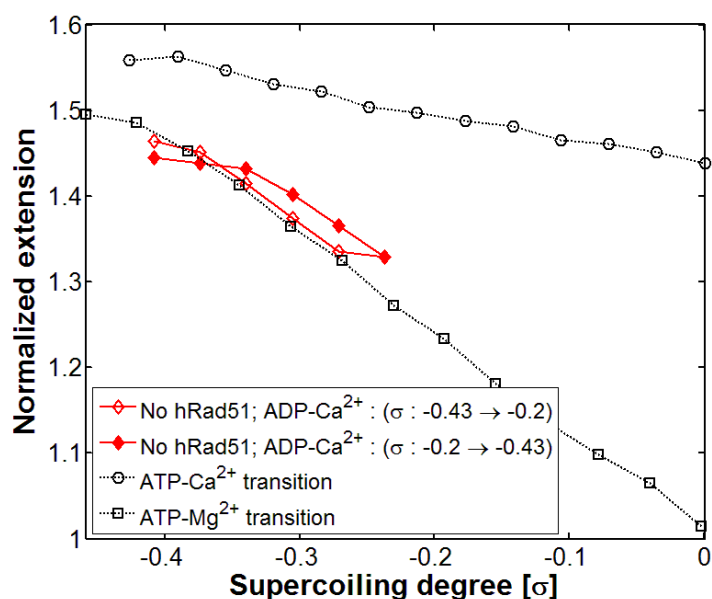


**Figure 129:** Response to torsion a filament formed in ADP and CaCl$_2$ no protein in solution. The filament was formed while imposing σ=-0.43 by adding a buffer containing 50nM hRad51, 100μM ADP, 2mM CaCl$_2$, 1mM DTT, 0.05% Tween 20, and 25mM NaCl. The protein was then evacuated by the same buffer protein-free prior to torsion modification. A pulling force of F=4pN was maintained during the experiment. The red profiles show the response of this filament. Shown in black are examples of transitions without protein present of filaments formed respectively in ATP-Ca$^{2+}$ and in ATP-Mg$^{2+}$.

These results lead us to two conclusions. The first is that ADP-bound conformations of the filaments are highly unstable, prone to protein dissociation. Taken together with the stability of the filaments in conditions preventing ATP hydrolysis, we can deduce that protein

- 145 -

dissociation most probably requires prior ATP hydrolysis. The second conclusion is that even though fully stretched ADP-bound conformations are possible, it is unlikely that this is their natural state; those conformations are most probably rendered possible only by supplying a yet to be defined amount of energy to the system by imposing the supercoiling degree. It is unclear at this point if the natural ADP-bound conformation is the previously shown condensed state with a null supercoiling degree or another state, less extended and less unwound than stretched.

# A.IV. Protein coverage and filament extension

## A.IV.1. Relative crystallographic extension

We've previously estimated the protein coverage of our filaments formed in the stretched state by making the three following assumptions:

1. The hRad51-nucleoprotein filaments are not fully covered with hRad51 proteins.

2. The covered parts are inelastic and have an extension of 1.5 times the crystallographic length of the B-DNA.

3. The non-covered parts behave like naked DNA and thus are elastic.

For some of our experiments, where we have probed the extension response to torsion, we then have simultaneously the filament's extension at different supercoiling degrees and the protein coverage deduced from the stretched state. Combining these results allows us to access the extension induced by hRad51 proteins relatively to crystallographic length without underestimating it because of protein coverage.

For this estimation, we will then consider, like before that the filament's extension may be expressed as follows:

$$l_{fil} = p \cdot \alpha \cdot l_{crys} + (1-p) \cdot l_{DNA}$$

Where $l_{fil}$ is the filament's extension, $l_{crys}$ is the crystallographic length of the DNA molecule, $l_{DNA}$ is the DNA molecule's extension at the used pulling force, $p$ is the protein coverage ($0 \leq p \leq 1$) and $\alpha$ is the relative extension induced by hRad51 proteins when compared to crystallographic length.

Since the extensions $l_{fil}$, $l_{crys}$ and $l_{DNA}$ are measured and the protein coverage $p$ is deduced, the relative extension α may be obtained through:

$$\boxed{\alpha = \frac{l_{fil} - (1-p) \cdot l_{DNA}}{p \cdot l_{crys}}}$$

## A.IV.2. Application to data

We may then apply the formula to our data to get the actual relative crystallographic extensions for the different states we've identified.

For the condensed state at σ=0 we obtain:

-   In presence of ATP and $Mg^{2+}$: Relative crystallographic extension of 0.962±0.011 (measured on 26 DNA molecules with a standard deviation of 0.054).

-   In presence of ATP and $Ca^{2+}$: Relative crystallographic extension of 0.970±0.038 (measured on 2 DNA molecules with a standard deviation of 0.053).

For the stretched state at σ=0 we obtain:

-   In presence of ATP and $Ca^{2+}$: Relative crystallographic extension of 1.340±0.008 (measured on 26 DNA molecules with a standard deviation of 0.040).

# B. A dynamic nucleoprotein filament

## B.I. Chemical co-factors and turnover

Conformations of hRad51 nucleoprotein filaments are heavily dependent on the nature of the chemical co-factors present during their formation. The question then arises if the cofactors are able to turnover, the nucleotides and cations in solution replacing those already in the filament. If so, does the process induce protein dissociation? The following experiments were conducted with this question in mind.

We have shown that nucleotide turnover is not required for most of the transitions between states except perhaps for the condensed to stretched transition in ATP-Mg$^{2+}$. Demonstrating the turnover of ATP in this case proved inconclusive due to experimental difficulties. The turnover of the cation was found to be always possible, in both ways, calcium to magnesium and vice-versa. We also found it was possible to transit from the null-torsion stretched state to the null-torsion condensed state while keeping the imposed supercoiling degree constant.

### B.I.1. Nucleotide turnover
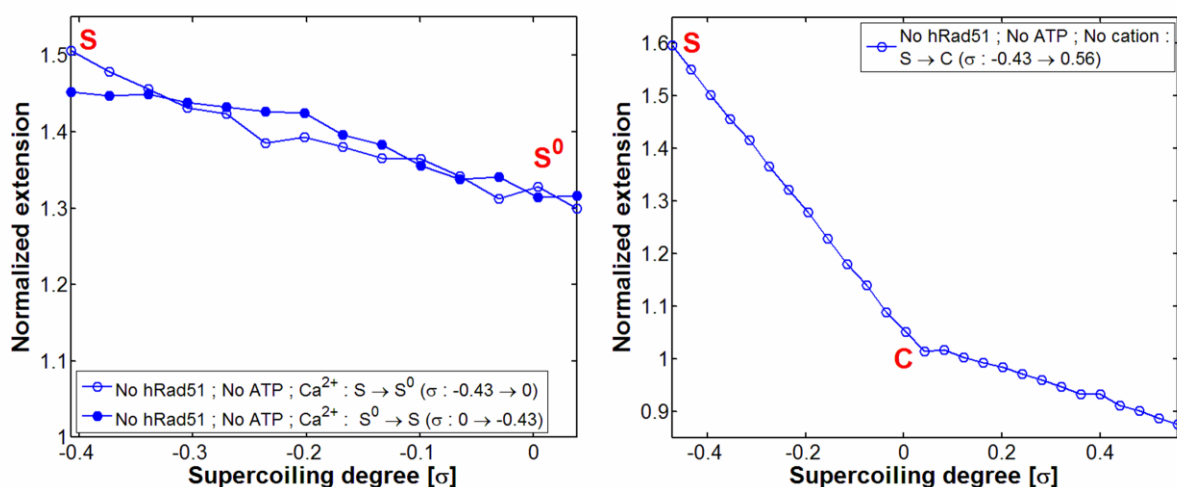


**Figure 130:** Experiments showing the behavior of hRad51-dsDNA complexes in the absence of various co-factors. On the left, the filament was formed in the presence of ATP-Ca$^{2+}$ at σ=-0.43 after which the chamber was rinsed with a buffer containing only Ca$^{2+}$ (no protein and no ATP). A pulling force of F=4pN was maintained throughout the experiment. On the right, the filament was formed in the presence of ATP-Mg$^{2+}$ at σ=-0.43 after which the chamber was rinsed with a buffer containing no co-factors (no protein, no Mg$^{2+}$ and no ATP). A pulling force of $F$=7.05pN was maintained throughout the experiment.

The possibility of nucleotide turnover within hRad51-dsDNA nucleoprotein filaments has been already convincingly proven in the existing literature [119]. So our aim here is not to prove the existence of nucleotide turnover but to understand how and when it happens during the different transitions of the filament.

We have shown that ATP hydrolysis is required only for the stretched to condensed transition; therefore ATP turnover should only be required for the reverse transition,

condensed to stretched. The two experiments presented in [**Figure 130**] aim to verify that ATP turnover is in fact not needed for the other transitions.

Thus we can observe that torsion response in calcium is unaffected by the absence of ATP in solution [**Figure 130 graph on the left**], which is not surprising since we suspect that $Ca^{2+}$-filaments are locked in an ATP-bound form. Since the ATP isn't hydrolyzed, it has no need to be renewed. The stretched to condensed transition of a filament formed in ATP-$Mg^{2+}$ is also unaffected by the absence of free nucleotides in solution [**Figure 130 graph on the right**]. If we assume that the condensed form is ADP-bound then the filament simply hydrolyzes the ATP it contains during the transition and doesn't require any additional supply of nucleotides. In this case it also seems it does not need any available $Mg^{2+}$ cations in solution.
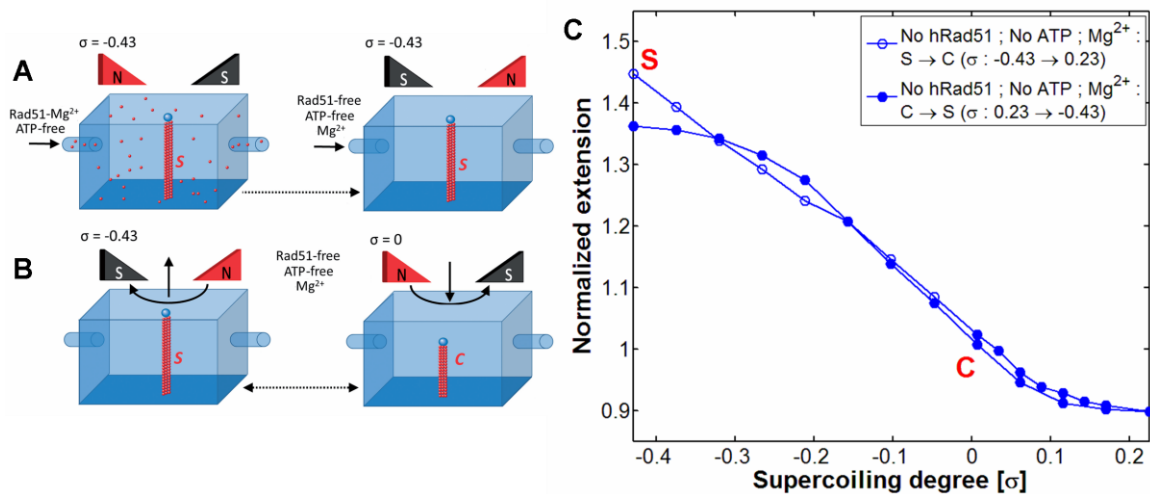


**Figure 131:** Experiment showing the behavior of hRad51-dsDNA nucleoprotein filaments formed in $Mg^{2+}$ and the absence of ATP. A buffer with 200nM hRad51, 2mM $MgCl_2$, 1mM DTT, 0.05% Tween 20, and 25mM NaCl was inserted into the flow chamber containing naked dsDNA molecules whose supercoiling degree was kept at $\sigma = -0.43$. Free proteins in solution were then washed away by the same buffer without the hRad51 proteins (**A**). The imposed supercoiling degree was increased gradually to reach $\sigma=0$ and then decreased back to $\sigma=-0.43$ (**B**). The torsion response of the filament, shown in (**C**), is similar to when ATP is present. A pulling force of $F=2.57$pN was maintained during the experiment.

If the condensed state of the filament is an ADP-bound form, then for the filament to be able to interconvert between the stretched state and the condensed state, as seen in the previous experiments [**Figure 123 and Figure 124**], the ATP in solution has to be able to replace the ADP within the filament. However, since filaments formed in ADP are able to adopt the stretched conformation in magnetic tweezers setups [**Figure 127**], the previous result in itself is not sufficient. Yet the fact that the ADP-bound stretched conformation is transitory could be enough to convince us that ATP turnover does occur. Unfortunately one of our control experiments show us that a nucleotide-free filament is also able to transit between the stretched and condensed forms , much like its ATP-bound counterpart [**Figure 131**]. Indeed in this experiment, hRad51-dsDNA complexes were formed in the absence of any nucleotides and the response to torsion was probed after evacuating the excess protein. The result showed no differences with the response of a filament formed with ATP present, except perhaps for a slight tendency for protein dissociation but no more than can be observed in filaments with filaments formed in ADP.

It is unclear at this point if this behavior is really possible in the absence of ATP or ADP, or if nucleotides are already present in the proteins prior to insertion in the chamber as

an aftereffect of the purification process. The presence of previously bound ATP in the purified protein could explain how filaments formed in ATP are able to perfectly mimic filaments formed in ATP when unbound proteins are in solution. Yet the behavior of ADP-filaments formed in conditions preventing hydrolysis (ADP-Ca$^{2+}$ **[Figure 129]**) is similar than with Mg$^{2+}$ which could suggest that no such ATP is present in the purified protein. The hypothesis remains nonetheless possible if we consider that the ATP within the purified protein could have been replaced by ADP present in solution. In order to settle the matter, we should have in hindsight tested the response of filaments formed in the absence of nucleotides with calcium cations present.

In the end, it is difficult for us to conclude on the role of nucleotide turnover during transitions using this experimental setup. We have shown as expected that no turnover is needed for most of the transitions but the question of if it is needed for the condensed to stretched transitions remains unanswered.

This experimental limit is the result of the fact that magnetic tweezers setups, by imposing the supercoiling degree with an almost infinite energy when compared to the biological system, may allow the formation of structures that may not be otherwise accessible. Thus the stretched forms in the presence of ADP or in the absence of nucleotides may simply be artifacts much like the null-torsion stretched form in ATP-Ca$^{2+}$ probably is.

## B.I.2. Cation turnover
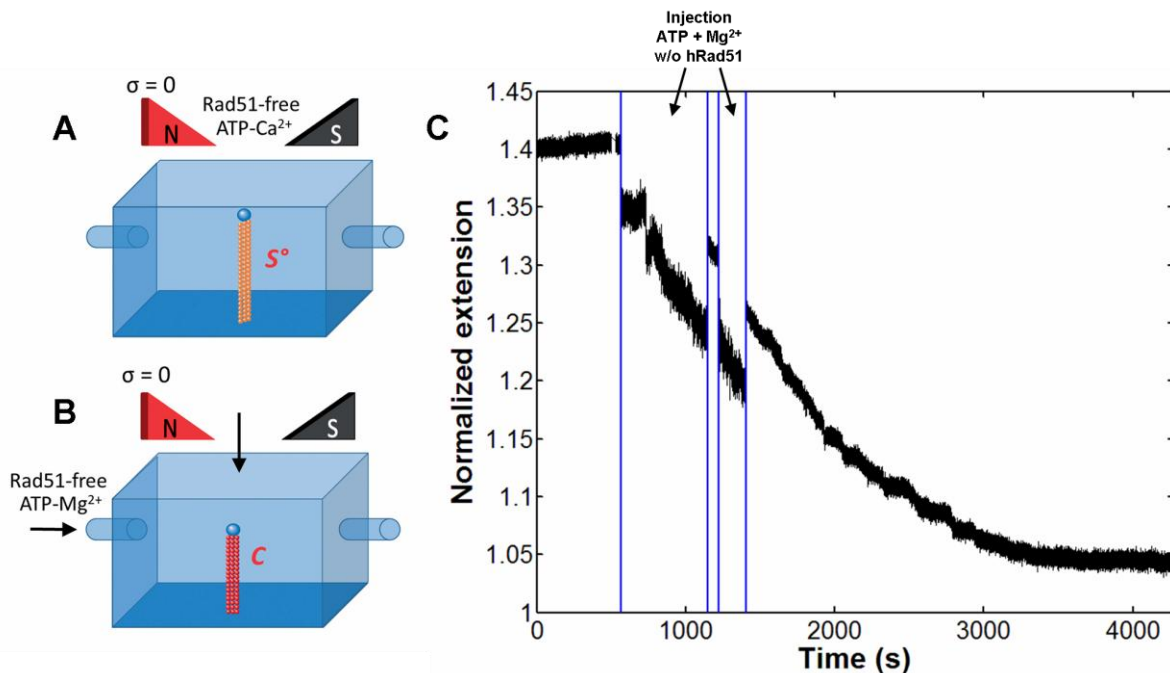


**Figure 132:** Experiment showing the transition from the null-torsion stretched state in ATP-Ca$^{2+}$ (S$^0$) to the condensed state in ATP-Mg$^{2+}$ (C) triggered by buffer exchange. The hRad51-dsDNA is initially shown at null torsion in a stretched state in a protein free buffer with ATP and Ca$^{2+}$ cations present (**A**). This state may be reached as shown in the experiment shown in **[Figure 125]**. The buffer was replaced by a similar one containing Mg$^{2+}$ cations instead of Ca$^{2+}$ (**B**). In (**C**) is shown the tracking of the elongation of a torsionally constrained DNA such as described in **A** and **B**. The buffer exchange resulted in a gradual shortening of the filament as it transitioned from the stretched null torsion state in (referred to as S$^0$) to the condensed null torsion state (referred to as C). For experimental reasons, the buffer exchange in this instance was made in two steps. During the experiment, a pulling force of $F$=4.63pN was maintained.
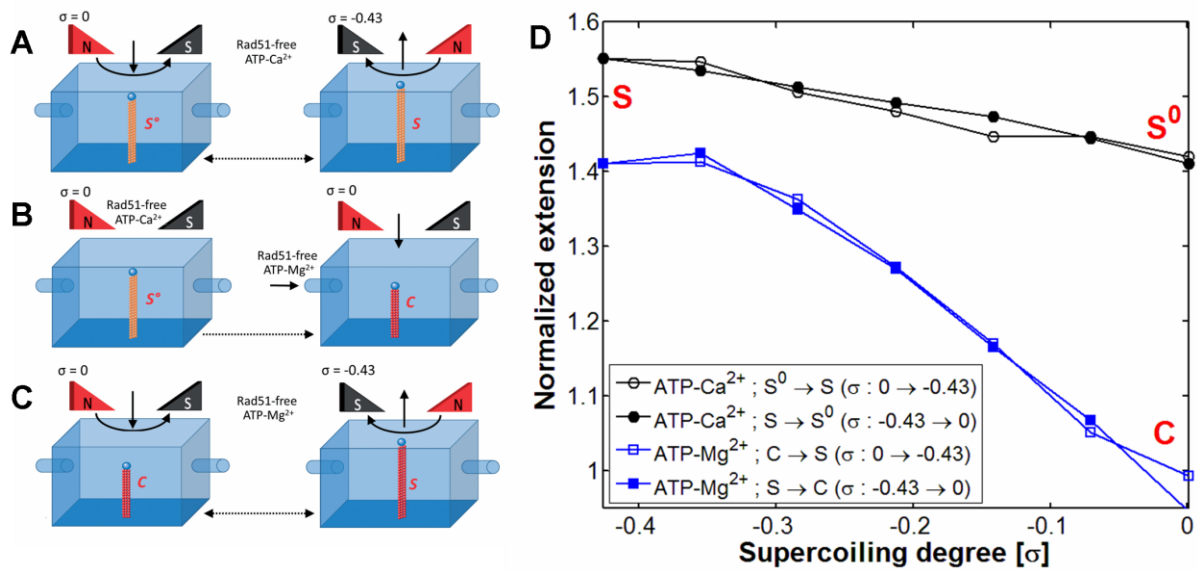
**Figure 133:** Experiment showing the difference in torsion response of a nucleoprotein filament before and after an ATP-$Ca^{2+}$ to ATP-$Mg^{2+}$ buffer exchange at a supercoiling degree of σ=0. The filament was initially in presence of ATP and $Ca^{2+}$ at null torsion. At such, it starts in a null torsion stretched stated ($S^0$). Unwinding and rewinding of the filament in these conditions resulted in a transition between the stretched unwound state (S) and $S^0$ (**A** and **D** ; black profiles). The ATP-$Ca^{2+}$ buffer was then exchanged for a ATP-$Mg^{2+}$ buffer while keeping a null supercoiling degree, resulting in a transition from $S^0$ to the null torsion condensed state (C) similarly to what is shown in [**Figure 132**]. Partial protein dissociation is probable during the buffer exchange (**B**). Unwinding and rewinding of the filament in these new conditions resulted in a transition between C and S as is expected from a filament formed ATP-$Mg^{2+}$ (**C** and **D** ; blue profiles). During the experiment, a pulling force of *F*=2pN was maintained.

The turnover of the cation is much easier to probe due to the great difference between the response in calcium and in magnesium. Particularly the null torsion stretched state (which will be referred to as $S^0$), seen in [**Figure 125**], is possible only in the presence of the $Ca^{2+}$ cation. In the experiment shown in [**Figure 132**], we tested the turnover of the cation for a filament which was brought to this particular state by forming the filament in the presence of ATP and $Ca^{2+}$ at a supercoiling degree of σ=-0.43 and winding it to impose σ=0. Since $S^0$ isn't reachable in the presence of $Mg^{2+}$, it is safe to assume that in these conditions the condensed state (referred to as C) is more favorable at σ=0 and therefore the turnover from $Ca^{2+}$ to $Mg^{2+}$ should trigger a transition from $S^0$ to C. Indeed we observe that the insertion of the protein-free buffer containing $Mg^{2+}$ while maintaining σ=0 triggers a relatively fast shortening of the filament length. In order to differentiate between state transition and protein dissociation, we probed the filament's response to torsion after the buffer exchange. In the experiment shown in [**Figure 133**], we can clearly see that the behavior before (black profiles) and after (blue profiles) the buffer exchange differ. In fact, apart from some apparent protein dissociation induced effects, the behavior after buffer exchange is identical to a filament formed in ATP and $Mg^{2+}$.

This turnover from calcium to magnesium is also possible when the filament is in the unwound stretched state (referred to as S) as can be seen in the experiment shown in [**Figure 134**]. Before the buffer exchange, the nucleoprotein filament is locked in a stretched (black profiles) as is typical of $Ca^{2+}$-filaments. The buffer exchange with a supercoiling of σ=-0.43 triggers no apparent transition, which is to be expected since the unwound stretched forms in calcium and magnesium do not differ in length. After buffer exchange, the filament's behavior is typical of $Mg^{2+}$-filaments, indicating that cation turnover has indeed happened.

The cation turnover while in the stretched form also seems less detrimental to the filament than at null torsion since no discernable protein dissociation occurred.
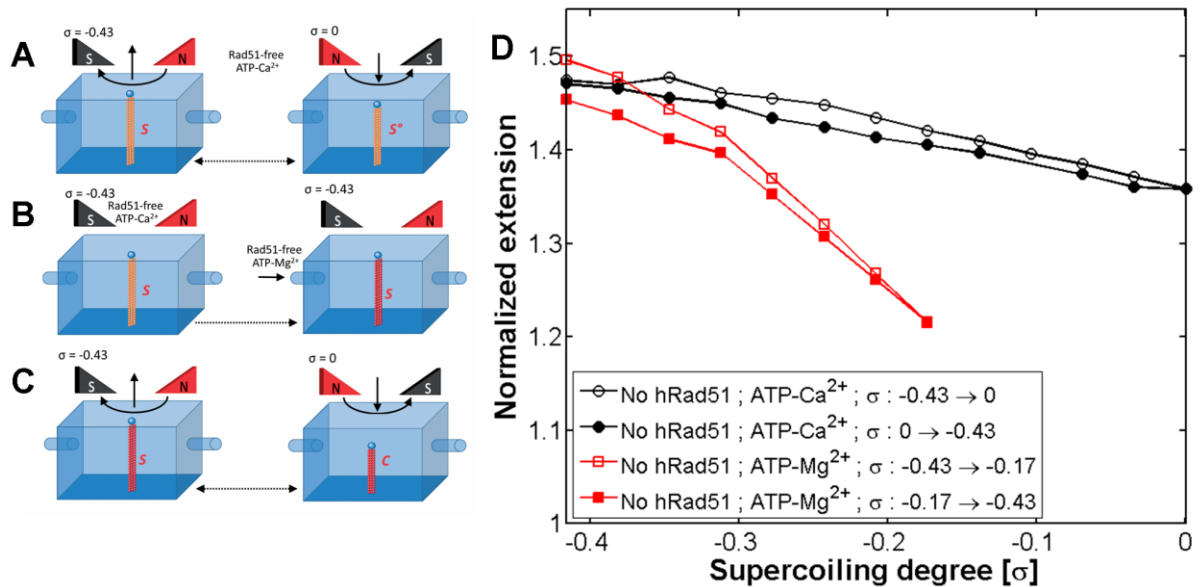


**Figure 134:** Experiment showing the difference in torsion response of a nucleoprotein filament before and after an ATP-$Ca^{2+}$ to ATP-$Mg^{2+}$ buffer exchange at a supercoiling degree of σ=-0.43. The filament was formed in ATP-$Ca^{2+}$, its torsion response was locked in a stretched form (**A** and **D** ; black profiles). The ATP-$Ca^{2+}$ buffer was then exchanged for a ATP-$Mg^{2+}$ buffer when the filament was in the stretched form (S at σ=-0.43), no discernable change to length was induced (**B**). Unwinding and rewinding of the filament in these new conditions resulted in a transition between C and S as is expected from a filament formed ATP-$Mg^{2+}$ (**C** and **D** ; blue profiles). For experimental reasons the red curve was not pushed up to σ=0. During the experiment, a pulling force of $F$=4pN was maintained.
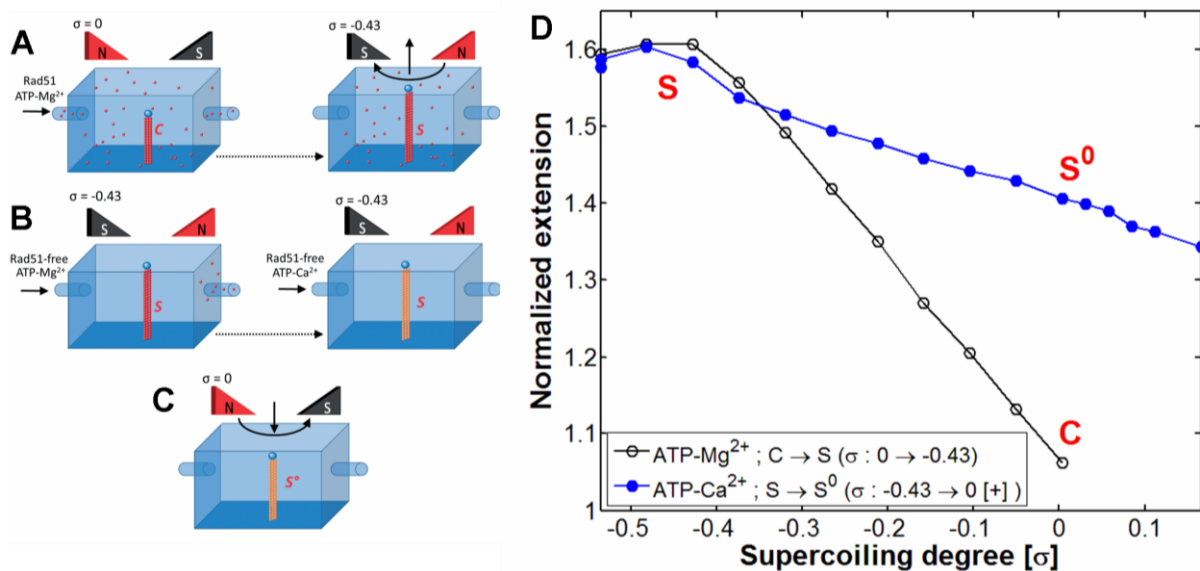


**Figure 135:** Turnover of the cation in hRad51-dsDNA from magnesium to calcium. The filament was formed at null torsion in presence of ATP and $Mg^{2+}$ and was unwound while leaving the protein in solution until it reached the extended S state (**A** and **D** ; black profile). Protein was rinsed from solution with an ATP-$Mg^{2+}$ protein-free buffer before being exchanged for a protein-free ATP-$Ca^{2+}$ buffer (**B**). No visible change of filament elongation was observed during this exchange. Winding of the filament in presence of calcium triggered a transition to the null torsion extended state $S^0$ as would be expected for a filament formed in ATP-$Ca^{2+}$ (**C** and **D**; blue profile). During the experiment, a pulling force of $F$=2.68pN was maintained.

Using the same method, we tested the turnover from magnesium to calcium with the filament in the stretched state [Figure 135]. The filament was formed at σ=0 in ATP-Mg$^{2+}$ and brought to the stretched state (σ=-0.43) while the protein (black profile). The chamber was then sequentially rinsed by a protein-free buffer containing ATP-Mg$^{2+}$ and then a protein-free buffer containing ATP-Ca$^{2+}$. Winding the filament back to σ=0 demonstrated a typical Ca$^{2+}$-filament response clearly indicating the occurrence of the cation turnover.

Taken together, these experiments demonstrate the possibility of cation turnover. The exchange may occur in both ways, from calcium to magnesium and vice-versa. We also showed a possible transition path from the null-torsion ATP-Ca$^{2+}$ stretched state to the ATP-Mg$^{2+}$ condensed stated with a constant imposed supercoiling degree of σ=0.

# B.II. Spontaneous evolution of the system

By not imposing the supercoiling degree, one may release the system and observe the spontaneous evolution of the hRad51-dsDNA nucleoprotein filaments. The residual energy applied by the pulling force is negligible and comparable to the forces applied on DNA *in vivo*. The observation of those spontaneous evolutions gives us information on the relative energy of the different states.

Releasing torsion in magnetic tweezers may be achieved by one of two ways. One may use nicked dsDNA molecules, on which single strand nicks have been created. Any excess torsion within the filament may then be released through rotation around the monovalent phosphodiester bonds [Figure 2] at the nick sites with little to no energy cost. Such a system is thus torsionally unconstrained even if its extremities are not allowed to rotate, which is the case in magnetic tweezers.

Another way is to modify the magnets in the magnetic tweezers setup in order to impose a vertical magnetic field [Figure 63] instead of a horizontal one [Figure 61]. In such a setup, no magnetic torque applied on the paramagnetic bead on the axis on the DNA molecule. Therefore, the extremity of the DNA attached is free to rotate through the beads rotation. Excess torsion release is then limited by the drag force during the bead's rotation.

In this section we will present experiments taking advantage of both these techniques, the first allowing the observation of the spontaneous elongation of the filaments and the second showing the spontaneous evolution of the twist.

We will show that the most favorable conformation for ATP-bound filaments is the stretched state regardless of the nature of the cation cofactor involved. The most favorable conformation of ADP-bound filaments is less certain but seems to be a condensed state with an elongation of approximately 1.2 times the length of B-DNA.

The observation of the filament induced twist change will allow us to confirm that the ATP-bound filaments spontaneously unwind themselves in order to reach the unwound stretched state. We will demonstrate that the application of small magnetic torque slows down or stalls this transition. We will propose a simple model for understanding the significance of this stall torque and reach the conclusion that it corresponds to the maximum torque applicable by a single hRad51 protein during the transition and thus is a measure of the energy difference between both states of the protein.

A series of experiments aiming to measure torques allowed us to characterize the different transitions observed. We will present different techniques for evaluating them and give our best estimations of each one.
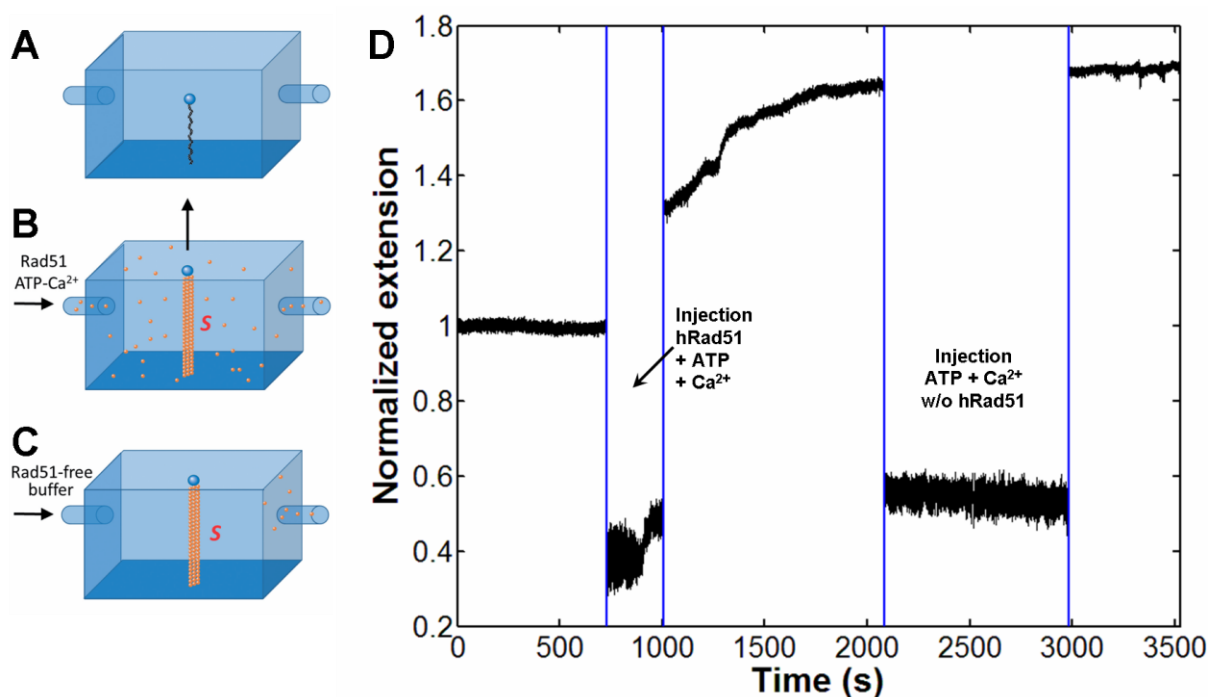
## B.II.1. Spontaneous elongation



**Figure 136:** Experiment showing the formation and stability of a stretched nucleoprotein filament formed on a nicked dsDNA in ATP-Ca$^{2+}$. The chamber was set up with nicked dsDNA molecules which are torsionally unconstrained (**A**). A buffer containing 200nM hRad51, 2mM CaCl$_2$, 1mM DTT, 0.05% Tween 20, and 25mM NaCl was inserted into the flow chamber (**B**). The protein was then rinsed out of the chamber (**C**). The graph in (**D**) shows the tracking of the elongation of one molecule. A pulling force of $F$=1.71pN was maintained throughout the experiment.

The formation of hRad51 filaments on nicked dsDNA yielded filaments in stretched form in both ATP-Ca$^{2+}$ [**Figure 136**] and ATP-Mg$^{2+}$ [**Figure 137**] suggesting that the unwound stretched form is the most energetically favorable regardless of the cation present when ATP is present. The behavior of the filaments, once the protein removed, differed greatly with the nature cation. In the case of Ca$^{2+}$, with which ATP hydrolysis is not permitted, the filament remained stable, locked in the stretched state. In the case of Mg$^{2+}$, protein removal triggered a slow protein dissociation process (approximately five hours for most of the process to occur). We know that this shortening is due to protein dissociation and not transition to the condensed state because of similar experiments performed on intact dsDNA molecules, on which we can probe the torsion response after the process (data not shown). However, since we know that ATP hydrolysis is required prior to protein dissociation, it is likely that transition from the stretched to the condensed state occurs transiently during the shortening observed in ATP-Mg$^{2+}$.

The formation of filaments in the presence of ADP-Mg$^{2+}$ resulted in the formation of a conformation shorter than the stretched state [**Figure 138**]. The normalized extension of this new conformation was measured to be 1.32±0.02 times the initial length of the DNA molecule (measured on 4 molecules ; STD of 0.02) when unbound proteins were available.

Evacuating the proteins from the chamber using the same buffer protein-free triggered a slight extension decrease resulting in conformation whose extension was $1.20\pm0.02$ times the initial length of the DNA molecule (measured on 4 molecules ; STD of 0.04). The reason for this shorter conformation when the protein is absent remains unclear. We know that this shortening is not solely caused by protein dissociation because exchanging the buffer for a buffer containing ATP-$Ca^{2+}$ immediately triggers a transition to the stretched state.
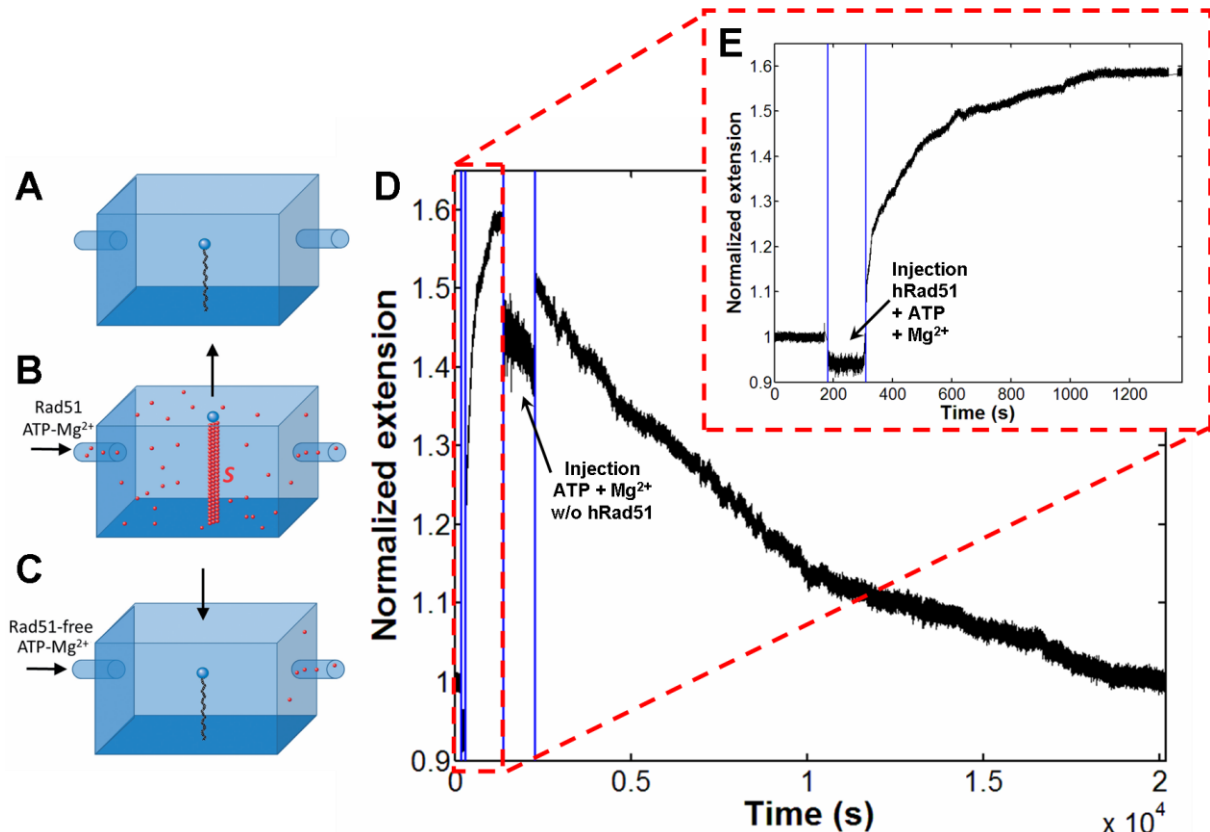


**Figure 137:** Experiment showing the formation and instability of a stretched nucleoprotein filament formed on a nicked dsDNA in ATP-$Mg^{2+}$. The chamber was set up with nicked dsDNA molecules which are torsionally unconstrained (**A**). A buffer containing 200nM hRad51, 2mM $MgCl_2$, 1mM DTT, 0.05% Tween 20, and 25mM NaCl was inserted into the flow chamber (**B**). The protein was then rinsed out of the chamber (**C**). The graph in (**D**) shows the tracking of the elongation of one molecule. A close-up of the first 20 minutes is shown in (**E**). A pulling force of $F$=3.85pN was maintained throughout the experiment.

Together these results indicate that the stretched state is the most stable conformation for the ATP bound form of a hRad51-dsDNA nucleoprotein filament. For the ADP bound form, we found two shorter stable states:

- In presence of ADP, $Mg^{2+}$ and hRad51: a state extended by $32\pm2\%$ (4 molecules; STD of 2%) when compared to the initial length of the DNA. Its relative crystallographic extension is estimated at $1.26\pm0.02$ (4 molecules; STD of 0.04).

- In presence of ADP, $Mg^{2+}$ without hRad51: a state extended by $20\pm2\%$ (4 molecules; STD of 4%) when compared to the initial length of the DNA. Its relative crystallographic extension is estimated at $1.14\pm0.03$ (4 molecules; STD of 0.06).

The conformation of those ADP-filaments seems to be affected by the presence of unbound proteins in solution for reasons we do not fully understand. It is likely that the stable form is the one observed in the absence of proteins. This last result should be used with caution, since we have not verified it to our satisfaction and it apparently contradicts known facts in literature where filaments are formed in ADP on dsDNA display a normalized extension of 1 [131][**Figure 45**] .
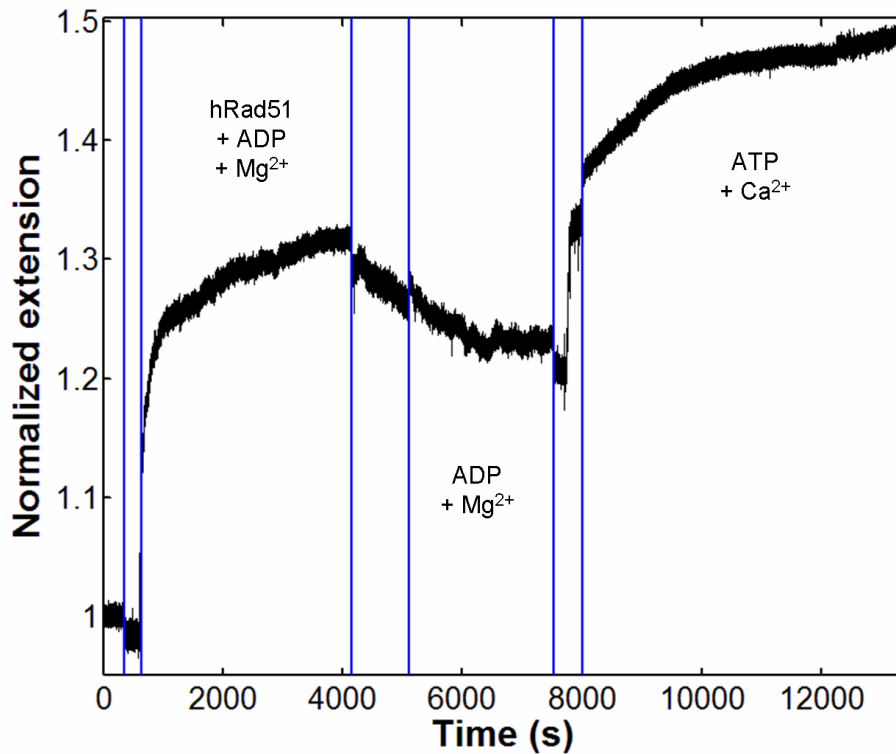


**Figure 138:** Experiment showing nucleotide turnover in a filament formed on a nicked dsDNA molecule. Around t≈350s, a buffer containing 200nM hRad51, 1mM ADP, 2mM MgCl$_2$, 1mM DTT, 0.05% Tween 20, and 25mM NaCl was introduced in the chamber. A partially stretched filament was formed with a stretching of ~30%. Free proteins in solution were then chased by the same buffer without hRad51 (t≈4150s). The molecule's extension decreases to a stretching of ~25%. After some time (t≈7525s), a buffer containing 1mM ATP, 2mM CaCl$_2$, 1mM DTT, 0.05% Tween 20, and 25mM NaCl was injected in the chamber. The molecule's extension reaches ~1.5 times its initial length, a fully stretched filament was formed. During the experiment, a pulling force of $F$=7.96pN was maintained.

## B.II.2. Spontaneous twist change

Changing the magnet configuration of the magnetic tweezers setup in the way described in [**Figure 63**] allows for the creation of a magnetic field mostly vertical with a minimal horizontal component. It is possible to minimize this horizontal component in order to lessen the magnetic torque applied to the paramagnetic beads. This torque may reduced to values inferior or comparable to torques applicable by Brownian motion (for an ambient temperature of 25°C, $k_BT$ = 4.12e-21J = 4.12 pN.nm).

Adding an extra pair of magnets such as described in [**Figure 65**] also allows the application of a variable magnetic torque. The value of this torque can be controlled by lowering or raising those magnets, reaching values ranging from 1pN.nm.rad$^{-1}$ to 5000pN.nm.rad$^{-1}$.

If the applied magnetic torque is low enough (typically under 10pN.nm.rad$^{-1}$), then the torque applied to bead by the nucleoprotein filament becomes no longer negligible and may induce its rotation. The observation of this spontaneous twist change gives us precious information on the rotational energy landscape. This landscape is the most pertinent when dealing with helicase proteins, in our case the hRad51 protein, where most of the energy is spent in the twist modification. A quick estimation of the energies involved is simple enough:

The work for DNA extension per protein can be estimated by $W_{extension}=L_{DNA}*Extension\_Factor*Force\_Applied$. One protein covers 3 base pairs so the corresponding length of the DNA in its B-form is $L_{DNA}=3*0.34nm$. The extension factor is of 50% and we'll assume for the argument's sake that the force applied by the protein is of the order of 1pN. In this case the work involved for the extension has a value of $W_{extension}=3*0.34e-9*0.5*1e-12 \approx 5e-22J$.

The work for DNA twist change per protein can be estimated by $W_{twist}=Rotation\_Angle*Torque\_Applied$. For one protein, the literature tells us that the twist induced is of 45° [145]. We'll assume for the argument that the torque applied is in the order of 10pN.nm.rad$^{-1}$. Then the work involved for the twist change has a value of $W_{twist}=45*\pi/180*10e-21 \approx 8e-21J$.

This estimation gives us a rotational energy at least one order of magnitude greater than the energy involved for extension. Moreover, the energy involved for extension is also one order of magnitude lower than thermal energy and can therefore be considered as negligible. Therefore, studying the energy landscape of the hRad51 protein comes down to investigating the way the twist changes and measuring the torques involved.

## Twist evolution of ATP-bound filaments



**Figure 139:** Experiment showing spontaneous twist change of a filament formed in ATP-Ca$^{2+}$. Initially the chamber was set up with dsDNA molecules inside and the horizontal magnetic field was nullified as much as possible (**A**). Brownian motion was sufficient to induce rotation of the beads as can be seen in the first 20 minutes in (**C**). At some point, a buffer containing hRad51 proteins, ATP and Ca$^{2+}$ cations was injected into the flow chamber (**B**). The rotation of the beads is blocked during buffer injection by a pair of magnets not shown. When released, the filament started unwinding itself toward $\sigma$=-0.43 (**C**). A pulling force of $F$=1.4pN was maintained during the experiment.

Filaments were formed on dsDNA molecules in a magnetic tweezers setup in which the horizontal field had been minimized as much as possible. The residual magnetic torque applied to the paramagnetic beads was inferior to thermal energy and thus the beads were able to rotate under the influence of both the torsion of the DNA and of the Brownian motion [**first 20 minutes in Figure 139**]. Initially, the supercoiling degree of those molecules is approximately that of the natural twist of B-DNA ($\sigma=0$). Buffers containing the hRad51 proteins, ATP and one of the two cations were inserted while blocking the beads' rotation by lowering the pair auxiliary magnets, thus applying a magnetic torque strong enough to stall any rotation. Protein insertion triggered filament unwinding for both ATP-Ca$^{2+}$ [**Figure 139**] and ATP-Mg$^{2+}$ filaments [**Figure 140**].
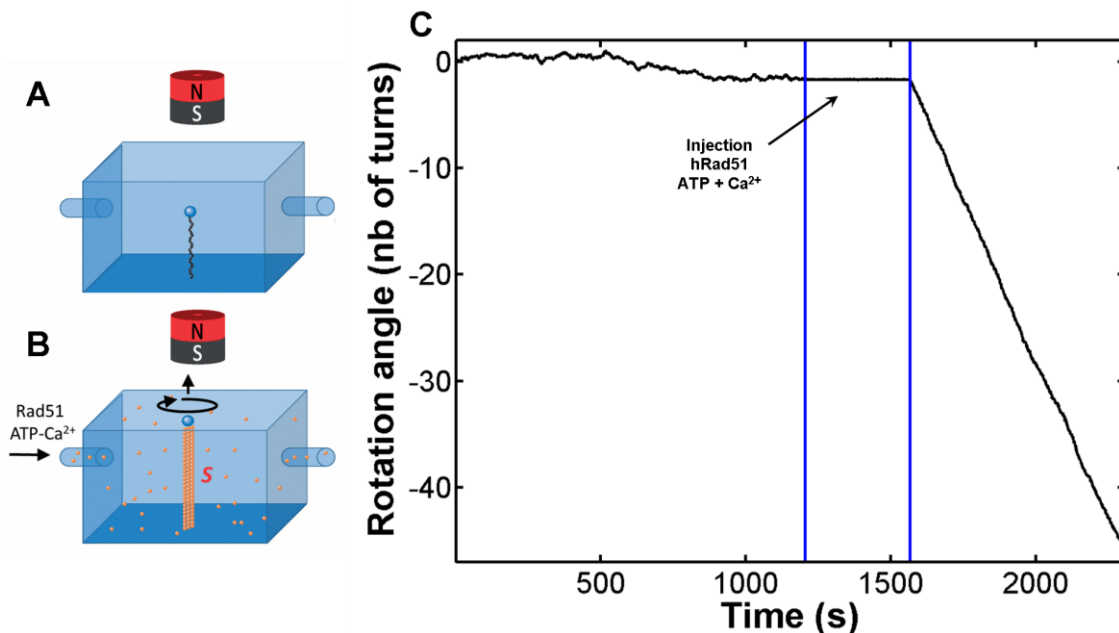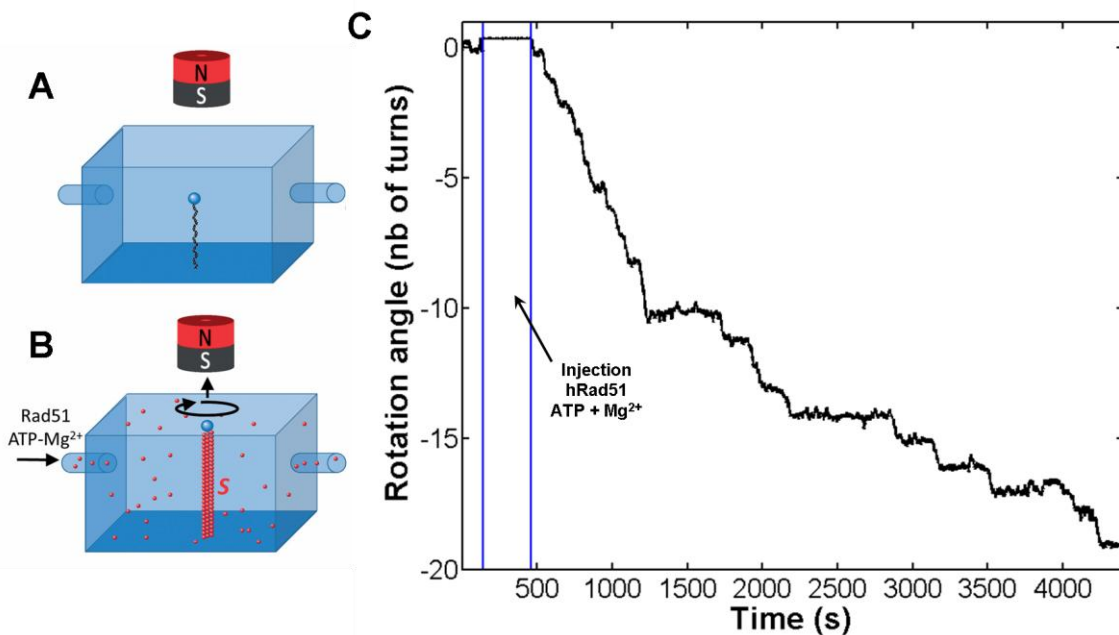


**Figure 140:** Experiment showing spontaneous twist change of a filament formed in ATP-Mg$^{2+}$. Initially the chamber was set up with dsDNA molecules inside and the horizontal magnetic field was nullified as much as possible (**A**). A buffer containing hRad51 proteins, ATP and Mg$^{2+}$ cations was injected into the flow chamber (**B**). When released, the filament started unwinding itself toward $\sigma=-0.43$ (**C**). A pulling force of $F=1.7$pN was maintained during the experiment.

The beads used in our experiments (M-280 Streptavidin Dynabeads) have a quite large diameter of 2.8µm. As a consequence, the drag force exerted on the beads during rotation is quite high resulting in slow filament unwinding. Indeed waiting for the filament to on its own from $\sigma=0$ to $\sigma=-0.43$ at the observed rotation speeds should take somewhere between 10 to 15 hours. This experimentation time is not only discouragingly long for the experimenter, but is also superior to the time required for protein dissociation from ATP-Mg$^{2+}$ filaments [**Figure 137**].

Therefore we made use of the auxiliary magnets in order to gradually unwind the filaments and thus observe twist change at different supercoiling degrees. Such an experiment with an ATP-Ca$^{2+}$ filament is shown in [**Figure 141**]. The red profiles indicate when the bead is free to rotate on its own whereas the black show when the magnets were lowered for twist manipulation. We could then observe that the tendency to unwind held true up to approximately $\sigma=-0.43$ corresponding to the supercoiling associated to the stretched state in ATP-Ca$^{2+}$. Once the filament unwound, we were able to gradually wind it back towards $\sigma=0$

in order to probe the filament's response once it was locked in the stretched conformation. The tendency was then also towards filament unwinding, back to the stretched state at σ=-0.43.

Results obtained for ATP-Mg$^{2+}$ filaments were not as clear cut as in ATP-Ca$^{2+}$ but overall the same tendency to unwind was found.
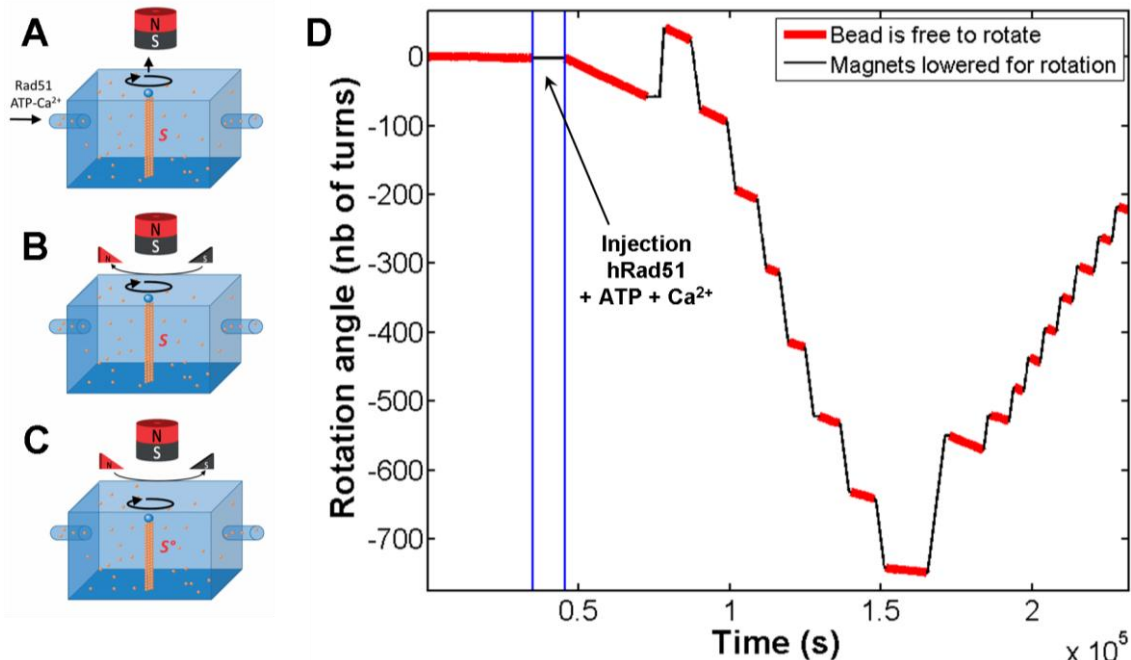


**Figure 141:** Experiment showing the rotation of ATP-Ca$^{2+}$ filament at different supercoiling degrees (**D**). The filament was formed in ATP-Ca$^{2+}$ (blue profile shows protein injection) and the proteins were left in solution (**A**). The residual horizontal magnetic field was nullified as much as possible. By lowering a pair of magnets to bring them closer to the system, we are able to apply a small magnetic torque to the bead; this torque may be used to control bead rotation by rotating the magnets. The black profiles show when the magnets are lowered. The filament is gradually unwound towards σ=-0.43 (**B**) .The exact supercoiling degree is unknown in this type of experiment, we only know that natural twist of the initial B-DNA should be composed of around 1200 turns. Once unwound, the filament is wound back to observe the behavior of the locked stretched conformations typical of ATP-Ca$^{2+}$-filaments (**C**). During filament induced rotation, a pulling force of F=1.4pN was maintained.

## Stalling torque

Let us consider the simplest model possible in the case of the ATP-Mg$^{2+}$ condensed to stretched state transition. We'll then assume the transition occurs with the hRad51 proteins applying a constant torque $\Gamma_{hRad51}$ throughout the transition. In order to induce twist modification, the proteins would then apply a differential torque over and under their position and the situation could be summarized as in the diagram in [**Figure 142 ; diagram on the left**]. The different torques would propagated by the torsional elasticity of the DNA inside the nucleoprotein filament resulting in the nullifying of the torques of one protein by the torques of the proteins over and under it. The situation is then equivalent to a single protein filament applying a differential torque equal to that one protein [**Figure 142 ; diagram on the right**].. The filament's end attached to the bottom of the chamber prevents any release of torsion on this end, thus the floor applies an appropriate torque equal to $\Gamma_{floor} = \Gamma_{hRad51}$. Thus the only torque left for the bead to feel is the torque of a single protein: $\Gamma_{bead} = \Gamma_{hRad51}$. The rotation of the

bead is then limited by the sum of the magnetic torque applied it and the torque resulting from drag force.

We define the stalling torque for the filaments' transition as the minimum magnetic torque that may be applied to the bead with which the filament induced rotation is stalled. This stalling torque is an indication of how much energy a hRad51 is able to deploy for a particular transition.
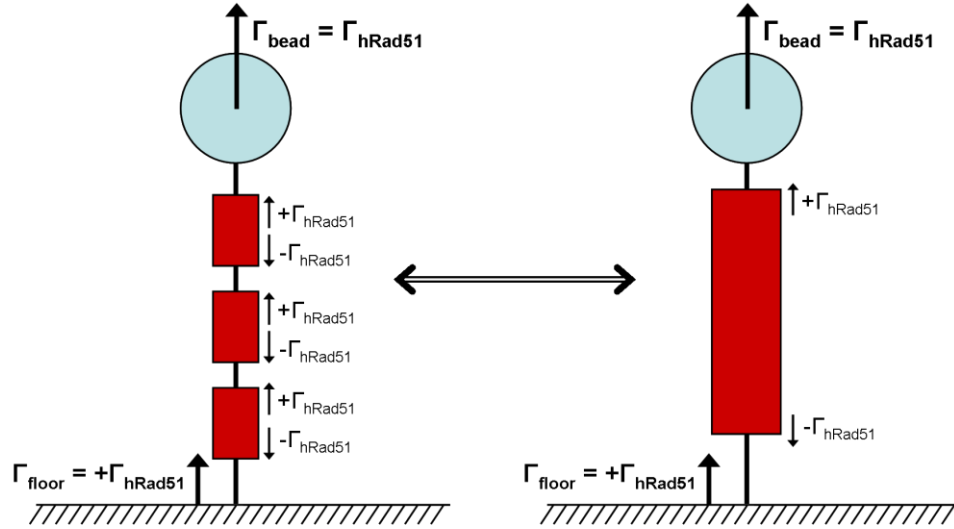


**Figure 142:** Diagram showing what torque is induced by the nucleoprotein filament on the paramagnetic bead. The hRad51 proteins (red boxes) induce a differential torque on the filament. The torque is propagated throughout the filament by the torsional elasticity, thus several proteins (on the left) is equivalent to a single protein filament applying the same torque as a normal protein. The filament's end attached to the bottom of the chamber is unable to rotate, so the floor responds by applying the necessary torque of one protein in order to compensate. In the end, the torque felt by the bead is the sum of torques and is equal to the torque of one protein.

This hold true of course only if the torques are propagated by elasticity and this the case only if the system is far enough from the final state to induce throughout the filament a torque equal to $\Gamma_{hRad51}$. If we consider that the DNA within the filament has an elastic response, than the torque it may apply is given by the following expression:

$$\Gamma_{DNA} = \frac{C_{rot}}{L_{DNA}}\left(\theta_{DNA} - \theta_0\right)$$

Where $\Gamma_{DNA}$ is the torque within the DNA, $C_{rot}$ the torsion constant per length, $L_{DNA}$ the length of the DNA, $\theta_0$ the natural twist of the DNA and $\theta_{DNA}$ the current twist of the DNA.

If there are $N$ proteins in a filament, a number $N_C$ of which are still in the condensed ATP-Mg$^{2+}$ state and that they all wish to reach the stretched state, then the twist remaining for the transition is equal to:

$$\theta_{transition} = N_C \cdot \theta_{hRad51}$$

Where $\theta_{hRad51}$ is the twist induced by one protein from the condensed to the condensed state ($\theta_{hRad51}$ = -45°).

The torque felt by the bead will be then equal to the torque of one protein as long as:

$$\Gamma_{hRad\,51} \leq \frac{C_{rot}}{L_{DNA}}\left(N_C \cdot \theta_{hRad\,51} - \theta_0\right)$$

If measured far enough from equilibrium, the stalling torque is therefore an indication of the maximum torque applicable by a single hRad51 protein in the transition it is stalled in. Since we are able to apply variable torques in the pertinent range ($1\text{pN.nm.rad}^{-1}$ to $100\text{pN.nm.rad}^{-1}$), we experimented stopping transitions by applying the smallest torque possible. Such an experiment is shown for a filament formed in ATP-Mg$^{2+}$ **[Figure 143]**. The bead is initially shown in conditions where the torque was minimized as much as possible and there the filament has no problem inducing rotation. We then lowered the auxiliary magnets in order to increase the magnetic torque, and for an intermediate value (here $17.2\text{pN.nm.rad}^{-1}$) the rotation continues more slowly with short pauses in between turns (when the bead is trapped at an angle for which the magnetic torque is maximum). Lowering the magnets further, thus applying a higher torque (here $27.3\text{pN.nm.rad}^{-1}$) stalls rotation completely. It may be resumed by raising the magnets allowing us to confirm that rotation has been stalled solely by the magnetic torque. The operation is repeatable many times. This type of experiments allows us to obtain a fork within which the stall torque is comprised. Here we measured the stall torque was somewhere in between $17.2\text{pN.nm.rad}^{-1}$ and $27.3\text{pN.nm.rad}^{-1}$.
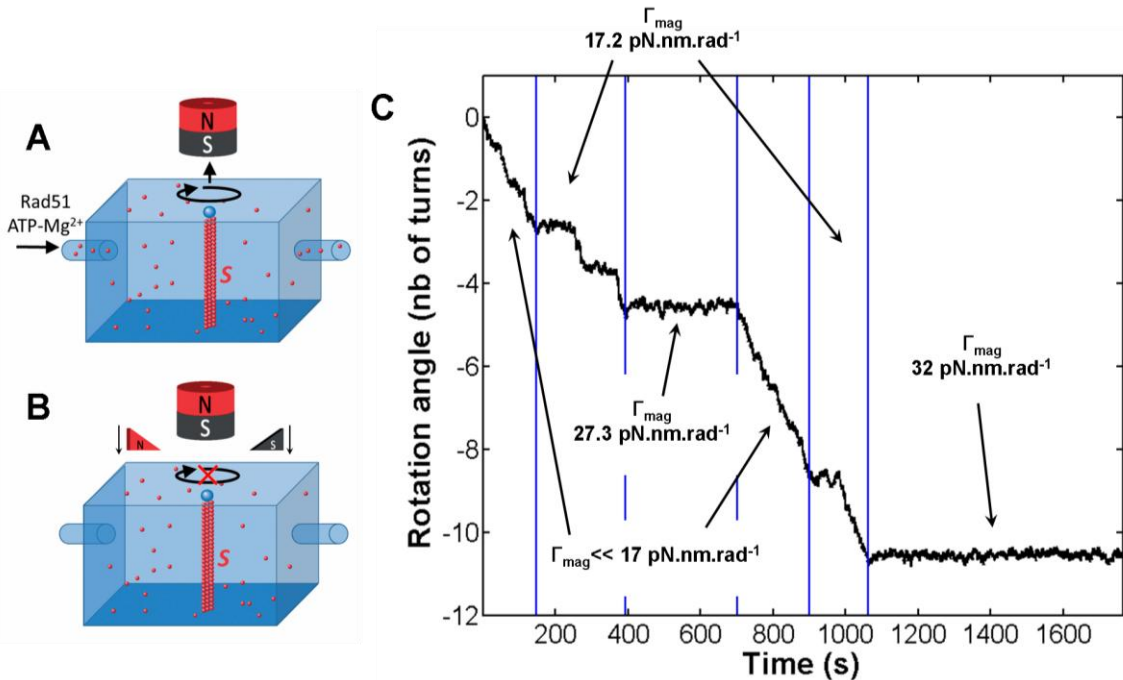


**Figure 143:** Experiment showing the stalling of rotation of a ATP-Mg$^{2+}$ filament by the application of a small magnetic torque on the paramagnetic bead (**C**). The filament was formed in ATP-Mg$^{2+}$ and the proteins were left in solution (**A**). The residual horizontal magnetic field was nullified as much as possible but could not be measured, we can only know it is negligible. The filament has no problem inducing bead rotation in these conditions. By lowering a pair of magnets to bring them closer to the system, we are able to apply a small magnetic torque to the bead (**B**). If the stronger the torque, the more laborious the rotation becomes up to a point where it is completely stalled. Lowering the torque by raising the magnets triggers the resuming of bead rotation. The lowering of the extra magnets increase the applied pulling force, during the experiment it was maintained in the following range: $0.5\text{pN}<F<1.3\text{pN}$.

## B.II.3. Transition torques

### Estimating the stall torque

By repeating experiments such as shown in [**Figure 143**], we've tried narrowing down the value of the stall torque for the ATP-Mg$^{2+}$ condensed to stretched state transition. Due to the nature of the experiment, in which one cannot know the magnetic torque applied until after the experiment is over, added to the fact that a good measure of torque requires a long acquisition time, the whole process is one strenuous trial and error. We've nonetheless concluded from our data [**Figure 144**] that the value of this stall torque should be over 22pN.nm.rad$^{-1}$ and under 24pN.nm.rad$^{-1}$. The uncertainty of this estimation is then of 1pN.nm.rad$^{-1}$ to which must be added the mean uncertainty of torque measures (2pN.nm.rad$^{-1}$). Taken together, our best estimation of the stall torque of the condensed to stretched transition in ATP-Mg$^{2+}$ is:

$$\Gamma_{stall\ C\rightarrow S\ ATP-Mg^{2+}} = 23\pm3\,pN.nm.rad^{-1}$$
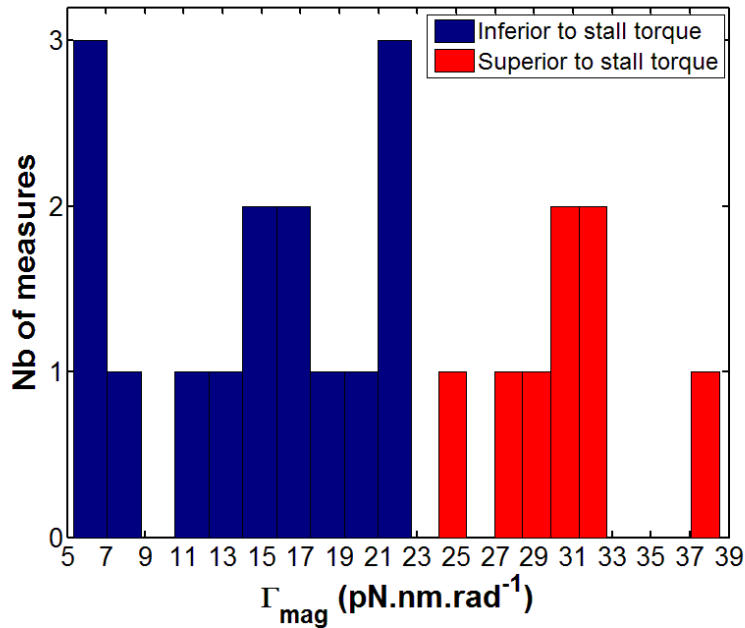


**Figure 144:** Histogram of the magnetic torque measures taken for the ATP-Mg$^{2+}$ condensed to stretched transition. In blue are the values of the magnetic that were inferior to the stall torque and in red are the values that were superior.

### Static torque

Another possibility for estimating the torque applied by the hRad51 proteins on the bead is to fit the energy potential of stalled beads with a static torque model. This model assumes that when rotation is stalled, the proteins continue to apply a constant static torque $\Gamma_{stat}$ to the bead. Thus the total torque felt by the bead in such a situation would be the sum of the magnetic torque and the static torque:

$$\Gamma_{bead} = \Gamma_{mag} + \Gamma_{stat} = -MB\sin(\theta-\theta_0) + \Gamma_{stat}$$

Adding a constant torque to the equation comes down to slanting the energy potential $U(\theta)$ in the direction of the torque:

$$U(\theta) = -MB\cos(\theta - \theta_0) - \Gamma_{stat} * (\theta - \theta_0)$$

The form of the potential given by this model allows accounting for the dissymmetry of the energy potentials measured on stalled beads [**Figure 145**]. Since the fit model contains four free parameters ($MB$, $\Gamma_{stat}$, $\theta_0$ and the energy constant), the coefficient values obtained may be a bit fickle and too dependent on the starting position of the fitting algorithm. For the values measured to be considered reliable, one should input a previously measured value of the magnetic field orientation $\theta_0$ which is the parameter which seems the influence results the most and is also an easy to measure parameter on beads linked to naked DNA molecules before starting the experiment. Analyzing our data yielded the following value for the static torque of the condensed to stretched ATP-$Mg^{2+}$:

$$\boxed{\Gamma_{stat\ C \to S\ ATP-Mg^{2+}} = 19.60 \pm 1.40\,pN.nm.rad^{-1}}$$

This value has been obtained over 12 measures with a standard deviation of 4.82pN.nm.rad$^{-1}$.
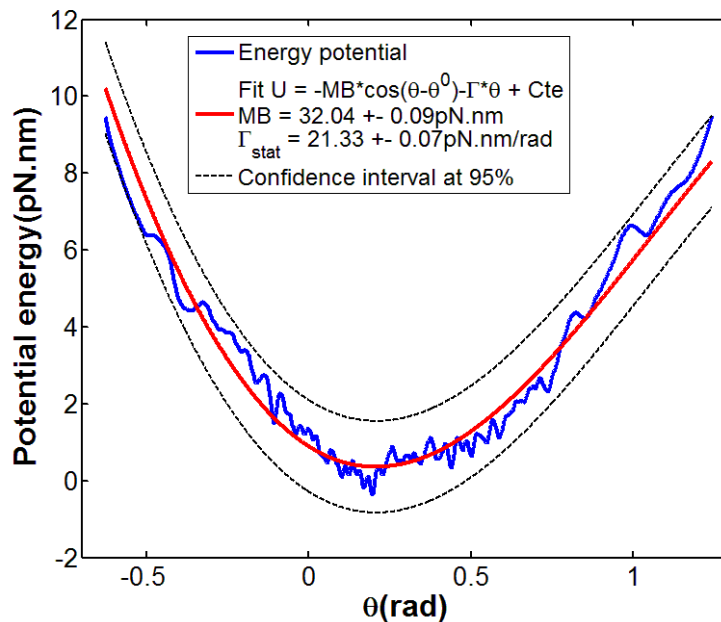


**Figure 145:** Fitting of the fluctuations of the bead shown in [**Figure 143; 1100s $< t <$ 1700s**] with the static torque model. Rotation is stalled and hRad51 proteins are present in solution with ATP and $Mg^{2+}$ as cofactors.

## Dynamic torque

The last solution we found for measuring the transition torques proved to be easiest one to apply. Compared with the two others, it requires more extensive calibration prior to starting the experiment but afterwards, measurements are much faster since the method doesn't require knowledge of the value of the magnetic torque nor of the form of the energy potential.

The method involves using the bead's drag force to measure the transition torque while the bead rotates. One must then just apply a small enough magnetic torque to allow protein induced rotation and measure the bead's angular speed $\omega$. Obtaining the transition torque then becomes a matter of solving the kinetic equation:

$$m_{bead}\frac{d^2\theta(t)}{dt^2} - \xi_{bead}\frac{d\theta(t)}{dt} - \Gamma_{hRad\,51}(t) - \Gamma_{mag}(t) = \eta(t)$$

Where $\theta(t)$ is the angular position of the bead, $m_{bead}$ its mass, $\xi_{bead}$ its rotational drag coefficient, $\Gamma_{hRad51}(t)$ the torque applied by the proteins on the bead , $\Gamma_{mag}$ the torque resulting from the magnetic field and $\eta(t)$ the torque resulting from Brownian motion.

The magnetic torque applied is known and, since the Reynolds number in our situation is very low, we are able to neglect the inertial component of the equation:

$$-\xi_{bead}\frac{d\theta(t)}{dt} - \Gamma_{hRad51}(t) + MB\sin(\theta(t) - \theta_0) = \eta(t)$$

By averaging the equation in time, we'll be able to dismiss both the Brownian motion component whose average is always null. If we assume that the speed is of a constant value $\omega$ in average, the time average of the magnetic torque is also null if the time period considered is long enough for the bead to rotate several times. The equation then becomes:

$$\Gamma_{dyn} = -\xi_{bead}*\omega$$

Where we'll define $\Gamma_{dyn}$ as the dynamic torque of the protein, which represents the average torque applied by the protein on the bead.

In the end, measuring this dynamic torque comes down to measuring the average angular speed and ascertaining the bead's drag coefficient $\xi_{bead}$. The latter is where the whole process becomes tricky and requires extensive calibration prior to protein insertion in order to measure the drag coefficient when the beads are linked to naked dsDNA molecules. This coefficient is the sum of two different contributions, a rotation drag component and a translational component resulting from the bead's off-centered rotation:

$$\xi_{bead} = \xi_{rot} + \xi_{off}$$

The rotational component $\xi_{rot}$ may be obtained through the form of the power spectrum density of the angular fluctuations resulting from Brownian motion as we have done for force measurements. The translational component $\xi_{off}$ has to be calculated as being the product of the translational drag coefficient $\xi_{trans}$ and the radius of the off-centered rotation $R_{off}$:

$$\xi_{off} = R_{off}*\xi_{trans}$$

The radius of the off-centered rotation is obtainable through a circular fit of the plot in a XY plane of the fluctuation of the bead's center. Accessing the translational drag coefficient can be done by analyzing the power spectrum density of the fluctuation of the bead's center.

In order to uncorrelate the angular fluctuations from the transition fluctuation, only the direction of the radius is considered ($\mathbf{u_r}$ in polar coordinates). And so once these four different parameters have been measured, the dynamic torque may be calculated through:

$$\Gamma_{dyn} = (\xi_{trans} + R_{off} * \xi_{trans}) * \omega$$

In our experiments, the diameter of the paramagnetic beads used (2.8µm) is quite large and so the drag force is substantial. This works in our advantage because in these conditions the dynamic torque should be quite close to the static torque previously considered. Indeed, in the case of the ATP-Mg$^{2+}$ condensed transition, the value obtained is fairly close to what we measured before:

$$\boxed{\Gamma_{dyn\ C \to S\ ATP-Mg^{2+}} = 20.92 \pm 0.71\,pN.nm.rad^{-1}}$$

This value has been obtained over 24 measures with a standard deviation of 3.48pN.nm.rad$^{-1}$.

Since the method was simple enough to implement, we've also applied it in the case of the ATP-Ca$^{2+}$ condensed to stretched transition and obtained the following value:

$$\boxed{\Gamma_{dyn\ C \to S\ ATP-Ca^{2+}} = 25.56 \pm 0.72\,pN.nm.rad^{-1}}$$

This value has been obtained over 26 measures with a standard deviation of 3.64pN.nm.rad$^{-1}$.
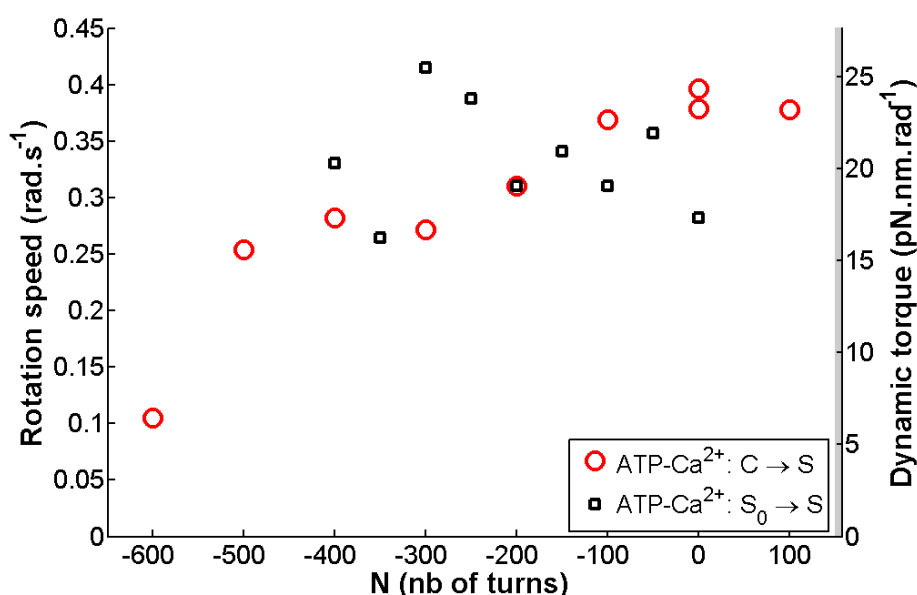


**Figure 146:** Rotation speeds (**axis on the left**) and the deduced dynamic torques (**axis on the right**) taken during the experiment shown in [**Figure 141**], associated with the condensed to stretched transition is ATP-Ca$^{2+}$ (red data points) and the transition from the null-torsion stretched state to the unwound stretched state also in ATP-Ca$^{2+}$ (black profiles data points).The naked dsDNA molecule contains in its B-forms approximately 1200 turns which means that N=-600 corresponds approximately to σ=-0.5.

By unwinding a ATP-Ca$^{2+}$ nucleoprotein filament up to the unwound stretched state and then winding it back towards σ=0, we were able to probe the transition from the null-torsion stretched state to the unwound stretched state which occurs when the filament is locked in stretched conformations in ATP-Ca$^{2+}$. The torque obtained was as follows:

$$\Gamma_{dyn\ S_0 \rightarrow S\ ATP-Ca^{2+}} = 20.72 \pm 0.78\, pN.nm.rad^{-1}$$

This value has been obtained over 24 measures with a standard deviation of 3.48pN.nm.rad$^{-1}$. This last value corroborates well with a recent measure achieved using a similar magnetic tweezers setup of $\Gamma_{S0 \rightarrow S\ ATP-Ca}$=20±13pN.nm.rad$^{-1}$ [145] **[Figure 147]**.
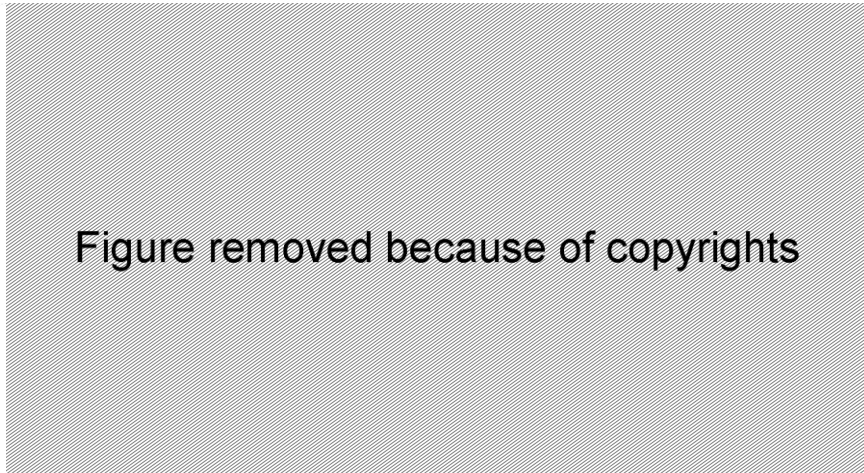


**Figure 147:** Extracted from [145]. Torque as a function of the imposed number of turns in a hRad51-dsDNA nucleoprotein filament in ATP-Ca$^{2+}$. The reference for the turns N=0 is set for a supercoiling degree of σ=-0.43. Torque values saturate upon over- and under- winding at -20±13pN.nm and 24±14pN.nm respectively. The difference between the plateaus is 43±3pN.nm. The linear response regime is fitted to a torsional persistence length of $C$=504±57nm. The data was obtained for a pulling force of $F$=3.5pN on a nucleoprotein filament with a length of $L_{filament}$ = 4.1±0.1μm formed on a dsDNA molecule with a length of $L_{DNA}$ = 2.74±0.08μm.

A behavior difference between the two ATP-Ca$^{2+}$ transitions is to be noted. In the case of the ATP-Ca$^{2+}$ condensed to stretched, we may observe a decrease of the dynamic torque as the filament is unwound **[Figure 146 ; red data points]**. We expected this effect due to the elastic behavior of the DNA within the filament and so dynamic torques were calculated near the condensed state's supercoiling degree. In the case of the ATP-Ca$^{2+}$ null-torsion stretched to unwound stretched transition however, the torque remained more or less constant at different supercoiling degrees **[Figure 146 ; black data points]**. The fact that it remains constant tells us that the torque applied is not the result of the filament's elastic behavior, where the torque would increase linearly with the supercoiling degree. The reason why it does not decrease however as is the case for the other transition is yet to be understood.

# Chapter 4: Drawing the energy landscape of hRad51

## A. Extrapolating the energy landscape

### A.I. The ATP-bound nucleoprotein filament

With the information we've obtained, we can now try to draw the energy landscape in which the nucleoprotein filament evolves when it passes from one conformation to another. We've identified three states for the ATP-bound hRad51 nucleoprotein filament which we'll call $S_{ATP}$, $C_{ATP}$ and $S^0_{ATP}$:

- **$S_{ATP}$**: A stretched unwound state with a normalized extension of 1.552±0.012 (1.424±0.014 in relative crystallographic extension) and a supercoiling degree of σ=-0.43. We'll assume in the following argument that the actual normalized extension of this state is 1.5 times the crystallographic length, as is generally accepted in the literature [119], [127], [129], [135], [139]. The actual value of the supercoiling degree could not be ascertained with precision with our experiments, but nothing in our data seems to contradict the value given by existing literature [127], [128], [145].

- **$C_{ATP}$**: A condensed null-torsion state with a normalized extension of 1.115±0.035 and a supercoiling of σ=0. We've estimated its relative crystallographic extension to 0.970±0.038. This value may be underestimated if we consider that the proteins are actually trying to unwind the DNA molecule in this state, despite the strong magnetic trap. Therefore positive torsion is applied to the naked regions of the DNA which would then form plectonems. We will then assume for the following that the actual extension induced in this state is the crystallographic length.

- **$S^0_{ATP}$**: A stretched null-torsion state with a normalized extension of 1.384±0.045 and a supercoiling degree of σ=0. Its relative crystallographic length has been estimated at 1.34±0.01. We should keep in mind that like for the condensed state, this value is probably slightly underestimated.

We know from our experiments in spontaneous elongation **[Figure 136]** and from the ones in spontaneous rotation **[Figure 139]** that the filament spontaneously converts from the condensed state $C_{ATP}$ to the stretched state $S_{ATP}$. Therefore it stands to reason that the energy associated to the stretched state is lower than the energy associated with the condensed one:

$$U_{S_{ATP}} < U_{C_{ATP}}$$

With the same reasoning stemming from experiments in spontaneous rotation [**Figure 141**], we deduce that the energy associated with null-torsion stretched state $S^0_{ATP}$ is superior to the energy associated with the stretched state $S_{ATP}$:

$$U_{S_{ATP}} < U_{S_{0\,ATP}}$$

From our experiments with an imposed supercoiling degree, we've shown that, once unwound to $S_{ATP}$, the filament will never go back to the condensed state $C_{ATP}$ upon winding. It prefers instead to reach the null-torsion stretched state $S^0_{ATP}$ [**Figure 125**]. We then know that the energy associated with $S^0_{ATP}$ is inferior to the energy associated with $C_{ATP}$:

$$U_{S_{0\,ATP}} < U_{C_{ATP}}$$

We've measured the torques $\Gamma$ associated with the transitions $S^0_{ATP} \rightarrow S_{ATP}$ and $C_{ATP} \rightarrow S_{ATP}$. Those measured torques represent the average torques induced by one protein in the nucleoprotein filament as it convert from one state to the other. As such, we consider that these torques are representative of the difference in free energy between the different states. Thus we deduce the mechanical energy required to move between these states from the product between the torque and the angle between the states to which we subtract the energy stemming from the magnetic pulling force in our experiments:

$$\Delta U = \Gamma \cdot \theta_{hRad51} - F \cdot \Delta l$$

Where $\theta_{hRad51}$ is the angle induced by one hRad51 protein when converting the filament from the condensed state to the stretched state, $\Delta l$ is the extension difference between the two considered states and $F$ is the pulling force exerted by the magnetic tweezers on the nucleoprotein filament during the transition. We'll use $\theta_{hRad51}$=-45° as a value of the angle which assumes that the supercoiling degree of the stretched state is σ=-0.43 and that the stochiometry is of three base pairs of dsDNA per hRad51 protein [100]–[102]. In doing so, we choose to ignore the measurement of $\theta_{hRad51}$ done within our unit by Arata *and al.* [142], which yielded a value of -65° and is currently in contradiction with most of the existing literature.

For the energy difference between the condensed state $C_{ATP}$ and the stretched $S_{ATP}$, the extension difference for one protein is equal to 0.5 times the crystallographic length of 3 base pairs in the dsDNA B-form:

$$\Delta l_{C \rightarrow S} = 0.5 * 3 * 0.34 nm = 0.51 nm$$

Thus taking as a reference the dynamic torques we have measured taken with their associated pulling forces, the energy difference between $S_{ATP}$ and $C_{ATP}$ then becomes:

$$U_{C_{ATP}} - U_{S_{ATP}} = \Gamma_{dyn\ C \rightarrow S\ ATP-Ca^{2+}} \cdot \theta_{hRad51} - F \cdot \Delta l_{C \rightarrow S}$$

$$= 19.2 \pm 0.6\, pN.nm$$

(Average on 26 measures with a standard deviation of 2.79pN.nm).

In the same way, we can characterize the energy difference between the two stretched states. Since we don't know if the $S^0_{ATP}$ is actually a state, the angle to apply for the conversion is unknown. It is pertinent however to estimate the energy required to reach null-torsion in that transition in order to compare it with the energy of the condensed state. In that case, we'll use the same angle $\theta_{hRad51}$ as before. We estimate the extension difference between the $S^0_{ATP}$ and the $S_{ATP}$ state by:

$$\Delta l_{S_0 \to S} = (1.5 - 1.34) * 3 * 0.34 nm = 0.1632 nm$$

The energy difference between the stretched states stemming from our measured dynamic torques then becomes:

$$U_{S_{0\,ATP}} - U_{S_{ATP}} = \Gamma_{dyn\ S_0 \to S\ ATP-Ca^{2+}} \cdot \theta_{hRad51} - F \cdot \Delta l_{S_0 \to S}$$

$$= 16.0 \pm 0.7\, pN.nm$$

(Average on 20 measures with a standard deviation of 2.72pN.nm).

## A.I.1. Does the $S^0_{ATP}$ state exist?

In the literature, there are no previous reports supporting the existence of the null-torsion stretched state $S^0_{ATP}$. For sake of simplicity, we hypothesize that the extension of the $S^0_{ATP}$ state is the result of a hybrid nucleoprotein filament made of hRad51 proteins in the two different states $C$ and $S$. In this framework, the extension $L_{S0\ ATP}$ would be a linear combination of the condensed null-torsion state $C_{ATP}$ and a fully stretched null-torsion state with an extension similar to the unwound stretched $S_{ATP}$ state. Thus a portion $p$ of the proteins in the filament would display a normalized extension of $L_{S\ ATP} = 1.5$ whereas the other $(1-p)$ proteins would display a condensed extension of $L_{C\ ATP} = 1$:

$$L_{S_{0\,ATP}} = p * L_{S_{ATP}} + (1-p) * L_{C_{ATP}} = 1.34 \pm 0.01$$

This hypothesis yields a value of **$p = 0.68 \pm 0.02$**.

At thermal equilibrium, the distribution between both states should obey a Maxwell-Boltzmann statistics. If so, their energy difference is linked to the distribution probability $p$ by:

$$U_{C_{ATP}} - U_{S_{0\,ATP}} = -k_B T \ln\left(\frac{1-p}{p}\right)$$

The energy difference between the $C_{ATP}$ and the $S^0_{ATP}$ states may be deduced from the difference of the two previous measured energy differences stemming from our experimental data:

$$U_{C_{ATP}} - U_{S_{0\,ATP}} = \left(U_{C_{ATP}} - U_{S_{ATP}}\right) - \left(U_{S_{0\,ATP}} - U_{S_{ATP}}\right) = 3.2 \pm 1.3\, pN.nm$$

On the other hand, the energy difference between both states assuming a Maxwell-Boltzmann distribution explaining the extension of the $S^0_{ATP}$ state would be given for a proportion of fully stretched proteins $p = 0.68\pm0.02$:

$$-k_B T \ln\left(\frac{1-p}{p}\right) = 3.10 \pm 0.39 \, pN.nm$$

These values are compatible with the hypothesis of the $S^0_{ATP}$ state being the result of an equilibrium between a fully stretched null torsion state with a extension of $L_S = 1.5$ and the condensed null-torsion state $C_{ATP}$.

## A.I.2. Stability of the state $C_{ATP}$

We measured that the energy associated with the condensed state $C_{ATP}$ is higher than the one associated with the null-torsion stretched state $S^0_{ATP}$. In these conditions, one would expect the filament to change its conformation from $C_{ATP}$ to $S^0_{ATP}$ when the filament is formed on a dsDNA molecule whose supercoiling degree at is kept at σ=0. However no such transitions are observed, the transition between those two conformations requires the nucleoprotein filament to be unwound to the $S_{ATP}$ state before being wound back to σ=0 **[Figure 125]**.

In order to understand this point, we make the simple hypothesis that only the two states $S_{ATP}$ and $C_{ATP}$ exist for the hRad51 protein and that there is no continuous transition between them. In this two-state model, we assume that the energy difference at σ = 0 is the one measured above: **$\Delta U_{S0 \to C} = 3.2\pm1.3$ pN.nm**. A gentle traction on a hRad51 protein in the $C_{ATP}$ state would then not immediately induce the transition to the $S_{ATP}$ state, but only apply an elastic deformation. In the same way, a gentle compression on a hRad51 protein in the $S_{ATP}$ state would put it under stress.
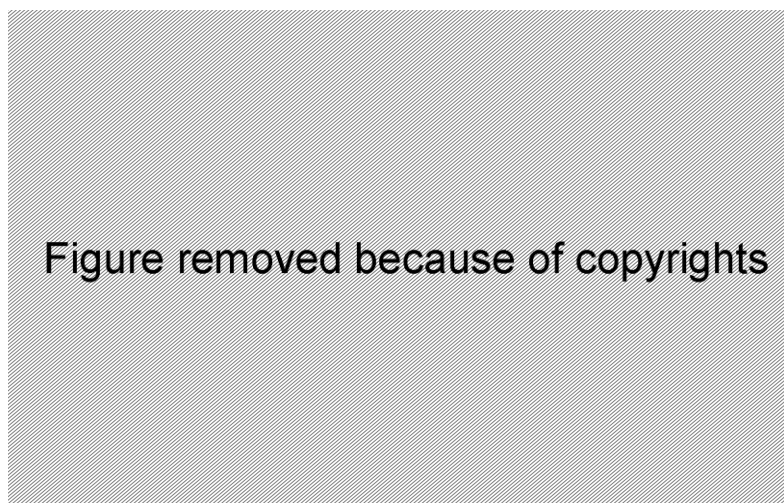


**Figure 148:** Adapted from [136]. Force-extension curve of a continuous zone in a hRad51-dsDNA nucleoprotein filament. This region of the filament is thought to be completely covered by hRad51 proteins; therefore its elastic response is solely due to the filament and not from bare DNA regions. By fitting the data with an elastic response (**red profile**), we estimate the stiffness of one protein in the filament to $k_L = 348\pm25$pN.nm$^{-1}$.

The elastic stiffness of a hRad51-dsDNA nucleoprotein filament may be evaluated using the force-extension curve measured by van Mameren *and al.* [136]. The measure of the extension of a continuous zone of the nucleoprotein filament allows the access to its elastic stiffness without the contribution of any bare DNA regions. By fitting the figure with a linear elastic response **[Figure 148]**, we estimate the stiffness of one hRad51 protein in a hRad51-dsDNA nucleoprotein filament to $k_L = \mathbf{348 \pm 25 pN.nm^{-1}}$.
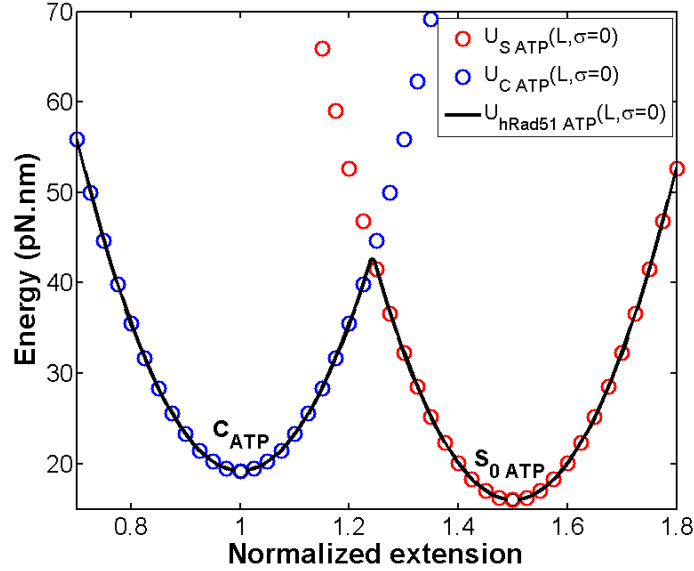


**Figure 149:** Representation of the energy potentials for a hRad51 protein with a bound ATP in the *S* state (**red profile**) and in the *C* state (**blue profile**) for an imposed supercoiling degree $\sigma = 0$. The resulting potential for a hRad51 protein (**black profile**) is the minimum of the $U^S_{ATP}$ and $U^C_{ATP}$ potentials. The resulting barrier is situated at $L=1.24 \pm 0.02$ with a height of $H_B = 23.9 \pm 4.4 pN.nm$ when compared to the minimum of the *C* state.

If both the *S* and the *C* state have a similar compressibility, the energy potentials of the proteins for a given supercoiling degree $\sigma$ may be written as follows:

$$U_S(L,\sigma) = \frac{K_{LU}}{2}(L - L_S)^2 + U_S(L_S,\sigma)$$

$$U_C(L,\sigma) = \frac{K_{LU}}{2}(L - L_C)^2 + U_C(L_C,\sigma)$$

Where $U_S$ and $U_C$ are the energies associated to respectively the *S* and *C* states, $L_S=1.5$ and $L_C=1$ are their normalized extensions and $K_{LU}$ is the normalized stiffness for longitudinal deformations. The value of $K_{LU}$ may be deduced from the previous value of $k_L$ by normalizing it with the square of the extension of a hRad51 protein in the *S* state. This leads to an estimation of $\mathbf{K_{LU} = 816 \pm 60 pN.nm}$. Using these assumptions, we can draw the two elastic potentials of the nucleoprotein filament for a supercoiling degree of $\sigma=0$. We do so assuming that $U_S(L_S,\sigma=0) = 16.0 \pm 0.7 pN.nm$ and $U_C(L_C,\sigma=0) = 19.2 \pm 0.6 pN.nm$ **[Figure 149]**. The resulting potential for the protein is the minimum of both potentials, as the protein will jump from one potential to another as soon the energy of the state it is in is superior to the energy of the other state. For ease of representation, we'll arbitrarily set the energy associated to the stretched state $S_{ATP}$ to zero, which we can do because potential energy is defined up to an additive constant.

We notice that with such a simple assumption, an energy barrier of approximately $6k_BT$ appears midway between the $C$ and $S$ states. This finding is in agreement with the fact that a pulling force up to $F=10pN$ is insufficient to allow transition between those two states. The work gained by passing from the condensed state to the null-torsion state under such a pulling force $F$ can be estimated by:

$$W_{C_{ATP} \to S_{0\,ATP}}(F) = 3bp * 0.34nm * (1.5-1) * F$$

$$W_{C_{ATP} \to S_{0\,ATP}}(10\,pN) = 5.1\,pN.nm$$

Therefore a barrier situated midway between both states would see its height reduced by approximately 2.45pN.nm by the application of such a pulling force. This reduced barrier has to be high enough to prevent passing from the $C$ state to the $S$ state and thus should be higher than 3 to $4k_BT$.

On another hand, we observed that the condensed state in ATP-Ca$^{2+}$ is systematically more extended that the condensed state in ATP-Mg$^{2+}$, the former having a normalized extension of 1.11±0.04 whereas the latter has only an extension of 1.05±0.05. The longer extension in the case of ATP-Ca$^{2+}$ could be due to the thermally activated transition of some proteins to the null-torsion stretched state $S_0$ under the added effect of entropy. This would be impossible if the barrier was much higher than $10k_BT$. Therefore a barrier of $6k_BT$ is reasonable if one is to explain the phenomena we've observed.

However if this barrier is high enough to prevent the passage from the $C$ state to the $S$ state, then it comes logically that the reverse passage for which the barrier is even higher ( $U_S(L=1.5,\sigma=0) < U_C(L=1,\sigma=0)$ ) should also be prevented. This last fact is in apparent contradiction with our hypothesis that the $S^0_{ATP}$ state is a linear combination of both states. This paradox may be resolved by considering that the $S^0_{ATP}$ state may only be reached by increasing the supercoiling degree $\sigma$ from the $S_{ATP}$ state. As such, the protein could be able to jump across the barrier at an intermediate value of the supercoiling degree ($-0.43 < \sigma < 0$) for which the barrier height is lower.

## A.I.3. The ATP-bound hRad51 potential

### The constant torque model

We've seen empirically constant torque transitions between the $C_{ATP}$ and $S_{ATP}$ states and between the $S^0_{ATP}$ and $S_{ATP}$ states. The model we'll propose here will then impose constant torques along the transitions paths and set elastic boundaries if the filament is extended or compressed. Following our previous hypothesis where the extension decrease of the $S^0_{ATP}$ state is due to a linear combination of a fully stretched state and of a condensed state, we'll suppose that the $S^0_{ATP}$ to $S_{ATP}$ transition occurs at constant length of $L_S=1.5$. Therefore, the potential $U_S$ for the stretched states $S$ may be written as follows:

$$U_S(L,\sigma) = \frac{K_{LU}}{2}(L-L_S)^2 + K_{\sigma US}(\sigma - \sigma_S) + U_S(L_S,\sigma_S)$$

Where $K_{LU}$ is the longitudinal elastic stiffness, with a value of $K_{LU}=816\pm60pN.nm$ as calculated before, and $K_{\sigma US}$ is the torsional stiffness between the $S^0_{ATP}$ and $S_{ATP}$ states, deduced from the constant torque we've measured, with a value of:

$$K_{\sigma US} = \frac{U_{S_{0\,ATP}} - U_{S_{ATP}}}{\sigma_{S_0} - \sigma_S} = 37.2 \pm 1.7\,pN.nm$$
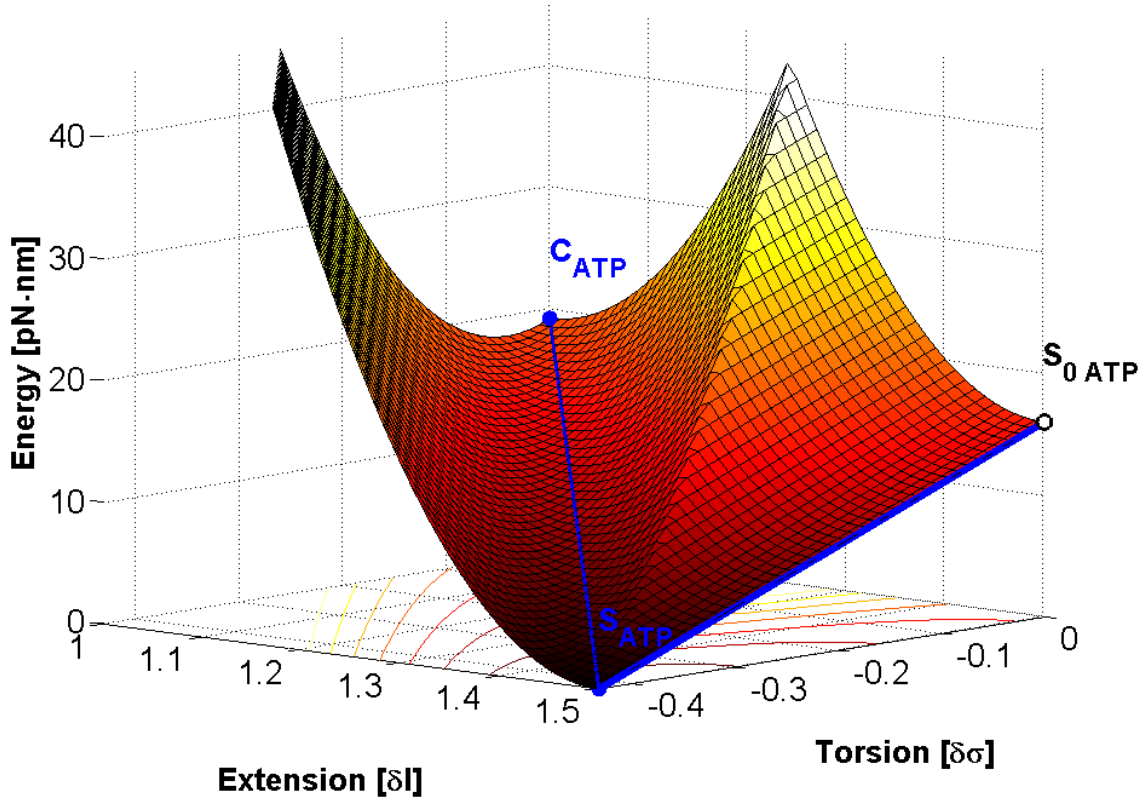


**Figure 150:** Representation of the ATP-bound energy landscape of the hRad51 protein with the hypothesis of constant torque transitions.

For the transition between the $C_{ATP}$ and the $S_{ATP}$ states, we'll assume that the path is a straight line with longitudinal elastic boundaries. Thus the potential for the condensed states $C$ has the following expression:

$$U_C(L,\sigma) = \frac{K_{LU}}{2}\left(L - L_{C_{min}}(\sigma)\right)^2 + K_{\sigma UC}(\sigma - \sigma_C) + U_C(L_C, \sigma_C)$$

Where $K_{LU}$ is the same longitudinal elastic stiffness as for the $U_S$ potential and $K_{\sigma UC}$ is the torsional stiffness between the $C_{ATP}$ and $S_{ATP}$ states, deduced from the constant torque we've measured, with a value of:

$$K_{\sigma UC} = \frac{U_{C_{ATP}} - U_{S_{ATP}}}{\sigma_C - \sigma_S} = 44.7 \pm 1.7\,pN.nm$$

The straight line path imposed between the two states results in the following expression for the minimums $L_{Cmin}$ of longitudinal elastic potentials:

$$L_{C_{\min}}(\sigma) = L_C + \frac{L_S - L_C}{\sigma_S - \sigma_C}(\sigma - \sigma_C)$$

The resulting energy landscape for the ATP-bound hRad51 protein is the minimum of both potentials **[Figure 150]**.

## Energy differences and Maxwell-Boltzmann distribution

In this framework, for a given supercoiling degree σ, the nucleoprotein filament's energy potential presents two local minimums: one for the $U_S$ potential at $L=L_S$ and one for the $U_C$ potential at $L=L_{Cmin}(\sigma)$, exactly like in the previous situation for σ=0 **[Figure 149]**. Thus assuming that the filament is able to cross the barrier between both minimums, the distribution at thermal equilibrium between both states should obey a Maxwell-Boltzmann statistics. Therefore the proportion $p(\sigma)$ of hRad51 proteins that are in the fully stretched state ($L=L_S$) at a given supercoiling degree σ is given by:

$$p(\sigma) = \frac{1}{1 + \exp\left(-\dfrac{U_C(L_{C_{\min}}(\sigma), \sigma) - U_S(L_S, \sigma)}{k_B T}\right)}$$
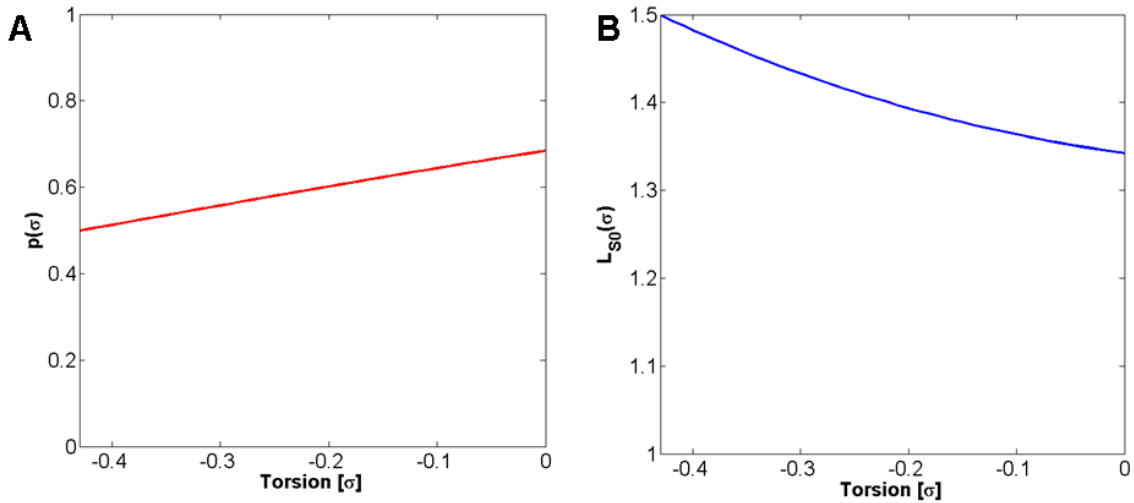


**Figure 151:** Proportion $p$ of hRad51 proteins in the $S$ state stemming from a Maxwell-Boltzmann distribution (**A**) and the resulting normalized extension $L_{S0}$ of the $S^0_{ATP}$ state (**B**) as a function of the supercoiling degree σ.

For this argument, we are working under the assumption that the filament is able to cross the barrier when going through the $S^0_{ATP}$ to $S_{ATP}$ transition. We figure that it may do so because the $S^0_{ATP}$ state may only be reached from the $S_{ATP}$ state where the barrier is very low. Thus a proportion $p$ of the proteins in the filament would display a normalized extension of

$L=L_S=1.5$ whereas the other $(1-p)$ proteins would display a condensed extension of $L=L_{Cmin}(\sigma)$ resulting in an extension $L_{S0\ ATP}$ of:

$$L_{S_{0\ ATP}}(\sigma) = p(\sigma)*L_S + [1-p(\sigma)]*L_{C_{min}}(\sigma)$$

Calculating the proportion $p(\sigma)$ resulting from the energy difference allows us to deduce the extension of the filament during the transition to $S^0_{ATP}$ **[Figure 151]**. We notice that the extension $L_{S0}$ decreases almost linearly from $L=1.5$ at $\sigma=-0.43$ to $L=1.34$ at $\sigma=0$. This linear decrease is coherent with our experimental observations **[Figure 125]** confirming that our hypothesis of a transition to $S^0_{ATP}$ at a constant length of $L=L_S$ is not incompatible with our experimental data.

## A.II. The ADP-bound nucleoprotein filament

We've identified that ADP-bound filaments are able, much like the ATP-$Mg^{2+}$ filaments, to pass from a null-torsion condensed state to an unwound stretched state when the supercoiling degree is imposed **[Figure 127]**. We'll call these two states respectively $C_{ADP}$ and $S_{ADP:}$

- **$C_{ADP}$**: A condensed null-torsion state with a normalized extension of $1.05\pm0.01$ and a supercoiling degree of $\sigma=0$. There is a remarkable similarity of the normalized extension of this condensed ADP-bound state when compared to the one observed in the case of ATP-bound filaments ($C_{ATP}$). We suppose that these states are resulting from the same protein conformation even though the energies associated with each state most probably differ due to the nature of the bound nucleotide. We'll thus assume that the relative crystallographic extension of the $C_{ADP}$ state is 1, like for $C_{ATP.}$

- **$S_{ADP}$**: A stretched unwound state with a normalized extension of $1.49\pm0.04$ and a supercoiling degree of $\sigma=-0.43$. Much like for the condensed state, we propose that this state $S_{ADP}$ is actually the same as the stretched one in ATP ($S_{ATP}$) apart from the nature of the bound nucleotide. It is probably measured shorter as a result of a number of proteins within the filament contracting in their effort to reach a more condensed state despite the imposed supercoiling degree. For this reason we'll assume in the following argumentation that its normalized extension is also of 1.5 as for $S_{ATP.}$

### A.II.1. Existence of an intermediate state $M_{ADP}$?

The formation in ADP of hRad51-dsDNA nucleoprotein filaments has already been studied by other teams. In TIRFM experiments [131] and in optical tweezers [135], filaments formed in ADP on unconstrained dsDNA molecules were found to have an extension of respectively 1.04 and 1.07 with pulling forces of $0.6\pm0.1pN$ and $0.9\pm0.1pN$. These extensions corroborate well with our measured normalized extension of $1.05\pm0.01$ for the condensed state in ADP ($C_{ADP}$).

In both these experiments, the supercoiling degree was left free to evolve. Our experiments involving spontaneous elongation in ADP **[Figure 138]** were thus conducted in similar conditions. However we obtained very different results. Our experiments seemed to suggest a stable intermediate conformation with a normalized extension of 1.20±0.02. We did not verify this surprising result to our satisfaction and do not understand why the presence of unbound hRad51 proteins in solution would change the length of the stable conformation to 1.32±0.02. We do know that partial depolymerization is not solely the reason for this state shorter than the extended $S_{ADP}$ state because of the filament extension triggered by the insertion of ATP nucleotides.

This intermediate extension of 1.20 is compatible with the ones obtained when ATP is left to hydrolyze inside the filaments in TIRFM experiments conducted by Robertson *and al.* [119] or in optical tweezers experiments conducted by Hilario *and al.* [135]. They showed that ATP-bound filaments contracted to extensions of 1.25 in TIRFM, 1.26 for the fluorescent hRad51 and 1.16 for the wild-type protein in optical tweezers, with pulling forces of $F$=0.6±0.1pN for the TIRFM experiments and $F$=0.9±0.1pN in the optical tweezers.

Thus there seems to be two different stable ADP bound conformations:

- $\mathbf{C_{ADP}}$: A fully condensed conformation attainable by forming hRad51-dsDNA filaments directly on unconstrained DNA molecules or by imposing the supercoiling degree to σ=0 in our torsion-extension experiments.

- $\mathbf{M_{ADP}}$: A partially condensed conformation attainable by allowing hydrolysis in unconstrained ATP-bound filaments or by imposing the supercoiling degree σ = -0.12±0.03 in our torsion-extension experiments[1]. Its normalized extension is of 1.20±0.02 (relative crystallographic extension of 1.14±0.03).

The history of the nucleoprotein filament seems to be determinant for the final conformation. This difference of behavior between ADP-bound filaments and hydrolyzed ATP-bound filaments is well illustrated within the same set of experiments conducted by Hilario *and al.* **[Figure 58]**.

On one hand, those findings indicate that the condensed states $C_{ADP}$ and $M_{ADP}$ are energetically more stable than the stretched state $S_{ADP}$:

$$ U_{C_{ADP}} < U_{S_{ADP}} \quad \text{and} \quad U_{M_{ADP}} < U_{S_{ADP}} $$

On the other hand, the *history dependency* suggests that the transition $S_{ADP} \rightarrow C_{ADP}$ is not direct and the protein may be stuck in an intermediate state $M_{ADP}$. The natural question is whether $M_{ADP}$ is a new conformational state of the nucleoprotein filament ($U^M_{ADP} < U^C_{ADP}$) or if there is a local minimum $U^M_{ADP}$ in the energy landscape between $S_{ADP}$ and $C_{ADP}$ ($U^C_{ADP} < U^M_{ADP}$).

---

[1] Surprisingly in our experiments, the $M_{ADP}$ state was attained by forming nucleoprotein filaments in ADP-$Mg^{2+}$ on unconstrained dsDNA molecules with a pulling force of 8pN and evacuating unbound proteins from solution.

Interestingly van Mameren *and al.* **[Figure 56]** have shown that the dissociation rate k depends exponentially on the tension *F* applied to the nucleoprotein filament.

$$k(F) = k(0)\exp\left(-\frac{x_B F}{k_B T}\right) \quad \text{with} \quad x_B = 0.27 \pm 0.04 nm$$

In which *k(F)* is the decrease rate and $k_B T$ is the thermal energy. This *Arrhenius-like* law suggests the presence of a single energy barrier, between the two states. This barrier is situated at a distance $x_B$ from the stretched state. In normalized extension, it becomes:

$$l_{Barrier_{norm}} = (1.02nm*1.5 - x_B)/1.02nm = 1.24 \pm 0.04$$

Thus, its presence may occasion a local minimum in the energy landscape, between the two states $S_{ADP}$ and $C_{ADP}$. Admitted that after ATP hydrolysis the stable conformation is the compact state, the nucleoprotein filament would not undergo the S→C transition spontaneously and would get stuck in this local minimum.

In this framework, the $M_{ADP}$ state would not correspond to a structural conformation of the nucleoprotein filament, but more likely to a $S_{ADP}$ conformation under compression. Eventually, we know that the barrier can be overtaken by forcing the topology of nucleoprotein filament to σ=0.

## A.II.2. Energy difference between $C_{ADP}$ and $S_{ADP}$

To characterize the energies involved for the ADP-bound filament, we'll use the results produced by van Mameren *and al.* [137] in correlation with ours. Their results **[Figure 56]** show that they stalled protein dissociation by applying a pulling force of 48±3pN on the extremities of the filaments. All previous studies suggest that ATP hydrolysis precedes protein dissociation. Furthermore, the ATP hydrolysis rate did not seem to be dependent of the pulling force applied. We think it therefore reasonable to assume that the protein was stalled in this case because the proteins were kept in the stretched ADP state by the pulling force. This relies on the assumption that protein dissociation occurs from the condensed ADP state. If so, then the measure of the stalling pulling force gives us a measure of the energy difference between those two states.

There is an extension difference of $\Delta l = 0.51$nm per protein between the stretched $S_{ADP}$ and the condensed $C_{ADP}$ states. Taken together with a pulling force of 48pN to stall dissociation, we get an energy difference equal to:

$$U_{S_{ADP}} - U_{C_{ADP}} = 48 \pm 3pN * 0.51nm = 24.48 \pm 1.53 pN.nm$$

## A.II.3. Plotting the ADP-bound hRad51 potential

We now have a value for the energy difference $U^S_{ADP}$ - $U^C_{ADP}$ which we will try to use in order to draw the ADP-bound energy potential of the hRad51-dsDNA nucleoprotein filament. We'll hypothesize here that the hydrolysis of the ATP nucleotide into ADP releases

the elastic energy of the dsDNA molecule. In this framework, the ADP-bound energy would be derived from the ATP-bound potential by the addition of the dsDNA molecule's elastic potential energy. The dsDNA molecule would then strive to reach its natural B-DNA state at $\sigma = \sigma_C = 0$ and $L = L_C = 1$, therefore the expression of its potential energy would be:

$$U_{spring}(L,\sigma) = \frac{k_L}{2} \cdot (L - L_C)^2 + \frac{k_\sigma}{2} \cdot (\sigma - \sigma_C)^2 + U_{spring}(L = L_C, \sigma = \sigma_C)$$

Where $U_{spring}$ is the elastic potential energy of the dsDNA molecule, $k_L$ its stiffness in extension and $k_\sigma$ its stiffness in rotation. For the sake of the argument, we will assume that this spring is homogeneous ($k_L = k_\sigma = k_{spring}$):

$$U_{spring}(L,\sigma) = \frac{k_{spring}}{2} \cdot \left( (L - L_C)^2 + (\sigma - \sigma_C)^2 \right) + U_{spring}(L = L_C, \sigma = \sigma_C)$$

Furthermore, for the construction of the potential, we'll consider that $U^S_{ATP} = U^S_{ADP} = 0$, which just comes down to defining both the ATP and ADP-bound potentials relatively to the energy of the stretched conformations. This second assumption leads to the two following conclusions. First the energy minimum of the spring's potential energy is defined by the difference in energy between both condensed states:

$$U_{spring}(L = L_C, \sigma = \sigma_C) = U_{C_{ADP}} - U_{C_{ATP}}$$

$$= \left( U_{C_{ADP}} - U_{S_{ADP}} \right) - \left( U_{C_{ATP}} - U_{S_{ATP}} \right) = -43.68 \pm 2.13\, pN.nm$$

Second, the spring's stiffness $k_{spring}$ is imposed by the fact that the elastic energy at the stretched conformation is null:

$$U_{spring}(L = L_S, \sigma = \sigma_S) = 0$$

$$\Rightarrow k_{spring} = -2 \frac{U_{spring}(L = L_C, \sigma = \sigma_C)}{(\sigma_S - \sigma_C)^2 + (L_S - L_C)^2} = 201 \pm 10\, pN.nm$$

With these assumptions, we may now draw the energy potential for the ADP-bound filament from the expression for the ATP-bound filament through the following transformation:

$$U_{ADP}(L,\sigma) = U_{ATP}(L,\sigma) + U_{spring}(L,\sigma)$$

Where $U_{ADP}$ is the potential energy for the ADP-bound nucleoprotein filament, $U_{ATP}$ is the previously proposed potential energy for the ATP-bound filament and $U_{spring}$ is the elastic energy of the dsDNA molecule. The modeling of such an energy potential is plotted in [**Figure 152**].
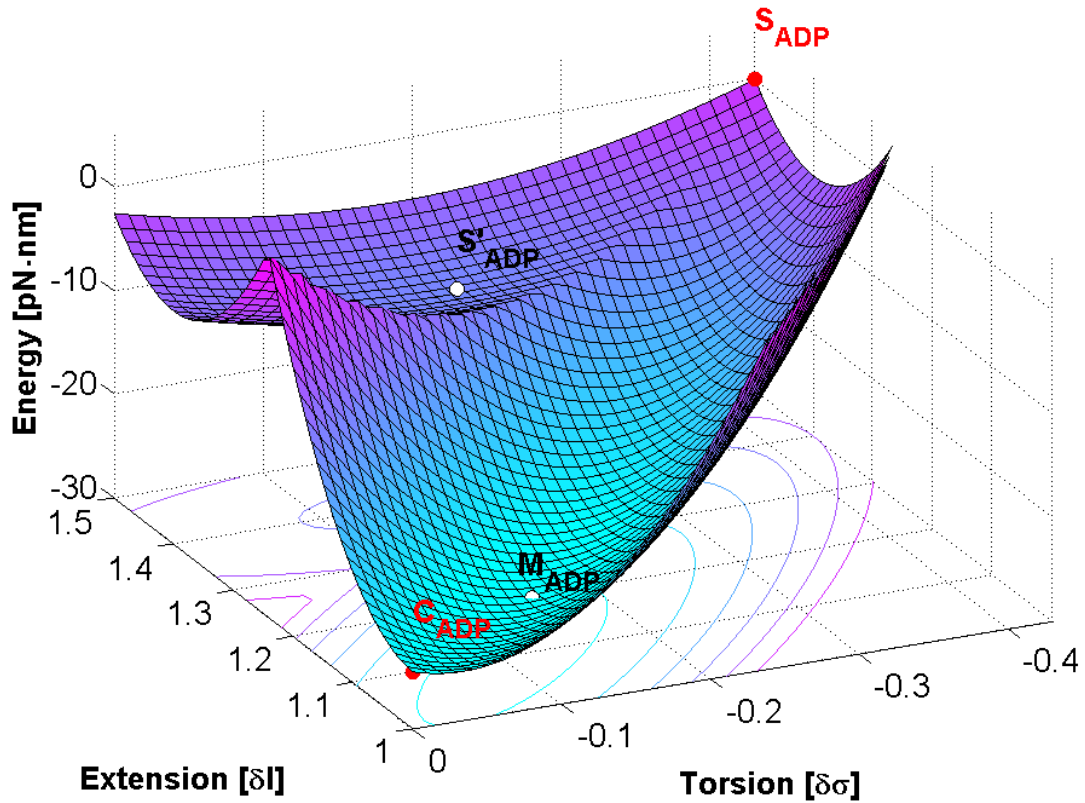
**Figure 152:** Representation of the ADP-bound energy landscape of the hRad51 protein derived from constant torque transitions and from an added spring energy centered on the natural state for B-DNA ($L=1,\sigma=0$).

## A.II.4. Validity of the model

### The DNA molecule's elastic energy

Due to the arbitrary nature of certain of our assumptions in constructing this energy landscape, the model proposed here for the ADP-bound potential is qualitative at best. However the hypothesis that the dsDNA molecule acts as a spring would explain the behavior of hRad51-ssDNA nucleoprotein filaments formed in ADP. It has been reported [128] that those filaments display an intermediately condensed extension (helical pitch of 76Å which converts into a normalized extension of $L=1.16$ if compared to the length of a dsDNA molecule in its B-DNA form). Contrarily to what happens with hRad51-dsDNA filaments, the contraction of the ssDNA filaments occurs without modifying the helicity (6.43 hRad51 proteins per helical turn which converts to $\sigma=-0.46$ if compared to the torsion of dsDNA in its B-DNA form). This helicity is similar to the one found in hRad51-dsDNA filaments in ATP-bound conformations (6.39 hRad51 proteins per helical turn for filaments formed in ADP-AlF$_4^-$ [128] and 6.4 hRad51 per turn in AMP-PNP [127]). This contraction could then be explained by the elastic energy contained in the ssDNA molecule much as is the case with dsDNA. However since no torsional elastic energy is contained in ssDNA, there is no reason why the helicity would be modified.

We assume in this argument that the helicity of ADP-bound hRad51-dsDNA filaments is modified in condensed conformations because of the correlation between the supercoiling degree and the extension that we have observed in our experiments.

## Energy minimums

In our model, we observe the apparition of a local minimum for a stretched conformation [**S'$_{ADP}$ in Figure 152**] found at an extension of $L = 1.4$ and $\sigma = -0.185$. An energy minimum [**M$_{ADP}$ in Figure 152**] is also found at an extension of $L = 1.1$ and $\sigma = -0.11$. The extension and torsion of this energy minimum is compatible with the intermediate condensed state M$_{ADP}$. However, in this framework, no barrier prevents the passage from the C$_{ADP}$ to the M$_{ADP}$ state whose energy is lower (U$^C_{ADP}$ - U$^M_{ADP}$ ≈ 2.31pN.nm with our numeric values). In this our model is in contradiction with the existing literature because hRad51-dsDNA filaments formed in ADP would then be expected display the extension of the M$_{ADP}$ state. It is however coherent with our results in ADP [**Figure 138**] where the extension of ADP filaments is found to be 1.20 (1.14 in relative crystallographic extension). We did not however verify this result sufficiently to be confident enough to contradict several other experiments conducted by others teams.

## The energy barrier
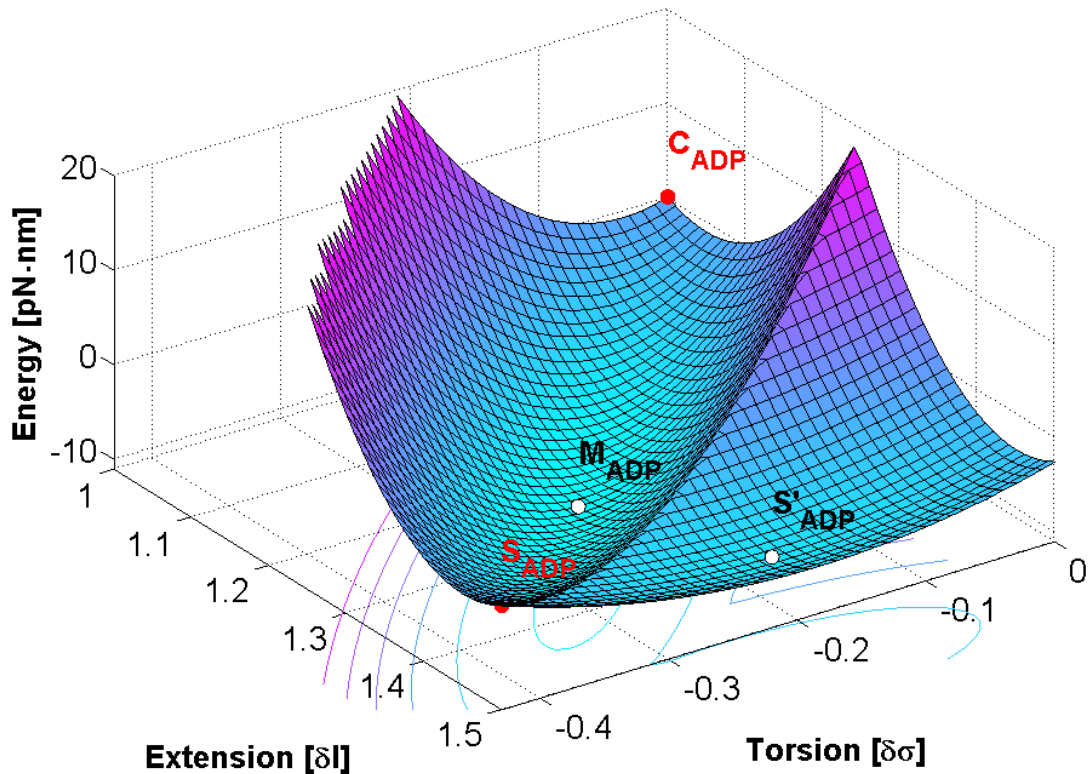


**Figure 153:** Representation of the ADP-bound energy landscape of the hRad51 protein under a pulling force of $F$=48pN.

Furthermore, our model would not explain the previously discussed barrier observed by van Mameren *and al* since there is no barrier between the S$_{ADP}$ and M$_{ADP}$ states. This last matter can nonetheless be explained in our model's framework. In their experiment, the torsion of the filament is left free to evolve which means the filament will naturally adopt a conformation corresponding to an energy minimum. Their filament is originally formed in ATP-Ca$^{2+}$ resulting in a stretched ATP-bound conformation which would correspond to the S$_{ATP}$ state. Hydrolysis of the ATP nucleotides within the filament is then allowed by transferring the filament in a buffer containing no free nucleotides and Mg$^{2+}$ cations. As the

hydrolysis occurs, part of the filament contracts resulting in a building up of an extreme tension at the extremities of the filament up to a pulling force of $F=48\pm3$pN at which protein dissociation is stalled. The energy potential under such a pulling force would then be within our framework as represented in [**Figure 153**]. In this energy potential, a significant portion of the hRad51 proteins in the filament would then adopt the conformation corresponding to the local minimum of $S'_{ADP}$. Since the energy of the $S'_{ADP}$ conformation is lower than the energy associated with the $S_{ADP}$ state ($U^S_{ADP} - U^{S'}_{ADP} \approx 9.8$pN.nm in the absence of pulling force), upon tension release, the proteins in the $S'_{ADP}$ would then have to cross the barrier between the stretched and the condensed states to reach $M_{ADP}$. The position of this barrier goes from $L=1.5$ at $\sigma=-0.43$ to $L=1.24$ at $\sigma=0$ with a minimum in height at $L=1.38$ and $\sigma=-0.24$. This phenomenon would explain why a barrier is observed for protein dissociation in van Mameren *and al*'s experiment.

## Passage of the barrier at σ=0

We know from our experiments that filaments may not pass from the $C_{ATP}$ to the $S^0_{ATP}$ state (which has a lower energy) without changing the supercoiling degree [**Figure 125**]. We've explained this phenomenon by the presence of a barrier of ~$6k_BT$ in between both states preventing such a passage [**Figure 149**]. Furthermore, we've observed that filaments that are maintained in the $S^0_{ATP}$ state by imposing a supercoiling of $\sigma=0$ go through a slow transition from $S^0_{ADP}$ to $C_{ADP}$ as soon ATP hydrolysis is allowed [**Figure 132**]. This last result suggests that ATP hydrolysis drastically modifies the energy difference between the stretched and condensed states at $\sigma=0$. Indeed in the framework of our model, the energy of the condensed state $C_{ADP}$ is significantly lower than that of the stretched state [**Figure 154**]. The height of the energy barrier in between both states is also greatly reduced to ~$3k_BT$. This value for the barrier height (when compared to the $S^0_{ADP}$ state) is still quite high but should allow passage between the both states. Its relatively high value would explain why the transition to $C_{ADP}$ occurs slowly.
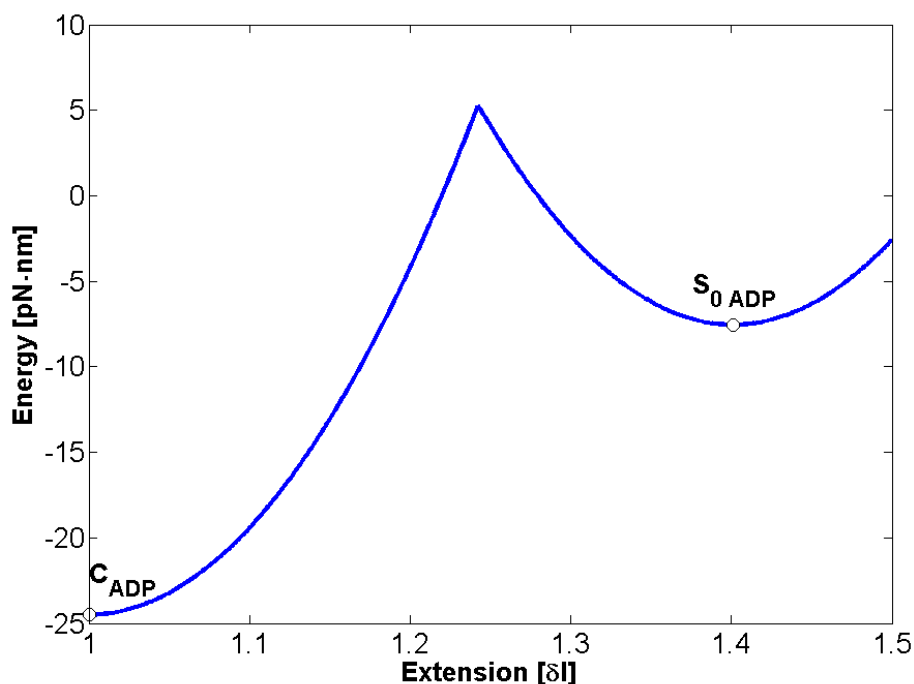


**Figure 154:** Representation of the ADP-bound potential for an imposed supercoiling degree of σ=0.

# Maxwell-Boltzmann distribution and extension

Much as we have done previously for the ATP-bound filaments, we hypothesize that the extension of ADP-bound filaments for a given supercoiling degree is the result of a Maxwell-Boltzmann distribution between a stretched state and a condensed state. The extensions of these states for a given supercoiling degree are defined by the local energy minimums of the potential as shown in [**Figure 152**]. Therefore if $p(\sigma)$ is the proportion of proteins in the stretched state, this proportion decreases as the supercoiling increases as a result of an increasing energy difference between the stretched and condensed states [**Figure 155; A**]. The resulting length for the ADP-bound filament decreases almost linearly from $L\approx1.4$ at $\sigma$=-0.43 to $L\approx1$ at $\sigma$=0 **Figure 155; B**]. These conclusions are compatible with the slightly reduced extensions found both for the $S_{ATP}$ state in ATP-Mg$^{2+}$ ($L$=1.531±0.014 in ATP-Mg$^{2+}$ versus $L$=1.552±0.014 in ATP-Ca$^{2+}$) and for the $S_{ADP}$ state ($L$=1.487±0.033 at $\sigma$=-0.43 in ADP).
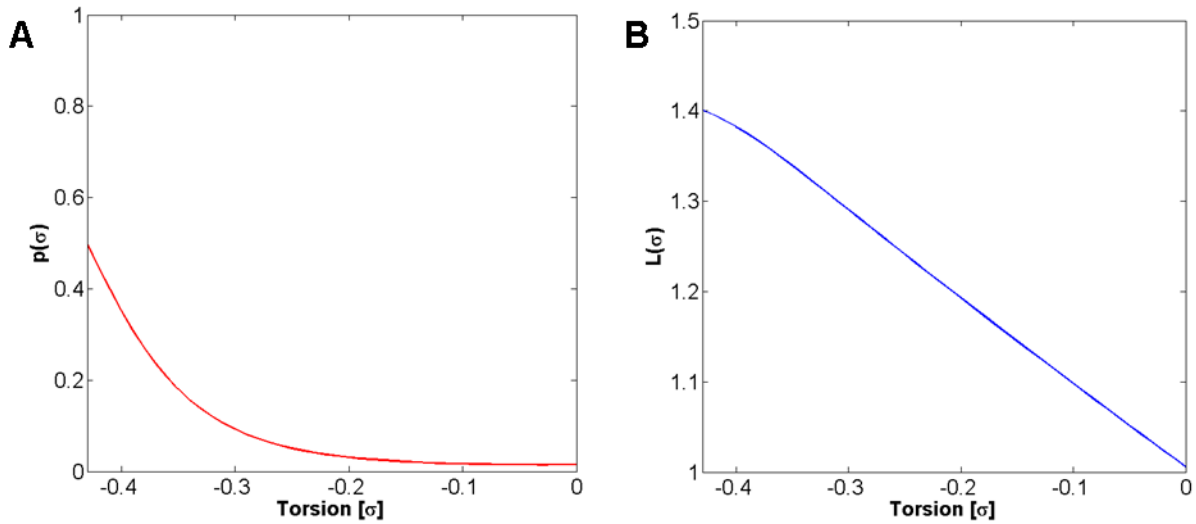


**Figure 155:** Proportion $p$ of hRad51 proteins in the $S$ state stemming from a Maxwell-Boltzmann distribution (**A**) and the resulting normalized extension $L$ of the ADP-bound filament (**B**) as a function of the supercoiling degree $\sigma$.

# B. Steric effect for the filament

This section is dedicated to the consideration of the steric effects for different filament conformation which we have considered possible based on our results in magnetic tweezers. We will focus especially on two structures which are currently unobserved in existing literature: the null-torsion condensed structure $C_{ADP}$ and the null-torsion stretched structure $S^0_{ATP}$.

## B.I. Resolved structures

### B.I.1. The stretched conformation

These structures were previously presented in **[Chapter1.C.II]**. The available 3D-reconstructions stemming from electron microscopy yield the structures of the stretched hRad51 filaments formed on ssDNA with ADP-AlF$_4^-$ [128] and on dsDNA in AMP-PNP [127]. Those structures showed respectively 6.39 and 6.4 hRad51 proteins per helical turn with helical pitches of respectively 99Å and 100Å. Assuming of stochiometry of 3 base pairs per protein, one can convert these values into normalized extensions and supercoiling degrees in order to compare them with our results. The structures will be compared to the parameters for the B-form of dsDNA even when the substrate is ssDNA. Therefore we have for the structure on ssDNA with ADP-AlF$_4^-$:

$$\sigma_{ssDNA\ ADP-AlF_4^-} = \frac{10.5bp/turn}{3bp*6.39hRad51/turn} - 1 \approx -0.45$$

$$L_{ssDNA\ ADP-AlF_4^-} = \frac{9.9nm/turn}{3bp*0.34nm*6.39hRad51/turn} \approx 1.52$$

Similar values are obtained for the structure on dsDNA with AMP-PNP:

$$\sigma_{dsDNA\ AMP-PNP} \approx -0.45$$

$$L_{dsDNA\ AMP-PNP} \approx 1.53$$

With a supercoiling degree of σ=-0.45 and normalized extensions around 1.5, these structures correspond to the unwound stretched state $S_{ATP}$ we have observed and measured in our experiments. For experimental reasons, the structures in electron microscopy were achieved by using non-hydrolysable analogs of ATP; the similarities of the values obtained and results from our experiments **[Figure 126; B]** demonstrate that this difference has little to no effect on filament extension and torsion. Furthermore, the stretched conformation seems to exist with very similar parameters on both ssDNA and dsDNA substrates. This stands to

reason when one considers that in the homologous recombination process, the joint molecule conformation needs to host three strands of DNA in order to conduct the homology search. Unwinding and stretching the dsDNA and the ssDNA molecules to the same extent will allow to easily insert the third strand into the double-stranded structure for sequence comparison. This ATP-bound structure is widely believed to be the active form of the nucleoprotein filament.

## B.I.2. A condensed conformation?

Another more condensed structure was resolved by electron microscopy on ssDNA with ATP-γS [128]. This structure displayed 6.43 hRad51 proteins per turn and a helical pitch of 76Å. Converted into normalized values, it yields:

$$\sigma_{ssDNA\ ATP-\gamma S} \approx -0.46$$

$$L_{ssDNA\ ATP-\gamma S} \approx 1.16$$

With a normalized extension of 1.16, this structure makes us think of the intermediately stretched conformation found for hydrolyzed ATP-bound filaments. This is surprising, first because the structure was obtained using a non-hydrolysable analog of ATP, and secondly because the supercoiling degree of -0.46 doesn't even come close to the value of σ=-0.12±0.03 that we've measured for this structure on dsDNA.

Since very similar structures were found for filaments formed with ADP, this structure was thought to be the condensed ADP conformation on ssDNA. It is however possible that the authors suffered from the same problem we've encountered during our experiments while forming filaments in ADP. Since we have not yet solved the problem for ourselves, we are unfortunately unable to shed more light on this matter.

# B.II. Extrapolating other structures

## B.II.1. The condensed state C$_{ADP}$

Our results seem to suggest that the stretched states S$_{ATP}$ and the condensed state C$_{ADP}$ are in fact allosteric form of the same dsDNA-hRad51 complex. To conserve the stochiometry between those states, the filament must be able convert from an extended helix with ~19.2 base pairs per 100Å pitch to a B-DNA-like helix with ~10.5 base pairs per 36Å pitch. Hence the filaments would need to change from a structure with ~6.4 hRad51 monomers per 100Å pitch to a structure with ~3.5 hRad51 monomers per 36Å pitch. Such a change would require ~52% increase in the linear density of filaments. Furthermore, if one is to conserve the protein to protein distance in the 3D-space, the diameter of the helix is then reduced by roughly 40%. This results in a protein density in the condensed state which is 4 to 5 times higher than in the stretched state. The question whether such a conformation is possible in consideration of steric effects is the focus of this section.
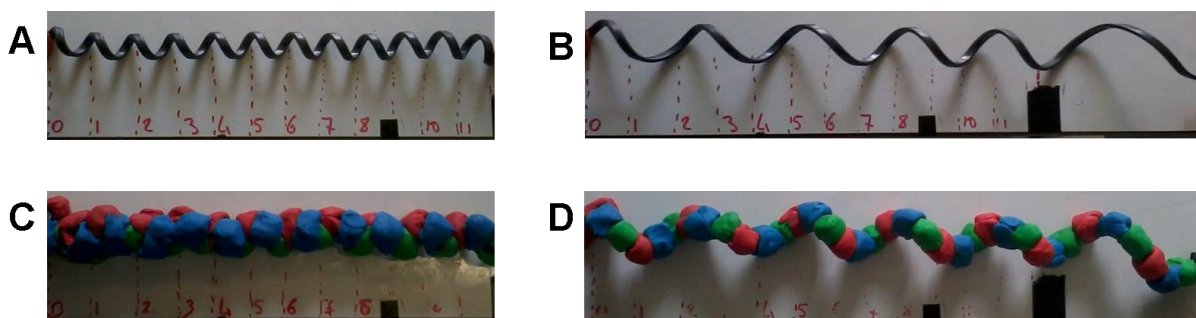
# Playing with modeling clay



**Figure 156:** Simple model using modeling clay and a right-handed telephone wire to illustrate the differences between the stretched unwound state $S_{ATP}$ and the null-torsion condensed state $C_{ADP}$. Our fictional dsDNA has originally 12 turns in its B-form with a normalized extension of 1 (**A**). If unwound to σ=-0.5 and extended to an extension of 1.5, the structure is then comprised of 6 turns and the helical pitch is multiplied by 3 (**B**). The structure of the nucleoprotein filament in the $S_{ATP}$ state thus has 6 turns each containing 6 hRad51 proteins (lumps of modeling clay) (**D**). In order to conserve the stochiometry when forming the $C_{ADP}$ state, the structure must have 12 turns each containing 3 hRad51 proteins (**C**). The linear density increases by 52% and in order to conserve the protein to protein distance, the diameter of the helix is reduced by roughly 40%. Overall, the protein density is multiplied by approximately 4.6.

In an attempt to elucidate the matter, we've considered a naïve 3D model involving a right-handed helix formed by a telephone wire on which are latched lumps of modeling clay standing for the monomers of hRad51 **[Figure 156]**. In order to keep the model pertinent, we've tried as much as possible to keep the model to scale. The telephone wire being inelastic, it naturally conserves the protein to protein distance along the curve of the molecule.

We've chosen a model dsDNA molecule formed of 12 helical turns. The unwound stretched state was chosen for the sake of simplicity with a supercoiling of σ=-0.5, which corresponds to 6 turns in the molecule, and a normalized extension of 1.5. To form the stretched unwound hRad51-dsDNA nucleoprotein filament in the $S_{ATP}$ state, 6 proteins were positioned on each of the 6 helical turns of the unwound and stretched DNA molecule. Winding the filament back to σ=0 in these conditions naturally results in its contraction. The end result is a highly dense structure where the lumps of clay are compressed by one another in order to make room for the others. This simple model tells us that if the structure is possible, it is obviously pushing limits of what is allowed sterically. This highly dense structure would explain why electron microscopy images of the condensed state seem stressed and display much less regular structures than the stretched states **[Figure 118]**.



**Figure 157:** Modeling clay model of one helical turn of the stretched unwound state $S_{ATP}$ (**A**) and of two helical turns of the null-torsion condensed state $C_{ADP}$ (**B**).

Another aspect to consider is modification of the angle between one protein and the next. A simple calculation yields that in the stretched state, the angle between the proteins is of ~56° whereas the angle imposed by the theoretical $C_{ADP}$ state would be of ~103°. Such an

angle would require a great flexibility of the filament for the sections comprised in between the proteins **[Figure 157]**.

## 3D modeling

The simple modeling clay model obviously has its limitations as it does not take into account the size and shape of the hRad51 proteins. In order to get a better idea of the steric effects, we've resorted to 3D-modeling using the 3D-reconstruction stemming from electron microscopy of a hRad51-ssDNA filament formed with ADP-AlF$_4^-$ **[Figure 158; A]**. The size and shape of a hRad51 monomer was thus approximated to scale to a 3D object roughly 3nm wide, 3.4nm thick and 6.3nm high **[Figure 158; B]**. The helical parameters were both measured on the 3D reconstruction and taken from the provided values in the article [128]. As a control, we reproduced the structure of the unwound stretched state S$_{ATP}$ **[Figure 158; C]**; the result is not perfect but should be sufficient for our purpose.
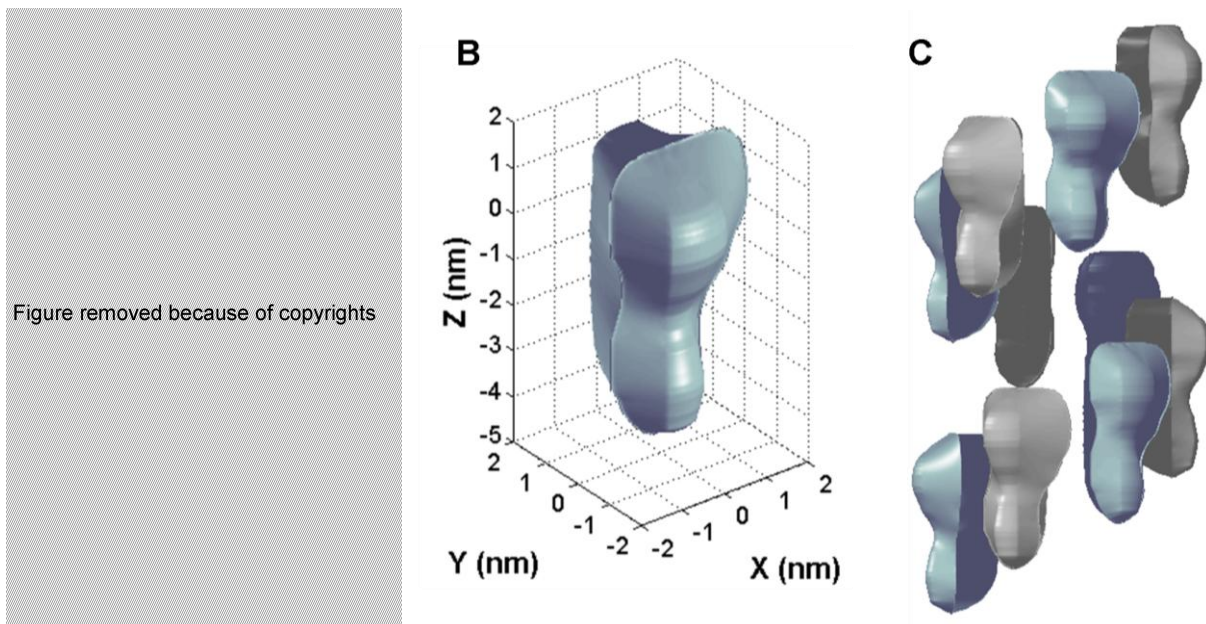


**Figure 158:** The image in (**A**), adapted from [128], shows the structure of a hRad5-ssDNA filament when in the ATP-bound stretched state S$_{ATP}$. The shape of the protein (**B**) was approximated from this structure on which the helical parameters were measured to reproduce the structure in 3D (**C**).

We then used the deduced protein shape to construct our theoretical null-torsion condensed state C$_{ADP}$ **[Figure 159]**. This structure has an extension and a twist equal to a dsDNA molecule in its B-form. As such, it contains 10.5 base pairs per helical turn which corresponds to 3.5 hRad51 monomers if a stochiometry of 3 base pairs per protein is considered. Its helical pitch is of 10.5bp*0.34nm = 3.57nm. The diameter of the helix was deduced from the one in the S$_{ATP}$ state by imposing a constant distance between the monomers along the strands of the DNA molecule. Hence the diameter of the helix for the S$_{ATP}$ state was of D$_S$=7.61nm and the helix diameter of the C$_{ADP}$ state was D$_C$=4.76nm.

Intuitively from the modeling clay model, we thought that the thickness (Y direction) of the protein be problematic for the formation of the condensed structure because of the reduced helix diameter. However observing our model from a top view **[Figure 159; B]** and from a rear view **[Figure 159; C]** shows us that there should be more than enough space to accommodate the proteins into this smaller helix. In fact, from this model it becomes apparent

that the main obstacle to the realization of this structure resides with the pendular lobes of the proteins. This lobe lodges itself in between the main bodies of the two neighboring proteins located on the helical turn below it. With our chosen parameters, the lobe partially co-exist in the same 3D space as the main bodies of the two neighbors which of course is a physical absurdity. Therefore for the structure to be possible, these lobes would have to be pushed out of the way.
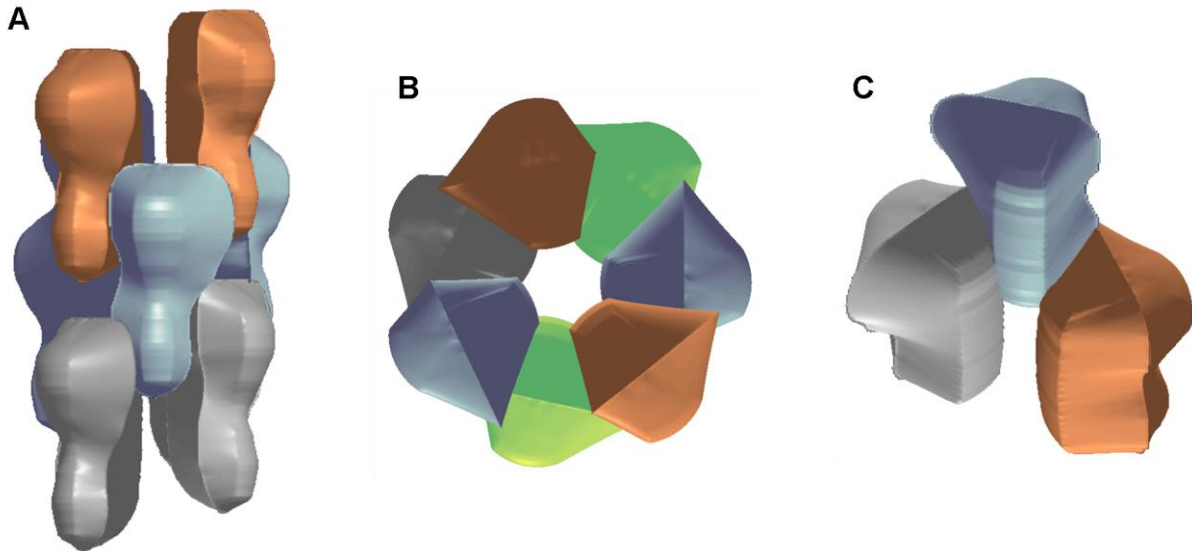


**Figure 159:** Model of the theoretical structure for the null-torsion condensed state $C_{ADP}$ (**A**). The same structure is viewed from the top (**B**) and from the rear with only one protein with its two neighbors from the below helical turn (**C**).

The model of the structure we've constructed was achieved by using the shape of the hRad51 protein in its ATP-bound state. In conditions where ATP hydrolysis is allowed or when the filament is formed in ADP, it has been shown that main difference in the shape of the protein is a shift of the pendular lobe [**Figure 29**]. This shift could be enough to accommodate the new condensed $C_{ADP}$ structure. At the very least, it shows that these lobes are capable of flexibility which is dependent on the state of the bound nucleotide. In the end, this condensed structure could be possible, but a more detailed and perhaps less naïve study of the matter is required to get a definite answer.

## B.II.2. The null-torsion stretched state $S^0_{ATP}$

The second unobserved structure our results seemed to suggest is the null-torsion stretched state $S^0_{ATP}$. As with the condensed structure, the filaments could reversibly convert from $S_{ATP}$ to $S^0_{ATP}$ and vice-versa. If so the structure should contain the same number hRad51 proteins as in the unwound stretched state. This structure should have the same twist as B-DNA and should thus be similar to the $C_{ADP}$ structure except for the helical pitch and the helix diameter. The relative crystallographic extension of this new state is 1.34±0.01, this corresponds to a helical pitch of 4.78±0.04nm. Imposing a constant protein to protein distance yields a helix diameter of $D_{S0}$=4.37nm.

As before, we used these parameters to construct a theoretical 3D model of the structure [**Figure 160**]. The pendular lobes in this configuration no longer pose a problem due to the increased helical pitch. A top and rear views show no major obstacle for the placement of

the proteins in this even smaller helix. Sterically, we see no reason why this structure couldn't exist. Choosing a relative crystallographic extension of 1.5 instead of 1.34, such as we have previously hypothesized, yields similar results (data not shown). The question then becomes whether or not the nucleoprotein filament is flexible enough to allow for such a conformation.



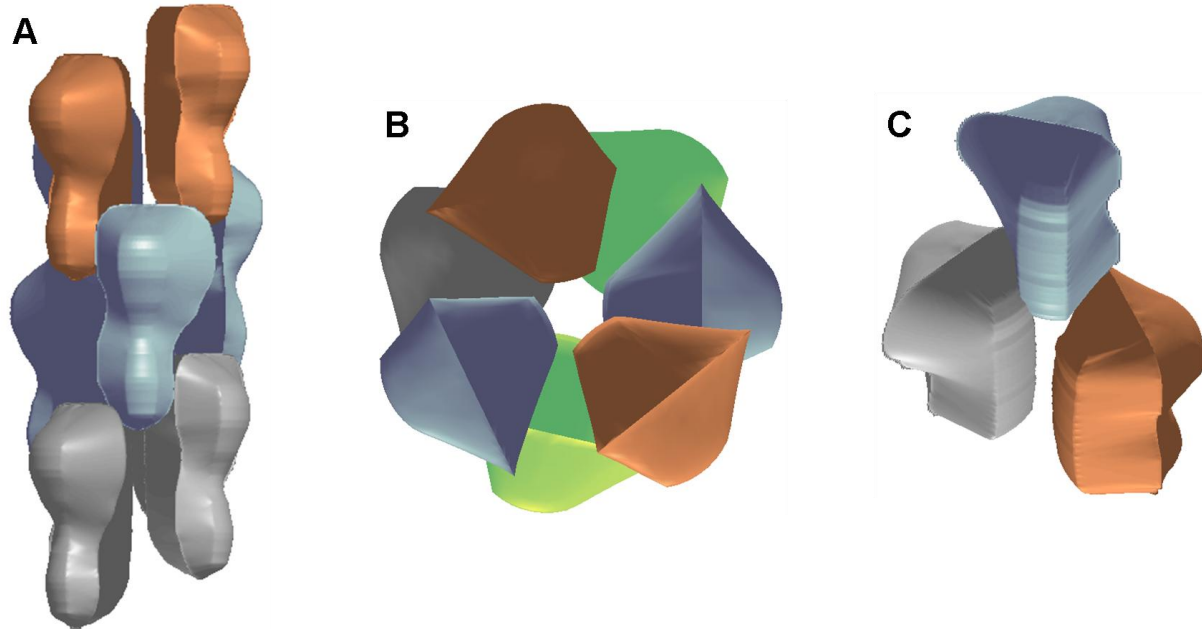**Figure 160:** Model of the theoretical structure for the null-torsion stretched state $S^0_{ATP}$ (**A**). The same structure is viewed form the top (**B**) and from the rear with only one protein with its two neighbors from the below helical turn (**C**).

# Conclusion

We have studied the hRad51 protein using two different types of magnetic tweezers. Our main conclusion is that the response of hRad51-dsDNA nucleoprotein filaments in extension is function only of the imposed supercoiling degree as long as ATP hydrolysis is allowed. This implies that the transitions are actually conversions of the filament from one conformation to another, all containing the same number of proteins and thus probably conserving the base pairs per protein stochiometry. The behavior of the filaments varies depending on the nature of the cofactors. It is our belief that only the nature of the bound nucleotide matters; the nature of the cation cofactor only has an effect on the ability of the protein to hydrolyze ATP. By measuring the torques associated with the different transitions, we explain this difference in behavior through the unlocking of the elastic energy of the dsDNA molecule by the hydrolysis of the ATP nucleotides within the filament.

Drawing the energy potentials required making many hypotheses that we can not yet verify. Hence we foresee that our model might very well be partially invalidated by future studies. Specifically, we lacked the ability to apply pulling forces ranging up to 120pN, our setups currently being limited to forces up to 15pN. Further magnetic tweezers studies could for example measure the height of the barrier present between the $C_{ATP}$ and the $S^0_{ATP}$ states. The new version of the magnetic tweezers I have developed during my thesis could also be used for the measure of the torques associated with transitions for the ADP-bound filaments. Unfortunately time was lacking to conduct such a study.

Our results suggested the existence of several conformations of the nucleoprotein filaments. We have succinctly discussed the possibility of their existence by considering the steric effects. Pushing this line of study further would require cooperating with structural experts to ascertain the validity of our conclusions.

# Bibliography

[1]     R. Sinden, *DNA structure and function*. Gulf Professional Publishing., 1994.

[2]     K. Grzeskowiak, K. Yanagi, G. G. Privé, and R. E. Dickerson, "The structure of B-helical CGATCGATCG and comparison with CC-AACGTTGG. The effect of base pair reversals," *J. Biol. Chem.*, vol. 266, no. 14, pp. 8861–8883, May 1991.

[3]     K. Yanagi, G. G. Privé, and R. E. Dickerson, "Analysis of local helix geometry in three B-DNA decamers and eight dodecamers.," *J. Mol. Biol.*, vol. 217, no. 1, pp. 201–214, 1991.

[4]     G. G. Privé, K. Yanagi, and R. E. Dickerson, "Structure of the B-DNA decamer CCAACGTTGG and comparison with isomorphous decamers CCAAGATTGG and CCAGGCCTGG.," *J. Mol. Biol.*, vol. 217, no. 1, pp. 177–199, 1991.

[5]     V. A. Bloomfield, D. M. Crothers, I. Tinoco, and I. Tinocio Jr, *Nucleic Acids: Structures, Properties, and Functions*. University Science Books, 2000.

[6]     V. A. Bloomfield, D. M. Crothers, I. Tinoco, and I. Tinocio Jr, *Nucleic Acids: Structures, Properties, and Functions*. University Science Books, 2000.

[7]     M. C. Wahl and M. Sundaralingam, "Crystal structures of A-DNA duplexes.," *Biopolymers*, vol. 44, no. 1, pp. 45–63, Jan. 1997.

[8]     A. H.-J. Wang, G. J. Quigley, F. J. Kolpak, J. L. Crawford, J. H. Van Boom, G. van der Marel, and A. Rich, "Molecular structure of a left-handed double helical DNA fragment at atomic resolution," *Nature*, vol. 282, pp. 680–686, 1979.

[9]     J. L. Crawford, F. J. Kolpak, A. H.-J. Wang, G. J. Quigley, J. H. van Boom, G. der Marel, A. Rich, and G. van der Marel, "The tetramer d(CpGpCpG) crystallizes as a left-handed double helix," *Proc. Natl. Acad. Sci. U. S. A.*, vol. 77, no. 7, pp. 4016–4020, Jul. 1980.

[10]    H. R. Drew, T. Takano, S. Tanaka, K. Itakura, and R. E. Dickerson, "High-salt d (CpGpCpG), a left-handed Z DNA double helix," *Nature*, vol. 286, pp. 567–573, 1980.

[11]    L. Pauling and R. B. Corey, "Structure of the nucleic acids," *Nature*, vol. 171, p. 346, 1953.

[12]    J.-F. Allemand, D. Bensimon, R. Lavery, and V. Croquette, "Stretched and overwound DNA forms a Pauling-like structure with exposed bases.," *Proc. Natl. Acad. Sci. U. S. A.*, vol. 95, no. 24, pp. 14152–7, Nov. 1998.

[13]   C. Prévost, M. Takahashi, and R. Lavery, "Deforming DNA: from physics to biology," *ChemPhysChem*, vol. 10, no. 9–10, pp. 1399–1404, Jul. 2009.

[14]   M. H. Wilkins, R. G. Gosling, and W. E. Seeds, "Nucleic acid: an extensible molecule," *Nature*, vol. 167, pp. 759–760, 1951.

[15]   P. Cluzel, A. Lebrun, C. Heller, R. Lavery, J.-L. Viovy, D. Chatenay, and F. Caron, "DNA: an extensible molecule," *Science*, vol. 271, no. 5250, p. 792, Feb. 1996.

[16]   a Lebrun and R. Lavery, "Modelling extreme stretching of DNA.," *Nucleic Acids Res.*, vol. 24, no. 12, pp. 2260–7, Jun. 1996.

[17]   J. Morfill, F. Kühner, K. Blank, R. A. Lugmaier, J. Sedlmair, and H. E. Gaub, "B-S transition in short oligonucleotides.," *Biophys. J.*, vol. 93, no. 7, pp. 2400–9, Oct. 2007.

[18]   C. H. Albrecht, G. Neuert, R. A. Lugmaier, and H. E. Gaub, "Molecular force balance measurements reveal that double-stranded DNA unbinds under force in rate-dependent pathways.," *Biophys. J.*, vol. 94, no. 12, pp. 4766–74, Jun. 2008.

[19]   C. Danilowicz, C. Limouse, K. Hatch, A. Conover, V. W. Coljee, N. Kleckner, and M. Prentiss, "The structure of DNA overstretched from the 5'5' ends differs from the structure of DNA overstretched from the 3'3' ends.," *Proc. Natl. Acad. Sci. U. S. A.*, vol. 106, no. 32, pp. 13196–201, Aug. 2009.

[20]   L. Shokri, M. J. McCauley, I. Rouzina, and M. C. Williams, "DNA overstretching in the presence of glyoxal: structural evidence of force-induced DNA melting.," *Biophys. J.*, vol. 95, no. 3, pp. 1248–55, Aug. 2008.

[21]   C. Bustamante, Z. Bryant, and S. B. Smith, "Ten years of tension: single-molecule DNA mechanics.," *Nature*, vol. 421, no. 6921, pp. 423–7, Jan. 2003.

[22]   S. P. Jackson and J. Bartek, "The DNA-damage response in human biology and disease.," *Nature*, vol. 461, no. 7267, pp. 1071–8, Oct. 2009.

[23]   S. C. Kowalczykowski, "Initiation of genetic recombination and recombination-dependent replication," *Trends Biochem. Sci.*, vol. 25, no. 4, pp. 156–165, Apr. 2000.

[24]   K. K. Khanna and S. P. Jackson, "DNA double-strand breaks: signaling, repair and the cancer connection.," *Nat. Genet.*, vol. 27, no. 3, pp. 247–54, Mar. 2001.

[25]   L. Krejci, V. Altmannova, M. Spirek, and X. Zhao, "Homologous recombination and its regulation.," *Nucleic Acids Res.*, vol. 40, no. 13, pp. 5795–818, Jul. 2012.

[26]   T. Misteli and E. Soutoglou, "The emerging role of nuclear architecture in DNA repair and genome maintenance," *Nat. Rev. Mol. Cell Biol.*, vol. 10, no. 4, pp. 243–254, Apr. 2009.

[27]   S. Burma, B. P. C. Chen, and D. J. Chen, "Role of non-homologous end joining (NHEJ) in maintaining genomic integrity," *DNA Repair (Amst).*, vol. 5, no. 9–10, pp. 1042–1048, Sep. 2006.

[28]  J. M. Daley, P. L. Palmbos, D. Wu, and T. E. Wilson, "Nonhomologous end joining in yeast," *Annu. Rev. Genet.*, vol. 39, pp. 431–451, Jan. 2005.

[29]  A. Chavez, A. M. Tsou, and F. B. Johnson, "Telomeres do the (un)twist: helicase actions at chromosome termini.," *Biochim. Biophys. Acta*, vol. 1792, no. 4, pp. 329–40, Apr. 2009.

[30]  J.-Y. Bleuyard, M. E. Gallego, and C. I. White, "Recent advances in understanding of the DNA double-strand break repair machinery of plants.," *DNA Repair (Amst).*, vol. 5, no. 1, pp. 1–12, Jan. 2006.

[31]  E. Sonoda, M. S. Sasaki, J. M. Buerstedde, O. Y. Bezzubova, A. Shinohara, H. Ogawa, M. Takata, Y. Yamaguchi-Iwai, and S. Takeda, "Rad51-deficient vertebrate cells accumulate chromosomal breaks prior to cell death.," *EMBO J.*, vol. 17, no. 2, pp. 598–608, Jan. 1998.

[32]  M. Lisby, R. J. Rothstein, and U. H. Mortensen, "Rad52 forms DNA repair and recombination centers during S phase.," *Proc. Natl. Acad. Sci. U. S. A.*, vol. 98, no. 15, pp. 8276–82, Jul. 2001.

[33]  J. W. Szostak, T. L. Orr-Weaver, R. J. Rothstein, and F. W. Stahl, "The double-strand-break repair model for recombination," *Cell*, vol. 33, no. 1, pp. 25–35, May 1983.

[34]  N. Nassif, J. Penney, S. Pal, W. R. Engels, and G. B. Gloor, "Efficient copying of nonhomologous sequences from ectopic sites via P-element-induced gap repair.," *Mol. Cell. Biol.*, vol. 14, no. 3, pp. 1613–25, Mar. 1994.

[35]  D. O. Ferguson and W. K. Holloman, "Recombinational repair of gaps in DNA is asymmetric in Ustilago maydis and can be explained by a migrating D-loop model.," *Proc. Natl. Acad. Sci. U. S. A.*, vol. 93, no. 11, pp. 5419–24, May 1996.

[36]  T. Allers and M. Lichten, "Differential Timing and Control of Noncrossover and Crossover Recombination during Meiosis," *Cell*, vol. 106, no. 1, pp. 47–57, Jul. 2001.

[37]  N. Hunter and N. Kleckner, "The Single-End Invasion," *Cell*, vol. 106, no. 1, pp. 59–70, Jul. 2001.

[38]  E. Kraus, W. Y. Leung, and J. E. Haber, "Break-induced replication: a review and an example in budding yeast.," *Proc. Natl. Acad. Sci. U. S. A.*, vol. 98, no. 15, pp. 8255–62, Jul. 2001.

[39]  W. L. Santivasi and F. Xia, "The role and clinical significance of DNA damage response and repair pathways in primary brain tumors.," *Cell Biosci.*, vol. 3, no. 1, p. 10, Jan. 2013.

[40]  T. Helleday, "Homologous recombination in cancer development, treatment and development of drug resistance.," *Carcinogenesis*, vol. 31, no. 6, pp. 955–60, Jun. 2010.

[41]   S. J. Xia, M. A. Shammas, and R. J. Shmookler Reis, "Elevated recombination in immortal human cells is mediated by HsRAD51 recombinase.," *Mol. Cell. Biol.*, vol. 17, no. 12, pp. 7151–8, Dec. 1997.

[42]   H. Maacke, S. Opitz, K. Jost, W. Hamdorf, W. Henning, S. Krüger, a C. Feller, a Lopens, K. Diedrich, E. Schwinger, and H. W. Stürzbecher, "Over-expression of wild-type Rad51 correlates with histological grading of invasive ductal breast cancer.," *Int. J. Cancer*, vol. 88, no. 6, pp. 907–13, Dec. 2000.

[43]   E. Raderschall, K. Stout, S. Freier, V. Suckow, S. Schweiger, and T. Haaf, "Elevated levels of Rad51 recombination protein in tumor cells.," *Cancer Res.*, vol. 62, no. 1, pp. 219–25, Jan. 2002.

[44]   S. C. Short, S. Giampieri, M. Worku, M. Alcaide-German, G. Sioftanos, S. Bourne, K. I. Lio, M. Shaked-Rabi, and C. Martindale, "Rad51 inhibition is an effective means of targeting DNA repair in glioma models and CD133+ tumor-derived cells.," *Neuro. Oncol.*, vol. 13, no. 5, pp. 487–99, May 2011.

[45]   J. S. Russell, K. Brady, W. E. Burgan, M. A. Cerra, K. A. Oswald, K. Camphausen, and P. J. Tofilon, "Gleevec-mediated inhibition of Rad51 expression and enhancement of tumor cell radiosensitivity.," *Cancer Res.*, vol. 63, no. 21, pp. 7377–83, Nov. 2003.

[46]   F. Huang, N. A. Motlekar, C. M. Burgwin, A. D. Napper, S. L. Diamond, and A. V Mazin, "Identification of Specific Inhibitors of Human RAD51 Recombinase Using High-Throughput Screening," *ACS Chem. Biol.*, vol. 6, pp. 628–635, 2011.

[47]   F. Huang, O. M. Mazina, I. J. Zentner, S. Cocklin, and A. V Mazin, "Inhibition of Homologous Recombination in Human Cells by Targeting RAD51 Recombinase," *J. Med. Chem.*, vol. 55, pp. 3011–3020, 2012.

[48]   T. Ohnishi, T. Taki, S. Hiraga, N. Arita, and T. Morita, "In vitro and in vivo potentiation of radiosensitivity of malignant gliomas by antisense inhibition of the RAD51 gene.," *Biochem. Biophys. Res. Commun.*, vol. 245, no. 2, pp. 319–24, Apr. 1998.

[49]   J.-C. Ko, J.-H. Hong, L.-H. Wang, C.-M. Cheng, S.-C. Ciou, S.-T. Lin, M.-Y. Jheng, and Y.-W. Lin, "Role of repair protein Rad51 in regulating the response to gefitinib in human non-small cell lung cancer cells.," *Mol. Cancer Ther.*, vol. 7, no. 11, pp. 3632–41, Nov. 2008.

[50]   J. C. Game and R. K. Mortimer, "A genetic study of X-ray sensitive mutants in yeast," *Mutat. Res. Mol. Mech. Mutagen.*, vol. 24, no. 3, pp. 281–292, Sep. 1974.

[51]   A. Shinohara, H. Ogawa, Y. Matsuda, N. Ushio, K. Ikeo, and T. Ogawa, "Cloning of human, mouse and fission yeast recombination genes homologous to RAD51 and recA.," *Nat. Genet.*, vol. 4, no. 3, pp. 239–43, Jul. 1993.

[52]   R. Kanaar, C. Troelstra, S. M. Swagemakers, J. Essers, B. Smit, J. H. Franssen, a Pastink, O. Y. Bezzubova, J. M. Buerstedde, B. Clever, W. D. Heyer, and J. H. Hoeijmakers, "Human and mouse homologs of the Saccharomyces cerevisiae RAD54

DNA repair gene: evidence for functional conservation.," *Curr. Biol.*, vol. 6, no. 7, pp. 828–38, Jul. 1996.

[53] G. M. Dolganov, R. S. Maser, A. Novikov, L. Tosto, S. Chong, D. A. Bressan, and J. H. Petrini, "Human Rad50 is physically associated with human Mre11: identification of a conserved multiprotein complex implicated in recombinational DNA repair.," *Mol. Cell. Biol.*, vol. 16, no. 9, pp. 4832–41, Sep. 1996.

[54] D. F. R. Muris, O. Bezzubova, J.-M. Buerstedde, K. Vreeken, A. S. Balajee, C. J. Osgood, C. Troelstra, J. H. J. Hoeijmakers, K. Ostermann, H. Schmidt, A. T. Natarajan, J. C. J. Eeken, P. H. M. Lohman, and A. Pastink, "Cloning of human and mouse genes homologous to RAD52, a yeast gene involved in DNA repair and recombination," *Mutat. Res. Repair*, vol. 315, no. 3, pp. 295–305, Nov. 1994.

[55] S. L. Hays, a a Firmenich, and P. Berg, "Complex formation in yeast double-strand break repair: participation of Rad51, Rad52, Rad55, and Rad57 proteins.," *Proc. Natl. Acad. Sci. U. S. A.*, vol. 92, no. 15, pp. 6925–9, Jul. 1995.

[56] R. D. Johnson and L. S. Symington, "Functional differences and interactions among the putative RecA homologs Rad51, Rad55, and Rad57.," *Mol. Cell. Biol.*, vol. 15, no. 9, pp. 4843–50, Sep. 1995.

[57] E. I. Golub, O. V Kovalenko, R. C. Gupta, D. C. Ward, and C. M. Radding, "Interaction of human recombination proteins Rad51 and Rad54.," *Nucleic Acids Res.*, vol. 25, no. 20, pp. 4106–10, Oct. 1997.

[58] P. Baumann and S. C. West, "Role of the human RAD51 protein in homologous recombination and double-stranded-break repair.," *Trends Biochem. Sci.*, vol. 23, no. 7, pp. 247–51, Jul. 1998.

[59] G. Chen, S. S. Yuan, W. Liu, Y. Xu, K. Trujillo, B. Song, F. Cong, S. P. Goff, Y. Wu, R. Arlinghaus, D. Baltimore, P. J. Gasser, M. S. Park, P. Sung, and E. Y. Lee, "Radiation-induced assembly of Rad51 and Rad52 recombination complex requires ATM and c-Abl.," *J. Biol. Chem.*, vol. 274, no. 18, pp. 12748–52, Apr. 1999.

[60] F. Pâques and J. E. Haber, "Multiple pathways of recombination induced by double-strand breaks in Saccharomyces cerevisiae.," *Microbiol. Mol. Biol. Rev.*, vol. 63, no. 2, pp. 349–404, Jun. 1999.

[61] P. Sung, K. M. Trujillo, and S. Van Komen, "Recombination factors of Saccharomyces cerevisiae," *Mutat. Res. Mol. Mech. Mutagen.*, vol. 451, no. 1–2, pp. 257–275, Jun. 2000.

[62] Y. Liu and N. Maizels, "Coordinated response of mammalian Rad51 and Rad52 to DNA damage," *EMBO Rep.*, vol. 1, no. 1, pp. 85–90, Jul. 2000.

[63] J. Essers, A. B. Houtsmuller, L. van Veelen, C. Paulusma, A. L. Nigg, A. Pastink, W. Vermeulen, J. H. J. Hoeijmakers, and R. Kanaar, "Nuclear dynamics of RAD52 group homologous recombination proteins in response to DNA damage.," *EMBO J.*, vol. 21, no. 8, pp. 2030–7, Apr. 2002.

[64] T. L. Tan, J. Essers, E. Citterio, S. M. Swagemakers, J. de Wit, F. E. Benson, J. H. J. Hoeijmakers, and R. Kanaar, "Mouse Rad54 affects DNA conformation and DNA-damage-induced Rad51 foci formation.," *Curr. Biol.*, vol. 9, no. 6, pp. 325–8, Mar. 1999.

[65] M. Tarsounas, A. a Davies, and S. C. West, "RAD51 localization and activation following DNA damage.," *Philos. Trans. R. Soc. Lond. B. Biol. Sci.*, vol. 359, no. 1441, pp. 87–93, Jan. 2004.

[66] E. Raderschall, E. I. Golub, and T. Haaf, "Nuclear foci of mammalian recombination proteins are located at single-stranded DNA regions formed after DNA damage.," *Proc. Natl. Acad. Sci. U. S. A.*, vol. 96, no. 5, pp. 1921–6, Mar. 1999.

[67] R. Scully, J. Chen, a Plug, Y. Xiao, D. Weaver, J. Feunteun, T. Ashley, and D. M. Livingston, "Association of BRCA1 with Rad51 in mitotic and meiotic cells.," *Cell*, vol. 88, no. 2, pp. 265–75, Jan. 1997.

[68] J. Chen, D. P. Silver, D. Walpita, S. B. Cantor, a F. Gazdar, G. Tomlinson, F. J. Couch, B. L. Weber, T. Ashley, D. M. Livingston, and R. Scully, "Stable interaction between the products of the BRCA1 and BRCA2 tumor suppressor genes in mitotic and meiotic cells.," *Mol. Cell*, vol. 2, no. 3, pp. 317–28, Sep. 1998.

[69] D. S. Shin, L. Pellegrini, D. S. Daniels, B. Yelent, L. Craig, D. Bates, D. S. Yu, M. K. Shivji, C. Hitomi, A. S. Arvai, N. Volkmann, H. Tsuruta, T. L. Blundell, A. R. Venkitaraman, and J. a Tainer, "Full-length archaeal Rad51 structure and mutants: mechanisms for RAD51 assembly and control by BRCA2.," *EMBO J.*, vol. 22, no. 17, pp. 4566–76, Sep. 2003.

[70] A. J. Clark and A. D. Margulies, "Isolation and characterization of recombination-deficient mutants of Escherichia coli K12," *Proc. Natl. Acad. Sci. U. S. A.*, vol. 53, pp. 451–459, 1965.

[71] A. Aboussekhra, R. Chanet, A. Adjiri, and F. Fabre, "Semidominant suppressors of Srs2 helicase mutations of Saccharomyces cerevisiae map in the RAD51 gene, whose sequence predicts a protein with similarities to procaryotic RecA proteins.," *Mol. Cell. Biol.*, vol. 12, no. 7, pp. 3224–34, Jul. 1992.

[72] G. Basile, M. Aker, and R. K. Mortimer, "Nucleotide sequence and transcriptional regulation of the yeast recombinational repair gene RAD51.," *Mol. Cell. Biol.*, vol. 12, no. 7, pp. 3235–46, Jul. 1992.

[73] D. K. Bishop, D. Park, L. Xu, and N. Kleckner, "DMC1: a meiosis-specific yeast homolog of E. coli recA required for recombination, synaptonemal complex formation, and cell cycle progression.," *Cell*, vol. 69, no. 3, pp. 439–56, May 1992.

[74] D. F. Muris, K. Vreeken, a M. Carr, B. C. Broughton, a R. Lehmann, P. H. Lohman, and a Pastink, "Cloning the RAD51 homologue of Schizosaccharomyces pombe.," *Nucleic Acids Res.*, vol. 21, no. 19, pp. 4586–91, Sep. 1993.

[75]   T. Ogawa, X. Yu, A. Shinohara, and E. H. Egelman, "Similarity of the yeast RAD51 filament to the bacterial RecA filament.," *Science*, vol. 259, no. 5103, pp. 1896–9, Mar. 1993.

[76]   A. Shinohara, H. Ogawa, and T. Ogawa, "Rad51 protein involved in repair and recombination in S. cerevisiae is a RecA-like protein.," *Cell*, vol. 69, no. 3, pp. 457–70, May 1992.

[77]   M. Terasawa, a Shinohara, Y. Hotta, H. Ogawa, and T. Ogawa, "Localization of RecA-like recombination proteins on chromosomes of the lily at various meiotic stages.," *Genes Dev.*, vol. 9, no. 8, pp. 925–934, Apr. 1995.

[78]   K. Maeshima, K. Morimatsu, a Shinohara, and T. Horii, "RAD51 homologues in Xenopus laevis: two distinct genes are highly expressed in ovary and testis.," *Gene*, vol. 160, no. 2, pp. 195–200, Jul. 1995.

[79]   T. Morita, Y. Yoshimura, a Yamamoto, K. Murata, M. Mori, H. Yamamoto, and a Matsushiro, "A mouse homolog of the Escherichia coli recA and Saccharomyces cerevisiae RAD51 genes.," *Proc. Natl. Acad. Sci. U. S. A.*, vol. 90, no. 14, pp. 6577–80, Jul. 1993.

[80]   Y. Yoshimura, T. Morita, A. Yamamoto, and A. Matsushiro, "Cloning and sequence of the human RecA-like gene cDNA," *Nucleic Acids Res.*, vol. 21, no. 7, p. 1665, Apr. 1993.

[81]   J. K. De Zutter and K. L. Knight, "The hRad51 and RecA proteins show significant differences in cooperative binding to single-stranded DNA," *J. Mol. Biol.*, vol. 293, no. 4, pp. 769–780, Nov. 1999.

[82]   J. M. Sage, O. S. Gildemeister, and K. L. Knight, "Discovery of a Novel Function for Human Rad51," *J. Biol. Chem.*, vol. 285, no. 25, pp. 18984–18990, 2010.

[83]   T. Haaf, E. I. Golub, G. Reddy, C. M. Radding, and D. C. Ward, "Nuclear foci of mammalian Rad51 recombination protein in somatic cells after DNA damage and its localization in synaptonemal complexes.," *Proc. Natl. Acad. Sci. U. S. A.*, vol. 92, no. 6, pp. 2298–302, Mar. 1995.

[84]   R. Scully, J. Chen, R. L. Ochs, K. Keegan, M. Hoekstra, J. Feunteun, and D. M. Livingston, "Dynamic changes of BRCA1 subnuclear location and phosphorylation state are initiated by DNA damage.," *Cell*, vol. 90, no. 3, pp. 425–35, Aug. 1997.

[85]   D. K. Bishop, U. Ear, a Bhattacharyya, C. Calderone, M. Beckett, R. R. Weichselbaum, and a Shinohara, "Xrcc3 is required for assembly of Rad51 complexes in vivo.," *J. Biol. Chem.*, vol. 273, no. 34, pp. 21482–8, Aug. 1998.

[86]   M. Takata, M. S. Sasaki, E. Sonoda, T. Fukushima, C. Morrison, J. S. Albala, S. M. Swagemakers, R. Kanaar, L. H. Thompson, and S. Takeda, "The Rad51 paralog Rad51B promotes homologous recombinational repair.," *Mol. Cell. Biol.*, vol. 20, no. 17, pp. 6476–82, Sep. 2000.

[87] M. Takata, M. S. Sasaki, S. Tachiiri, T. Fukushima, E. Sonoda, D. Schild, L. H. Thompson, and S. Takeda, "Chromosome instability and defective recombinational repair in knockout mutants of the five Rad51 paralogs.," *Mol. Cell. Biol.*, vol. 21, no. 8, pp. 2858–66, Apr. 2001.

[88] V. P. Yu, M. Koehler, C. Steinlein, M. Schmid, L. A. Hanakahi, A. J. van Gool, S. C. West, and A. R. Venkitaraman, "Gross chromosomal rearrangements and genetic exchange between nonhomologous chromosomes following BRCA2 inactivation.," *Genes Dev.*, vol. 14, no. 11, pp. 1400–6, Jun. 2000.

[89] P. O'Regan, C. Wilson, S. Townsend, and J. Thacker, "XRCC2 is a nuclear RAD51-like protein required for damage-dependent RAD51 focus formation without the need for ATP binding.," *J. Biol. Chem.*, vol. 276, no. 25, pp. 22148–53, Jun. 2001.

[90] T. Tsuzuki, Y. Fujii, K. Sakumi, Y. Tominaga, K. Nakao, M. Sekiguchi, A. Matsushiro, Y. Yoshimura, and MoritaT, "Targeted disruption of the Rad51 gene leads to lethality in embryonic mice.," *Proc. Natl. Acad. Sci. U. S. A.*, vol. 93, no. 13, pp. 6236–40, Jun. 1996.

[91] D. S. Lim and P. Hasty, "A mutation in mouse rad51 results in an early embryonic lethal that is suppressed by a mutation in p53.," *Mol. Cell. Biol.*, vol. 16, no. 12, pp. 7133–43, Dec. 1996.

[92] S. Tashiro, J. M. Walter, A. Shinohara, N. Kamada, and T. Cremer, "Rad51 accumulation at sites of DNA damage and in postreplicative chromatin.," *J. Cell Biol.*, vol. 150, no. 2, pp. 283–91, Jul. 2000.

[93] S. Tashiro, N. Kotomura, A. Shinohara, K. Tanaka, K. Ueda, and N. Kamada, "S phase specific formation of the human Rad51 protein nuclear foci in lymphocytes.," *Oncogene*, vol. 12, no. 10, pp. 2165–70, May 1996.

[94] M. Tarsounas, D. Davies, and S. C. West, "BRCA2-dependent and independent formation of RAD51 nuclear foci.," *Oncogene*, vol. 22, no. 8, pp. 1115–23, Feb. 2003.

[95] P. Baumann, F. E. Benson, N. M. Hajibagheri, and S. C. West, "Purification of human Rad51 protein by selective spermidine precipitation," *Mutat. Res. Repair*, vol. 384, no. 2, pp. 65–72, Aug. 1997.

[96] V. M. Navadgi, A. Shukla, R. K. Vempati, and B. J. Rao, "DNA mediated disassembly of hRad51 and hRad52 proteins and recruitment of hRad51 to ssDNA by hRad52," *FEBS J.*, vol. 273, no. 1, pp. 199–207, Jan. 2006.

[97] D. E. Urena, Z. Zhang, Y. Tsai, Y. Wang, and J. Chen, "From Strand Exchange to Branch Migration ; Bypassing of Non-homologous Sequences by," *J. Mol. Biol.*, vol. 405, no. 1, pp. 77–91, 2011.

[98] M. J. McIlwraith, E. Van Dyck, J.-Y. Y. Masson, A. Z. Stasiak, and S. C. West, "Reconstitution of the strand invasion step of double-strand break repair using human Rad51 Rad52 and RPA proteins," *J. Mol. Biol.*, vol. 304, no. 2, pp. 151–164, Nov. 2000.

[99] F. E. Benson, A. Stasiak, and S. C. West, "Purification and characterization of the human Rad51 protein, an analogue of E. coli RecA.," *EMBO J.*, vol. 13, no. 23, pp. 5764–71, Dec. 1994.

[100] P. Baumann, F. E. Benson, and S. C. West, "Human Rad51 protein promotes ATP-dependent homologous pairing and strand transfer reactions in vitro.," *Cell*, vol. 87, no. 4, pp. 757–66, Nov. 1996.

[101] P. Baumann and S. C. West, "The human Rad51 protein: polarity of strand transfer and stimulation by hRP-A," *EMBO J.*, vol. 16, no. 17, pp. 5198–5206, Sep. 1997.

[102] R. C. Gupta, L. R. Bazemore, E. I. Golub, and C. M. Radding, "Activities of human recombination protein Rad51.," *Proc. Natl. Acad. Sci. U. S. A.*, vol. 94, no. 2, pp. 463–8, Jan. 1997.

[103] C. Wyman, D. Ristic, and R. Kanaar, "Homologous recombination-mediated double-strand break repair.," *DNA Repair (Amst).*, vol. 3, no. 8–9, pp. 827–33, 2004.

[104] S. Sigurdsson, K. M. Trujillo, B. W. Song, S. Stratton, and P. Sung, "Basis for avid homologous DNA strand exchange by human Rad51 and RPA," *J. Biol. Chem.*, vol. 276, no. 12, pp. 8798–8806, Mar. 2001.

[105] A. V Mazin, A. A. Alexeev, and S. C. Kowalczykowski, "A novel function of Rad54 protein. Stabilization of the Rad51 nucleoprotein filament," *J. Biol. Chem.*, vol. 278, no. 16, p. 14029, Apr. 2003.

[106] T. L. L. Raoul Tan, R. Kanaar, and C. Wyman, "Rad54, a Jack of all trades in homologous recombination," *DNA Repair (Amst).*, vol. 2, no. 7, pp. 787–794, Jul. 2003.

[107] A. A. Alexeev, A. V Mazin, and S. C. Kowalczykowski, "Rad54 protein possesses chromatin-remodeling activity stimulated by the Rad51-ssDNA nucleoprotein filament.," *Nat. Struct. Biol.*, vol. 10, no. 3, pp. 182–6, Mar. 2003.

[108] M. Lisby, J. H. Barlow, R. C. Burgess, and R. J. Rothstein, "Choreography of the DNA damage response: spatiotemporal relationships among checkpoint and repair proteins," *Cell*, vol. 118, no. 6, pp. 699–713, Sep. 2004.

[109] K.-S. Shim, G. Tombline, C. D. Heinen, N. Charbonneau, C. Schmutte, and R. Fishel, "Magnesium influences the discrimination and release of ADP by human Rad51," *DNA Repair (Amst).*, vol. 5, no. 6, pp. 704–717, Jun. 2006.

[110] G. Tombline and R. Fishel, "Biochemical characterization of the human RAD51 protein. I. ATP hydrolysis.," *J. Biol. Chem.*, vol. 277, no. 17, pp. 14417–25, Apr. 2002.

[111] D. V Bugreev and A. V Mazin, "Ca2+ activates human homologous recombination protein Rad51 by modulating its ATPase activity.," *Proc. Natl. Acad. Sci. U. S. A.*, vol. 101, no. 27, pp. 9988–93, Jul. 2004.

[112] M. M. Cox and I. R. Lehman, "recA protein-promoted DNA strand exchange. Stable complexes of recA protein and single-stranded DNA formed in the presence of ATP and single-stranded DNA binding protein.," *J. Biol. Chem.*, vol. 257, no. 14, pp. 8523–32, Jul. 1982.

[113] P. Chi, S. Van Komen, M. G. Sehorn, S. Sigurdsson, and P. Sung, "Roles of ATP binding and ATP hydrolysis in human Rad51 recombinase function," *DNA Repair (Amst).*, vol. 5, no. 3, pp. 381–391, Mar. 2006.

[114] A. L. Forget, M. S. Loftus, D. a McGrew, B. T. Bennett, and K. L. Knight, "The human Rad51 K133A mutant is functional for DNA double-strand break repair in human cells.," *Biochemistry*, vol. 46, no. 11, pp. 3566–75, Mar. 2007.

[115] C. W. Fung, G. S. Fortin, S. E. Peterson, and L. S. Symington, "The rad51-K191R ATPase-defective mutant is impaired for presynaptic filament formation.," *Mol. Cell. Biol.*, vol. 26, no. 24, pp. 9544–54, Dec. 2006.

[116] C. Morrison, A. Shinohara, E. Sonoda, Y. Yamaguchi-Iwai, M. Takaku, R. R. Weichselbaum, S. Takeda, and M. Takata, "The essential functions of human Rad51 are independent of ATP hydrolysis.," *Mol. Cell. Biol.*, vol. 19, no. 10, pp. 6891–7, Oct. 1999.

[117] J. M. Stark, P. Hu, A. J. Pierce, M. E. Moynahan, N. Ellis, and M. Jasin, "ATP hydrolysis by mammalian RAD51 has a key role during homology-directed DNA repair.," *J. Biol. Chem.*, vol. 277, no. 23, pp. 20185–94, Jun. 2002.

[118] H.-K. Kim, K. Morimatsu, B. Nordén, M. Ardhammar, and M. Takahashi, "ADP stabilizes the human Rad51-single stranded DNA complex and promotes its DNA annealing activity.," *Genes Cells*, vol. 7, no. 11, pp. 1125–34, Nov. 2002.

[119] R. B. Robertson, D. N. Moses, Y. H. Kwon, P. Chan, P. Chi, H. Klein, P. Sung, and E. C. Greene, "Structural transitions within human Rad51 nucleoprotein filaments.," *Proc. Natl. Acad. Sci. U. S. A.*, vol. 106, no. 31, pp. 12688–93, Aug. 2009.

[120] Y. Tsai, Y. Wang, D. E. Urena, S. Kumar, and J. Chen, "Heterology tolerance and recognition of mismatched base pairs by human Rad51 protein," *DNA Repair (Amst).*, vol. 10, no. 4, pp. 363–372, 2011.

[121] G. Tombline, K.-S. Shim, and R. Fishel, "Biochemical characterization of the human RAD51 protein. II. Adenosine nucleotide binding and competition.," *J. Biol. Chem.*, vol. 277, no. 17, pp. 14426–33, Apr. 2002.

[122] G. Tombline, C. D. Heinen, K.-S. Shim, and R. Fishel, "Biochemical characterization of the human RAD51 protein. III. Modulation of DNA binding by adenosine nucleotides.," *J. Biol. Chem.*, vol. 277, no. 17, pp. 14434–42, Apr. 2002.

[123] K. -i. Yoshioka, Y. Yumoto-Yoshioka, F. Fleury, and M. Takahashi, "pH-and salt-dependent self-assembly of human Rad51 protein analyzed as fluorescence resonance energy transfer between labeled proteins," *J. Biochem.*, vol. 133, no. 5, p. 593, May 2003.

[124] V. M. Navadgi, A. Shukla, and B. J. Rao, "Effect of DNA sequence and nucleotide cofactors on hRad51 binding to ssDNA: role of hRad52 in recruitment.," *Biochem. Biophys. Res. Commun.*, vol. 334, no. 2, pp. 696–701, Aug. 2005.

[125] M. M. Cox, "Motoring along with the bacterial RecA protein," *Nat. Rev. Mol. Cell Biol.*, vol. 8, no. 2, pp. 127–138, Feb. 2007.

[126] L. H. Fornander, K. Frykholm, A. Reymer, A. Renodon-Cornière, M. Takahashi, and B. Norde, "Ca 2 + improves organization of single-stranded DNA bases in human Rad51 filament , explaining stimulatory effect on gene recombination," *Nucleic Acids Res.*, vol. 40, no. 11, pp. 4904–4913, 2012.

[127] V. E. Galkin, F. Esashi, X. Yu, S. Yang, S. C. West, and E. H. Egelman, "BRCA2 BRC motifs bind RAD51-DNA filaments.," *Proc. Natl. Acad. Sci. U. S. A.*, vol. 102, no. 24, pp. 8537–42, Jun. 2005.

[128] X. Yu, S. a Jacobs, S. C. West, T. Ogawa, and E. H. Egelman, "Domain structure and dynamics in the helical filaments formed by RecA and Rad51 on DNA.," *Proc. Natl. Acad. Sci. U. S. A.*, vol. 98, no. 15, pp. 8419–24, Jul. 2001.

[129] D. Ristic, M. Modesti, T. van der Heijden, J. van Noort, C. Dekker, R. Kanaar, and C. Wyman, "Human Rad51 filaments on double- and single-stranded DNA: correlating regular and irregular forms with recombination function.," *Nucleic Acids Res.*, vol. 33, no. 10, pp. 3292–302, Jan. 2005.

[130] M. Modesti, D. Ristic, T. van der Heijden, C. Dekker, J. van Mameren, E. J. G. Peterman, G. J. L. Wuite, R. Kanaar, and C. Wyman, "Fluorescent human RAD51 reveals multiple nucleation sites and filament segments tightly associated along a single DNA molecule.," *Structure*, vol. 15, no. 5, pp. 599–609, May 2007.

[131] T. K. Prasad, C. C. Yeykal, and E. C. Greene, "Visualizing the assembly of human Rad51 filaments on double-stranded DNA.," *J. Mol. Biol.*, vol. 363, no. 3, pp. 713–28, Oct. 2006.

[132] A. Granéli, C. C. Yeykal, R. B. Robertson, and E. C. Greene, "Long-distance lateral diffusion of human Rad51 on double-stranded DNA.," *Proc. Natl. Acad. Sci. U. S. A.*, vol. 103, no. 5, pp. 1221–6, Jan. 2006.

[133] R. B. Robertson, D. N. Moses, Y. H. Kwon, P. Chan, W. Zhao, P. Chi, H. Klein, P. Sung, and E. C. Greene, "Visualizing the disassembly of S. cerevisiae Rad51 nucleoprotein filaments," *J. Mol. Biol.*, vol. 388, no. 4, pp. 703–720, May 2009.

[134] A. Granéli, C. C. Yeykal, T. K. Prasad, and E. C. Greene, "Organized arrays of individual DNA molecules tethered to supported lipid bilayers.," *Langmuir*, vol. 22, no. 1, pp. 292–9, Jan. 2006.

[135] J. Hilario, I. Amitani, R. J. Baskin, and S. C. Kowalczykowski, "Direct imaging of human Rad51 nucleoprotein dynamics on individual DNA molecules.," *Proc. Natl. Acad. Sci. U. S. A.*, vol. 106, no. 2, pp. 361–8, Jan. 2009.

[136] J. Van Mameren, M. Modesti, R. Kanaar, C. Wyman, G. J. L. Wuite, and E. J. G. Peterman, "Dissecting elastic heterogeneity along DNA molecules coated partly with Rad51 using concurrent fluorescence microscopy and optical tweezers.," *Biophys. J.*, vol. 91, no. 8, pp. L78–80, Oct. 2006.

[137] J. van Mameren, M. Modesti, R. Kanaar, C. Wyman, E. J. G. Peterman, G. J. L. Wuite, and J. Van Mameren, "Counting RAD51 proteins disassembling from nucleoprotein filaments under tension," *Nature*, vol. 457, no. 7230, pp. 745–748, Feb. 2008.

[138] J. van Mameren, E. J. G. Peterman, and G. J. L. Wuite, "See me, feel me: methods to concurrently visualize and manipulate single DNA molecules and associated proteins.," *Nucleic Acids Res.*, vol. 36, no. 13, pp. 4381–9, Aug. 2008.

[139] T. van der Heijden, R. Seidel, M. Modesti, R. Kanaar, C. Wyman, and C. Dekker, "Real-time assembly and disassembly of human RAD51 filaments on individual DNA molecules," *Nucleic Acids Res.*, vol. 35, no. 17, pp. 5646–5657, Jan. 2007.

[140] J. Miné, L. Disseau, M. Takahashi, G. Cappello, M. Dutreix, and J.-L. Viovy, "Real-time measurements of the nucleation, growth and dissociation of single Rad51-DNA nucleoprotein filaments.," *Nucleic Acids Res.*, vol. 35, no. 21, pp. 7171–87, Jan. 2007.

[141] L. Disseau, "Étude de l'association et de la dynamique de filaments nucléoprotéiques Rad51-ADN individuels dans les pinces magnétiques," *Thèse UPMC*, 2010.

[142] H. Arata, A. Dupont, J. Miné, L. Disseau, A. Renodon-Cornière, M. Takahashi, J.-L. Viovy, and G. Cappello, "Direct observation of twisting steps during Rad51 polymerization on DNA.," *Proc. Natl. Acad. Sci. U. S. A.*, vol. 106, no. 46, pp. 19239–44, Nov. 2009.

[143] A. Dupont, "La recombinaison homologue sur molécule unique d'ADN : mesures de torsion et de couple.," *Thèse Paris7*, 2008.

[144] Y. Harada, O. Ohara, a Takatsuki, H. Itoh, N. Shimamoto, and K. Kinosita, "Direct observation of DNA rotation during transcription by Escherichia coli RNA polymerase.," *Nature*, vol. 409, no. 6816, pp. 113–5, Jan. 2001.

[145] M. Lee, J. Lipfert, H. Sanchez, C. Wyman, and N. H. Dekker, "Structural and torsional properties of the RAD51-dsDNA nucleoprotein filament.," *Nucleic Acids Res.*, vol. 41, no. 14, pp. 7023–30, Aug. 2013.

[146] J. Lipfert, M. Wiggin, J. W. J. Kerssemakers, F. Pedaci, and N. H. Dekker, "Freely orbiting magnetic tweezers to directly monitor changes in the twist of nucleic acids.," *Nat. Commun.*, vol. 2, no. may, p. 439, Jan. 2011.

[147] A. B. Conway, T. W. Lynch, Y. Zhang, G. S. Fortin, C. W. Fung, L. S. Symington, and P. a Rice, "Crystal structure of a Rad51 filament.," *Nat. Struct. Mol. Biol.*, vol. 11, no. 8, pp. 791–6, Aug. 2004.

[148] A. Reymer, K. Frykholm, K. Morimatsu, M. Takahashi, and B. Nordén, "Structure of human Rad51 protein filament from molecular modeling and site-specific linear

dichroism spectroscopy.," *Proc. Natl. Acad. Sci. U. S. A.*, vol. 106, no. 32, pp. 13248–53, Aug. 2009.

[149]  L. Pellegrini, D. S. Yu, T. Lo, S. Anand, M. Lee, T. L. Blundell, and A. R. Venkitaraman, "Insights into DNA recombination from the structure of a RAD51-BRCA2 complex.," *Nature*, vol. 420, no. 6913, pp. 287–93, Nov. 2002.

[150]  H. Aihara, Y. Ito, H. Kurumizaka, S. Yokoyama, and T. Shibata, "The N-terminal domain of the human Rad51 protein binds DNA: structure and a DNA binding surface as revealed by NMR.," *J. Mol. Biol.*, vol. 290, no. 2, pp. 495–504, Jul. 1999.

[151]  C. Prévost and M. Takahashi, "Geometry of the DNA strands within the RecA nucleofilament: role in homologous recombination," *Q. Rev. Biophys.*, vol. 36, no. 4, pp. 429–453, Nov. 2003.

[152]  Z. Chen, H. Yang, and N. P. Pavletich, "Mechanism of homologous recombination from the RecA--ssDNA/dsDNA structures," *Nature*, vol. 453, no. 7194, pp. 489–494, May 2008.

[153]  A. Renodon-Cornière, Y. Takizawa, S. Conilleau, V. Tran, S. Iwai, H. Kurumizaka, and M. Takahashi, "Structural analysis of the human Rad51 protein-DNA complex filament by tryptophan fluorescence scanning analysis: transmission of allosteric effects between ATP binding and DNA binding.," *J. Mol. Biol.*, vol. 383, no. 3, pp. 575–87, Nov. 2008.

[154]  Y. Matsuo, I. Sakane, Y. Takizawa, M. Takahashi, and H. Kurumizaka, "Roles of the human Rad51 L1 and L2 loops in DNA binding.," *FEBS J.*, vol. 273, no. 14, pp. 3148–59, Jul. 2006.

[155]  A. V Hill, "The Combinations of Haemoglobin with Oxygen and with Carbon Monoxide. I.," *Biochem. J.*, vol. 7, no. 5, pp. 471–80, Oct. 1913.

[156]  J. N. Weiss, "The Hill equation revisited: uses and misuses.," *FASEB J.*, vol. 11, no. 11, pp. 835–41, Sep. 1997.

[157]  J. Miné, "Recombinaison homologue à l'échelle de la molécule unique," *Thèse UPMC*, 2007.

[158]  T. R. Strick, J.-F. Allemand, D. Bensimon, A. Bensimon, and V. Croquette, "The Elasticity of a Single Supercoiled DNA Molecule," *Science*, vol. 271, no. 5257, pp. 1835–1837, Mar. 1996.

[159]  A. Bancaud, "Dynamique et structure de fibres de chromatine individuelles," Université Paris 6 - Pierre et Marie Curie, 2004.

[160]  G. Fonnum, C. Johansson, A. Molteberg, S. Mørup, and E. Aksnes, "Characterisation of Dynabeads® by magnetization measurements and Mössbauer spectroscopy," *J. Magn. Magn. Mater.*, vol. 293, no. 1, pp. 41–47, May 2005.

[161] P. Recouvreux, "Influence de l'histone de liaison sur la dynamique de fibres de chromatine individuelles," Université Paris 7 - Denis Diderot, 2009.

[162] T. R. Strick, J.-F. Allemand, V. Croquette, and D. Bensimon, "Twisting and stretching single DNA molecules," *Prog. Biophys. Mol. Biol.*, vol. 74, no. 1–2, pp. 115–140, Jan. 2000.

[163] P.-G. de Gennes, *Scaling concepts in Polymer Physics*. Cornell University Press, 1979.

[164] J. F. Leger, G. Romano, A. Sarkar, J. Robert, L. Bourdieu, D. Chatenay, J. F. Marko, and J. Léger, "Structural transitions of a twisted and stretched DNA molecule," *Phys. Rev. Lett.*, vol. 83, no. 5, pp. 1066–1069, Aug. 1999.

[165] JPK Instruments, "DNA elasticity measurement." [Online]. Available: http://www.jpk.com/dna-elasticity-measurement.409.en.html.

[166] M. Fixman, "Polymer conformational statistics. III. Modified Gaussian models of stiff chains," *J. Chem. Phys.*, vol. 58, no. 4, p. 1564, 1973.

[167] J. Kovac and C. C. Crabb, "Modified Gaussian model for rubber elasticity. 2. The wormlike chain," *Macromolecules*, vol. 15, no. 2, pp. 537–541, Mar. 1982.

[168] C. Bustamante, J. F. Marko, E. D. Siggia, and S. B. Smith, "Entropic elasticity of lambda-phage DNA," *Science*, vol. 265, no. 5178, pp. 1599–1600, Sep. 1994.

[169] J. F. Marko and E. D. Siggia, "Stretching DNA," *Macromolecules*, vol. 28, no. 26, pp. 8759–8770, Dec. 1995.

[170] C. Bouchiat, M. D. Wang, J. Allemand, T. R. Strick, S. M. Block, and V. Croquette, "Estimating the persistence length of a worm-like chain molecule from force-extension measurements.," *Biophys. J.*, vol. 76, no. 1, pp. 409–13, Jan. 1999.

[171] M. D. Wang, H. Yin, R. Landick, J. Gelles, and S. M. Block, "Stretching DNA with optical tweezers," *Biophys. J.*, vol. 72, no. 3, pp. 1335–1346, Mar. 1997.

[172] J. H. White, "Self-linking and the Gauss integral in higher dimensions," *Am. J. Math.*, vol. 91, no. 3, pp. 693–728, 1969.

[173] T. R. Strick, J.-F. Allemand, D. Bensimon, and V. Croquette, "Stress-induced structural transitions in DNA and proteins.," *Annu. Rev. Biophys. Biomol. Struct.*, vol. 29, pp. 523–43, Jan. 2000.

[174] M. Abramowitz and M. W. Davidson, "Microscope Objectives: Immersion Media," *Olympus Microscopy Resource Center*, 2002. .

[175] J.-F. Allemand, "Micro-manipulations de molécules d'ADN isolées," *Thèse UPMC*, 1997.

[176] T. R. Strick, M.-N. N. Dessinges, G. Charvin, N. H. Dekker, J.-F. Allemand, D. Bensimon, and V. Croquette, "Stretching of macromolecules and proteins," *Reports Prog. Phys.*, vol. 66, no. 1, pp. 1–45, Jan. 2003.

[177] J. D. Moroz and P. Nelson, "Torsional directed walks, entropic elasticity, and DNA twist stiffness," *Proc. Natl. Acad. Sci. U. S. A.*, vol. 94, no. 26, p. 14418, Dec. 1997.

[178] J. D. Moroz and P. Nelson, "Entropic elasticity of twist-storing polymers," *Macromolecules*, vol. 31, no. 18, pp. 6333–6347, Sep. 1998.

[179] J. F. Marko, "Torque and dynamics of linking number relaxation in stretched supercoiled DNA.," *Phys. Rev. E*, vol. 76, no. 2, p. 021926, 2007.

[180] F. Mosconi, J.-F. Allemand, D. Bensimon, and V. Croquette, "Measurement of the Torque on a Single Stretched and Twisted DNA Using Magnetic Tweezers," *Phys. Rev. Lett.*, vol. 102, no. 7, pp. 1–4, Feb. 2009.

[181] J. Lipfert, J. W. J. Kerssemakers, T. Jager, and N. H. Dekker, "Magnetic torque tweezers: measuring torsional stiffness in DNA and RecA-DNA filaments.," *Nat. Methods*, vol. 7, no. 12, pp. 977–80, Dec. 2010.

[182] Z. Bryant, M. D. Stone, J. Gore, S. B. Smith, N. R. Cozzarelli, and C. Bustamante, "Structural transitions and elasticity from torque measurements on DNA.," *Nature*, vol. 424, no. 6946, pp. 338–41, Jul. 2003.

[183] E. H. Egelman and A. Stasiak, "Electron microscopy of RecA-DNA complexes: Two different states, their functional significance and relation to the solved crystal structure," *Micron*, vol. 24, no. 3, pp. 309–324, 1993.

[184] A. Stasiak and E. Di Capua, "The helicity of DNA in complexes with RecA protein," *Nature*, vol. 229, pp. 185–186, 1982.

[185] J. P. Menetski, D. G. Bear, and S. C. Kowalczykowski, "Stable DNA heteroduplex formation catalyzed by the Escherichia coli RecA protein in the absence of ATP hydrolysis.," *Proc. Natl. Acad. Sci. U. S. A.*, vol. 87, no. 1, pp. 21–5, Jan. 1990.

[186] S. M. Honigberg, D. K. Gonda, J. Flory, and C. M. Radding, "The pairing activity of stable nucleoprotein filaments made from recA protein, single-stranded DNA, and adenosine 5'-(gamma-thio)triphosphate.," *J. Biol. Chem.*, vol. 260, no. 21, pp. 11845–51, Sep. 1985.

[187] G. Reddy, B. Burnett, and C. M. Radding, "Uptake and processing of duplex DNA by RecA nucleoprotein filaments: insights provided by a mixed population of dynamic and static intermediates.," *Biochemistry*, vol. 34, no. 32, pp. 10194–204, Aug. 1995.

[188] X. Yu and E. H. Egelman, "Structural data suggest that the active and inactive forms of the RecA filament are not simply interconvertible," *J. Mol. Biol.*, vol. 227, no. 1, pp. 334–346, 1992.

[189] A. Stasiak, E. Di Capua, and T. Koller, "Elongation of duplex DNA by recA protein.," *J. Mol. Biol.*, vol. 151, no. 3, pp. 557–64, Sep. 1981.

[190] P. Howard-Flanders, S. C. West, and A. Stasiak, "Role of RecA protein spiral filaments in genetic recombination.," *Nature*, vol. 309, no. 5965, pp. 215–9, 1984.

[191] J. Heuser and J. Griffith, "Visualization of RecA protein and its complexes with DNA by quick-freeze/deep-etch electron microscopy.," *J. Mol. Biol.*, vol. 210, no. 3, pp. 473–84, Dec. 1989.

## Résumé

Hautement conservé, de la bactérie jusqu'à l'Homme, la recombinaison homologue est indispensable à la survie de tout organisme vivant. Chez l'humain, la protéine hRad51 (human Rad51) y joue un rôle clé en s'autoassemblant au site de cassure sur les extrémités simple-brin d'une molécule d'ADN endommagée pour former le filament nucléoprotéique. Ce filament est capable à lui seul d'effectuer la plupart des opérations nécessaires au bon déroulement de la recombinaison homologue; il va permettre la reconnaissance d'homologie, l'appariement des séquences homologues et l'invasion de brins requise pour la synthèse de l'ADN manquant.

La recombinaison homologue est un processus complexe impliquant de multiples partenaires. Pour mieux comprendre le rôle du filament nucléoprotéique au sein de la réaction, on se propose d'étudier ce dernier en l'absence de tout partenaire. Plus précisément, on observe le comportement mécanique de filaments hRad51-ADNdb en fonction des conditions chimiques.

La formation du filament nucléoprotéique modifie la conformation de l'ADN sur lequel il s'assemble, l'allongeant de 50% et le déroulant de 43% dans le cas d'une molécule double-brin. Les pinces magnétiques sont un outil permettant de contrôler la force et la torsion appliquées à une unique molécule d'ADN double-brin (ADNdb), elles sont donc l'outil idéal pour sonder les propriétés mécaniques de filaments nucléoprotéiques. Le système des pinces magnétiques a été modifié afin de mesurer des paramètres mécaniques précédemment inaccessibles tel que le couple ressenti ou exercé par le filament. Le but de cette thèse a été d'étudier les propriétés mécano-chimiques des filaments nucléoprotéiques tout en essayant de tracer le paysage énergétique qui régit les transitions de ces systèmes.


## Abstract

Highly conserved throughout the species, homologous recombination is crucial to the survival of any living organism. In humans, the hRad51 protein (human Rad51) plays a key role by self-assembling at the break site on the single stranded extremities of damaged DNA molecules thus forming the nucleoprotein filament. This filament is able by itself to accomplish most of the necessary operations of homologous recombination; it allows the homology search, the pairing of the homologous sequences and the strand exchange.

Homologous recombination is a complex process involving many partners. In order to better understand the role of the nucleoprotein filament in this process, we propose to study it in the absence of any partners. We will focus on the study of the mechanical properties of hRad51-dsDNA filaments as a function of chemical conditions.

The formation of the nucleoprotein filament modifies the conformation of the DNA molecule on which it assembles, stretching it by 50% and unwinding it by 43% in the case of a double stranded DNA. The magnetic tweezers are a tool allowing the control of the force and torsion applied to a single dsDNA molecule; they are therefore the ideal tool to probe the mechanical properties of nucleoprotein filaments. We modified the magnetic tweezers as to allow the measurement of previously inaccessible mechanical parameters such as the torque applied or felt by the filament. The goal of this thesis has been to study the mechano-chemical properties of nucleoprotein filaments while drawing the energy landscape that governs the various transitions of these systems.